

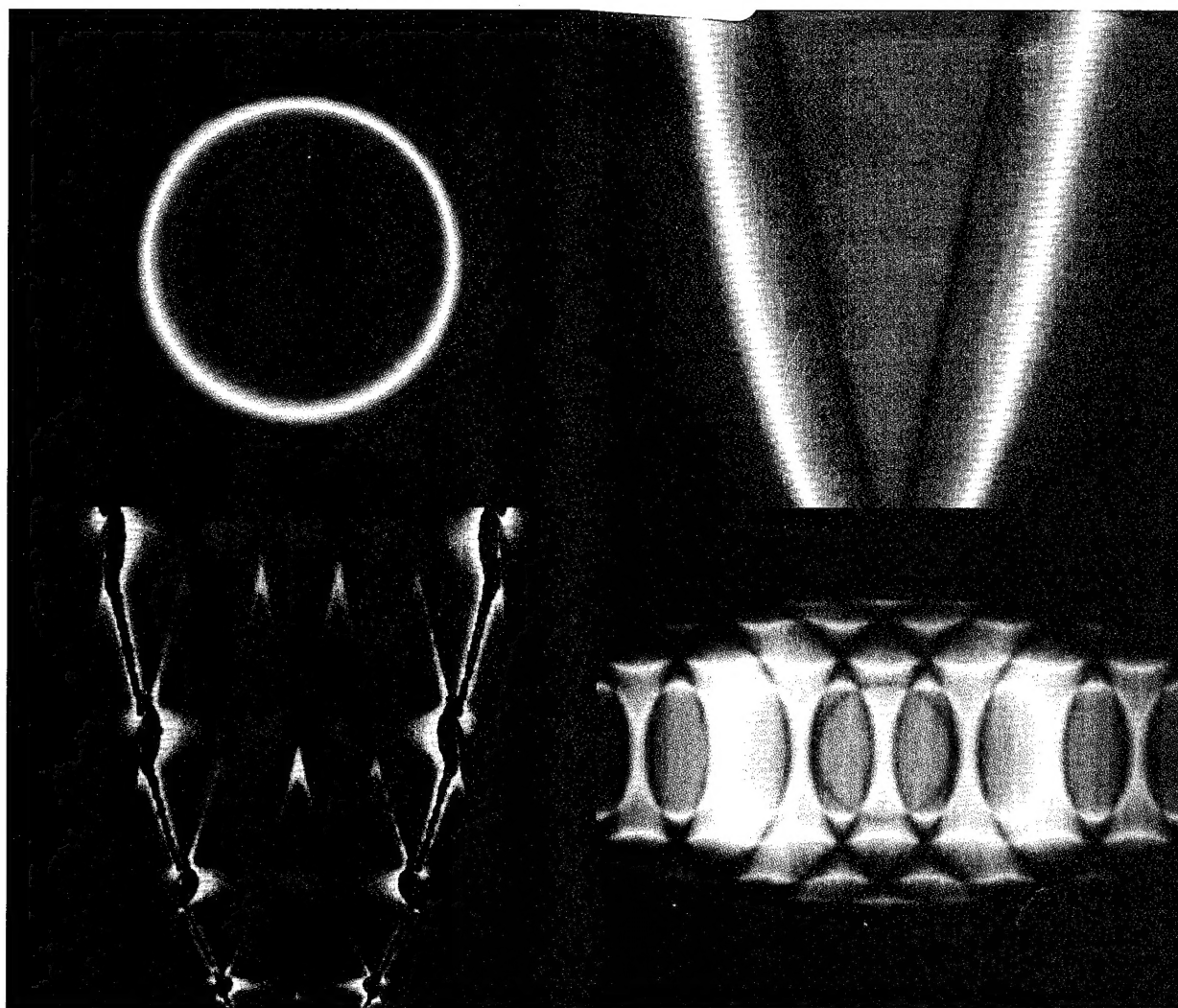
Naval Undersea Warfare Center Division Newport

Technical Digest

June 1995

19951113 010

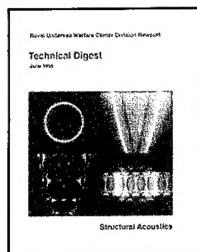
NAVY
SECRETARY
OFFICE
B



Structural Acoustics

NAVY
SECRETARY
OFFICE
B

NAVY
SECRETARY
OFFICE
B



The cover illustrations depict the wavevector-frequency spectra of unstiffened and stiffened fluid-loaded plates. Responses of periodically rib-stiffened plates to line (left) and point (right) force excitations are shown in the lower figures. The upper figures correspond to the structural response of unstiffened plates. (See "Structural and Acoustic Response of Stiffened Plates," by Dr. Benjamin A. Cray, page 16.)

Editorial Board

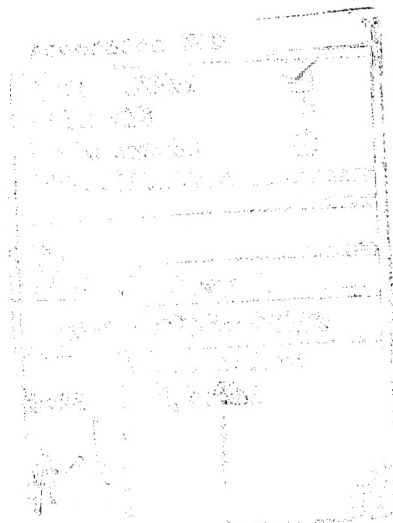
Dr. Richard H. Nadolink, Chairman
 Dr. Ding Lee
 Dr. James C. S. Meng
 Dr. Albert H. Nuttall
 Dr. Norman L. Owsley
 Dr. Bruce E. Sandman
 Dr. Paul D. Scully-Power

Guest Editor

Dr. Azriel Harari

Managing Editor

Ms. Mary A. Cowell



THE NAVAL UNDERSEA WARFARE CENTER (NUWC) DIVISION, Newport, RI, provides research, development, test and evaluation, engineering, and Fleet support for submarines, autonomous underwater systems, undersea offensive and defensive weapon systems, and countermeasures associated with undersea warfare. Through its **Technical Digest**, NUWC Division Newport reports on progress and innovations in its mission-related programs, as well as on breakthroughs in science and technology. In addition, the **Digest** devotes a special section to selected test facilities operated by Division Newport and available to the scientific community. Written by Division scientists and engineers, the **Digest's** articles focus on selected research and development efforts and on unique Division facilities, capabilities, and accomplishments.

Correspondence concerning the **Technical Digest** should be addressed to:

Naval Undersea Warfare Center Division Newport
 Director for Science and Technology
 1176 Howell Street
 Newport, RI 02841-1708
 Tel: (401) 841-6760

Approved for public release; distribution is unlimited.

Naval Undersea Warfare Center Division Newport

Technical Digest

June 1995

- 1 Guest Editor's Introduction

Azriel Harari

STRUCTURAL ACOUSTICS

- 7 Analytical and Experimental
Determination of the Vibration and
Pressure Radiation from a Submerged,
Stiffened, Cylindrical Shell with Two
End Plates

*Azriel Harari,
Bruce E. Sandman, and
John A. Zaldonis **

- 16 Structural and Acoustic Response
of Stiffened Plates

Benjamin A. Cray

- 22 An Overview of Developments
in Computational Fluid-
Structure Interaction

*Donald L. Cox, Robert T. Chapman,
Anthony J. Kalinowski, and
Jayant S. Patel*

- 41 Turbulent Flow Noise Estimates for Hull
Arrays

Sunghwan Ko

- 60 Compressive Strength of Continuous Fiber-
Reinforced Composite Components in the
Hydrospace Environment

*Francis C. Spicola and
Neil J. DuBois*

- 65 Simplified Structural Acoustic
Characterization of External
Compliant Coatings on Submerged
Surfaces

*Bruce E. Sandman and
Jeffrey E. Boisvert*

- 72 Considerations on the Use of Advanced
Materials in a Marine Environment

Wayne C. Tucker

- 79 Low Frequency Target Physics

Carlos M. Godoy

- 82 The Modal Decomposition of an Impedance Tube

Andrew J. Hull

ACOUSTIC FACILITIES

- 97 Target Response Measurement System (TRMS)

David M. Deveau

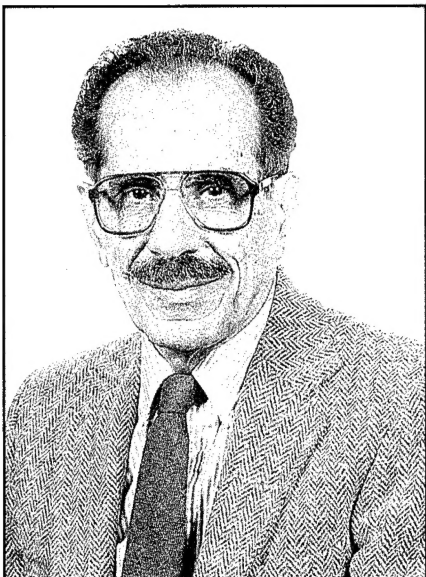
- 104 Acoustic Test Facility

- 106 Acoustic Wind Tunnel

- 108 Anechoic Chamber

- 110 Materials Analysis Laboratory

* John A. Zaldonis is a staff member of Westinghouse Electric Corporation



Guest Editor's Introduction

Azriel Harari is a member of the Advanced Technology Division at the Naval Undersea Warfare Center Division Newport. Since joining the organization in 1974, he has become one of the Division's key technologists in the areas of shell vibration, acoustic radiation from submerged structures, fluid/structure interaction analysis, buckling of deep submerged vehicles, and nonlinear shell vibration. In his present position, Dr. Harari is responsible for establishing fundamental theoretical concepts for advanced torpedo technology, including composite and laminated shells with surface coatings. He is also responsible for analyzing and predicting the performance of active surface vibration control to reduce radiated noise from the torpedo.

Dr. Harari's previous work at the Division involved analyzing vibration and acoustic radiation from composite and laminated shells, nonlinear vibration of shells under pressure, transmission of noise via the hull of the torpedo, and radiation from hull-mounted transducers.

Dr. Harari has been recognized for his accomplishments through many publication awards, performance awards, letters of appreciation, and commendations. In 1985, he received the NUSC (NUWC Division Newport's predecessor

organization) Science Award for his contributions to the theoretical mathematical modeling of turbulent flow and fluid-structure interaction.

He has published 25 journal articles in the areas of structural mechanics and acoustics and has presented numerous scientific papers at engineering conferences and international symposia, including several invited papers at Acoustical Society of America meetings. In addition, Dr. Harari has produced many computer codes for analysis in his area of expertise. In 1989, he received a patent for his invention titled "Semi-Active Self-Noise Reducer," which reduces self-noise interference with the functioning of the torpedo's transducer. He is a member of the American Society of Mechanical Engineers. Dr. Harari received his Bachelor of Science degree and his Master of Science degree in Structural Engineering from Technion, Israel Institute of Technology. He earned a Ph.D. degree in Engineering Mechanics from Columbia University.

• • •

The theme of this issue of the Naval Undersea Warfare Center Division Newport's *Technical Digest* is structural acoustics and composite structures. Structural acoustics is that field of physics dealing with the propagation of time-wise varying motion in solid bodies and their interaction with acoustic media. The practical application of structural acoustics is in noise control. The problems in this area of engineering science are complex because, unlike acoustic fluids, there are two types of propagating waves in solids. Additional complexity is introduced by the geometric shape of the structures. For submerged structures, the fluid/structure interface requires additional conditions that must be imposed before a solution can be found. The subjects covered in this issue are radiation, scattering, self-noise, target physics, turbulent flow excitation, and composite structures. Composite materials are included because they play an important role in many marine structures. The topics are intended to be instructive and address the

fundamental physical issues useful to the design of underwater vehicles. In addition to the theoretical articles presented, the *Digest* devotes a special section to selected test facilities operated by Division Newport and available to the scientific community. These test facilities explore/validate concepts, theories, and analyses developed at Division Newport and provide an essential link in the process that starts with an idea and ends with hardware.

Reduction of pressure radiation from submerged vehicles is important to the mission of the torpedo and submarine, while the study of mobility transfer is important to the functioning of the instruments on the vehicle. The article by Harari, Sandman, and Zaldonis describes an analysis and experimental validation of a vibration and radiation model of a torpedo shell. The analysis and the testing are a product of a joint effort between NUWC and Westinghouse Electric Corporation on active cancellation of torpedo radiated noise.

Division Newport developed the analytical model and Westinghouse conducted the test at their Naval System Division's test lake.

The article by Cray investigates the feasibility of using stiffened plates as underwater sound projectors. Theoretical models have shown that strong directional radiation can be achieved at low frequencies by adjusting the stiffener spacing and plate thickness.

Acoustic modeling is of fundamental importance to the Navy. In addition to the analytical models, Division Newport has developed several finite element programs to address many complicated problems. The article by Cox, Chapman, Kalinowski, and Patel describes three of these general analysis tools.

Flow-induced noise interferes with the functioning of hydrophone arrays mounted on the ship's hull. The article by Ko describes a method to lower the flow noise using wavenumber filters, such as a finite hydrophone, an array of hydrophones, and a layer of elastomer.

Composite materials can produce lightweight structural elements. The ability of composite materials to withstand stress is essential data to any designer of a structure made from composites. One of the difficult problems regarding the structural integrity of composite materials is the compressive strength of thick structural elements and the microbuckling of the fiber. The compressive strength of composite structures and microbuckling of the fiber is discussed in the article by Spicola and DuBois.

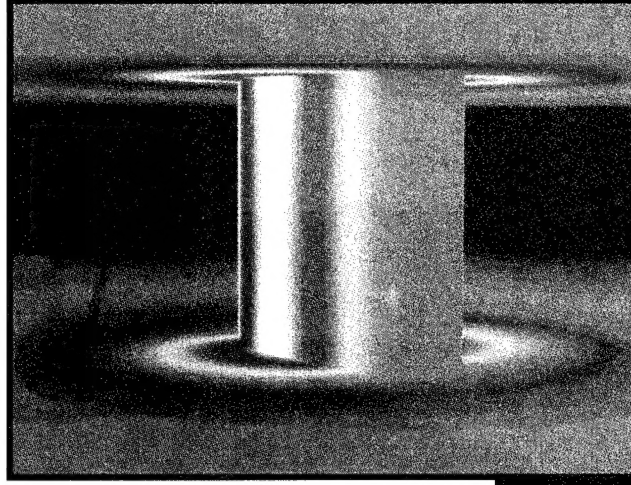
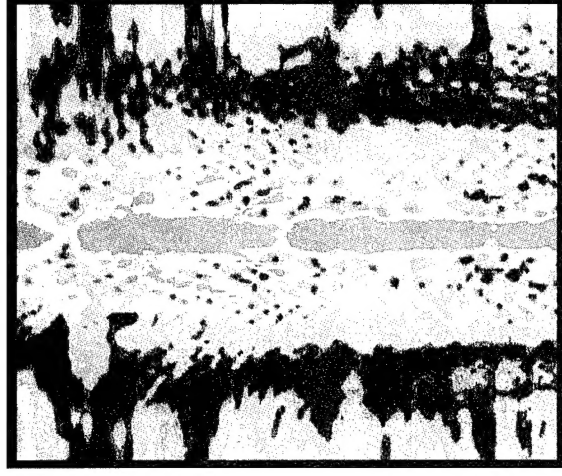
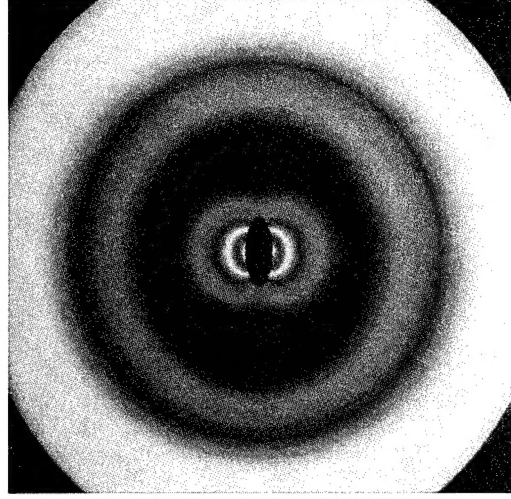
Experimental and theoretical analysis has demonstrated that the introduction of a compliant layer at the interface between the structure and the fluid medium provides a substantial reduction in radiated noise. The article by Sandman and Boisvert derives the appropriate equations in a simplified first-order analysis that identifies the essential parameters governing external compliant coating performance.

Glass-reinforced plastic has a substantial history of use in seawater. With the advent of high performance graphite fibers offering greater stiffness than glass, some marine applications may be implemented where glass was unsuitable. The article by Tucker discusses the problems associated with the nobility of graphite in the galvanic series.


Target physics is a branch of structural acoustics that studies the detection and classification of submerged vehicles by insonifying the vehicle at selected frequencies. At low and intermediate frequencies, an elastic structure will absorb power from the incoming wave and reradiate it back into the acoustic medium. The article by Godoy investigates the path by which incident power gets into the submarine and studies mitigating solutions to the problem of acoustic power reradiation into the fluid.

Impedance tubes are commonly used for determining the acoustic impedance of a material, transmission loss, echo reduction, and for testing and calibrating of microphones. The article by Hull extends the modeling of impedance tubes by developing an eigenvalue-based model of the tube in modal space that can incorporate transient or steady-state response of velocity sources on the spatial domain and pressure sources at the end of the tube.

Division Newport has four primary test facilities for structural acoustics experiments that enable the scientific community to evaluate the acoustic and dynamic characteristics of underwater vehicles. The Acoustic Test Facility in Newport consists of a large test tank and associated support systems. It provides this capability to measure the acoustic characteristics of a complete underwater weapon system, as well as the individual system components. The Acoustic Wind Tunnel is capable of evaluating hydrodynamics parameters and hydroacoustics of full-scale tactical undersea vehicles. The Anechoic Chamber is used for research in active noise cancellation, target strength studies, acoustic directivity and measurement of the sound power level, and electromagnetic signature produced by full-scale small-diameter vehicles. The walls of the anechoic chamber are covered with acoustic wedges, which reduce the reflections to an extremely low level. Electromagnetic shielding is accomplished by surrounding the measurement volume with a contiguous metallic enclosure. The Materials Analysis Laboratory has the capacity to measure the dynamic properties of elastomers using the Metravib test machine. In addition to the above, it is involved in the study of corrosion and fatigue mechanisms as they pertain to Navy applications.



Structural Acoustics



The top figure on the divider is taken from "Low Frequency Target Physics," by Carlos M. Godoy (page 79). The middle figure and the bottom figure are taken from "An Overview of Developments in Computational Fluid-Structure Interaction," by Donald L. Cox, Robert T. Chapman, Anthony J. Kalinowski, and Jayant S. Patel (page 22).

Analytical and Experimental Determination of the Vibration and Pressure Radiation from a Submerged, Stiffened, Cylindrical Shell with Two End Plates

*Azriel Harari and Bruce E. Sandman
Naval Undersea Warfare Center Division Newport*

*John A. Zaldonis
Westinghouse Electric Corporation
Science and Technology Center*

Abstract

An analytical model of a finite, stiffened, cylindrical shell with two end plates submerged in fluid was developed. Results obtained for the pressure at various points in the fluid, as well as the drive point and transfer point acceleration, are compared with experimental results. Good agreement was found between the analytical and experimental results.

Introduction

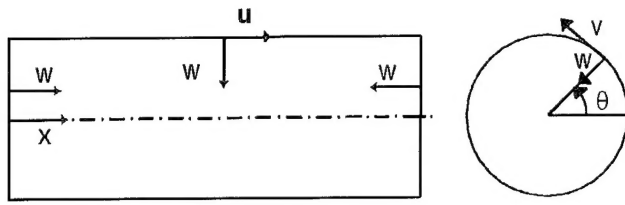
The analysis presented here uses classical techniques to find the vibration and acoustic radiation from a finite, stiffened, cylindrical shell with two end plates. This analysis considers Sanders-Koiter shell equations for the cylindrical part of the structure and classical bending and plane stress equations for the end plates and the rectangular stiffeners. The shell is excited by harmonic forces. The force acting on the shell may be a distributed force, a line force, or a discrete force, and it may have components in three directions and a moment in the axial direction. Shell displacements and the pressure on the surface of the shell are expanded by Fourier series in the circumferential direction. Because the structure is axisymmetric and the fluid infinite, the solution can be found for each circumferential mode separately. The shell is segmented at each stiffener location and at any location where a discrete force is acting. End plates are also segmented if a discrete force is acting on one of the plates. Homogeneous and particular solutions are found for each segment of the shell and the end plates. Values are found for the constants associated with the homogeneous solution by enforcing the boundary condition between the various structural elements. The boundary conditions between the various structural elements are the continuity of displacements/rotation and balance of forces/moment at each interface. Fluid loading is approximated by considering a cylindrical cavity with rigid extensions for the fluid loading of the cylindrical part of the surface and a half-space with a rigid extension for the fluid loading on the end plates. This approximation neglects the

interaction between the cylindrical surface and the two end surfaces via the fluid. For the purpose of solving the fluid/structure interaction problem, the normal to the surface displacement and the pressure on the shell are expanded by orthogonal surface functions, and the interaction is solved in terms of the coefficients of the expansion. Once the coefficients of the expansion are found, the displacement/velocity of the shell or the pressure anywhere in the fluid can be found. The analysis in this article is an extension of previous papers by the authors [1]-[3].

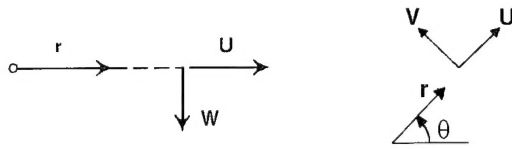
Cylindrical Shell Analysis

Consider a thin cylindrical shell of thickness h and mean radius a . The midsurface of the shell is described in terms of an (x, θ) coordinate system, with the x coordinate being taken in the axial direction of the shell and the θ coordinate in the circumferential direction. The components of the midsurface of the shell are designated by u , v , w (see Figure 1). The equations of shell motion governing u , v , and w are the Sanders-Koiter shell equations. The shell displacements are expanded in the Fourier series:

$$\begin{aligned} w(x, \theta, t) &= \sum_{n=0}^{\infty} w_n(x) \cos(n\theta) e^{i\omega t}, \\ u(x, \theta, t) &= \sum_{n=0}^{\infty} u_n(x) \cos(n\theta) e^{i\omega t}, \\ v(x, \theta, t) &= \sum_{n=0}^{\infty} v_n(x) \sin(n\theta) e^{i\omega t}. \end{aligned} \quad (1)$$



(a) Cylindrical Shell and End Plates



(b) Plate

Figure 1. Shell and Plate Coordinates and Displacements

Because the shell is axisymmetric, the circumferential modes are uncoupled and the solution can be found for each circumferential mode separately. For the purpose of this analysis, the shell is divided into separate segments at each stiffener location and at the location where the force is applied.

The equations of plate motion are the plate classical bending equations and the plate classical plane stress equation. The plate displacements are expanded similarly in the Fourier series:

$$\begin{aligned} w(r, \theta, t) &= \sum_{n=0}^{\infty} w_n(r) \cos(n\theta) e^{i\omega t} , \\ u(r, \theta, t) &= \sum_{n=0}^{\infty} u_n(r) \cos(n\theta) e^{i\omega t} , \\ v(r, \theta, t) &= \sum_{n=0}^{\infty} v_n(r) \sin(n\theta) e^{i\omega t} . \end{aligned} \quad (2)$$

Boundary Conditions

Let D and S be four-element column matrices describing the displacements and the stress resultants that are to be specified on the boundary $x=\text{const.}$ of the cylindrical shell or $r=\text{const.}$ on the plate, respectively. Let the subscript c or p indicate association with the cylindrical shell or the plate, respectively. The column matrices associated with the cylindrical shell are

$$D_c = \begin{bmatrix} w & u & v & a \frac{dw}{dx} \end{bmatrix}^T ,$$

$$S_c = \begin{bmatrix} Q & N_x & N & M_x \end{bmatrix}^T . \quad (3)$$

The column matrices associated with the plate are

$$\begin{aligned} D_p &= \begin{bmatrix} w & U & V & a \frac{dw}{dr} \end{bmatrix}^T , \\ S_p &= \begin{bmatrix} Q & N_r & N & \frac{M_r}{a} \end{bmatrix}^T . \end{aligned} \quad (4)$$

The boundary condition enforces the continuity of displacements and balance of forces at each interface and is written in terms of the matrices D and S described above, where the value of the elements of each matrix is composed of the homogeneous and the particular solutions. The superscripts L and R indicate that the displacement matrix D or the stress resultant matrix S is associated with the segment to the left or to the right of the interface between the two segments.

Line Force Boundary Condition. The boundary condition for a line force excitation can be written as follows:

$$\begin{aligned} D_c^L - D_c^R &= 0 , \\ S_c^L - S_c^R &= F_n , \end{aligned} \quad (5)$$

where F_n is a four-element column matrix whose elements are the n^{th} Fourier components in the circumferential direction of the forces in the normal, axial, and circumferential direction, and the moment in the axial direction:

$$F_n = \begin{bmatrix} f_w & f_u & f_v & m \end{bmatrix}^T . \quad (6)$$

Cylindrical Shell/End Plate Boundary Condition. The boundary condition between the cylindrical shell and end plate on the left side is

$$\begin{aligned} D_c^R - OD_p &= 0 , \\ S_c^R - OS_p &= 0 ; \end{aligned} \quad (7)$$

the boundary condition between the cylindrical shell and the end plate on the right side is

$$\begin{aligned} D_c^L - \bar{O}D_p &= 0 , \\ S_c^L + \bar{O}S_p &= 0 , \end{aligned} \quad (8)$$

where O and \bar{O} are 4×4 matrices defined as follows:

$$O = \begin{bmatrix} 0 & -1 & 0 & 0 \\ 1 & 0 & 0 & 0 \\ 0 & 0 & 1 & 0 \\ 0 & 0 & 0 & 1 \end{bmatrix}, \quad \bar{O} = \begin{bmatrix} 0 & -1 & 0 & 0 \\ 1 & 0 & 0 & 0 \\ 0 & 0 & 1 & 0 \\ 0 & 0 & 0 & 1 \end{bmatrix}. \quad (9)$$

Stiffener Boundary Condition. The boundary condition at each stiffener junction on the cylindrical shell is as follows:

$$D_c^L - D_c^R = 0, \quad S_c^L - S_c^R + ZD^R = 0, \quad (10)$$

where Z is a 4×4 impedance matrix associated with the stiffener [1].

Change of Thickness/Material Boundary Condition. The boundary condition at a discrete change of thickness or material properties is as follows:

$$D^L - D^R = 0, \quad S^L - S^R = 0. \quad (11)$$

Solution to the Shell Equations

The shell is segmented at each stiffener location and at the location where a discrete force is acting on the shell. The end plates are also segmented if a discrete force is acting on one of the end plates. The homogeneous and the particular solutions are found for each segment of the shell or end plates. Each segment of the shell contains eight unknown constants. The end plate segment that contains the origin has four unknown constants, because the singular solutions are omitted. Enforcing the boundary condition between the segments of the structure leads to a set of nonhomogeneous algebraic equations,

$$BC = A, \quad (12)$$

where B is a square matrix containing the elements associated with the homogeneous equations of the shell and plate, C is a column matrix containing the unknown constants, and A is a column matrix containing the contribution of the particular solutions and the discrete forces on the cylindrical

shell or end plates. There are eight constants associated with each segment of the cylindrical shell and end plates. The inner plate has four constants, because the singular solutions are omitted. Once the solution to Eq. (12) is found and the matrix C is obtained, the displacements on the shell or the end plates can be determined.

Fourier/Bessel Spatial Decomposition of the Shell Mobility and the Fluid Cavity Impedance

For the purpose of solving the fluid/structure interaction problem, the normal to the surface displacement and the normal to the surface force/pressure are expanded in the following manner:

$$w(s, \theta) = \sum_{n=0}^{\infty} \sum_{i=1}^I a_{ni} \varphi_{ni}(s, \theta), \quad f(s, \theta) = \sum_{n=0}^{\infty} \sum_{i=1}^I b_{ni} \varphi_{ni}(s, \theta), \quad \varphi_{ni}(s, \theta) = \psi_i(s) \cos(n\theta), \quad (13)$$

where s is a general surface coordinate along the generator line of the axisymmetric structure, a_{ni} and b_{ni} are constants, $I = I_1 + I_2 + I_3$ is the sum of three integer constants, and the functions $\psi_i(s)$ are defined below.

For $1 \leq i \leq I_1$, $m = i - 1$:

$$\psi_i(s) = \begin{cases} \cos\left(\frac{m\pi x}{L}\right) & \text{on the cylindrical shell} \\ 0 & \text{elsewhere} \end{cases}$$

For $I_1 < i \leq I_1 + I_2$, $k = i - I_1$:

$$\psi_i(s) = \begin{cases} J_n\left(\lambda_k \frac{r}{a}\right) & \text{on the left plate} \\ 0 & \text{elsewhere} \end{cases}$$

For $I_1 + I_2 < i \leq I_1 + I_2 + I_3$, $k = i - (I_1 + I_2)$:

$$\psi_i(s) = \begin{cases} J_n\left(\lambda_k \frac{r}{a}\right) & \text{on the right plate} \\ 0 & \text{elsewhere} \end{cases}. \quad (14)$$

The constants λ_k are the zero roots of $J_n(\lambda)$.

The functions φ_{ni} are orthogonal over the surface A of the shell:

$$\int_A \varphi_{ni}(s, \theta) \varphi_{mj}(s, \theta) dA = 0, \quad \text{for } n \neq m \text{ or } i \neq j. \quad (15)$$

The value of the Fourier/Bessel coefficients a_{ni} and b_{nj} can be obtained by multiplying both sides of Eq. (13) by φ_{ni} and integrating over the entire surface of the shell:

$$a_{nj} = \frac{\int_A w(s, \theta) \varphi_{nj}(s, \theta) dA}{\int_A \varphi_{nj}^2(s, \theta) dA}, \quad b_{nj} = \frac{\int_A f(s, \theta) \varphi_{nj}(s, \theta) dA}{\int_A \varphi_{nj}^2(s, \theta) dA}. \quad (16)$$

Fourier/Bessel Decomposition of the Shell Mobility Matrix

Let F_n and W_n be column matrices containing the Fourier/Bessel coefficients of a force $f(x, \theta)$ acting normal to the surface of the shell and the coefficients of the displacement $w(x, \theta)$, Eq. (16), respectively. The subscript n indicates association with the n^{th} circumferential mode. Let G_n be a matrix whose elements relate the Fourier/Bessel coefficients of the displacement $w(x, \theta)$ and the coefficients of the force $f(x, \theta)$:

$$W_n = G_n F_n. \quad (17)$$

The elements g_{ik} of the matrix G_n are obtained by finding, in the manner described previously, the response of the shell to excitation by a force $f(x, \theta)$ that is spatially described by the functions $\varphi_{nk}(x, \theta)$ and calculating the Fourier/Bessel coefficients a_{ni} of the displacement $w(x, \theta)$. The matrix G_n is obtained here for forces normal to the surface for the purpose of solving the fluid/structure interaction problem.

Fourier/Bessel Decomposition of the Cylindrical Cavity Impedance Matrix

Let P_n be a column matrix containing the coefficients of the Fourier/Bessel expansion of the pressure on the surface of the fluid cavity. Let H be the impedance matrix of the fluid cavity whose elements relate the Fourier/Bessel coefficients of the displacement w and the coefficients of the pressure p on the shell surface for the n^{th} circumferential mode:

$$P_n = H_n W_n. \quad (18)$$

The elements h_{ik} of the matrix H_n are obtained by finding the pressure p on the surface of the cavity due to a prescribed displacement distribution described by the functions φ_{nk} and calculating the Fourier/Bessel coefficients b_{ni} of the pressure p . The elements of the matrix H are approximated here by neglecting the cross influence between the cylindrical surface of the shell and the end plate surfaces. This is accomplished by considering a cylindrical cavity with rigid extensions for the vibration of the cylindrical surface and a half-space configuration that consists of a circular vibrating surface with a rigid extension for each end of the cylindrical cavity.

Solution to the Fluid/Structure Interaction Problem

Let W_n^o be a column matrix whose elements are the Fourier/Bessel coefficients of $w(x, \theta)$ for a shell in a vacuum that is excited by arbitrary forces. (The solution for the response of the shell in a vacuum to excitation by arbitrary forces was given earlier in this article.) For the special case where all the forces acting on the shell are normal to the surface of the shell, W_n^o can be calculated by using the matrix G_n :

$$W_n^o = G_n F_n, \quad (19)$$

where F_n is a column matrix containing the coefficients of the Fourier/Bessel expansion of the excitation forces.

Let W_n be a column matrix whose elements are the Fourier/Bessel coefficients of $w(x, \theta)$ for the submerged shell. The response of the submerged shell can be written as

$$W_n = G_n P_n + W_n^o, \quad (20)$$

where P_n is a column matrix containing the coefficients of the Fourier/Bessel expansion of the pressure on the surface of the shell. By eliminating P_n from Eqs. (20) and (18), one obtains the solution to the fluid/structure interaction problem:

$$W_n = (I - GH)^{-1} W_n^o. \quad (21)$$

Once the column matrix W_n is found, the displacements on the shell and the pressure anywhere in the fluid can be found.

Power Output from the Shell

Power output from the shell is found by integrating the time-averaged product of the

pressure and the velocity on the surface of the shell. For a shell without structural damping, the total power output from the shell is equal to the input power of the excitation force. The equality of the input and output power is used here to check the accuracy of the numerical calculations. For the purpose of conducting parametric studies, such as the effects of various geometric and material properties or various forcing functions on pressure radiation from the shell, it is beneficial to construct one entity that represents the average pressure radiation from the shell. The entity suggested here is the *equivalent spherical spreading pressure*, which gives a measure of the average pressure radiation from the shell and is obtained from a simple source that has the same total power output as the shell.

Numerical Calculation and Experimental Results

Numerical calculations and an experimental test were conducted on a submerged cylindrical shell with two end plates. The experimental test was conducted by the Westinghouse Electric Corporation at its Naval System Division's test lake at Columbia Station, OH. The geometric description of the shell and position of the accelerometers are shown in Figure 2. The force F_1 is acting normal to the surface of the shell on the middle stiffener. The material properties of the cylindrical shell and the two end plates are those of aluminum. The accelerometers in Figure 2 are marked as A_k , $k = 1, 6$, and the circumferential angle θ of the accelerometers is marked in the figure for all cases where $\theta \neq 0$. The excitation force is at $\theta = 0$. Figure 3 shows the location of the two hydrophones P_1 and P_2 . The circumferential angle of hydrophone P_1 is $\theta = 0$, while hydrophone P_2 is located on the axis of the shell. Figure 4 compares the numerically calculated pressure of hydrophone P_1 with the experimentally obtained values. Figure 5 compares the *equivalent spherical spreading pressure*, described previously, with the test results at hydrophones P_1 and P_2 . The

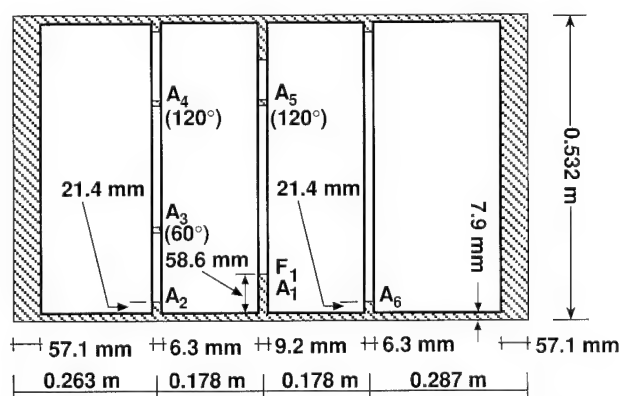


Figure 2. Shell Data and Accelerometer Positions Used in the Test

pressure was evaluated at the same distance from the center of the shell as hydrophones P_1 and P_2 . The results in Figure 5 show that the *equivalent spherical spreading pressure* is a valuable measure of the average pressure radiation from the shell. Figures 6 through 11 compare the acceleration at various points between the experimental results and the numerical calculation.

The second study performed was to determine the percentage of power emitted from the three surfaces of the shell, i.e., the cylindrical surface and the two end plate surfaces. The length of the shell considered for this study is $L = 2.54$ m, the shell radius is 0.254 m, and the shell thickness is $h = 5.08$ mm. The thickness of the end plates is $h = 0.051$ m, and the force is acting at a distance of $L/10$ from the left edge of the shell. The material properties of the shell and end plates are those of aluminum. The results of the study are shown in Figures 12 through 14. The two graphs in each figure divide the ordinate into three segments. The lower segment of the ordinate β_1 indicates the fraction of power output emitted from the left plate. The middle segment of the ordinate β_2 indicates the fraction of power from the cylindrical surface. The top segment of the ordinate β_3 indicates the fraction of power output from the right plate. Figure

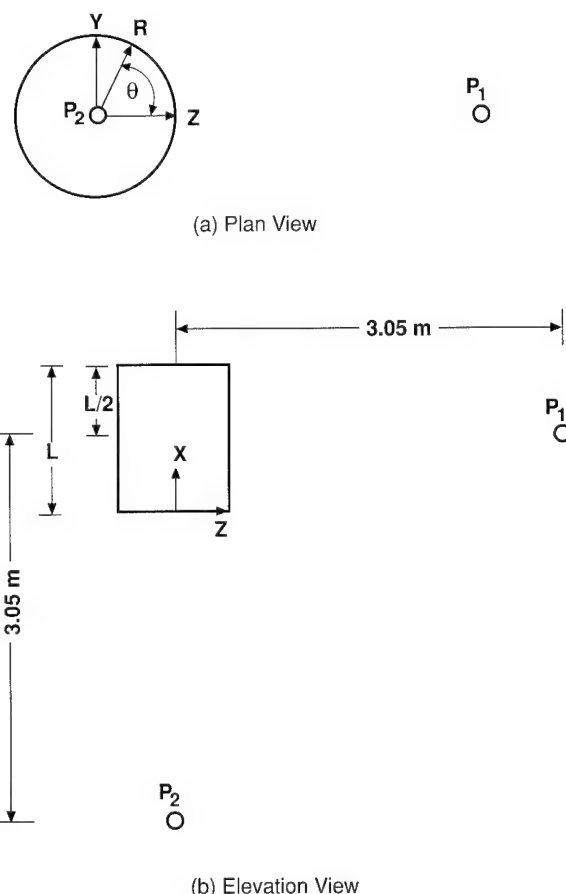


Figure 3. Location of Hydrophones P_1 and P_2

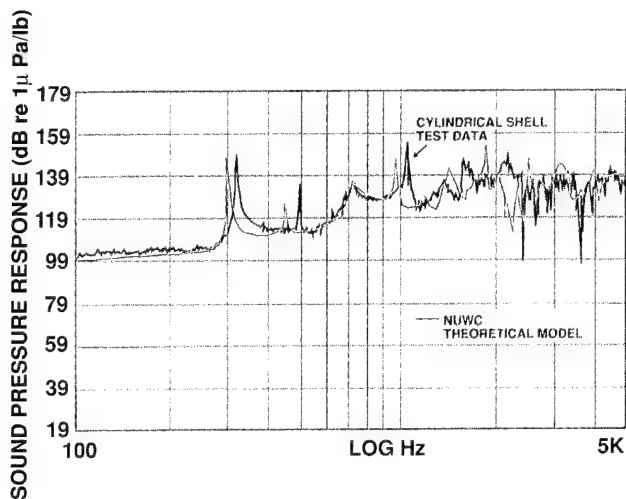


Figure 4. Comparison of the Experimental Test Data and the Numerical Calculation Results of the Pressure at Hydrophone P_1

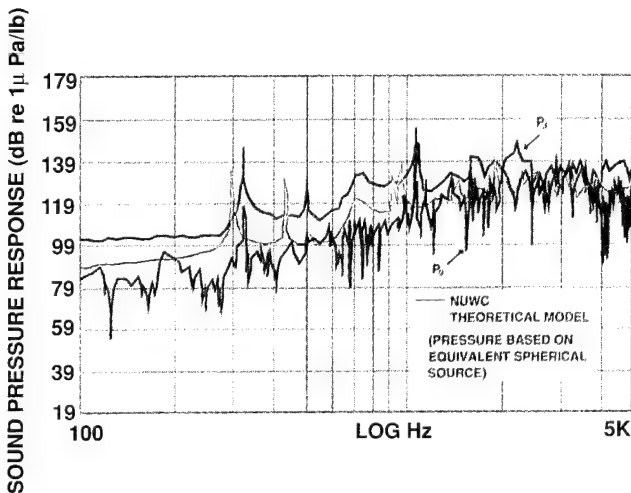


Figure 5. Comparison of the Equivalent Spherical Spreading Pressure Obtained by the Numerical Calculations and the Pressure at Hydrophones P_1 and P_2

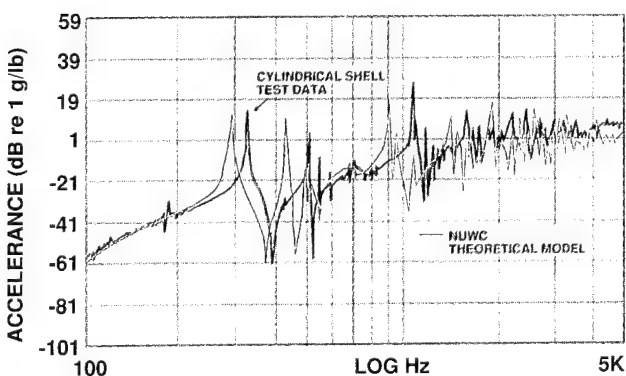


Figure 6. Comparison of the Experimental Test Data and the Numerical Calculation's Output of the Drive Point Acceleration at Point 1

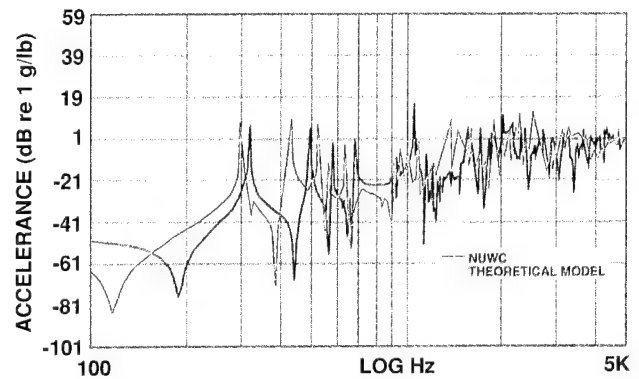


Figure 7. Comparison of the Experimental Test Data and the Numerical Calculation's Output of the Drive Point Acceleration at Point 2

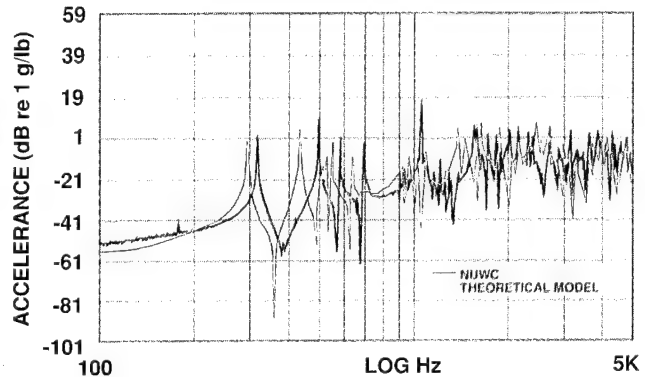


Figure 8. Comparison of the Experimental Test Data and the Numerical Calculation's Output of the Drive Point Acceleration at Point 3

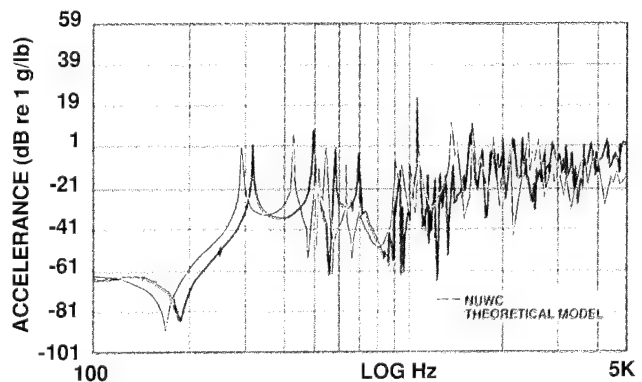


Figure 9. Comparison of the Experimental Test Data and the Numerical Calculation's Output of the Drive Point Acceleration at Point 4

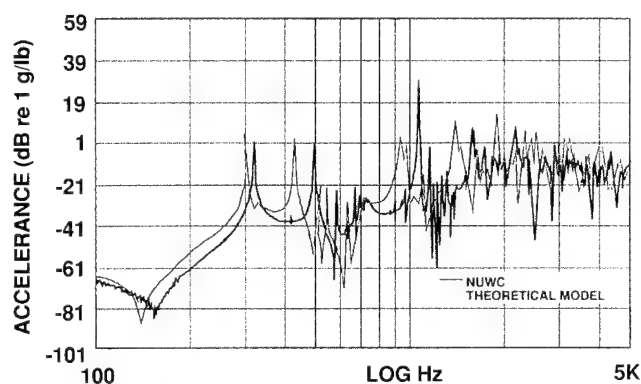


Figure 10. Comparison of the Experimental Test Data and the Numerical Calculation's Output of the Drive Point Acceleration at Point 5

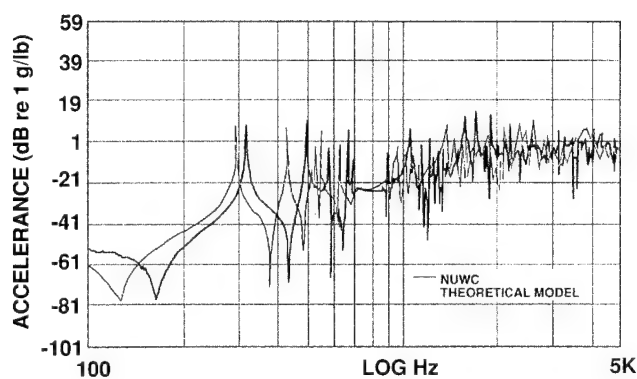


Figure 11. Comparison of the Experimental Test Data and the Numerical Calculation's Output of the Drive Point Acceleration at Point 6

12 shows the results for radial force excitation; Figure 13, for axial excitation; and Figure 14, for circumferential excitation. The results indicate that radiation from the end plates is substantial for axial excitation and that radiation from end plates cannot be neglected for circumferential excitation, except at low frequencies. For radial excitation, radiation from the end plates can be neglected, except at frequencies of the accordion mode. The effects of stiffeners and boundary condition on radiation from the shell are not discussed here; a partial account of these effects is presented in Harari and Sandman [4].

Conclusions

An analytical model of a finite, submerged, cylindrical shell with two end plates was developed. Results obtained from the analytical model were compared with an experimental test conducted by Westinghouse Electric Corporation. Numerical studies were conducted to find the relative importance of radiation from the end plates when compared with the radiation from the cylindrical part of the shell.

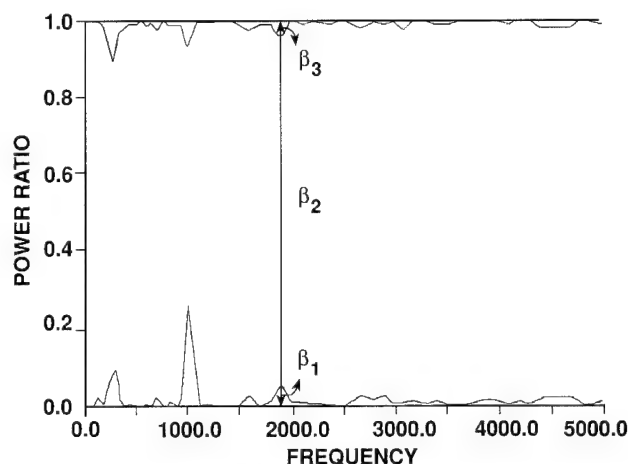


Figure 12. Ratios of Power Emitted from the Surface of the Cylindrical Shell and End Plates to the Total Power Emitted from the Shell due to Radial Force Excitation

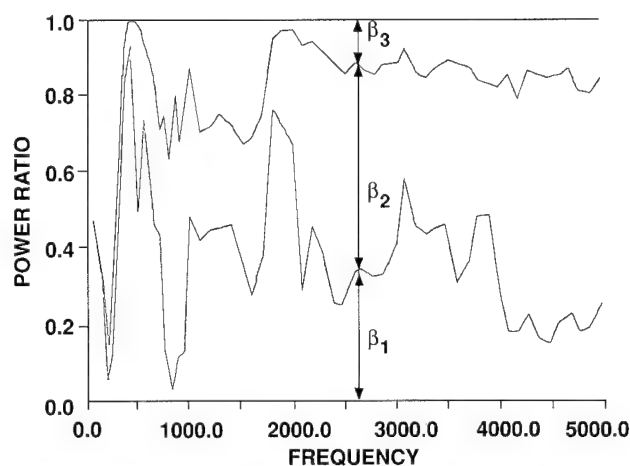


Figure 13. Ratios of Power Emitted from the Surface of the Cylindrical Shell and End Plates to the Total Power Emitted from the Shell due to Axial Force Excitation

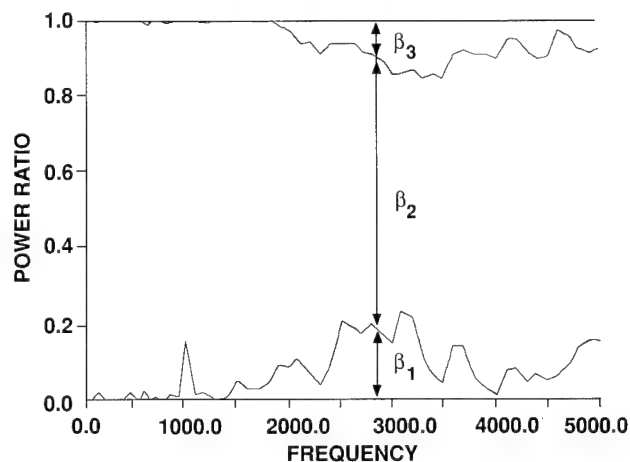


Figure 14. Ratios of Power Emitted from the Surface of the Cylindrical Shell and End Plates to the Total Power Emitted from the Shell due to Circumferential Force Excitation

Acknowledgments

The analytical and numerical work was supported by NUWC Division Newport's Independent Research/Independent Exploratory Development Program. The authors wish to thank the Westinghouse Electric Corporation Oceanic Division and Naval Systems Division for supporting the experimental measurements on the cylindrical shell in water.

References

- [1] A. Harari and B. E. Sandman, "Radiation and Vibrational Properties of Submerged Stiffened Cylindrical Shells," *Journal of the Acoustical Society of America*, vol. 88, 1990, pp. 1817-1830.
- [2] B. E. Sandman, "Numerical Fluid Loading Coefficients for the Modal Velocities of Cylindrical Shells," *Computational Structures*, vol. 6, 1976, pp. 467-473.
- [3] A. Harari and B. E. Sandman, "Vibratory Response of Laminated Cylindrical Shells Embedded in an Acoustic Fluid," *Journal of the Acoustical Society of America*, vol. 60, 1976, pp. 117-128.
- [4] A. Harari and B. E. Sandman, "The Role of Stiffeners in the Vibration and Acoustic Radiation of Submerged Cylindrical Shells," *Proceedings of the International Noise and Vibration Control Conference*, NOISE-93, St. Petersburg, Russia, vol. 5, 1993, pp. I33-I36.



AZRIEL HARARI is a member of the Structural Technology Branch in the Weapons Systems Directorate at NUWC Division Newport. Since joining the NUWC staff in 1974, he has become one of the Center's key technologists in the areas of shell vibration, acoustic radiation from submerged structures, fluid/structure interaction analysis, buckling of deep submerged vehi-

cles, and nonlinear shell vibration. In his present position, Dr. Harari is responsible for establishing fundamental theoretical concepts for advanced torpedo technology, including composite and laminated shells with surface coatings. Dr. Harari received his B.S. and M.S. degrees in Structural Engineering from Technion, Israel Institute of Technology. He earned a Ph.D. degree in Engineering Mechanics from Columbia University.



BRUCE E. SANDMAN is head of NUWC Division Newport's Advanced Technology Division. He directs broad programs of research and exploratory development in the areas of structureborne acoustic energy damping, flow-noise damping, and composite materials as they apply to the Navy's critical programs in torpedoes, missiles, submarine launching

systems, and submarine sonar systems. Dr. Sandman has published more than 40 scientific reports and journal articles in the areas of structural mechanics and acoustics and is an internationally recognized expert in flow-noise generation and structural noise propagation. He earned a B.S. degree in Mathematics from Cornell University, and a M.S. in Mechanical Engineering and a Ph.D. in Applied Mechanics from Kansas State University.



JOHN A. ZALDONIS is a senior engineer in the Dynamics and Acoustics section at the Westinghouse Science and Technology Center (formerly the R&D Center) in Pittsburgh. Since joining Westinghouse in 1980, Mr. Zaldonis has worked on various analytical and experimental investigations. His analytical work examines active structural/acoustic

control (ASAC) of submerged structures, torpedo propulsion system noise transmission paths, and sonar array self-noise. Other areas of interest include combustion induced oscillation and modeling the dynamics of various other Westinghouse products. His experimental work examines flow-induced vibration, low cycle fatigue, and damping treatment performance. He has also measured transfer functions (structural and acoustic) on a submerged cylindrical shell in support of his ASAC modeling. Mr. Zaldonis earned his B.S. degree in Engineering Science from Pennsylvania State University (1980) and his M.S. degree in Mechanical Engineering from Carnegie-Mellon University (1986).

Structural and Acoustic Response of Stiffened Plates

Benjamin A. Cray
Naval Undersea Warfare Center Division Newport

Abstract

A summary of the analytical methods used to study the structural and acoustic behavior of rib-stiffened plates is presented. Common results from these models are discussed; in particular, Bragg diffraction patterns are presented for line and point force excitations of fluid-loaded plates. Expressions dependent on the Bloch wavenumber, the wavenumber associated with the bay length spacing between stiffeners, are shown in detail. A formulation is given for deriving the farfield acoustic radiation from periodic, rib-stiffened plates of infinite extent. The theoretical formulation accounts for fluid loading and allows the stiffeners to exert both reactive forces and angular moments upon the plate, though the results presented consider reactive forces only. A preliminary investigation of the feasibility of using stiffened plates as efficient, low frequency (far below the critical frequency), underwater sound projectors is considered. Theoretical models for both infinite and finite stiffened plates have shown that strong directional radiation can be achieved at low frequency by adjusting the stiffener spacing and plate thickness. The investigation determined that a finite, periodically stiffened plate can have farfield sound pressure levels 25 dB greater than those of a comparable unribbed plate. These levels were obtained at low frequency and with relatively high radiation efficiency.

Introduction

Many engineered structures, such as aircraft cabins and submarine pressure hulls, are composed of rib-stiffened plates or stiffened cylindrical shells. Consequently, considerable effort has been made to understand how these structures respond to dynamic excitation. Typically, these engineered structures have support beams or stiffeners attached in a periodic arrangement, even though structural integrity may be maintained without periodic stiffening. Hence, the vibrational and sound radiation characteristics of periodically stiffened structures have been a subject of investigation for many years [1]-[4].

Recently, researchers have examined arbitrarily or nonperiodic stiffened structures of finite and infinite extent [5]-[8]. Maidanik [5] and Photiadis [6] studied localization phenomena on free wave propagation and on scattering of acoustic waves from fluid-loaded, irregularly stiffened, infinite plates. The analysis requires that the stiffened structure have extended disorder, i.e., the distance from stiffener to stiffener be randomly perturbed by a relatively small amount about a mean periodic spacing over a significant distance. The results predict that even a small amount of disorder can produce significant normal mode localization. Essentially, localization may be considered as an additional mechanism for damping the spatial

vibration of a stiffened system. Therefore, the spatial vibrations of a rib-stiffened structure will decay with distance from the point of excitation due to both structural damping and, if not perfectly periodic, vibrational confinement or localization.

Cray [7] examined the sound radiation from an infinite plate having sectionally aperiodic attached stiffeners. A companion study was completed by Keltie [8] of a finite, fluid-loaded plate with completely arbitrary attached rib stiffeners. All of these analytical models revealed that periodically stiffened plates exhibited *stop band* behavior, frequency regions at which propagating waves could not exist. Similarly, *pass bands* existed where waves would propagate unattenuated.

The analytical models used to investigate stiffened structures are frequently based on theoretical formulations that assume thin, isotropic structures. For plates, the transverse motion is assumed to be governed by the Euler-Bernoulli equation of motion. Typically, the plates or cylindrical shells are fluid-loaded by water and are driven by either harmonic line or point forces or pressures that are convected over the plate's surface. The stiffeners are modeled as a set of reactive normal forces acting upon the plate at discrete spatial locations. Eatwell [9] has presented a formulation

that allows for angular displacements or rotations of the rib stiffeners. Many of the analytical models use Fourier theory to obtain an algebraic, wavevector-frequency description of the structural response of the plate along with the construction of a suitable Green function to examine acoustic radiation. Asymptotic analysis (specifically, the method of stationary phase) is used to approximate the farfield radiated pressure.

Mead [10] and others have developed formulations based on propagation constants that use supports having well-known boundary conditions to model the effect of the attached rib stiffeners. These formulations consider only the response within a "bay" separated by two supports that have known transmission and reflection coefficients (which vary with frequency) for a propagating wave. For a given frequency, the change in phase and rate of amplitude decay in the plate's response, from one bay to an adjacent one, can be related to a constant, denoted the propagation constant.

This article, which relies on the formulation presented by Cray [7], describes universal trends in the structural and acoustic behavior of stiffened plates and summarizes an application that takes advantage of a periodically stiffened plate's farfield radiation characteristics. The application utilizes a submerged stiffened plate as an efficient, low frequency, deep water sound projector. An initial feasibility study [11] has shown that enhanced radiation — namely, increases in both radiated sound pressure level and directivity — can be obtained with a regularly stiffened plate of finite extent.

Cheng [12] has developed another use for an arbitrarily ribbed, finite plate that relies on rib stiffeners to reduce the vibrational levels over a given area on the structure. The method, based on Levenberg-Marquardt optimization, determines the optimal number, size, and spacing required of the stiffeners to produce a minimum in the plate displacement over a region of the plate's surface. An extension of this work is currently being investigated at NUWC Division Newport. A potentially inexpensive method to control the vibration and sound radiation from stiffened structures is being developed. The method will specify optimal stiffener configurations that maximize or minimize the magnitude of the structure's wavenumber spectra within some wavenumber region.

Results and Discussion

A thin, elastic, rib-stiffened plate of infinite extent is shown in Figure 1. The plate's motion, neglecting rotary inertia and shear deformation, is

assumed to be governed by the classical plate equation:

$$D \left(\frac{\partial^2}{\partial x^2} + \frac{\partial^2}{\partial y^2} \right)^2 w(x, y) - m \omega^2 w(x, y) = P_e(x, y) - P_a(x, y, 0) - \{P_1(x, y) + P_2(x, y) + P_3(x, y)\}, \quad (1)$$

where D is the plate's rigidity, $w(x, y)$ is the transverse plate displacement, m is the plate's mass per unit area, and ω is the applied excitation frequency.

The pressure produced by the applied point force is denoted $P_e(x, y)$. The acoustic pressure acting on the upper surface of the plate is $P_a(x, y, 0)$. Each set of stiffeners ($P_1(x, y)$, $P_2(x, y)$, and $P_3(x, y)$) is

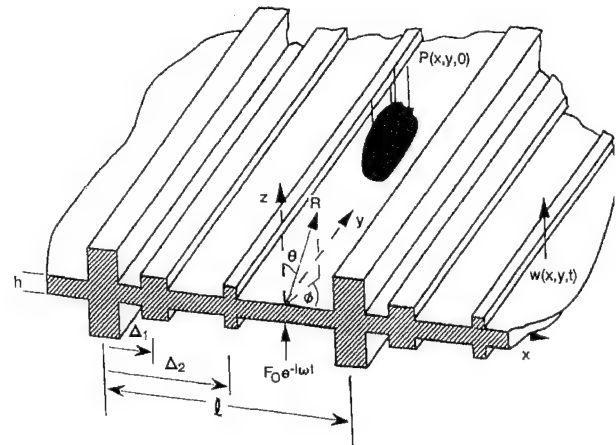


Figure 1. Geometry of Point-Driven, Sectionally Aperiodic, Rib-Stiffened Infinite Plate with Three Sets of Stiffeners of Different Cross-Sectional Area

modeled as Euler beams that exert reactive forces over the attachment area upon the plate. The harmonic time dependence $e^{-i\omega t}$ is suppressed.

A two-dimensional Fourier transform is performed on Eq. (1), shown below, and simplified by introducing vectors $\underline{x} = \{x, y\}$ and $\underline{k} = \{k_x, k_y\}$:

$$D(\mathbf{k}^4 - k_b^4) \tilde{w}(\underline{k}) = \tilde{P}_e(\underline{k}) - \tilde{P}_a(\underline{k}) - \{\tilde{P}_1(\underline{k}) + \tilde{P}_2(\underline{k}) + \tilde{P}_3(\underline{k})\}, \quad (2)$$

where $\mathbf{k} = |\underline{k}|$ and $k_b^4 = m \omega^2 / D$ is the free *in vacuo* plate wavenumber. The details of obtaining an algebraic expression from Eq. (2) will not be presented here. The algebraic complexity increases with each additional set of stiffeners (three sets are shown in Figure 1, two having offsets Δ_1 and Δ_2)

and with permitting angular moments to be exerted by the beams on the plate.

For sectionally aperiodic stiffening with two sets of stiffeners, an expression for the plate's wavevector response $\tilde{w}(\underline{k})$ is given by Cray [7]. For the special case of identical rib stiffeners spaced periodically ($\Delta_1 = \Delta_2 = 0$), with distance ℓ , the wavevector response becomes

$$\tilde{w}(\underline{k}) = F(\underline{k}) - \{Y(\underline{k})K_1F_o(\underline{k})\} / \{1 + K_1Y_o(\underline{k})\}, \quad (3)$$

where K_1 is the stiffeners' transformed reactive stiffness, $F(\underline{k})$ and $F_o(\underline{k})$ are algebraic expressions of the transformed excitation, and $Y(\underline{k})$ and $Y_o(\underline{k})$ are expressions that describe the admittance of the fluid-loaded plate. The farfield radiated pressure is obtained from Eq. (3) by introducing spherical coordinates, as shown in Figure 1, and employing the method of stationary phase.

The wavevector-frequency characteristics of $\tilde{w}(\underline{k})$, for both unribbed ($K_1 = 0$) and periodically ribbed plates, with line and point force excitations, are shown in Figures 2 through 5. In general, the structural acoustic behavior of elastic systems is characterized by two wavenumber regions, the acoustic or supersonic wavenumber region and the subsonic region. Supersonic wavenumbers generate acoustic fields that propagate into the farfield, whereas subsonic wavenumber components rapidly decay away from the surface of the structure. The regions are demarked by the acoustic wavenumber $k_o = \omega / c_o$. Radiation damping at the acoustic

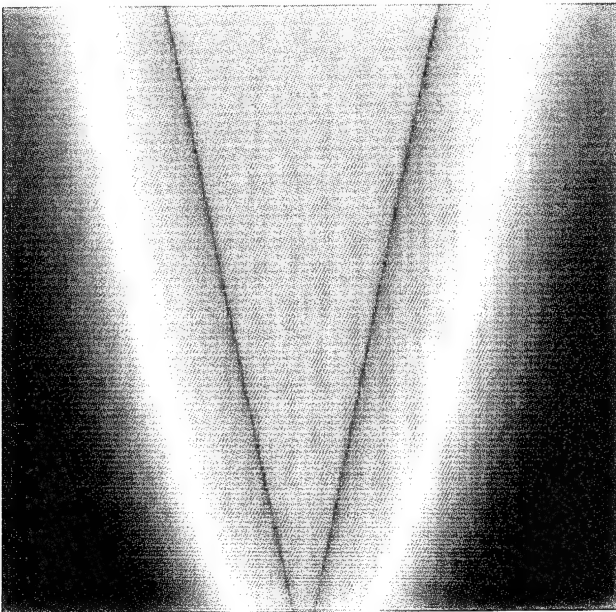


Figure 2. Magnitude of Unribbed Plate Wavenumber Response vs. Frequency (Ordinate) and Wavenumber (Abcissa) due to Line Force Excitation

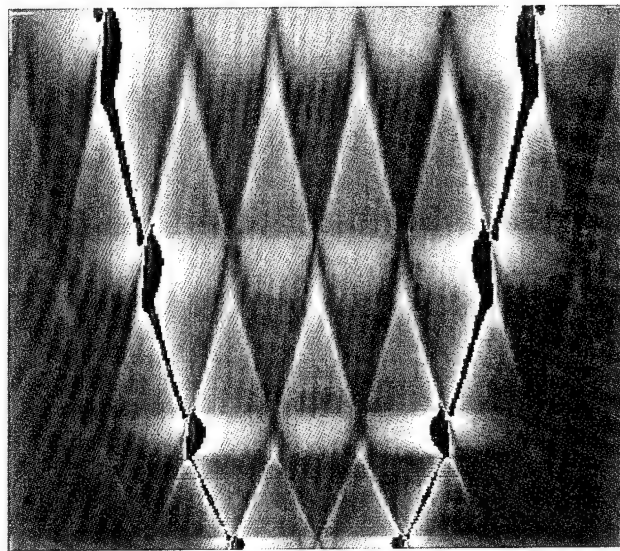


Figure 3. Magnitude of Periodically Ribbed Plate Wavenumber Response vs. Frequency (Ordinate) and Wavenumber (Abcissa) due to Line Force Excitation

wavenumber k_o can be seen clearly in the figures as minima (sharp dark lines and circles) in the plate's spectral response. Also apparent in the figures is the dispersive nature of the fluid-loaded, flexural wavenumber k_{fl} and the large spectral response (shown bright) at this wavenumber.

For an unribbed plate, shown in Figures 2 and 4 (fixed frequency), the response in the supersonic wavenumber region is relatively flat, with an even distribution of wavenumbers. The subsonic region is dominated by a large spectral peak at the plate's flexural wavenumber. Specifying these wavenumbers k_o and k_{fl} provides a qualitative description of the unribbed plate's response.

The periodic configurations shown in Figure 3 for line force excitation and in Figure 5 (fixed frequency) for point force excitation have, in addition to the acoustic and flexural wavenumbers, an aliasing or Bloch wavenumber $k_\ell = 2\pi / \ell$, where ℓ is the bay length between stiffeners. Local maxima and minima (Bragg diffraction [6]) in the wavenumber response occur at predictable multiples of k_ℓ . Hence, bay spacing ℓ is seen to be fundamental in determining the response of stiffened elastic systems.

For negligible fluid loading, the minima and maxima seen in Figure 5 for point force excitation obey, respectively, the wavenumber relationships

$$\{(k_x + nk_\ell)^2 + k_y^2\}^2 = k_b^4, \quad (4)$$

and

$$\{(k_x + nk_\ell)^2 + k_y^2\}^2 = k_b^4 + k_r^4, \quad (5)$$

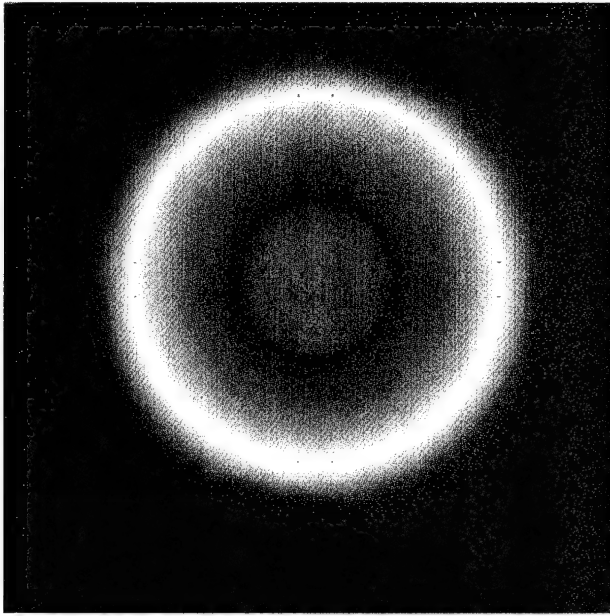


Figure 4. Magnitude of Unribbed Plate Wavenumber Response vs. k_y -Wavenumber (Ordinate) and k_x -Wavenumber (Abcissa) due to Point Force Excitation

where $k_r^4 = \frac{m_1 \omega^2}{D \ell}$ is defined as the *in vacuo* rib-stiffener wavenumber.

The above expressions are simpler for line force excitation, since this type of forcing precludes any spatial variation of the plate's displacement in a direction parallel to the stiffener, or in the y -direction shown in Figure 1. Hence, for an applied line force, k_y is set to zero in Eqs. (4) and (5).

The frequencies where the wavenumber maxima, given by Eq. (5), intersect within the supersonic wavenumber region are particularly important. Figure 3 shows these intersections, which produce strong directional acoustic radiation from the plate, as discrete, large (bright) spectral peaks within the acoustic region. The angular frequencies for these spectral peaks are given in Eq. (6):

$$\omega_p = (p\pi)^2 \sqrt{\frac{D}{\ell^4(m_1 + (m_1/\ell))}}, \quad p = 2, 3, 4, \dots, P, \quad (6)$$

where m_1 is the mass per unit length of a stiffener and integer P is less than or equal to twice the ratio (to the nearest integer) of the plate's flexural wavenumber to the Bloch wavenumber. The form of the above expression is the same as that given by classical resonant frequency analysis of a simply-supported plate of length ℓ , with the additional inclusion of the mass of a single rib stiffener. If the

stiffeners had been allowed to exert angular moments on the plate, resonant frequencies closer to that of a clamped-clamped plate would have been derived.

The even indices of Eq. (6) specify frequencies at which the farfield pressure radiates in a direction normal, or on-axis, to the plate's surface. To first order, Eq. (7) can be used to account for the downward shift in the angular frequencies due to heavy (water) fluid loading:

$$\omega_p' = \frac{\omega_p}{1 + \rho_o / 2m_1 \sqrt{\omega_p}} \left(\frac{D}{m} \right)^{1/4}, \quad (7)$$

where ρ_o is the density of the acoustic medium. Eqs. (6) and (7) indicate that these frequencies of enhanced radiation will decrease with increasing bay spacing ℓ , with increasing rib mass m_1 , or with decreasing plate thickness h .

Currently, no expressions similar to those given above exist for aperiodic stiffened or arbitrarily stiffened structures. For the simplest of sectionally aperiodic systems, two additional wavenumbers are assumed to be important, $k_\Delta = 2\pi/\Delta$ and $k_{(\ell-\Delta)} = 2\pi/(\ell-\Delta)$, where Δ is the offset of a set of stiffeners. In realistic systems, such as fluid-loaded, aperiodic, stiffened plates, the wavenumber expression for $\bar{w}(\underline{k})$ involving ℓ and Δ is quite complicated and cumbersome.

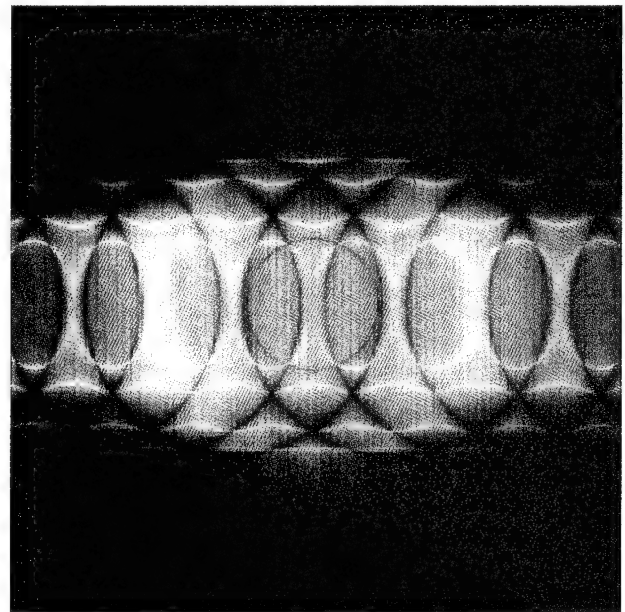


Figure 5. Magnitude of Periodically Ribbed Plate Wavenumber Response vs. k_y -Wavenumber (Ordinate) and k_x -Wavenumber (Abcissa) due to Point Force Excitation

Deriving any interdependence between these parameters is difficult. Simpler models (for example, the response of an infinite string with mass-like stiffening) may eventually be used to illuminate the underlying physics of nonperiodicity.

The application discussed in the introduction of this article concluded that enhanced acoustic radiation effects associated with the addition of regularly-spaced stiffeners on to an infinite plate are also observed in finite plates. For the geometry considered in the study, it was found that a 28-foot-long stiffened plate demonstrated radiated sound pressure levels that were 25 dB more than that of a similar unribbed plate at approximately 400 Hz. Furthermore, the radiated sound levels and directivity values were nearly identical to those observed from the infinite plate model. A partial radiation efficiency value of 46 percent was calculated from the infinite plate model.

Conclusions

For light fluid loading (air), it has been shown that Eqs. (4) and (5) predict, respectively, minima and maxima in the wavevector-frequency response of periodically stiffened plates. These equations, as well as Eqs. (6) and (7), are valid for periodic rib spacing and become invalid for aperiodic spacing.

Similar trends in the wavevector-frequency response have been observed in sectionally aperiodic stiffened plates, i.e., the Bragg diffraction pattern is generally characterized by the sectional spacing ℓ . However, small changes from periodic spacing generate additional spectra minima and maxima that disrupt the wavenumber symmetry seen in Figures 3 and 5. It is surmised that the wavevector-frequency behavior of a plate stiffened in two orthogonal directions (periodic stiffening parallel to the y -axis and the x -axis) will have a Bragg diffraction pattern comprising shifted concentric spectra minima and maxima aligned along the x -axis (as shown in Figure 5) and along the y -axis.

Finite ribbed plates have a potential application as efficient, low frequency sound projectors. The enhanced radiation effect is noted at certain frequencies at which the dominant structural response wavenumber coincides with the Bloch wavenumber k_ℓ . It should be noted that uniform rib stiffeners with equal spacing were used in the study. For enhanced acoustic radiation, such stiffener configurations may not be optimal. Aperiodic stiffening may provide a mechanism to shunt energy for the subsonic wavenumber region into the supersonic wavenumber region and thereby improve the plate's radiation efficiency.

References

- [1] M. Heckl, "Wave Propagation in Beam-Plate Systems," *Journal of the Acoustical Society of America*, vol. 33, 1961, pp. 640-651.
- [2] V. N. Evseev, "Sound Radiation from an Infinite Plate with Periodic Inhomogeneities," *Sov. Phys. Acoust.*, vol. 57, 1973, pp. 370-373.
- [3] B. R. Mace, "Sound Radiation from a Plate Reinforced by Two Sets of Parallel Stiffeners," *Journal of Sound Vibration*, vol. 71, no. 3, 1980, pp. 435-441.
- [4] C. B. Burroughs, "Acoustic Radiation from Fluid-Loaded Infinite Circular Cylinders with Doubly Periodic Ring Supports," *Journal of the Acoustical Society of America*, vol. 75, no. 3, 1984, pp. 715-722.
- [5] G. Maidanik and J. Dickey, "Quadratic and Energy Estimates of the Partial Response of Ribbed Panels," *Journal of the Acoustical Society of America*, vol. 94, no. 3, 1993, pp. 1435-1444.
- [6] D. M. Photiadis, "The Effect of Irregularity on the Scattering of Acoustic Waves from a Ribbed Plate," *Journal of the Acoustical Society of America*, vol. 91, no. 4, 1991, pp. 1897-1903.
- [7] B. A. Cray, "Acoustic Radiation from Periodic and Sectionally Aperiodic Rib-Stiffened Plates," *Journal of the Acoustical Society of America*, vol. 95, no. 1, 1994, pp. 256-264.
- [8] R. F. Keltie, "Structural Acoustic Response of Finite Rib-Reinforced Plates," *Journal of the Acoustical Society of America*, vol. 94, no. 1, 1993, pp. 880-887.
- [9] G. P. Eatwell, "The Response of a Fluid-Loaded, Beam Stiffened Plate," *Journal of Sound Vibration*, vol. 84, no. 3, 1982, pp. 371-388.
- [10] D. J. Mead, "Free Wave Propagation in Periodically Supported, Infinite Beams," *Journal of Sound Vibration*, vol. 11, no. 2, 1970, pp. 181-197.
- [11] R. F. Keltie and B. A. Cray, "Low Frequency Sound Radiation from Stiffened Plates," *ASME International Mechanical Engineering Congress and Exposition Proceedings*, Winter Annual Meeting, Chicago, IL, 1994.
- [12] C. Cheng, "Optimization of Ribbed Plate Vibration," Ph.D. Dissertation, North Carolina State University, 1994.



BENJAMIN A. CRAY

has been employed at NUWC's New London Detachment since August 1983, after receiving his B.S. degree in Mechanical Engineering from Tufts University, where he was a Wheelwright scientific scholar. Selected for NUWC-sponsored long-term training for the academic years 1985-86 and 1989-91, he earned an M.S. degree in

Mechanical Engineering from Yale University in 1987 and a Ph.D. degree in Mechanical Engineering from North Carolina State University in 1992. He has authored three refereed journal articles, six NUWC technical documents, numerous technical memoranda, and has two patents. He has presented two invited papers, one of them in St. Petersburg, Russia. His areas of technical expertise are structural acoustics and acoustic array systems.

An Overview of Developments in Computational Fluid-Structure Interaction

Donald L. Cox, Robert T. Chapman, Anthony J. Kalinowski, and Jayant S. Patel
Naval Undersea Warfare Center Division Newport

Abstract

The Naval Undersea Warfare Center (NUWC) Division Newport has developed a number of computational tools in response to evolving acoustic modeling demands. These recent demands for shallow water require three-dimensional, time-dependent modeling of nonhomogeneous fluid/solid continua. This article describes three general analysis tools capable of addressing these complicated problems: (1) the FIST program for the analysis of axisymmetric structures; (2) the NOMAD program for the three-dimensional structural acoustics problems; and (3) the TURBO program, for the hydro-acoustic issues precipitated by turbulent flow over compliant surfaces.

Introduction

Acoustic modeling is of fundamental importance to the Navy. Historically, the areas of interest have included radiation or scattering from submerged, elastic structures and propagation of acoustic energy in the open ocean. In addition, and more recently, the need for acoustic modeling in shallow water has placed greater demands on acoustical analysis. What were once primarily axisymmetric problems limited to steady-state, harmonic analysis, are rapidly becoming three-dimensional, time-dependent problems. In fact, littoral warfare demands three-dimensional, time-dependent modeling of nonhomogeneous fluid/solid continua.

In response to evolving acoustic modeling demands, the Naval Undersea Warfare Center (NUWC) Division Newport has developed a number of computational tools capable of addressing these complicated problems. This article describes three of these general analysis tools. First, a program (Fluid Interacting with Structures (FIST)) developed for the analysis of axisymmetric structures is described. This is followed by a discussion of a program (No Matrix Decomposition (NOMAD)) being developed to address three-dimensional structural acoustics problems. The article concludes with a description of a tool (Turbulent Unsteady-Flow over Resilient Boundaries (TURBO)) developed for the more complicated problem concerning the hydro-acoustic issues precipitated by turbulent flow over compliant surfaces.

The FIST Program

FIST is a hybrid program that couples the finite element method with the boundary element method. The finite element method is used to model the

structure, and the boundary element method is used to model the acoustic media. The program was developed to analyze the response of any axisymmetric elastic structure immersed in an infinite fluid medium due to acoustic or mechanical excitations.

Structural Modeling. As noted, the finite element method is used to model the structure. In FIST two elements are available for structural modeling, a shell element and a stiffener element. The shell element is a two-noded, conforming axisymmetric element that includes transverse shear and rotary inertial terms. The user has the option of choosing either a lumped or consistent mass matrix. Although the nodes used to describe the shell surface also describe the cavity shape for the Helmholtz integral used in the acoustic modeling, the program has the capability of modeling interior components, e.g., bulkheads, stiffeners, etc., with "dry" nodes. A stiffener element that includes rotary inertia and shear correction terms is also available in the program. This element properly accounts for the eccentricity of its center of gravity relative to a reference point on the shell.

Acoustic Modeling. The Helmholtz integral, which represents the solution of the Helmholtz boundary value problem in an infinite acoustic medium, is used to model the infinite acoustic media. The surface Helmholtz integral is used to relate the velocity normal to the inclusion surface and the corresponding acoustic pressure at the same point. The cavity surface is represented by a series of axisymmetric doubly curved boundary elements. The $r-z$ coordinates and the slope of the tangent at each of the boundary element end points are used

to fit a cubic polynomial that represents the shape of each boundary element. Gaussian quadrature is used to evaluate each surface integral. The singularities of this representation that occur at the cavity's interior resonant frequencies are handled by using a system of overdetermined equations. Once the surface velocity and pressure are calculated, the farfield or nearfield acoustic pressure in the fluid medium is calculated using the Helmholtz integral.

Capabilities. Currently, the FIST program permits solution of the following cases:

1. Given a normal velocity on the cavity surface, the program will calculate the surface and field point acoustic pressures, with the cavity assumed rigid.
2. Both the structural and acoustic response for the case of
 - a plane acoustic wave impinging from any direction on the structure;
 - a spherical, acoustical source;
 - mechanical forces applied to the structure;
 - a piston-type transducer mounted on the structure; and
 - a multiple source representing turbulence excitation.

Those cases listed under item 2 above, in general, represent nonsymmetric loading for which the solution is decomposed into N axisymmetric harmonic components. Each of these harmonic components is analyzed separately and the results are then superposed for the final results.

Figure 1 compares the results of the FIST program with those of the "exact" solution, given in [4].

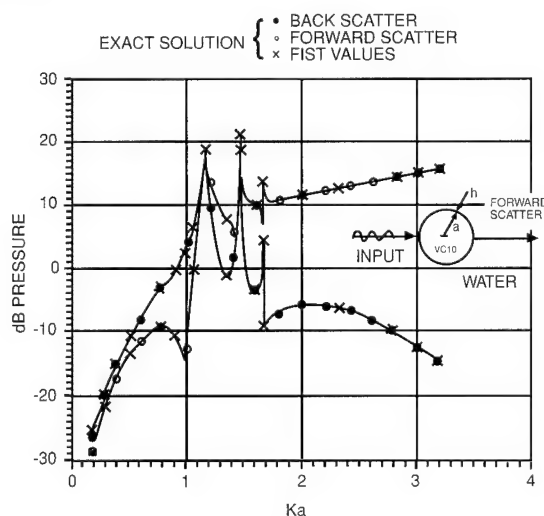


Figure 1. Results of Undamped Elastic Sphere Using "Junger Text"

The NOMAD Program

NOMAD is a finite element program developed at NUWC Division Newport under Independent Research/Independent Exploratory Development (IR/IED) funding. It is from the description No Matrix Decomposition that NOMAD's strength and uniqueness derive. By making use of an iterative solver, the Element-by-Element Preconditioned Conjugate Gradient (EBE-PCG) algorithm, NOMAD has the ability to solve problems without ever assembling a large coefficient matrix. This permits the solution of problems that have always been theoretically solvable by the finite element method. Previously, this process was impossible due to storage limitations, those limitations that continue to exist on today's supercomputers.

Historically, applications have been limited mostly to two-dimensional problems, either planar or axisymmetric. This has not been due to any three-dimensional theoretical shortfall but, as noted, to computer storage limitations. Ironically, as supercomputer availability has grown, so too has the apparent potential for extending finite element fluid/structure analysis to realistic three-dimensional geometries. Unfortunately, the storage necessary for the direct solution of the coupled set of equations resulting from three-dimensional finite element discretization outpaces that routinely available, even on supercomputers. This is due to the geometric growth in storage that results in the storage of assembled global stiffness matrices as mesh size increases. With NOMAD, an analyst has the power of the finite element method, which includes the ability to model continua of any shape, capture any variation in material property, and apply it to large three-dimensional geometries.

Although other programs are being developed and released with this advertised capability, none are known that have the potential of NOMAD. For example, a popular approach to minimizing storage requirements uses an infinite element to terminate the outer boundary for infinite acoustic domains, rather than use the more classical plane wave absorbers. This is a sound tactic in that the infinite elements do not require nearly as large an acoustic mesh because one does not have to model far enough out from the structure to approach a plane wave condition. This was an overpowering advantage for axisymmetric problems in which the acoustic media easily dominated the storage requirements. However, in three-dimensional analysis, the structure alone can overpower available resources, thus suggesting alternate solution strategies for more efficient storage. This is becoming recognized by commercial vendors, as programs such as MARC and MSC/NASTRAN are adding iterative solvers in order to take advantage of storage savings inherent in iterative solvers (no back fill) even after

assembling a global stiffness matrix. As yet, however, no commercial program is available that addresses the fluid/structure interaction problem using EBE strategy.

We describe the general EBE-PCG algorithm used in our program and describe the acoustical fluid/structure interaction problem. The resulting formulation is symmetrical and in the scattering analyses, scattered rather than total pressure is obtained. Our adaptation of the EBE-PCG algorithm for the coupled fluid/structure problems is then described in detail and two example problems are presented: (1) the required, analytically verifying, sphere scattering problem and (2) radiation analysis of a piezoelectric transducer.

General Form of the EBE-PCG Algorithm. The linear system of equations to be solved using the EBE-PCG method can be written generally as

$$Ax = b. \quad (1)$$

Using traditional solution algorithms, both A and b are constructed from the assembly of element contributions, i.e.,

$$A = \sum_{e=1}^n A^e \quad (2)$$

$$b = \sum_{e=1}^n b^e, \quad (3)$$

where A^e and b^e are element matrices, A is an assembly operator, n is the number of elements, and x is a vector of unknowns.

A standard form of the preconditioned conjugate gradient is given below.

- | | |
|-----|---|
| (a) | $p_1^T A p_1 = \text{a large number}$ |
| (b) | $x_1 = 0.0$ |
| (c) | $z_1 = r_0$
for $i = 1, \text{max. no. of iterations}$ |
| (d) | $z_i = z_i W^{-1/2}$ |
| (e) | $\tilde{z}_i = M^{-1} z_i$ |
| (f) | $\tilde{z}_i = \tilde{z}_i W^{-1/2}$ |

$$(g) \quad \beta = \frac{\tilde{z}_i^T A p_i}{p_i^T A p_i}$$

$$(h) \quad p_{(i+1)} = \tilde{z}_i - \beta p_i$$

$$(i) \quad \alpha = \frac{\tilde{z}_i^T r_i}{p_{(i+1)}^T A p_{(i+1)}}$$

$$(j) \quad x_{(i+1)} = x_{(i)} + \alpha p_{(i+1)}$$

$$(k) \quad r_{(i+1)} = r_{(i)} - \alpha A p_{(i+1)}$$

$$(l) \quad z_{(i+1)} = r_{(i+1)}$$

$$(m) \quad \text{if } \frac{\|r_{(0)}\|}{\|r_{(i+1)}\|} < \delta$$

YES \rightarrow STOP

NO $\rightarrow i = i + 1$.

In this algorithm, p is the search vector, W is the diagonal of the global matrix, M is a preconditioner, r is the residual vector, and x is the solution vector. The EBE computations are performed in solution steps d through g, i, and k. The Ap product is constructed one element at a time making use of the equality

$$Ap = \sum_{e=1}^n A^e p^e. \quad (4)$$

Diagonal Scaling and Winget Regularization. The diagonal scaling, sometimes cited as pre-preconditioning, operates on all terms in the element matrix by performing a pre- and post-multiplicative scaling by the inverse square root of the globally assembled matrix, and has the added feature of making the system dimensionally homogeneous. The Winget regularization of the element matrices is a required step for EBE preconditioning. It removes the zero eigenvalues of the element matrices A^e and prepares them for factorization [1]. Entries of the element matrix diagonal are assigned values of unity. The regularized, scaled matrix, \bar{A} , is then given as

$$\bar{A} = I + W^{-1/2} [A^e - W^e] W^{-1/2}. \quad (5)$$

EBE Preconditioners. The effectiveness of a preconditioner depends on how efficiently it can be formed and on how well $M^{-1} \approx A^{-1}$. As implied by the description of EBE, the preconditioner M , an approximation to A of Eq. (1), is never computed globally. For the preconditioning step, the matrix M may take several forms. Examples drawn from product decompositions include the following:

Crout Factorized - EBE Preconditioner

$$M = W^{1/2} \prod_{j=1}^n L(\bar{A}) \prod_{j=1}^n D(\bar{A}) \prod_{j=n}^1 L(\bar{A})^T W^{1/2} \quad (6)$$

and

Cholesky Factorized - EBE Preconditioner

$$M = W^{1/2} \prod_{j=1}^n L(\bar{A}) \prod_{j=n}^1 L(\bar{A})^T W^{1/2} \quad (7)$$

These product decomposition preconditioners are similar in structure and require identical storage. Historically, the Crout version has generally been found to be the most effective and, as a result, is the preconditioner used in this work.

A symmetrized sum decomposition has also been documented and takes the form

Gauss-Seidel - EBE Preconditioner

$$M = W^{1/2} \prod_{j=1}^n \left\{ I + L(\bar{A})_j \right\} \prod_{j=n}^1 \left\{ I + U(\bar{A})_j^T \right\} W^{1/2} \quad (8)$$

Details of the Gauss-Seidel preconditioner can be found in [1]. The primary reason for interest in this sum decomposition is its efficient storage of element matrix data, requiring 50 percent less storage than either the symmetric Cholesky or Crout factorizations. However, this preconditioning strategy is reportedly not as effective as the Crout product preconditioner in accelerating convergence.

Vectorization and Element Blocking. Vectorization of the preconditioner is essential to the computational speed of the EBE algorithm. Vectorization of the preconditioning phase of the algorithm and the $[A]\{p\}$ product can be achieved by incorporating an element blocking algorithm [2] that rennumbers the elements of the finite element connectivity array such that blocks of internally disjoint element blocks can be formed. The purpose of element blocking is to eliminate recursive degrees-of-freedom from the otherwise fully vectorizable computations of forward reduction and back substitution. Hence, each internally disjoint element block contains element matrices that share no degrees-of-freedom. Generally, the maximum

element block size is 64, which means that a maximum of 64 elements is maintained in an element block; as a result, 64 is the maximum vector loop length. Sequences of vector computations of either the forward reduction or back substitution phases are driven by an exterior nonvectorizable do-loop, serving to initialize the number of elements (or loop length) of the element block [1]. The computationally modified preconditioner of Eq. (9) is

$$M = W^{1/2} \prod_{j=1}^{N_{block}} L(\bar{A})_j \prod_{j=1}^{N_{block}} D(\bar{A})_j \prod_{j=N_{block}}^1 L(\bar{A})_j^T W^{1/2} \quad (9)$$

Fluid/Structure Interaction

Fluid/Structure Interaction Formulation. Finite element modeling of an elastic medium yields a matrix equation of the form

$$[M]\{\ddot{u}\} + [B]\{\dot{u}\} + [K]\{u\} = \{F\} \quad (10)$$

where $[M]$, $[B]$, and $[K]$ are the mass, damping, and stiffness matrices, respectively. $\{F\}$ is a vector of external loads that can result from body forces, prescribed tractions, and/or point loads. In the fluid/structure interaction case, $\{F\}$ will include a force A_p due to the acoustic pressure, where A is the appropriate area for converting the nodal acoustic pressures p to a load.

Finite element modeling of an acoustic medium results in matrix equations of the form

$$[Q]\{\ddot{p}\} + [H]\{\dot{p}\} = \{F_{Ac}\} \quad (11)$$

where $[Q]$ and $[H]$ are fluid "mass" and "stiffness" matrices, respectively, $\{p\}$ is the total pressure, and $\{F_{Ac}\}$ are the acoustical "loads." The total pressure $\{p\}$ can be decomposed into the sum of the incident and scattered pressures, i.e.,

$$p = p_i + p_s \quad (12)$$

and, as a result, the matrix equations for the acoustic medium can be written in terms of the scattered pressure p_s :

$$[Q]\{\ddot{p}_s\} + [H]\{\dot{p}_s\} = \{F_{Ac}\} \quad (13)$$

The coupling of Eqs. (10) and (13), or coupling the fluid with the structure, occurs through the force

terms of Eqs. (10) and (15). The boundary condition at the fluid/structure interface is

$$\frac{\partial p}{\partial n} = -\rho \ddot{u}_n, \quad (14)$$

where n is the normal at the interface, ρ is the mass density of the fluid, and \ddot{u}_n is the normal component of fluid particle acceleration. Substituting Eq. (12) into Eq. (14) gives

$$\frac{\partial p_s}{\partial n} = \rho(\ddot{u}_{ni} - \ddot{u}_n), \quad (15)$$

where n is the outward unit normal from the structure into the fluid, and \ddot{u}_{ni} and \ddot{u}_n are the total and incident outward components of fluid particle acceleration at the interface.

Termination of the outer boundary of the acoustic medium requires a boundary condition that simulates infinity. In this work, the plane wave absorber or ρc damper was used. This is the simplest satisfactory boundary condition. However, a penalty is paid in that the acoustic mesh must be extended far enough to satisfy the plane wave approximation. Use of the plane wave absorber results in an additional force term that can be expressed as

$$F_c = \left(\frac{A}{c} \right) \dot{p}_s. \quad (16)$$

Using Eqs. (10), (13), (15), and (16), the matrix equation for the coupled problem becomes

$$\begin{bmatrix} M & 0 \\ -\rho A & Q \end{bmatrix} \begin{Bmatrix} \ddot{u} \\ \dot{p} \end{Bmatrix} + \begin{bmatrix} B & 0 \\ 0 & C \end{bmatrix} \begin{Bmatrix} \dot{u} \\ \dot{p} \end{Bmatrix} + \begin{bmatrix} K & A \\ 0 & H \end{bmatrix} \begin{Bmatrix} u \\ p \end{Bmatrix} = \begin{Bmatrix} -Ap_i \\ \rho A \ddot{u}_{ni} \end{Bmatrix}. \quad (17)$$

The symmetric formulation of the fluid/structure interaction problem is obtained from Eq. (17) by reformulating the pressure equation in terms of a velocity potential [3], where

$$p_s = \dot{q}. \quad (18)$$

This results in matrix equations of the form

$$\begin{bmatrix} M & 0 \\ 0 & Q \end{bmatrix} \begin{Bmatrix} \ddot{u} \\ \ddot{q} \end{Bmatrix} + \begin{bmatrix} B & A \\ A^T & C \end{bmatrix} \begin{Bmatrix} \dot{u} \\ \dot{q} \end{Bmatrix} + \begin{bmatrix} K & 0 \\ 0 & H \end{bmatrix} \begin{Bmatrix} u \\ q \end{Bmatrix} = \begin{Bmatrix} -Ap_i \\ Av_{ni} \end{Bmatrix}. \quad (19)$$

For the steady-state case, both the displacement and the potential can be expressed, using complex arithmetic, as

$$\begin{aligned} u &= \bar{u} e^{i\omega t} \\ \dot{u} &= (i\omega) \bar{u} e^{i\omega t} \\ \ddot{u} &= (-\omega^2) \bar{u} e^{i\omega t} \end{aligned} \quad (20a)$$

and

$$\begin{aligned} q &= \bar{q} e^{i\omega t} \\ \dot{q} &= (i\omega) \bar{q} e^{i\omega t} \\ \ddot{q} &= (-\omega^2) \bar{q} e^{i\omega t}. \end{aligned} \quad (20b)$$

Substituting these expressions into Eq. (19) and suppressing the time dependence yields, with some rearrangement,

$$\begin{bmatrix} -\omega^2 M + i\omega B + K & (i\omega) \delta A \\ (i\omega) \delta A^T & -\omega^2 Q + i\omega C + H \end{bmatrix} \begin{Bmatrix} \bar{u} \\ \bar{q} \end{Bmatrix} = \begin{Bmatrix} -Ap_i \\ Av_{ni} \end{Bmatrix}. \quad (21)$$

Form of the EBE-PCG Algorithm for the Coupled Problem. The computation of conjugate gradient vector information for the structure and the acoustic media are performed separately. However, the conjugate gradient vectors for both media share identical storage locations when required for computation. This is done primarily to avoid large core storage requirements. In doing this, particular attention must be paid in computing the α and β parameters, the convergence criteria, and the $[A]\{p\}$ product of the conjugate gradient algorithm. In the modified EBE-PCG algorithm for the coupled problem presented below, steps (g) and (i) comprise the computations of the scalar parameters. They differ from the standard implementation of the algorithm in that they consist of summed contributions from both structure and acoustical fluid conjugate gradient vector dot products. With α_T and β_T , the computation of the remaining conjugate gradient vectors proceeds separately and may be performed in parallel. Step (m) is the convergence check of the algorithm, which consists of summed contributions of the structure and acoustical residual norms.

- (a) $p_1^T A p_1 = \text{a large number}$
- (b) $x_1 = 0.0$
- (c) $z_1 = r_0$
for $i = 1, \text{max. no. of iterations}$
- (d) ${}^{St}z_i = {}^{St}z_i {}^{St}W^{-1/2}$
 ${}^{Ac}z_i = {}^{Ac}z_i {}^{Ac}W^{-1/2}$
- (e) ${}^{St}\tilde{z}_i = {}^{St}M^{-1} {}^{St}z_i$
 ${}^{Ac}\tilde{z}_i = {}^{Ac}M^{-1} {}^{Ac}z_i$
- (f) ${}^{St}\tilde{z}_i = {}^{St}\tilde{z}_i {}^{St}W^{-1/2}$
 ${}^{Ac}\tilde{z}_i = {}^{Ac}\tilde{z}_i {}^{Ac}W^{-1/2}$
- (g) $\beta_T = \frac{{}^{St}\tilde{z}_i^T {}^{St}(A \cdot p) + {}^{Ac}\tilde{z}_i^T {}^{Ac}(A \cdot p)}{{}^{St}p_i^T {}^{St}(A \cdot p) + {}^{Ac}p_i^T {}^{Ac}(A \cdot p)}$
- (h) ${}^{St}p_{(i+1)} = {}^{St}\tilde{z}_i - \beta_T {}^{St}p_i$
 ${}^{Ac}p_{(i+1)} = {}^{Ac}\tilde{z}_i - \beta_T {}^{Ac}p_i$
- (i) $\alpha_T = \frac{{}^{St}\tilde{z}_i^T {}^{St}r_i + {}^{Ac}\tilde{z}_i^T {}^{Ac}r_i}{{}^{St}p_{(i+1)}^T {}^{St}(A \cdot p) + {}^{Ac}p_{(i+1)}^T {}^{Ac}(A \cdot p)}$
- (j) ${}^{St}x_{(i+1)} = {}^{St}x_{(i)} + \alpha_T {}^{St}p_{(i+1)}$
 ${}^{Ac}x_{(i+1)} = {}^{Ac}x_{(i)} + \alpha_T {}^{Ac}p_{(i+1)}$
- (k) ${}^{St}r_{(i+1)} = {}^{St}r_{(i)} - \alpha_T {}^{St}(A \cdot p_{(i+1)})$
 ${}^{Ac}r_{(i+1)} = {}^{Ac}r_{(i)} - \alpha_T {}^{Ac}(A \cdot p_{(i+1)})$
- (l) $z_{(i+1)} = r_{(i+1)}$
- (m) if $\left(\frac{\|{}^{St}r_{(0)}\| + \|{}^{Ac}r_{(0)}\|}{\|{}^{St}r_{(i+1)}\| + \|{}^{Ac}r_{(i+1)}\|} \right) < \delta$
YES \rightarrow STOP
NO $\rightarrow i = i + 1$

For efficiency, modifications to the $[A]\{p\}$ product and to the preconditioning computations of the EBE-PCG algorithm, for the acoustical fluid/structure interaction problem, must maintain both the core storage efficiency (i.e., the EBE data structure) and the computational efficiency or degree of vectorization of the original algorithm. To circumvent storage difficulties, element matrix information for both the acoustic medium and structure are allowed to occupy identical locations in core storage and are input from secondary storage when required for EBE computation. The original vectorizable routines of the acoustical fluid and structure for the $[A]\{p\}$ product and preconditioning are used where possible.

Fluid/Structure EBE Preconditioning. The element matrices used for EBE preconditioning are

$${}^{St}A^e = {}^{St}(-\omega^2 M^e + i\omega B^e + K^e)$$

$${}^{Ac}A^e = {}^{Ac}(-\omega^2 Q^e + i\omega C^e + H^e) \quad (22)$$

In the current implementation, the Crout element factors used to generate the preconditioner matrix M do not incorporate the coupling δA terms. As a result, the preconditioner formed using the element matrices from both the structure and the acoustic medium are uncoupled. Further refinements may be made to this preconditioning strategy, where corresponding interface elements of the structure and acoustic medium could be assembled with the off-diagonal δA terms included. However, in this work, the coupling of the equations appears only in the $[A]\{p\}$ product of the conjugate gradient algorithm and then, as a by-product, coupling becomes entrained in the EBE preconditioning via the residual vector (steps (g) through (k)).

Diagonal Scaling and Winget Regularization. As before, this preconditioning step operates on all terms in the element matrix by performing a pre- and post-multiplicative scaling by the inverse square root of the global diagonal. The scaling step differs from Eq. (5) in that two global diagonals are generated, one structure and one acoustic, and remain uncoupled. The regularized, scaled matrices, ${}^{St}\bar{A}$ and ${}^{Ac}\bar{A}$, are defined as

$${}^{St}\bar{A} = {}^{St} \left[I + W^{-1/2} [A^e - W^e] W^{-1/2} \right]$$

$${}^{Ac}\bar{A} = {}^{Ac} \left[I + W^{-1/2} [A^e - W^e] W^{-1/2} \right] \quad (23)$$

Fluid/Structure EBE Product Decomposition.

The Crout factorization preconditioners of the structure and the acoustic medium are defined as follows:

$$\begin{aligned}
 {}^{St}M &= \left[W^{1/2} \prod_{j=1}^{Nblock} L(\bar{A})_j \prod_{j=1}^{Nblock} D(\bar{A})_j \right] \\
 &\times \left[\prod_{j=Nblock}^1 L(\bar{A})_j^T W^{1/2} \right] \\
 {}^{Ac}M &= \left[W^{1/2} \prod_{j=1}^{Nblock} L(\bar{A})_j \prod_{j=1}^{Nblock} D(\bar{A})_j \right] \\
 &\times \left[\prod_{j=Nblock}^1 L(\bar{A})_j^T W^{1/2} \right]. \quad (24)
 \end{aligned}$$

Fluid/Structure EBE [A]{p} Product. The EBE product for the fluid/structure algorithm uses the matrix equation

$$\begin{bmatrix} {}^{St}(-\omega^2 M + i\omega B + K) & i\omega \delta A \\ i\omega \delta A^T & {}^{Ac}(-\omega^2 Q + i\omega C + H) \end{bmatrix} \times \begin{Bmatrix} {}^{St}p_i \\ {}^{Ac}p_i \end{Bmatrix} = \begin{Bmatrix} {}^{St}(A \cdot p) \\ {}^{Ac}(A \cdot p) \end{Bmatrix}. \quad (25)$$

The structural and acoustic products, ${}^{St}(A \cdot p_{(i)})$ and ${}^{Ac}(A \cdot p_{(i)})$ in steps (g), (i), and (k), contain the coupling terms and are given by

$$\begin{aligned}
 {}^{St}(A \cdot p_{(i)}) &= {}^{St}A \cdot {}^{St}p_i + {}^{St}\Delta A \cdot {}^{Ac}p_i \\
 {}^{Ac}(A \cdot p_{(i)}) &= {}^{Ac}A \cdot {}^{Ac}p_i + {}^{Ac}\Delta A \cdot {}^{St}p_i. \quad (26)
 \end{aligned}$$

The diagonal terms of Eq. (25) are stored element-wise for both the structure and fluid. The $[A]\{p\}$ product of the fluid/structure equations is constructed by performing an EBE $[A]\{p\}$ product for both media separately, yielding the uncoupled portion of the fluid/structure $[A]\{p\}$ product. The off-diagonal terms of Eq. (25) are stored corresponding to interface or wetted perimeter

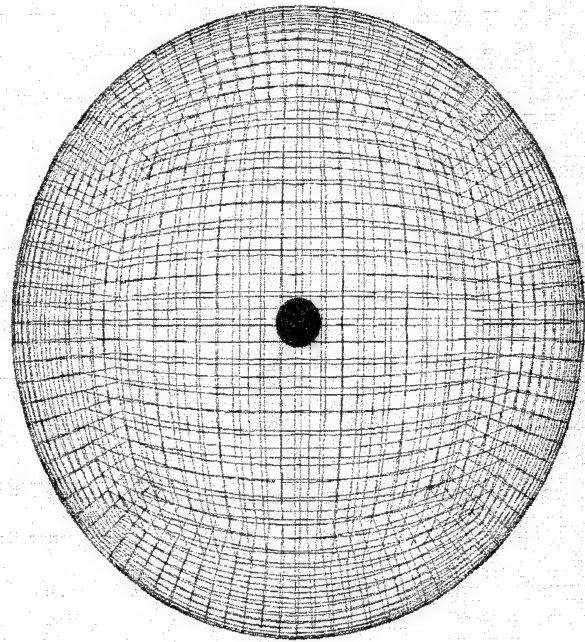


Figure 2. Acoustic Medium

degree-of-freedom number. To complete the fluid/structure matrix vector product, the search vector of either the acoustical fluid or structure must be read in from secondary storage, all interface degree-of-freedom locations of the search vector identified, the $\Delta A\{p\}$ computation performed, and the initial structural or acoustical fluid $[A]\{p\}$ product updated. This computation is performed at the degree-of-freedom level with a vectorizable do-loop length of the maximum number of degrees-of-freedom in the model. This resolves the complete fluid/structure $[A]\{p\}$ product, which must be computed exactly, utilizing EBE matrix-vector products and the vectorized EBE code associated with them.

Examples. As a first step in program validation, and to demonstrate the effectiveness and potential of the NOMAD program, a three-dimensional analysis of an elastic sphere subjected to an incident plane wave at a nondimensional ka value of 1.07 was performed. The entire sphere was modeled using 3456 bilinear degenerate continuum-based shell elements, resulting in a mesh with 3458 nodes or a total degree-of-freedom count of 20,748 for the structure. The acoustic medium (Figure 2) was extended two acoustic wavelengths out from the structure with plane wave absorbers applied at the outer boundary. This resulted in a mesh with 138,240 elements and 141,778 nodes. Hence, the finite element discretization of the problem resulted in 162,526 degrees-of-freedom.

The problem was executed on a Cray X-MP 28, which was limited to 5 megawords of core storage.

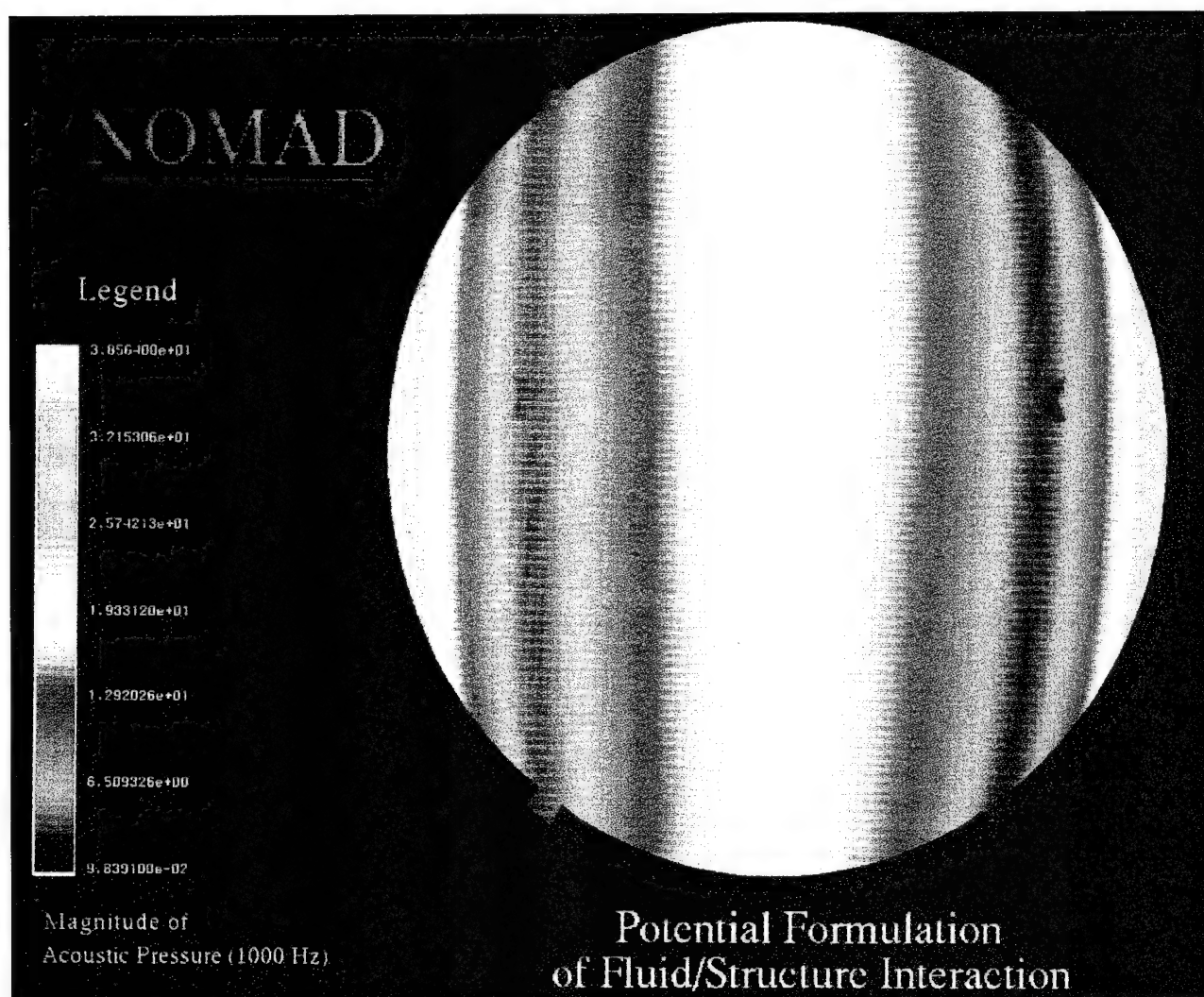


Figure 3. NOMAD Solution

For the sake of comparison, the acoustic mesh, after bandwidth minimization, had a half-bandwidth of 6905. This would require storage of approximately 1 billion words for the acoustic mesh alone if assembly of a global matrix were required. The NOMAD solution (Figure 3) was within 5 percent of the Junger and Feit [4] analytical solution programmed by Patel [5]. Total CPU time was approximately 4 hours.

The second example problem involves the modeling of a piezoelectric transducer. The fluid/structure analysis of this structure, a Class IV flexensional transducer, required a structural model with over 101,000 degrees-of-freedom and an acoustic mesh with approximately 90,000 degrees-of-freedom, for a total degree-of-freedom count of just over 190,000. Executed on a Cray Y-MP, this problem required 34 megawords of main memory and 1.4 hours of CPU time. The results of the analysis are shown in Figures 4 and 5. Figure 4 illustrates the response of the fluid-loaded structure to an enforced potential difference of 1 across each

layer of the three piezoelectric stacks. As shown in the figure, the transducer is responding as expected, with the maximum component of displacement, the y -translation, occurring along the minor axis of the ellipsoid as a result of the extension of the piezoelectric stack, shown as the z -translation. The real and imaginary components, as well as the magnitude of the radiated acoustic pressure, are shown in Figure 5. Also shown is the magnitude of the acoustic pressure at the surface of the transducer. Again, the response is as expected.

Planned Enhancements to the NOMAD Program. Two areas that should greatly increase the efficiency of the NOMAD program are currently being pursued. The addition of an infinite element for the termination of the acoustic mesh should greatly reduce both storage requirements and mesh generation time. It is also believed to yield more accurate results and faster convergence of the EBE-PCG algorithm. Also, because structure and acoustical fluid are operated on separately, the current algorithm described in this article contains

great potential for parallelism. This is being pursued for coarse-grained computers such as Cray Y-MPs.

The TURBO Program

The computational solution of fluid/structure interaction problems with shear flow involves the simultaneous solution of the nonlinear Navier-Stokes equations for the fluid and the appropriate linear dynamic structural equations (e.g., a continuum, plate, or shell representation). The intent here is to describe a formulation for treating the interaction phase for advancing the time step from time t_n to $t_n + \Delta t$. When the fluid and structure are solved with staggered time advancement schemes, unstable solutions might arise; therefore, emphasis is placed on advancing the fluid time step and the structure time step simultaneously (e.g., in place of a staggered method). The formulation treats a general problem class; however, the solution strategy is slanted towards spectral type solutions, where Fourier transformed

quantities (in the spanwise and streamwise directions) are the primary unknown variables.

A class of problems, treated in this article, involves time-dependent hydrodynamic fluid flow passing over compliant surfaces modeled with finite elements. The motivation for such work is to investigate how turbulence-related quantities such as wall pressure, velocity profiles, surface drag, and vorticity are affected by the presence of a compliant interfacing wall as compared with, say, the same flow passing over an undeformable rigid surface. Further, when a weakly compressible form of the continuity equation is used by dropping the convective term $v_i \partial \rho / \partial x_i$ and retaining $\rho_0 \partial v_i / \partial x_i$ (e.g., [6]), the incompressible version reported would also work for hydro-acoustic interaction effects, but this version of TURBO is not treated in this article. Only hydro-interaction phenomena will be treated here.

The physical flow situation is depicted in Figure 6, where the streamwise fluid flow is bounded by a

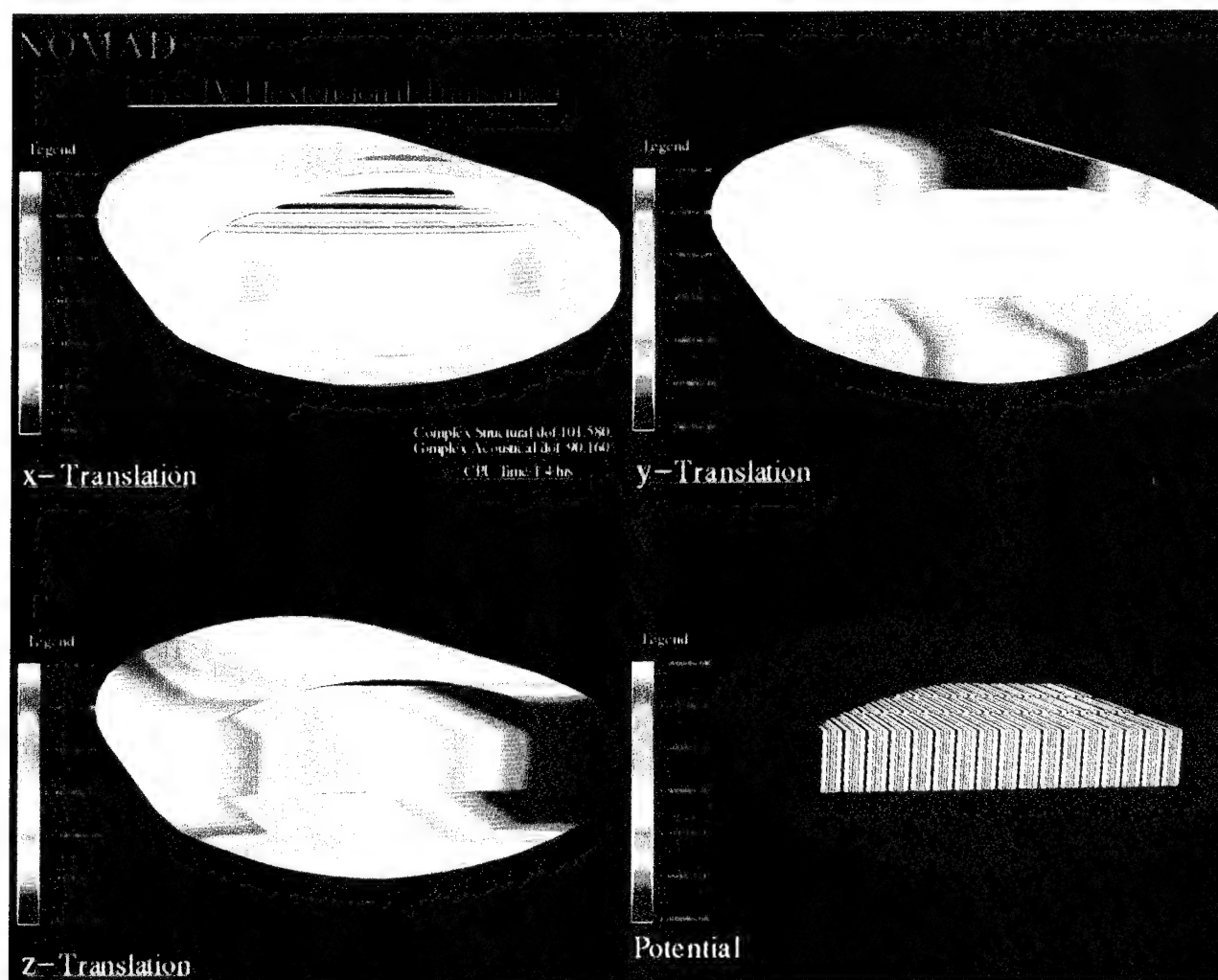


Figure 4. Response of the Fluid-Loaded Structure to an Enforced Potential Difference of 1 Across Each Layer of Three Piezoelectric Stacks

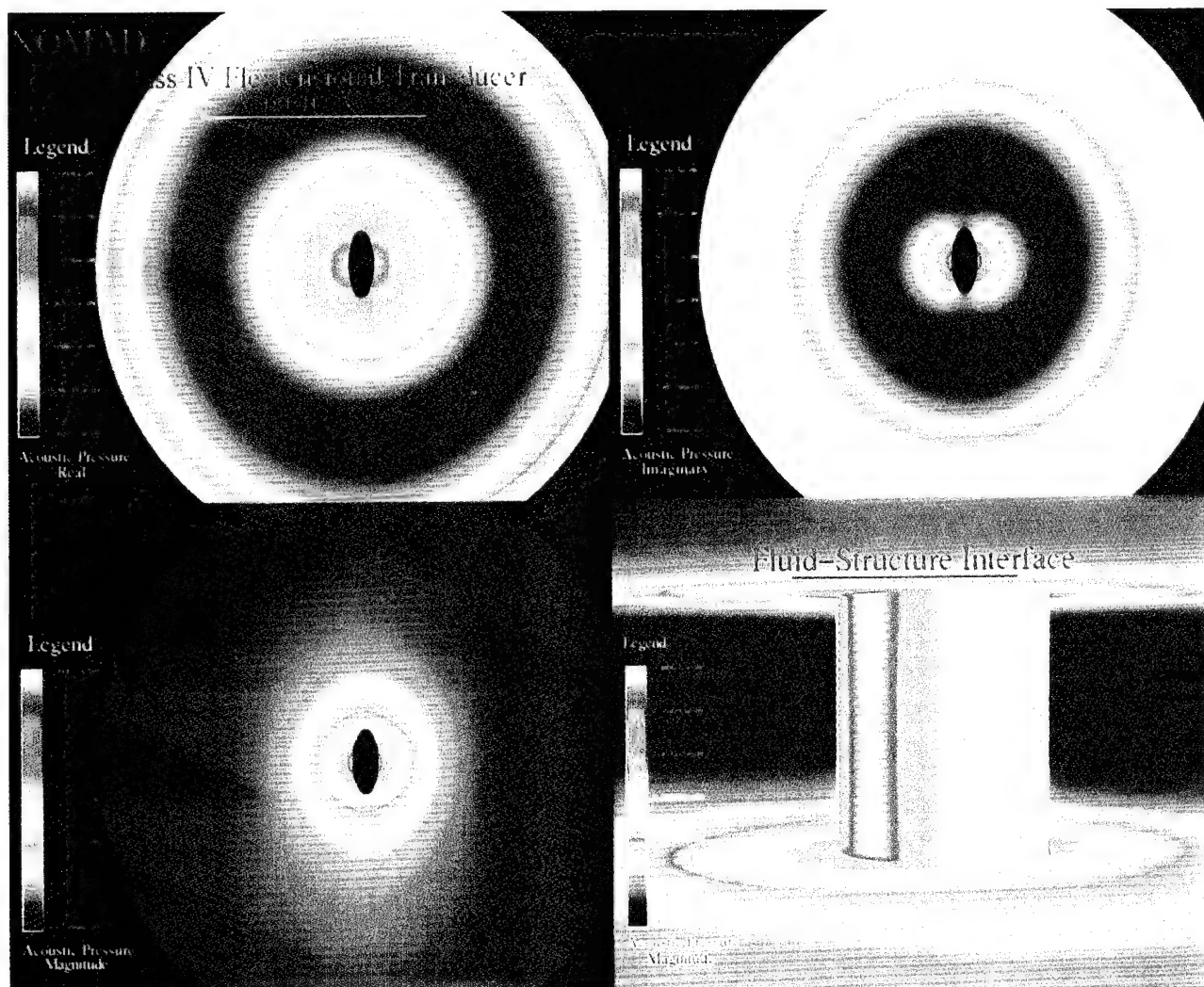


Figure 5. Real and Imaginary Components and Magnitude of Radiated Acoustic Pressure

deformable surface from below and by a rigid wall from above. The fluid portion of the response is assumed to be governed by the nonlinear Navier-Stokes partial differential equations (pdes) in conjunction with the continuity of mass equation. The corresponding interfacing structure is governed by the appropriate linear pdes of viscoelasticity where the discrete dynamic equations of motion are built from either a viscoelastic combined bending-stretching plate model or a three-dimensional isoparametric finite element model. The numerical treatment of hydrodynamic problems typically must consider how to handle the finite domain boundary cuts in the fluid field, and impose at these cuts the appropriate boundary conditions that would result in an undisturbed flowfield. One method for treating this boundary condition issue is with periodic boundary conditions, e.g., [7], [8]. Over a limited region of the fluid, experimental results suggest that streaking patterns in the flow tend to repeat in space in the streamwise and spanwise directions. Thus, by taking finite Fourier transforms in these two directions, the spatial periodicity is maintained. In

the direction normal to the structure, the response is not taken as periodic (e.g., in the semi-infinite domain case, the flow is bounded by the structure wall from below and by an unbounded fluid domain from above). The Fourier components of the

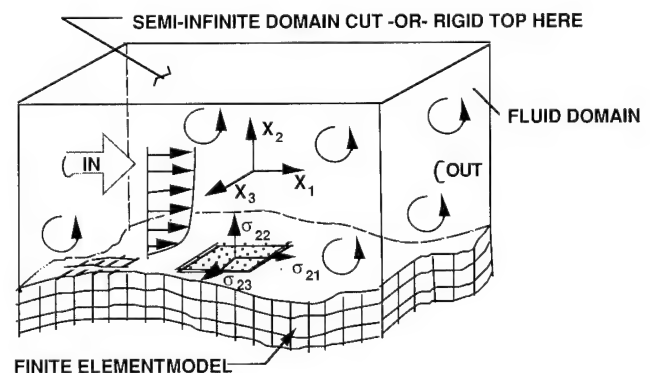


Figure 6. Computational Fluid/Structure Interaction Flow Domain

primitive state variables become the new unknowns in the problem formulation.

Governing Equations of Fluid Motion. For the incompressible version of TURBO, the fluid domain is governed by the standard incompressible Navier-Stokes equations and associated continuity of mass equations which, for a standard Eulerian fixed-frame coordinate system, are given by the relations

$$\rho \left(\frac{\partial v_i}{\partial t} \Big|_{\bar{x}=c} + \frac{\partial v_i}{\partial x_k} v_k \right) - \frac{\partial \sigma_{ik}}{\partial x_k} - b_i = 0 \quad (27)$$

$$\frac{\partial v_k}{\partial x_k} = 0, \quad (28)$$

where from here on the usual continuum mechanics summation convention is employed with repeated indices implying a summation from, say, $k = 1, 2, 3$. In the case where the fluid interfaces with a moving surface, such as for the hydrodynamic fluid/elastic structure interaction problem, the usual fixed grid Eulerian representation for the fluid and the "follow the particle" Lagrangian representation for the structure results in a mismatch at the fluid/solid interface and can take on the form of a gap or an overlap (as indicated in Figure 7, where \bar{u} denotes the gap or overlap) displacement vector spanning the structure to fluid distance.

The interfacing of the fluid/solid independent variables can be handled by the following methods such as (1) ignoring the gaps (or overlaps) that exist between the fluid and solid; (2) mating the Eulerian description fluid and Lagrangian description structure with an Arbitrary Lagrangian Eulerian (ALE) coordinate mapping; (3) using an approximate method, a Taylor expansion, on fluid state variables out to the fluid/solid interface (e.g., [9] for a free surface problem and [10] for a curved bottom problem); and (4) using a combination of these methods, such as ALE treatment for the normal to the surface direction and method (1) or (3) for the streamwise and spanwise directions.

Here, we consider the combination method (4), which uses the ALE method (2) for the displacement

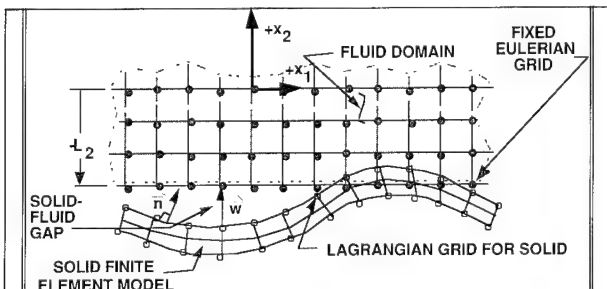


Figure 7. Eulerian Grid - Lagrangian Grid Gaps

direction normal to the structure interface and method (1) for the in-plane motion. In [11], another combination method of ALE (2) for the normal direction and Taylor (3) for the in-plane direction is considered. When spectral methods (i.e., taking finite Fourier transforms in a spatial direction) are used in the fluid domain for the streamwise direction and spanwise directions (e.g., [7],[8]), standard fast Fourier transforms dictate that equal spatial spacing be used in the directions; therefore, method (4) will be favored here.

To account for the gaps, the most general treatment involves a stretching of the coordinate system through a transformation of the form $\bar{x} = \bar{F}(\bar{\chi}, t)$. This type of ALE coordinate mapping was applied to moveable surfaces problems involving fluid/structure interactions [12]. The above governing Eqs. (27) and (28) can be rewritten in the form

$$\rho \left(\frac{\partial v_i}{\partial t} \Big|_{\bar{\chi}=c} + \frac{\partial v_i}{\partial \chi_k} \frac{\partial \chi_k}{\partial x_j} (v_j - v_j^G) \right) - \frac{\partial \sigma_{ik}}{\partial \chi_j} \frac{\partial \chi_j}{\partial x_k} - b_i = 0 \quad (29)$$

$$\frac{\partial v_k}{\partial x_j} \frac{\partial \chi_j}{\partial x_k} = 0, \quad (30)$$

where the variables χ_k, t are the new fluid-independent variables for space and time; x_k is the old Eulerian independent variable; ρ is the mass density/unit volume; v_i is the velocity vector; and σ_{ik} is the stress tensor, which is related to velocity through the following Stokes constitutive equation.

$$\sigma_{ik} = -p\delta_{ik} + \mu \left(\frac{\partial v_i}{\partial \chi_j} \frac{\partial \chi_j}{\partial x_k} + \frac{\partial v_k}{\partial \chi_j} \frac{\partial \chi_j}{\partial x_i} \right) - (2/3)\mu\delta_{ik} \left(\frac{\partial v_q}{\partial \chi_j} \frac{\partial \chi_j}{\partial x_q} \right). \quad (31)$$

Further, μ is the viscosity coefficient; $v_j^G = \partial F_j / \partial t$ is the "grid velocity"; b_i is the body force term; and the rate $\partial \chi_k / \partial x_j$ variable is computed from the inverse of the mapping function $\chi_k = F_k^{-1}(\bar{x}, t)$. When the mapping function $F_k(\bar{\chi}, t)$ is selected so that if $\bar{\chi} = \bar{x}$, then $v_j^G = 0$, then the fluid description is the usual Euler one for fixed grids.

In the case of the deformable surface, whose main deflection is normal to the surface of the solid, a simplified representation is taken. The mapping function is taken only on the vertical coordinate. Thus, $F_2(\bar{\chi}, t)$ is taken in the form $\chi_2 = x_2 B(x_1, x_3, t) + C(x_1, x_3, t)$ and $\chi_1 = x_1, \chi_3 = x_3$, where the functions $B(x_1, x_3, t), C(x_1, x_3, t)$ are

determined from the conditions that the Lagrangian description for the solid and the Eulerian description for the fluid meet at the solid-fluid interface. Thus, we require that at $x_2 = -L_2 + w_2$, $\chi_2 = -L_2$ is enforced at the bottom and at $x_2 = L_2 + 0$, $\chi_2 = L_2$ is enforced at the rigid wall top for all x_1, x_3, t in the spatial and time domain of interest. This mapping, in effect, results in the computational fluid flow having both flat top and bottom boundaries in the mapped $\bar{\chi}$ domain.

In a situation where ALE is required in all three coordinate directions, a much more complex mapping function would have to be determined to preserve both the flat interface surface and maintain equal grid spacing. These are not unlike the kind of body-fitted coordinate mappings used in computational fluid dynamics finite difference schemes (e.g., [13]).

Finally, there remains the issue of enforcing the velocity and surface traction physical boundary conditions at the fluid/solid interface $\bar{x} = \bar{x}^S \equiv -L_2 + \bar{w}$, namely

$$v_i(\bar{x}^S, t) = \frac{\partial w_i}{\partial t} \Big|_{ON-SURFACE}; \quad (32)$$

$$\sigma_{ij}(\bar{x}^S, t)n_j = \tilde{\sigma}_{ij}n_j \Big|_{ON-SURFACE}, \quad (33)$$

where σ_{ij} , $\tilde{\sigma}_{ij}$ are the interface stresses in the fluid and elastic body (tilde labeled), respectively, and n_j is the unit outward normal from the elastic body. When the structure deformation slopes are small, and the coordinate system is aligned parallel to the initial undeformed surface, then n_j can be approximated with $[0, 1, 0]^T$.

Equations of Motion for Finite Element Modeled Viscoelastic Solid. In the situation where the interfacing structure is complex with viscoelastic damping, its finite element representation can be used (e.g., [14]). Here, the continuous pdes have already been discretized in space. The solution for advancing the solid from t_n to $t_n + \Delta t$ involves solving the following set of discretized matrix equations:

$$[M]\{\ddot{D}\}_{n+1} + [C]\{\dot{D}\}_{n+1} + [K]\{D\}_{n+1} = \{F\}_{n+1}, \quad (34)$$

which are partitioned further into surface and interior nodes:

$$\begin{bmatrix} M_{SS} & M_{SI} \\ M_{IS} & M_{II} \end{bmatrix} \begin{bmatrix} \ddot{D}_S \\ \ddot{D}_I \end{bmatrix}_{n+1} + \begin{bmatrix} C_{SS} & C_{SI} \\ C_{IS} & C_{II} \end{bmatrix} \begin{bmatrix} \dot{D}_S \\ \dot{D}_I \end{bmatrix}_{n+1}$$

$$+ \begin{bmatrix} K_{SS} & K_{SI} \\ K_{IS} & K_{II} \end{bmatrix} \begin{bmatrix} D_S \\ D_I \end{bmatrix}_{n+1} = \begin{bmatrix} F_S \\ F_I \end{bmatrix}_{n+1}, \quad (35)$$

where $[D_S, D_I]^T$ denotes the structure displacement vector, which is partitioned into surface (subscript "S") and interior nodes, (subscript "I"); $[M]$, $[C]$, $[K]$ denote conventional mass, damping, and stiffness matrices, respectively; and $[F_S, F_I]^T$ denotes the surface forces (interface stress tractions) and the interior driver forces, should any exist. Also, "dotted" variables ($\dot{\cdot}$) denote time differentiation of the displacement, and a set of three orthogonal component direction values of $\{D_S\}$, for a given surface node, corresponds to \bar{w} in Figure 7. Next, we rewrite Eq. (34) in first-order form to facilitate a first-order form integration scheme:

$$\begin{aligned} \begin{bmatrix} \dot{\mathcal{W}} \\ \dot{\mathcal{V}} \\ \dot{\mathcal{U}} \end{bmatrix}_{n+1} &= \begin{bmatrix} \mathcal{A} \\ -[M]^{-1}[C] & -[M]^{-1}[K] \\ [I] & [0] \end{bmatrix} \begin{bmatrix} \mathcal{W} \\ \mathcal{V} \\ \mathcal{U} \end{bmatrix}_{n+1} \\ &+ \begin{bmatrix} \mathcal{F} \\ [M]^{-1}\{F\} \\ \{0\} \end{bmatrix}_{n+1}, \quad (36) \end{aligned}$$

where $\{\mathcal{W}\}_{n+1}$ is the new first-order unknown variable whose upper half partition $\{\mathcal{V}\}$ corresponds to the original velocity array $\{\dot{D}\}_{n+1}$, and the lower half partition $\{\mathcal{U}\}$ corresponds to the original displacement array $\{D\}_{n+1}$.

Simultaneous Solution Strategy for Coupled Fluid/Solid Field Equations. The solution scheme for solving coupled fluid and solids problems concentrates on a spectral analysis approach where finite Fourier transforms are taken in the streamwise and spanwise directions of the computational box of Figure 6. Thus, double spatial transformed variables will be denoted as single-hatted variables ($\hat{\cdot}$) in the development to follow.

The integration scheme begins with a startup idealized solution that corresponds to an Orr-Sommerfeld type onset of instability solution [15] for channel flow over a rigid surface. The potential form of solutions (normally used to compute eigenvalues for flow instabilities) taken from [15] was converted into the full primitive state variable form so that the full velocity, velocity gradients, and pressure distributions would be available for all

spatial points in the computational domain. Further, this eigenfunction type solution is adjusted so that the maximum amplitude of the streamwise fluctuating component is some small percentage, say 5 percent, of the centerline freestream velocity.

The Orr-Sommerfeld starting solution also provides the surface traction stresses σ_{ij} needed to compute the starting solid displacement and velocity, $\{D_S\}$, $\{\dot{D}_S\}$ for $n = 0$ in $t_{n+1} = t_n + \Delta t$. This surface traction acts as a time driver in the structure governing equations. To integrate the solid equations across the time step, the Fourier transformed surface stresses acting on the solid, $\hat{\sigma}_{2i}(t')$, are explicitly represented by

$$\hat{\sigma}_{2i}(t') = \hat{\sigma}_{2i}(t_n) + \frac{(\hat{\sigma}_{2i}(t_{n+1}) - \hat{\sigma}_{2i}(t_n))}{\Delta t} (t' - t_n) \quad (37)$$

for $t_n \leq t' \leq t_{n+1}$,

where the implicit unknowns are the solid surface tractions $\hat{\sigma}_{2i}(t_{n+1})$ at the end of the time step and the corresponding fluid interface velocity components $v_i(\bar{x}^S, t_{n+1})$.

Implicit Boundary Condition. The main step is to determine a relationship between surface stress and surface motion for the implicit time advancement solution of the linear structural solution. This is similar to the impedance relationship between surface motion and surface force employed during harmonic steady-state solutions used in linear acoustics problems [16]. For the class of problems at hand, we seek a relationship (in the Fourier transformed domain) that takes on the form

$$\hat{V}_i^S(\bar{m}, \bar{n})_{n+1} = \hat{\mathcal{A}}_i(\bar{m}, \bar{n}) + \hat{\mathcal{G}}_{ij} \hat{\sigma}_{2j}^S(\bar{m}, \bar{n})_{n+1}, \quad (38)$$

where \hat{V}_i^S is the structure surface velocity variable and $\hat{\sigma}_{2j}^S$ is a surface stress variable $\hat{\mathcal{A}}_i(\bar{m}, \bar{n})$, and $\hat{\mathcal{G}}_{ij}$ terms are known quantities involving the solid material constants and geometry for each wavenumber pair (\bar{m}, \bar{n}) . Specifically, the \hat{V}_i^S variable corresponds to the finite element method (FEM) surface velocity \hat{D}_S for solutions to Eq. (35).

The development of Eq. (38) for the FEM case is not as straightforward as dealing with continuous pdes, because we already have discretized the spatial distribution via the shape functions within the FEM; therefore, there is no continuous pde on which we can directly perform the finite Fourier transform

operations. There is the further complication of dealing with both internal and external displacement unknowns, and the enforcement of a periodic boundary condition in the x_1 and x_3 directions must also be satisfied. A first-order form predictor-corrector scheme that uses Adams Bashforth for the predictor and the trapezoidal rule [17] for the corrector has been selected as the method to develop Eq. (38) for the FEM. The method was chosen because it is an explicit time advancement scheme for the solid motion (but the yet unknown surface loading $\hat{\sigma}_{2i}(t')$ can be treated implicitly) and further, because it *does* allow a nondiagonal damping matrix since the algorithm does not require $[C]^{-1}$. However, the algorithm does require the evaluation of $[M]^{-1}$; therefore, from an efficiency point of view, we employ a lumped mass matrix so that the evaluation of $[M]^{-1}$ is a trivial step. The development of Eq. (38) is not limited to this particular time integrator; however, it has the advantage of dealing with a nondiagonal damping matrix often encountered in models with structural damping. A second-order version of the integrator, which also avoids the need for $[C]^{-1}$, was used in [11], which was based on the explicit predictor-corrector of [18]. The full displacement vector, denoted $\{D\}_{n+1}$, contains both internal and surface nodes; it is also noted that nodal displacements at periodic streamwise and spanwise periodic cutting planes *are not* treated as independent values, since they are connected by the periodicity.

Thus, the first-order version of Eq. (36) is given by

$$\{\mathcal{W}\}_{n+1} + [\mathcal{A}]\{\mathcal{W}\}_{n+1} = \{\mathcal{F}\}_{n+1}, \quad (39)$$

where the predictor phase (denoted by underscore tilde terms $\{\mathcal{W}\}$) of the integration process is given by

$$\begin{aligned} \{\mathcal{W}\}_{n+1} &= \{\mathcal{W}\}_n + \Delta t \left(\frac{3}{2} [\mathcal{A}]\{\mathcal{W}\}_n + \frac{3}{2} \{\mathcal{F}\}_n \right. \\ &\quad \left. - \frac{1}{2} [\mathcal{A}]\{\mathcal{W}\}_{n-1} - \frac{1}{2} \{\mathcal{F}\}_{n-1} \right) \end{aligned} \quad (40)$$

and the corrector phase is given by

$$\begin{aligned} \{\mathcal{W}\}_{n+1} &= \{\mathcal{W}\}_n + \Delta t \left(\frac{1}{2} [\mathcal{A}]\{\mathcal{W}\}_n + \frac{1}{2} \{\mathcal{F}\}_n \right. \\ &\quad \left. + \frac{1}{2} [\mathcal{A}]\{\mathcal{W}\}_{n+1} + \frac{1}{2} \{\mathcal{F}\}_{n+1} \right). \end{aligned} \quad (41)$$

Substituting Eq. (40) into the velocity term Eq. (41) leads to Eq. (42), where the notation $\{ \}^U$ refers to the upper half of the first-order vector form of Eq. (41).

$$\begin{aligned} \{ \dot{D} \}_{n+1} = & \overbrace{\left\{ \left([I] + \frac{\Delta t}{2} [A] \right) \{ w \}_n \right\}^U}^{\text{KNOWN TERM}} + \frac{\Delta t}{2} \left\{ \left([A] \{ w \} \right)_{n+1} \right\}^U \\ & + \underbrace{\frac{\Delta t}{2} [M]^{-1} \{ F \}_n}_{\text{KNOWN TERM}} + \underbrace{\frac{\Delta t}{2} [M]^{-1} \{ F \}_{n+1}}_{\text{UNKNOWN TERM}}. \end{aligned} \quad (42)$$

Next, a simple rearrangement operation is performed on the terms in Eq. (42), where the full displacement vector is reordered into three $(\bar{m} \cdot \bar{n}) \times 1$ component displacement column-stacked arrays for the surface variables $\{ \dot{D}_S \}_i$ for $i = 1, 2, 3$ and a rearrangement into the column nodal display for the remaining interior nodes $\{ \dot{D}_I \}$. This results in

$$\begin{Bmatrix} \{ \dot{D}_S \}_i \\ \{ \dot{D}_I \} \end{Bmatrix}_{n+1} = \begin{Bmatrix} \{ A_S \}_i \\ \{ A_I \} \end{Bmatrix}_n + \frac{\Delta t}{2} [M]^{-1} \begin{Bmatrix} \Delta \mathcal{A}_S [\sigma_{2i}^s] \\ \{ F_I \} \end{Bmatrix}_{n+1}. \quad (43)$$

In Eq. (43), the nodal force has been rewritten as a product of the stress and a $\Delta \mathcal{A}_S$ factor which represents a local area factor for converting distributed stress values into lumped nodal finite element force, where implicit stress Eq. (37) is used in the $\{ F \}_{n+1}$ nodal force evaluation and the following explicit equation

$$\hat{\sigma}_{2i}(t') = \hat{\sigma}_{2i}(t_n) + \frac{(\hat{\sigma}_{2i}(t_n) - \hat{\sigma}_{2i}(t_{n-1}))}{\Delta t} (t' - t_n)$$

$$\text{for } t_n \leq t' \leq t_{n+1} \quad (44)$$

is used in the $\{ F \}_n$ nodal force evaluation. The final form of the boundary condition can be achieved if we restrict ourselves further to finite element solids whose upper region interfacing the fluid is of a uniform density material, so that when an equal spaced surface mesh is employed (as will be the case for the spectral method), all diagonal terms in $[M]^{-1}$ are the same, say $1/m_S$, for the interfacing surface nodes (nodes below the surface can, however, vary from internal node to internal node). Further, due to the connectivity topology implied by the periodic boundary condition (discussed later in this article), the net lumped masses at corners and edges also have the same m_S value. We extract three $(\bar{m} \cdot \bar{n}) \times 1$ sized column arrays from the top partition of Eq. (43) and feed each of these into the appropriate bin numbers of a two-dimensional spatial fast

Fourier transform algorithm. Thus, the top partition of Eq. (43) is rewritten as

$$i \dot{D}_S(\bar{m}, \bar{n})_{n+1} = \underbrace{i \hat{A}_S(\bar{m}, \bar{n})_n}_{\text{KNOWN}} + \frac{\Delta t}{2} \Delta \mathcal{A}_S \frac{1}{m_S} \hat{\sigma}_{2i}^S(\bar{m}, \bar{n})_{n+1}, \quad (45)$$

where the $i \hat{A}_S(\bar{m}, \bar{n})_n$, $0.5 \Delta t \Delta \mathcal{A}_S (1/m_S)$ coefficients correspond to the \hat{A}_i , \hat{G}_{ij} variables in the generalized velocity-surface stress relation in Eq. (38).

Enforcement of Two-Way Periodic Boundary Condition. The application of the two-way boundary condition to the fluid portion of the model is automatic by virtue of taking finite Fourier transforms in the x_1 and x_3 directions; however, the finite element model requires a different treatment wherein the displacements in, say, the x_1 direction front $x_3 - x_2$ plane must be equal to the displacements in the corresponding back $x_3 - x_2$ plane. These displacements are equal, but are yet unknown and are to be determined as part of the solution process. Similarly, the displacements in the x_3 direction front $x_3 - x_1$ plane must be equal to the displacements in the corresponding back $x_3 - x_1$ plane.

Construction of Fluid State Variable Boundary Condition. First, Eq. (45) must be converted into an interface boundary condition for the fluid as applied at the bottom grid points (i.e., $\chi_i = \chi_i^G$). This is accomplished by substituting Fourier transformed versions of Eq. (32) and Eq. (33) into Eq. (38) (i.e., its equivalent, Eq. (45)), obtaining

$$\hat{v}_i^G(\bar{m}, \bar{n})_{n+1} = \hat{A}_i(\bar{m}, \bar{n})_n + G \hat{\sigma}_{2i}^G(\bar{m}, \bar{n})_{n+1}, \quad (46)$$

where the coefficients \hat{A}_i , G are a result of the above-mentioned algebraic substitutions and \hat{v}_i^G , $\hat{\sigma}_{2i}^G$ are the Fourier transformed velocity and surface stress values, respectively, at the fluid-bottom interface grid points.

Next, the stress terms are replaced with their state variable equivalents via the hatted version of the stress-strain rate Eq. (31), leading to the expressions

$$\begin{aligned} \hat{\sigma}_{22}^G &= -\hat{p} - \frac{2}{3} \mu i (k_m \hat{v}_1 + k_n \hat{v}_3) + \frac{4}{3} \mu \hat{B} * \frac{\partial}{\partial \chi_2} \hat{v}_2 \\ \hat{\sigma}_{21}^G &= \mu \left(i k_m \hat{v}_2 + \hat{B} * \frac{\partial}{\partial \chi_2} \hat{v}_1 \right) \\ \hat{\sigma}_{23}^G &= \mu \left[i k_n \hat{v}_2 + \hat{B} * \frac{\partial}{\partial \chi_2} \hat{v}_3 \right], \end{aligned} \quad (47)$$

where \hat{B} is the Fourier transform of the ALE mapping function $B(x_1, x_3, t)$, and $*$ corresponds to the circular convolution operator resulting from the transform of a product [19]. Note that Eq. (47) corresponds to the simple ALE version involving coordinate stretching only in the direction normal to the solid, and ALE effects are neglected for the in-plane directions. Next, Eq. (47) is substituted into Eq. (46), resulting in the following relationship between fluid state variables at the fluid grid surface:

Bottom Boundary Condition

$$\sum_{j=1}^3 \alpha_{ij} \hat{v}_j^G(\bar{m}, \bar{n}) + \gamma_i \hat{p}^G(\bar{m}, \bar{n}) + \beta_i \hat{B} * \frac{d}{d\chi_2} \hat{v}_i^G = \hat{d}_i(\bar{m}, \bar{n}), \quad (48)$$

$i = 1, 2, 3 \quad \text{no sum on } i$

where α_{ij} , γ_i , β_i , \hat{d}_i are coefficients resulting from the algebraic substitutions mentioned above.

The corresponding boundary condition at the top rigid wall is simply

Top Boundary Condition

$$\hat{v}_i(\bar{m}, \bar{n})|_{\chi_2=+L_2} = 0 \quad i = 1, 2, 3. \quad (49)$$

Eqs. (48) and (49) constitute six boundary conditions that must be applied to the fluid solution time advancement phase. It is noted that for open top (semi-infinite) domains, Eq. (49) can be replaced with $\hat{v}_i(\bar{m}, \bar{n}) = U_\infty$, where U_∞ is some appropriate fraction of the freestream, depending on how far the upper boundary is located from the solid bottom.

In the case where no ALE method is used to account for the Eulerian-Lagrangian gap, Eq. (48) contains only wavenumber pairs (\bar{m}, \bar{n}) (e.g., it does not contain neighboring wavenumbers like $\bar{m} + 1$, $\bar{m} - 1$, $\bar{n} + 1$, $\bar{n} - 1$, ... etc.). We define this (\bar{m}, \bar{n}) pair as "dominant," which refers to the (\bar{m}, \bar{n}) combination that would be present if the stretching metric $B(x_1, x_3, t)$ had been identically 1.0. However, when ALE is used, then the convolution operation $*$ brings in other wavenumber pairs in addition to (\bar{m}, \bar{n}) . At the point of enforcing the boundary conditions, it is greatly advantageous to have Eq. (48) uncoupled (i.e., the implicit unknowns at $t + \Delta t$ only contain (\bar{m}, \bar{n})) and this is accomplished by an approximation that treats only the dominant term $B(1, 1, t) \partial \hat{v}_i(\bar{m}, \bar{n}) / \partial \chi_2$ implicitly and treats the remaining neighboring wavenumber terms as explicit knowns, which are absorbed into the \hat{d}_i term.

The enforcement of Eq. (48) and Eq. (49) boundary conditions involves specific details of the

spectral method of solution, which is beyond the scope of this article and, therefore, only an abbreviated outline of the steps necessary to implement these conditions is presented below.

Spectral Method Fluid Solution. The fluid portion of the response is assumed to be governed by the Navier-Stokes Eq. (29), in conjunction with the continuity equation (Eq. (30)). A mixed implicit-explicit time integration scheme is used, where for the nonlinear convective terms, an explicit Adams-Bashforth integrator is used as a predictor with an optional trapezoidal rule for the corrector; a trapezoidal rule scheme (i.e., Crank-Nicolson) is used for the linear terms.

Unlike full three-dimensional finite difference methods, where all of the primary unknowns are the physical quantities, such as the unhatted velocity components and pressure, here a pseudo-spectral approach is used. Complex Fourier amplitude components (denoted as hatted quantities), resulting from taking finite Fourier transforms in the streamwise and spanwise directions, become the problem unknowns. Therefore, after Fourier transforming the governing pdes and advancing the time step with a mixed implicit-explicit time integrator, such as the one described above, a set of ordinary second-order differential equations results:

$$\begin{aligned} \mathcal{L}(\hat{v}(\bar{m}, \bar{n}, \chi_2)_{n+1}, \hat{p}(\bar{m}, \bar{n}, \chi_2)_{n+1}) &= 0 \\ -L_2 \leq \chi_2 \leq L_2, \end{aligned} \quad (50)$$

with $d^2(\cdot)/d\chi_2^2$, $d(\cdot)/d\chi_2$ as the differential operators, denoted collectively by \mathcal{L} . Thus, in Eq. (50), the velocity and pressure \hat{v}_{n+1} , \hat{p}_{n+1} are the problem unknowns over a selected set of N variable spaced vertical planes ${}_k\chi_2$ taken at

$$\begin{aligned} {}_k\chi_2 &= \{ {}_1\chi_2 = -L_2 < {}_2\chi_2 < {}_3\chi_2 < {}_4\chi_2 < \dots < {}_N\chi_2 = L_2 \} \\ k &= 1, 2, 3, \dots, N. \end{aligned} \quad (51)$$

A variable plane spacing in Eq. (51) is selected (e.g., based on hyperbolic tangent distributions), so that a fine variation is used through the viscous sublayer near the fluid-solid interface, with an increasing coarse spacing away from the surface. The specific details of the solutions to Eq. (50) are too intricate for presentation here; therefore, only a rough outline of methodologies is given.

Equations such as Eq. (50) have been numerically solved by finite differences [20], where

a set of $N \times 4$ linear algebraic equations and $N \times 4$ unknowns is solved for each wavenumber pair (\bar{m}, \bar{n}) for a simple boundary condition of no-slip velocity (i.e., zero velocity). Similarly, the same type of equations have been solved by collocation methods employing Chebyshev polynomials as the expansion functions [13]. This also leads to a set of $N \times 4$ linear algebraic equations, where $N \times 4$ unknowns are determined for each wavenumber pair (\bar{m}, \bar{n}) . In both of these approaches, the six boundary conditions (e.g., Eq. (48) and Eq. (49) in this application) would have to be worked into the solution as constraints on the unknowns at the domain boundaries $\chi_2 = L_2, -L_2$.

Yet a different approach has been taken in [11], and can be classified as the method of lines (e.g., [21]). Here the eigenfunctions and eigenvalues of Eq. (50) are found for each wavenumber pair (\bar{m}, \bar{n}) . The eigenfunctions provide us with continuous functions through the χ_2 space; however, the nonhomogeneous portion of the differential equations Eq. (50) (appearing in $\mathcal{F}(\chi'_2)$ below) are known only discretely over the set of planes described by Eq. (51). Typically, the solutions for $\hat{v}_{n+1}, \hat{p}_{n+1}$ are constructed from integrals of the form

$$\int_{-L_2}^{\chi_2} e^{-\lambda(\chi_2 - \chi'_2)} \mathcal{F}(\chi'_2) d\chi'_2, \quad (52)$$

where the exponential and λ are related to the eigenfunctions and eigenvalues of Eq. (50). The application of the six boundary conditions, Eqs. (48) and (49), for the six corresponding arbitrary constants, needs to be determined for each wavenumber pair (\bar{m}, \bar{n}) . This then requires the solution to a 6×6 set of simultaneous linear equations, which, due to the relatively sparse nature of the coefficient matrix, has an explicit algebraic solution. Therefore, the solution for an $N \times 4$ set of simultaneous unknowns for each wavenumber pair encountered in the two previously mentioned approaches [20], [7] is replaced by N separate smaller 6×6 systems, for which we have the exact algebraic solution. Once the arbitrary constants are evaluated, the integrals of the type given by Eq. (52) are evaluated in a plane-by-plane sweep, which then provides the desired $\hat{v}_{n+1}, \hat{p}_{n+1}$ at all planes defined by Eq. (51). Some of the λ values are large, and special care must be taken in the numerical evaluation of the Eq. (52) type integrals, where the exponential part of the integrand is treated exactly.

Correction for Explicit ALE Metric Approximations. During the solution process, two approximations involving the ALE metric $B(x_1, x_3, t)$ are used, namely, (1) the explicit treatment of the

nondominant wavenumber convolution terms involved in products of the $B(x_1, x_3, t)$ and independent variables (e.g., terms like $\hat{B}(\bar{m}, \bar{n}, t) * \partial \hat{v}_i(\bar{m}, \bar{n}) / \partial \chi_2$ that appear in Eq. (47), and therefore, eventually in the governing differential equations); and (2) the use of the gap displacement vector $\bar{w}(t_n)$ evaluated at the past time $t = t_n$ instead of at $t = t_{n+1}$.

The fix for approximation (1) is made at the corrector phase of the fluid advancement time integration. Linear terms appearing in the governing differential equations of the type $\hat{B}(\bar{m}, \bar{n}, t) * \partial \hat{v}_i(\bar{m}, \bar{n}) / \partial \chi_2$ are treated analogously to the boundary condition treatment previously discussed. For the same uncoupling reasons, such product terms are split, where the dominant term $\hat{B}(1, 1, t_{n+1}) \partial \hat{v}_i(\bar{m}, \bar{n}) / \partial \chi_2$ remains implicit on the left and the remaining terms are treated explicitly on the right during the predictor pass, where later these explicit terms are updated on the subsequent corrector pass. It is noted that nonlinear convective terms involving B are treated as explicit during the whole integration process and, therefore, are never split into dominant and nondominant terms.

The fix for approximation (2) is treated differently, where a multiple pass (we call this global iteration) through the whole solution process would be made before moving on to the next time step. On the first pass, the B metric appearing in implicit terms, is evaluated with only the information known at that time, namely $\bar{w}(t_n)$. Once the $t = t_{n+1}$ time step is completed and the updated $\bar{w}(t_{n+1})$ is known, B is reevaluated and the time advancement step is recomputed as another global iteration pass through the solution process.

Recovery of Real State Variables. Once the solutions for the hatted variables in the fluid are obtained, there remains the "retrieval phase" of back-stepping through the process to reclaim all the unhatted physical variables in both the solid and the fluid. For the fluid variables, this is a simple matter of taking inverse Fourier transforms of the velocity and pressure at $t = t_{n+1}$. For the solid, we substitute the newly computed interface fluid velocities into Eq. (45) to solve for $\hat{\sigma}_{2i}^S(\bar{m}, \bar{n})$, which can then be used in Eq. (41) to compute the rest of the solid displacement and velocity unknowns at $t = t_{n+1}$.

Example Turbulent Velocity Profile. As an illustration, a channel flow configuration corresponding to the type of doubly wall-bounded flow illustrated in Figure 6 is considered next. The flow was initialized with a startup procedure as described above and corresponds to the velocity profile labeled V_1 Startup in Figure 8 (square solid symbol). As the flow develops into the turbulent range, the streamwise velocity profile flattens out

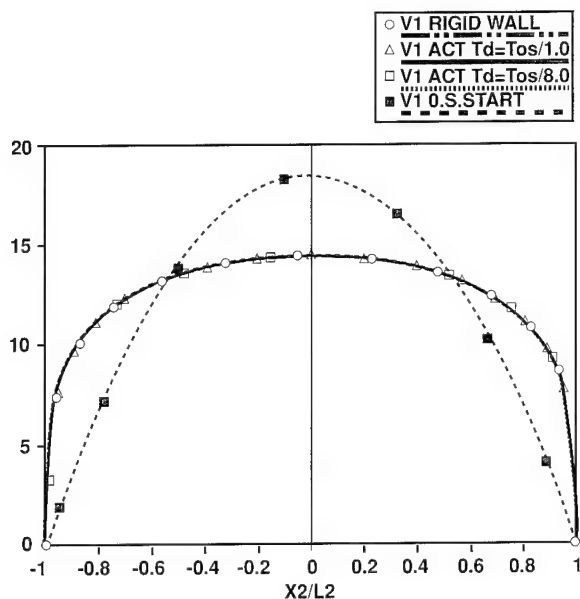


Figure 8. Streamwise Velocity Profile

as expected. Three flattened profiles are shown and correspond to the wall remaining rigid (hollow circle symbol), and the wall moving with a small prescribed motion of two different displacement

amplitudes (hollow triangle and hollow square, respectively). In this particular application, there was no important difference between the rigid and movable wall results for the streamwise velocity profiles; however, there were more important differences in other wave number components in the spanwise and vertical components. Furthermore, the rigid turbulent flow profile matched the law of the wall experimental data (particularly in the wall region from $x^+ = 1.0$ to 20.0 nondimensional wall units).

Acknowledgment for TURBO Code

The authors would like to acknowledge the funding received from NUWC's Independent Research/Independent Exploratory Development (IR/IED) Program. We also wish to thank Prof. Murray Wachman for his contributions to the Hydrodynamic Fluid/Structure Interaction work and to Robert Chapman for his implementation of the FEM first-order time integrator and periodic boundary condition into the computational computer code used to execute Hydrodynamic Fluid/Structure Interaction work, the solution methodology given here.

References

- [1] R. M. Ferencz, "Element-by-Element Preconditioning Techniques for Large-Scale, Vectorized Finite Element Analysis in Nonlinear Solid and Structural Mechanics," Ph.D. Dissertation, Stanford University, 1989.
- [2] T. J. R. Hughes, R. M. Ferencz, and J. O. Hallquist, "Large-Scale Vectorized Implicit Calculations in Solid Mechanics on a CRAY X-MP/48 Utilizing EBE Preconditioned Conjugate Gradients," *Computer Methods in Applied Mechanics and Engineering*, vol. 36, 1987, pp. 215-248.
- [3] G. C. Everstine, "Structural-Acoustic Finite Element Analysis with Application to Scattering," *Proceedings of the 6th Invitational Symposium on the Unification of Finite Elements - Finite Differences and Calculus of Variations*, H. Kardestuncer (ed.), University of Connecticut, 1982.
- [4] M. C. Junger and D. Feit, *Sound, Structures, and Their Interaction*, Second Edition, The MIT Press, Cambridge, MA, 1986.
- [5] J. S. Patel, "The Radiation from a Point Driven Thin Elastic Sphere and the Scattering of a Plane Wave by a Thin Elastic Sphere in an Infinite Acoustic Medium," NUSC Technical Memorandum No. 911041, Naval Underwater Systems Center, New London, CT, 1 March 1991.
- [6] S. H. Reitsmer, "Non-Reflective Boundary Conditions for Fluid-Acoustic Simulations Using a Finite Volume Formulation," Presented at the ASME Fluids Engineering Conference, Washington, DC, June 1993.
- [7] P. Moin and J. Kim, "On the Numerical Solution of Time-Dependent Viscous Incompressible Fluid Flows Involving Solid Boundaries," *Journal of Computational Physics*, vol. 35, no. 3, 1980, pp. 381-393.
- [8] J. Kim, P. Moin, and R. Moser, "Turbulence Statistics in Fully Developed Channel Flow at Low Reynolds Number," *Journal of Fluid Mechanics*, vol. 177, 1987, pp. 133-166.
- [9] Milne-Thompson, *Theoretical Hydrodynamics*, Macmillan Company, New York, 1960.
- [10] M. D. Kelleher and R. Balasubramanian, "On the Use of Linearized Boundary Conditions in the Computation of Flow Over Wavy Walls," ASME bound volume publication FED-vol. 11, (Presented at the Symposium on Laminar Turbulent Boundary Layers, ASME Energy Sources Technology Conference, New Orleans, LA), February 1984.
- [11] A. J. Kalinowski and M. Wachman, "A Combined Finite Element Method and Spectral Method for Shear Flow-Structure Interaction Problems," *Computational Methods In Fluid/Structure Interaction*, AMD-vol. 178, Proceedings of the ASME Winter Annual Meeting, New Orleans, LA, 1993.
- [12] T. Belytschko, D. P. Flanagan, and J. M. Kennedy, "Finite Element Methods with User-Controlled Meshes for Fluid-Structure Interaction," *Computer Methods in Applied Mechanics and Engineering*, vol. 33, nos. 1-3, 1982, pp. 669-688.
- [13] D. Kwak, J. L. C. Chang, S. P. Shanks, and S. R. Charkravathy, "An Incompressible Navier-Stokes Flow Solver in Three Dimensional Curvilinear Coordinate System Using Primitive Variables," AIAA Paper No. 84-0252, AIAA 22nd Aerospace Sciences Meeting, Reno NV, January, 1984.
- [14] R. D. Cook, D. S. Malkus, and M. E. Plesha, *Concepts and Applications of Finite Element Analysis*, Third Edition, John Wiley and Sons, New York, 1988.
- [15] P. G. Drazin and W. D. Reid, *Hydrodynamic Stability*, Cambridge University Press, New York, 1981.
- [16] M. C. Junger and D. Feit, *Sound, Structures and Their Interaction*, Second Edition, MIT Press, Cambridge, MA, 1972.
- [17] G. Strang, *Introduction to Applied Mathematics*, Wellesley-Cambridge Press, Cambridge, MA, 1986.
- [18] T. J. R. Hughes and W. K. Liu, "Implicit-Explicit Finite Elements in Transient Analysis: Implementation and Numerical Examples," *Journal of Applied Mechanics*, vol. 45, no. 2, 1978, pp. 375-378.
- [19] C. S. Burrus and T. W. Parks, *DFT/FFT and Convolution Algorithms Theory and Implementation*, John Wiley and Sons, New York, 1985.
- [20] P. Moin and J. Kim, "Numerical Investigation of Turbulent Channel Flow," *Journal of Fluid Mechanics*, vol. 118, 1982, pp. 341-377.
- [21] M. Holt, *Numerical Methods in Fluid Dynamics*, Springer Verlag, New York, 1984.



DONALD L. COX is a member of the Computational Analysis Branch at NUWC. He received his B.S. degree in 1974 and his M.S. degree in 1976, both in Engineering Mechanics, from North Carolina State University. In 1988, he received his Ph.D. in Mechanical Engineering from the University of Connecticut. His research interests are in computational methods for large-scale problems in 3-D fluid/

structure interaction, nonlinear solid mechanics, and dynamic contact. Of particular current interest is the application of the finite element method to problems in structural acoustics through a combination of hierarchical formulation methods and iterative solution techniques. Dr. Cox has published in the areas of computational methods applied to structural acoustics problems, and constitutive modeling of visco-hyperelastic solids. He is a co-author of the finite element program NOMAD.



ANTHONY J. KALINOWSKI is a mechanical engineer in the Computational Analysis Branch of NUWC's Engineering and Technical Services Department. His work is in the area of structural dynamics, wave propagation, acoustics, and fluid/structure interaction with primary emphasis on computational techniques, focusing on applications to supercomputers. He is currently chairman of the Dynamics of Structures and Systems

Committee for the Applied Mechanics Division of the American Society of Mechanical Engineers. Before joining the NUWC staff, Dr. Kalinowski worked at Pratt and Whitney Aircraft and at the Illinois Institute of Technology Research Institute. Dr. Kalinowski earned an M.S. degree in Mechanical Engineering from Rensselaer Polytechnic Institute and a Ph.D. degree in Applied Mechanics from the Illinois Institute of Technology. He and Professor Murray Wachman of the University of Connecticut are co-authors of the TURBO program.



ROBERT T. CHAPMAN is a member of the Computational Analysis Branch at NUWC. He received his B.S. degree in Civil Engineering from the University of Connecticut in 1984 and an M.S. degree in Civil Engineering and Applied Mechanics from the University of Virginia in 1990. His research interests are vector-parallel computational strategies, memory

management, and algorithm development of large-scale preconditioned iterative solution techniques for linear systems of equations. His experience ranges from industrial and domestic structural design and site planning to development of numerical solution strategies for engineering mechanics applications. Mr. Chapman has published papers in 3-D structural acoustics and shallow-water acoustics and is a co-author of the finite element program NOMAD.



JAYANT S. PATEL is a research mechanical engineer in the Computation Analysis Branch of the Mechanical Engineering Division at NUWC's Detachment in New London, CT. His areas of interest include continuum mechanics, structural analysis and dynamics, acoustics, material science, and computational mechanics. Dr. Patel earned a B.E. degree in Civil

Engineering from Sardar Patel University India, an M.E. degree in Civil Engineering from Yale University, and a Ph.D. degree in Engineering Mechanics from Pennsylvania State University. He is author of the FIST program.

Turbulent Flow Noise Estimates for Hull Arrays

Sunghwan Ko

Naval Undersea Warfare Center Division Newport

Abstract

This article presents techniques for reducing turbulent boundary layer pressure fluctuations using wavenumber filters, such as a finite hydrophone, an array of hydrophones, and a layer of elastomer (outer decoupler). The turbulent wall pressure spectrum that represents the flow excitation function is the Corcos model adjusted to fit a realistic estimate at the low wavenumber region. The occurrence of the convective ridge wavenumber (where most of the energy is carried) is estimated by using a convective flow speed that is a function of frequency.

Introduction

When a ship (submarine or surface ship) is in motion, the hydrophone arrays mounted on its hull are subject to a noisy environment. Figure 1 shows locations of the hull arrays mounted on a submarine (white rectangular apertures). It is desirable to reduce the noise associated with turbulent boundary layer pressure fluctuations. The flow-induced noise can be reduced by covering the hydrophone arrays with a layer of elastomer (frequently called an outer decoupler), or by using large hydrophones as well as large arrays. This article presents a method for reducing flow noise. The turbulent boundary layer flow noise can be lowered by filtering the wavenumber-frequency spectrum through wavenumber filters, such as a finite hydrophone, a hydrophone array, and an outer decoupler.

In this article, two mathematical models are used. The first is the analytical model that evaluates the response of an array of rectangular hydrophones flush-mounted on a rigid surface to the wavenumber-frequency turbulent wall pressure spectrum [1]. An approximate technique has been developed by Thompson and Montgomery [2] to perform the rapid evaluation of power spectral density integrals for an array of hydrophones mounted on a rigid surface.

The second is the theoretical model that evaluates the response of an array of rectangular hydrophones embedded within a layer of elastomer to the turbulent wall pressure spectrum [3],[4]. Calculation of the flow-induced noise received by a circular hydrophone beneath turbulent boundary layers has been made by Chase and Stern [5].

A technique for making measurements using an array of pressure sensors, called wavenumber filtering, was proposed by Maidanik and Jorgensen [6]. It was first implemented by Blake and Chase [7], who used a line array of four pressure sensors steered in two directions in wavevector space to determine the wavenumber-frequency spectra of a turbulent boundary layer on a wind tunnel wall.

The effectiveness of various wavenumber filtering components, such as a hydrophone, an array of hydrophones, and a layer of elastomer, in reducing turbulent flow noise is discussed. The main features of this work are the noise reductions compared with the calculated noise levels for a flush-mounted point hydrophone.

Theoretical Analysis

Turbulent Flow Noise Level. The turbulent flow noise level received by an array of finite hydrophones embedded within an outer decoupler (a layer of elastomer) can be obtained from the frequency spectral density, given by: (see Figure 2)

$$Q(\omega) = 2\pi \int_{-\infty}^{+\infty} \int_{-\infty}^{+\infty} P(k_x, k_y, \omega) S(k_x, k_y) \times A(k_x, k_y) T(k_x, k_y, \omega) dk_x dk_y, \quad (1)$$

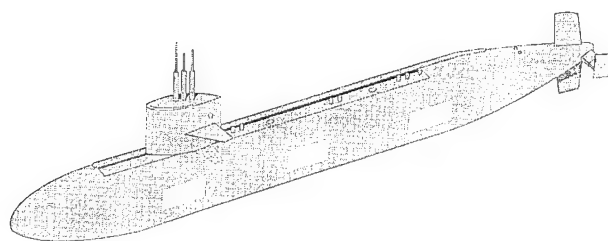


Figure 1. Hull-Mounted Hydrophone Arrays on a Submarine

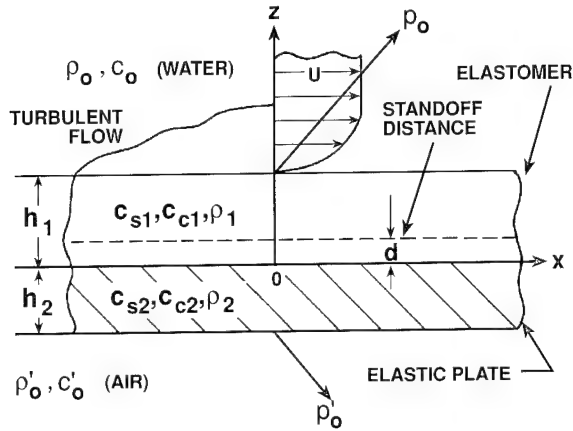


Figure 2. Theoretical Model (Hydrophone Array Embedded Within a Layer of Elastomer Backed by a Plate with Finite Thickness)

where $Q(\omega)$ is the frequency spectral density, $P(k_x, k_y, \omega)$ is the turbulent wall pressure spectrum, $S(k_x, k_y)$ is the hydrophone function, $A(k_x, k_y)$ is the array function, $T(k_x, k_y, \omega)$ is the transfer function, $\omega = 2\pi f$ is the angular frequency in radians/s, f is the frequency in Hz, and k_x and k_y are the wavenumbers in the x and y directions, respectively.

Turbulent-Boundary-Layer Wall Pressure Spectrum. It is important to define an excitation function to be used as a driving force in the analysis. A wavevector-frequency spectrum of wall pressure fluctuations beneath a turbulent boundary layer has been developed by some researchers to represent a proper turbulent flow excitation function [8]-[11]. Among currently available wall pressure spectrum models, that developed by Corcos [8] has been a convenient expression for use in the study of flow noise reduction.

Following Corcos [8], one may write the cross-spectrum of turbulent boundary layer pressure as

$$P(\zeta_x, \zeta_y, \omega) = \frac{1}{2\pi} \int_{-\infty}^{+\infty} R(\zeta_x, \zeta_y, \tau) \exp(-i\omega\tau) d\tau, \quad (2)$$

where $R(\zeta_x, \zeta_y, \tau)$ is the space-time cross-correlation function, ζ_x and ζ_y are the spatial separations in the x and y directions, respectively, and τ is the time interval. The space-time cross-correlation function of the pressures at two arbitrary points is given by

$$R(\zeta_x, \zeta_y, \tau) = \langle p(x, y, t) p(x + \zeta_x, y + \zeta_y, t + \tau) \rangle, \quad (3)$$

where $\langle \rangle$ denotes the time average, $p(x, y, t)$ is the wall pressure at (x, y) and t , and $p(x + \zeta_x, y + \zeta_y, t + \tau)$ is the wall pressure at

$(x + \zeta_x, y + \zeta_y)$ and $(t + \tau)$. The cross-spectrum shown in Eq. (3) is defined by Corcos [8]:

$$P(\zeta_x, \zeta_y, \omega) / P(\omega) = \Phi(\zeta_x \omega / u_c, \zeta_y \omega / u_c), \quad (4)$$

where $P(\omega)$ is the point spectrum ($\zeta_x = \zeta_y = 0$), $\Phi(\zeta_x \omega / u_c, \zeta_y \omega / u_c)$ is the narrowband cross-correlation function, and u_c is the convective flow speed. The restriction of Eq. (4) is that $\Phi(0, 0) = 1$ to ensure the identity for $(\zeta_x, \zeta_y) = (0, 0)$. The frequency-wavenumber spectrum is written as

$$\begin{aligned} P(k_x, k_y, \omega) &= \left(\frac{1}{2\pi} \right)^{2+\infty+\infty} \int_{-\infty}^{+\infty} \int_{-\infty}^{+\infty} P(\zeta_x, \zeta_y, \omega) \\ &\times \exp[i(k_x \zeta_x + k_y \zeta_y)] d\zeta_x d\zeta_y \\ &= \left(\frac{1}{2\pi} \right)^{2+\infty+\infty} \int_{-\infty}^{+\infty} \int_{-\infty}^{+\infty} P(\omega) \Phi\left(\frac{\zeta_x \omega}{u_c}, \frac{\zeta_y \omega}{u_c} \right) \\ &\times \exp[i(k_x \zeta_x + k_y \zeta_y)] d\zeta_x d\zeta_y. \end{aligned} \quad (5)$$

Further, using a similarity hypothesis, Corcos approximated the narrowband cross-correlation function as the product of two functions:

$$\begin{aligned} \Phi(\zeta_x \omega / u_c, \zeta_y \omega / u_c) \\ = A(\zeta_x \omega / u_c) B(\zeta_y \omega / u_c) \exp(-i\zeta_x \omega / u_c), \end{aligned} \quad (6)$$

where $A(\zeta_x \omega / u_c)$ and $B(\zeta_y \omega / u_c)$ are the longitudinal and lateral cross-spectra, and are defined by

$$A(\zeta_x \omega / u_c) = \exp(-\alpha_1 |\zeta_x| \omega / u_c) \quad (7)$$

and

$$B(\zeta_y \omega / u_c) = \exp(-\alpha_2 |\zeta_y| \omega / u_c), \quad (8)$$

where α_1 and α_2 are the constants that should be determined. Substituting Eq. (6) along with Eqs. (7) and (8) into Eq. (5) and performing the Fourier transform yields the frequency-wavenumber spectrum of the turbulent wall pressure (Corcos model):

$$P(k_x, k_y, \omega) = P(\omega) (\alpha_1 \alpha_2 k_c^2) /$$

$$\{\pi^2 [(k_x - k_c)^2 + (\alpha_1 k_c)^2] [k_y^2 + (\alpha_2 k_c)^2]\}, \quad (9)$$

where $k_c = \omega / u_c$ is the convective (hydrodynamic coincidence) wavenumber, and the point power spectrum is given by

$$P(\omega) = a_0 \rho_o^2 v_*^4 / \omega, \quad (10)$$

where $a_0 = 1$ (an approximate, experimental value derived from spectra measured by small hydrophones), ρ_o is the upper fluid density, and v_* is the friction velocity. In the low wavenumber region ($k_x = k_y = 0$), the turbulent wall pressure spectrum given by Eq. (9) reduces approximately to the wavenumber-white, scale-independent form given by Chase [9]:

$$P(k_x, k_y, \omega) \cong C_0 \rho_o^2 v_*^6 / \omega^3. \quad (11)$$

The parameter C_0 related to the low wavenumber is given by Eq. (90) of Chase [9] as

$$C_0 \cong \frac{a_0}{\pi^2} \left(\frac{\alpha_1}{\alpha_2} \right) \left(\frac{u_c}{v_*} \right)^2, \quad (12)$$

provided $\alpha_1^2 < 1$.

The convective flow velocity u_c is a function of frequency as shown by Bull [12] and an empirically fitted expression using Bull's measured data (Figure 15 in Bull [12]) is obtained as

$$u_c = U[0.6 + 0.4 \exp(-0.8\omega\delta^* / U)], \quad (13)$$

where $\delta^* = 0.35$ cm is the average value of the boundary layer displacement thicknesses shown in Bull's measurements. As can be seen in Eq. (13), the convective flow velocity asymptotically approaches the freestream velocity U as the frequency becomes smaller, and $0.6U$ as the frequency becomes larger.

The friction velocity is defined as

$$v_* = (c_f / 2)^{1/2} U, \quad (14)$$

where c_f is the skin friction coefficient. The friction coefficient used here is an empirical expression suggested by Schlichting [13] and is given by

$$c_f = 0.455 (\log R_x)^{-2.58}, \quad (15)$$

where R_x is the Reynolds number.

A recent work by Sherman et al. [14] has shown that the difference between the peak level (convective ridge) of the turbulent wall pressure spectrum and the level at the low wavenumber region is approximately 35 to 45 dB. This value has been estimated by adjusting the contamination due to the acoustic wavenumber and flexural wavenumber of the composite plate at the low wavenumber region. In their study, Martin and Leehey [15] showed that their measurements of low wavenumber wall pressure spectrum are 36 dB below corresponding convective ridge levels. Based on the work of [14],[15], albeit a limited study, the peak-to-low wavenumber difference of 40 dB yields the constants as follows:

$$\alpha_1 = 0.01 \text{ and } \alpha_2 = 1.0. \quad (16)$$

Eq. (9) along with Eq. (10) is the Corcos model representing a wavenumber-frequency turbulent wall pressure on a plane surface in the present study. However, the question of how to develop a proper flow excitation function remains unanswered for the reduction of turbulent boundary layer pressure fluctuations. Many fundamental questions regarding extremely complicated turbulence structures must be answered before an adequate turbulent wall pressure model is fully accepted.

Hydrophone Function. This section presents the development of the hydrophone function for a rectangular sensor (Figure 3). The average pressure acting on a rectangular sensor is written as [16], [17].

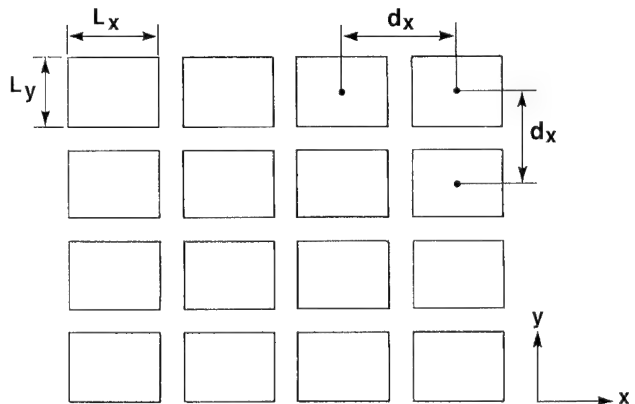


Figure 3. Configuration of Hydrophone Array

$$\langle p(x, y, t) \rangle = \frac{1}{L_x L_y} \int_{-L_x/2}^{+L_x/2} \int_{-L_y/2}^{+L_y/2} p(x, y, t) dx dy, \quad (17)$$

where $\langle \rangle$ denotes the spatial average, and L_x and L_y are the dimensions of the rectangular sensor in the x and y directions, respectively. The Fourier transform of the pressure field is written as

$$\hat{p}(k_x, k_y, \omega) = \frac{1}{(2\pi)^3} \int_{-\infty}^{+\infty} \int_{-\infty}^{+\infty} \int_{-\infty}^{+\infty} p(x, y, t) \times \exp[+i(k_x x + k_y y - \omega t)] dx dy dt, \quad (18)$$

and the inverse Fourier transform is written as

$$p(x, y, t) = \int_{-\infty}^{+\infty} \int_{-\infty}^{+\infty} \hat{p}(k_x, k_y, \omega) \times \exp[-i(k_x x + k_y y - \omega t)] dk_x dk_y d\omega. \quad (19)$$

If Eq. (19) is substituted into Eq. (17), then Eq. (17) is written as

$$\begin{aligned} \langle p(x, y, t) \rangle &= \frac{1}{L_x L_y} \int_{-L_x/2}^{+L_x/2} \exp(-ik_x x) dx \int_{-L_y/2}^{+L_y/2} \exp(-ik_y y) dy \\ &\times \int_{-\infty}^{+\infty} \int_{-\infty}^{+\infty} \int_{-\infty}^{+\infty} \exp(i\omega t) \hat{p}(k_x, k_y, \omega) dk_x dk_y d\omega \\ &= \int_{-\infty}^{+\infty} \int_{-\infty}^{+\infty} \int_{-\infty}^{+\infty} \exp(i\omega t) s(k_x, k_y) \hat{p}(k_x, k_y, \omega) dk_x dk_y d\omega. \end{aligned} \quad (20)$$

The pressure sensitivity $s(k_x, k_y)$ for the rectangular sensor is obtained as

$$s(k_x, k_y) = \frac{\sin(k_x L_x / 2)}{k_x L_x / 2} \times \frac{\sin(k_y L_y / 2)}{k_y L_y / 2}. \quad (21)$$

The frequency spectral density of the rectangular hydrophone response is written as

$$Q(\omega) = 2\pi \int_{-\infty}^{+\infty} \int_{-\infty}^{+\infty} S(k_x, k_y) \Phi_{pp}(k_x, k_y, \omega) dk_x dk_y, \quad (22)$$

where $\Phi_{pp}(k_x, k_y, \omega)$ is the wavenumber-frequency spectrum of the power and $S(k_x, k_y)$ is the hydrophone function of the rectangular sensor as follows:

$$S(k_x, k_y) = [s(k_x, k_y)]^2. \quad (23)$$

Note that in the present study the wavenumber-frequency spectrum of the power $\Phi_{pp}(k_x, k_y, \omega)$ corresponds to the Corcos turbulent wall pressure spectrum.

Array Function. This section presents the development of the array function for a rectangular array of sensors (Figure 3). The average pressure (sum of array outputs) received by $N_x \times N_y$ sensors is written as [16],[18]

$$\begin{aligned} \langle p(x, y, t) \rangle &= \frac{1}{N_x N_y} \iint p(x, y, t) dx dy \\ &= \frac{1}{N_x N_y} \sum_{m=1}^{N_x} \sum_{n=1}^{N_y} p[x + (m-1)d_x, y + (n-1)d_y], \end{aligned} \quad (24)$$

where $\langle \rangle$ denotes the spatial average, and d_x and d_y are the distances between adjacent sensors in the x and y directions, respectively. The Fourier transform of the pressure field is written as

$$\begin{aligned} \hat{p}(k_x, k_y, \omega) &= \frac{1}{(2\pi)^3} \int_{-\infty}^{+\infty} \int_{-\infty}^{+\infty} \int_{-\infty}^{+\infty} p(x, y, t) \\ &\times \exp[+i(k_x x + k_y y - \omega t)] dx dy dt, \end{aligned} \quad (25)$$

and if the rectangular array is realized, then the inverse Fourier transform is written as

$$\begin{aligned} p(x, y, t) &= \int_{-\infty}^{+\infty} \int_{-\infty}^{+\infty} \hat{p}(k_x, k_y, \omega) \\ &\times \exp\{-i[k_x(x + (m-1)d_x) \\ &+ k_y(y + (n-1)d_y) - \omega t]\} dk_x dk_y d\omega. \end{aligned} \quad (26)$$

If Eq. (26) is substituted into Eq. (24), then Eq. (24) is written as

$$\begin{aligned} \langle p(x, y, t) \rangle &= \frac{1}{N_x N_y} \sum_{m=1}^{N_x} \sum_{n=1}^{N_y} \exp\{ik_x[x + (m-1)d_x]\} \\ &\times \exp\{ik_y[y + (n-1)d_y]\} \\ &\times \int_{-\infty}^{+\infty} \int_{-\infty}^{+\infty} \int_{-\infty}^{+\infty} \exp(i\omega t) \hat{p}(k_x, k_y, \omega) dk_x dk_y d\omega \end{aligned}$$

$$= \int_{-\infty}^{+\infty} \int_{-\infty}^{+\infty} \int_{-\infty}^{+\infty} \exp(i\omega t) a(k_x, k_y) \hat{p}(k_x, k_y, \omega) dk_x dk_y d\omega. \quad (27)$$

The pressure sensitivity received by the rectangular array of sensors is written as

$$a(k_x, k_y) = \left[\frac{\sin(N_x k_x d_x / 2)}{N_x \sin(k_x d_x / 2)} \times \frac{\sin(N_y k_y d_y / 2)}{N_y \sin(k_y d_y / 2)} \right]. \quad (28)$$

The frequency spectral density of the total rectangular array response is written as

$$Q(\omega) = 2\pi \int_{-\infty}^{+\infty} \int_{-\infty}^{+\infty} A(k_x, k_y) \Phi_{pp}(k_x, k_y, \omega) dk_x dk_y, \quad (29)$$

where $\Phi_{pp}(k_x, k_y, \omega)$ is the wavenumber-frequency spectrum of the power, and $A(k_x, k_y)$ is the array function of the rectangular array as follows:

$$A(k_x, k_y) = [a(k_x, k_y)]^2. \quad (30)$$

Note that in the present study the wavenumber-frequency spectrum of the power $\Phi_{pp}(k_x, k_y, \omega)$ corresponds to the Corcos turbulent wall pressure spectrum.

Transfer Function. The transfer function is the wavenumber-frequency transform of the normal stress τ_{zz} acting at the standoff distance $z = d$ within the elastomer layer (Figure 2) compared to the wavenumber-frequency transform of the turbulent boundary layer pressure field f_o applied to the elastomer surface $z = h_1$ and is written as

$$T(k_x, k_y, \omega) = \left| \frac{(\tau_{zz})_{z=d}}{(f_o)_{z=h_1}} \right|^2 = \left| \frac{T_{zz}(k_x, k_y, \omega; z=d)}{F_o(k_x, k_y, \omega; z=h_1)} \right|^2, \quad (31)$$

where T_{zz} and F_o are the Fourier transforms of the normal stress τ_{zz} and the turbulent wall pressure field f_o , respectively. The noise reductions calculating the three-dimensional transfer function [19] are found to be approximately the same as those calculated using the two-dimensional transfer function. Therefore, in the present study, a two-dimensional analysis is made and its resulting expression is applied to the three-dimensional problem by approximating such that the wavenumber k_x corresponds to a radial wavenumber $(k_x^2 + k_y^2)^{1/2}$ to cover the $k_x k_y$ plane. The normal and tangential stresses in elastic media [20]-[22] (elastomeric layer and elastic backing plate)

are written as

$$\tau_{zz} = (\lambda + 2\mu) \frac{\partial u_z}{\partial z} + \lambda \frac{\partial u_x}{\partial x} \quad (32)$$

and

$$\tau_{zx} = \mu \left[\frac{\partial u_x}{\partial z} + \lambda \frac{\partial u_z}{\partial x} \right], \quad (33)$$

where λ and μ are Lamé constants, and u_z and u_x are the normal and tangential displacements, respectively, given by

$$u_z = \frac{\partial \phi}{\partial z} + \frac{\partial \psi}{\partial x} \quad (34)$$

and

$$u_x = \frac{\partial \phi}{\partial x} - \frac{\partial \psi}{\partial z}, \quad (35)$$

where ϕ (scalar potential) and ψ (y component of the vector potential) are the solutions of the following two-dimensional wave equations governing small elastic motions:

$$\frac{\partial^2 \phi}{\partial x^2} + \frac{\partial^2 \phi}{\partial z^2} = \frac{1}{c_c^2} \frac{\partial^2 \phi}{\partial t^2} \quad (36)$$

and

$$\frac{\partial^2 \psi}{\partial x^2} + \frac{\partial^2 \psi}{\partial z^2} = \frac{1}{c_s^2} \frac{\partial^2 \psi}{\partial t^2}, \quad (37)$$

where c_c and c_s are the complex compressional and shear wave speeds, respectively, and are given by

$$c_c = [(\lambda + 2\mu) / \rho]^{1/2} \quad (38)$$

and

$$c_s = (\mu / \rho)^{1/2}, \quad (39)$$

where ρ is the material density.

Let us assume that

$$\phi(x, z, t) = \Phi(z) \exp[-i(k_x x - \omega t)] \quad (40)$$

and

$$\psi(x, z, t) = \Psi(z) \exp[-i(k_x x - \omega t)]. \quad (41)$$

Substituting Eqs. (40) and (41) into Eqs. (36) and (37), respectively, gives

$$\frac{d^2\Phi}{dz^2} + (k_d^2 - k_x^2)\Phi = 0 \quad (42)$$

and

$$\frac{d^2\Psi}{dz^2} + (k_s^2 - k_x^2)\Psi = 0, \quad (43)$$

where $k_d = \omega / c_c$ and $k_s = \omega / c_s$ are the compressional (dilatational) and shear wavenumbers, respectively. The solutions of Eqs. (42) and (43) are written as

$$\Phi = A_1 \cos(\alpha z) + B_1 \sin(\alpha z) \quad (44)$$

and

$$\Psi = A_2 \cos(\beta z) + B_2 \sin(\beta z), \quad (45)$$

where $\alpha = (k_d^2 - k_x^2)^{1/2}$ and $\beta = (k_s^2 - k_x^2)^{1/2}$.

The boundary conditions to be satisfied at the interface between the elastomer layer and the fluid (upper medium) are as follows: (1) the pressure acting in the normal direction must be continuous, and (2) the shear stress on the flow surface is assumed to be zero. In the normal direction, we write

$$\left(\tau_{zz}^{(1)}\right)_{z=h_1} = -(p_o + f_o)_{z=h_1}, \quad (46)$$

where $\left(\tau_{zz}^{(1)}\right)_{z=h_1}$ is the normal stress on the elastomer layer surface ($z = h_1$), h_1 is the elastomer layer thickness, p_o is the acoustic pressure (that satisfies the radiation condition) acting on the surface in the water, and f_o is the excitation pressure field acting on the surface. Note that the superscript (1) refers to the elastomer layer. The acoustic pressure field is written as

$$p_o = A_o \exp(-\alpha_o z + i\omega t), \quad z \geq h_1, \quad (47)$$

where A_o is a constant, $\alpha_o = (k_x^2 - k_o^2)^{1/2}$, and $k_o = \omega / c_o$ is the acoustic wavenumber. Further, the acoustic pressure field is coupled to the displacement of the elastomer by

$$\left[\frac{\partial^2 u_z^{(1)}}{\partial^2 t}\right]_{z=h_1} = -\frac{1}{\rho_o} \left[\frac{\partial p_o}{\partial z}\right]_{z=h_1}, \quad (48)$$

where $u_z^{(1)}$ is the normal displacement of the elastomer. Using Eqs. (47) and (48), we obtain

$$(p_o)_{z=h_1} = -[\rho_o \omega^2 / \alpha_o] [u_z^{(1)}]_{z=h_1}. \quad (49)$$

Substituting Eq. (49) into Eq. (46), we obtain

$$\left(\tau_{zz}^{(1)}\right)_{z=h_1} \alpha_o - \rho_o \omega^2 (u_z^{(1)})_{z=h_1} = -\alpha_o f_o, \quad (50)$$

and the boundary condition for the shear stress at the interface is written as

$$\left(\tau_{zx}^{(1)}\right)_{z=h_1} = 0. \quad (51)$$

The boundary conditions to be satisfied at the interface between the elastomer layer and the elastic backing plate are that the normal and tangential stresses and the normal and tangential displacements must be continuous:

$$\left(\tau_{zx}^{(1)}\right)_{z=0} = \left(\tau_{zx}^{(2)}\right)_{z=0}, \quad (52)$$

$$\left(\tau_{zz}^{(1)}\right)_{z=0} = \left(\tau_{zz}^{(2)}\right)_{z=0}, \quad (53)$$

$$(u_x^{(1)})_{z=0} = (u_x^{(2)})_{z=0}, \quad (54)$$

$$(u_z^{(1)})_{z=0} = (u_z^{(2)})_{z=0}. \quad (55)$$

Note that the superscript (2) refers to the elastic backing plate. Using the boundary conditions to be satisfied between the backing plate and the fluid (lower medium), we obtain

$$\left(\tau_{zz}^{(2)}\right)_{z=-h_2} \alpha'_o + \rho'_o \omega^2 (u_z^{(2)})_{z=-h_2} = 0 \quad (56)$$

and

$$\left(\tau_{zx}^{(2)}\right)_{z=-h_2} = 0, \quad (57)$$

where h_2 is the backing plate thickness, $\alpha'_o = (k_x^2 - k_o'^2)^{1/2}$, and $k_o' = \omega / c_o'$. Substituting

Eqs. (32) through (35) into Eqs. (50) through (57), we obtain a system of linear algebraic equations to be solved for undetermined constants $A_1^{(1)}$, $B_1^{(1)}$, ..., $A_2^{(2)}$, and $B_2^{(2)}$ in terms of f_o as follows:

$$\begin{bmatrix} a_{11} & a_{12} & a_{13} & a_{14} & 0 & 0 & 0 & 0 \\ a_{21} & a_{22} & a_{23} & a_{24} & 0 & 0 & 0 & 0 \\ 0 & a_{32} & a_{33} & 0 & 0 & a_{36} & a_{37} & 0 \\ a_{41} & 0 & 0 & a_{44} & a_{45} & 0 & 0 & a_{48} \\ a_{51} & 0 & 0 & a_{54} & a_{55} & 0 & 0 & a_{58} \\ 0 & a_{62} & a_{63} & 0 & 0 & a_{66} & a_{67} & 0 \\ 0 & 0 & 0 & 0 & a_{75} & a_{76} & a_{77} & a_{78} \\ 0 & 0 & 0 & 0 & a_{85} & a_{86} & a_{87} & a_{88} \end{bmatrix} \times \begin{bmatrix} A_1^{(1)} \\ B_1^{(1)} \\ A_2^{(1)} \\ B_2^{(1)} \\ A_1^{(2)} \\ B_1^{(2)} \\ A_2^{(2)} \\ B_2^{(2)} \end{bmatrix} = \begin{bmatrix} b_1 \\ 0 \\ 0 \\ 0 \\ 0 \\ 0 \\ 0 \\ 0 \end{bmatrix}, \quad (58)$$

where

$$\begin{aligned} b_1 &= -\alpha_o f_o, \\ a_{11} &= \rho_1 c_{s_1}^2 (k_x^2 - \beta_1^2) \alpha_o \cos(\alpha_1 h_1) + \rho_o \omega^2 \alpha_1 \sin(\alpha_1 h_1), \\ a_{12} &= \rho_1 c_{s_1}^2 (k_x^2 - \beta_1^2) \alpha_o \sin(\alpha_1 h_1) - \rho_o \omega^2 \alpha_1 \cos(\alpha_1 h_1), \\ a_{13} &= 2i\rho_1 c_{s_1}^2 k_x \beta_1 \alpha_o \sin(\beta_1 h_1) + i\rho_o \omega^2 k_x \cos(\beta_1 h_1), \\ a_{14} &= -2i\rho_1 c_{s_1}^2 k_x \beta_1 \alpha_o \cos(\beta_1 h_1) + i\rho_o \omega^2 k_x \sin(\beta_1 h_1), \\ a_{21} &= 2i\rho_1 c_{s_1}^2 k_x \alpha_1 \sin(\alpha_1 h_1), \\ a_{22} &= -2i\rho_1 c_{s_1}^2 k_x \alpha_1 \cos(\alpha_1 h_1), \\ a_{23} &= -\rho_1 c_{s_1}^2 (k_x^2 - \beta_1^2) \cos(\beta_1 h_1), \\ a_{24} &= -\rho_1 c_{s_1}^2 (k_x^2 - \beta_1^2) \sin(\beta_1 h_1), \\ a_{32} &= -2i\rho_1 c_{s_1}^2 k_x \alpha_1, \\ a_{33} &= -\rho_1 c_{s_1}^2 (k_x^2 - \beta_1^2), \\ a_{36} &= 2i\rho_2 c_{s_2}^2 k_x \alpha_2, \\ a_{37} &= \rho_2 c_{s_2}^2 (k_x^2 - \beta_2^2), \\ a_{41} &= \rho_1 c_{s_1}^2 (k_x^2 - \beta_1^2), \\ a_{44} &= -2i\rho_1 c_{s_1}^2 k_x \beta_1, \\ a_{45} &= -\rho_2 c_{s_2}^2 (k_x^2 - \beta_2^2), \end{aligned}$$

$$\begin{aligned} a_{48} &= 2i\rho_2 c_{s_2}^2 k_x \beta_2, \\ a_{51} &= -ik_x, \\ a_{54} &= -\beta_1, \\ a_{55} &= ik_x, \\ a_{58} &= \beta_2, \\ a_{62} &= \alpha_1, \\ a_{63} &= -ik_x, \\ a_{66} &= -\alpha_2, \\ a_{67} &= ik_x, \\ a_{75} &= \rho_2 c_{s_2}^2 (k_x^2 - \beta_2^2) \alpha'_o \cos(\alpha_2 h_2) + \rho'_o \omega^2 \alpha_2 \sin(\alpha_2 h_2), \\ a_{76} &= -\rho_2 c_{s_2}^2 (k_x^2 - \beta_2^2) \alpha'_o \sin(\alpha_2 h_2) + \rho'_o \omega^2 \alpha_2 \cos(\alpha_2 h_2), \\ a_{77} &= -2i\rho_2 c_{s_2}^2 k_x \beta_2 \alpha'_o \sin(\beta_2 h_2) - i\rho'_o \omega^2 k_x \cos(\beta_2 h_2), \\ a_{78} &= -2i\rho_2 c_{s_2}^2 k_x \beta_2 \alpha'_o \cos(\beta_2 h_2) + i\rho'_o \omega^2 k_x \sin(\beta_2 h_2), \\ a_{85} &= -2i\rho_2 c_{s_2}^2 k_x \alpha_2 \sin(\alpha_2 h_2), \\ a_{86} &= -2i\rho_2 c_{s_2}^2 k_x \alpha_2 \cos(\alpha_2 h_2), \\ a_{87} &= -\rho_2 c_{s_2}^2 (k_x^2 - \beta_2^2) \cos(\beta_2 h_2), \\ a_{88} &= \rho_2 c_{s_2}^2 (k_x^2 - \beta_2^2) \sin(\beta_2 h_2), \end{aligned}$$

where α_1 and β_1 refer to the expressions of α and β (see Eqs. (44) and (45)) for the elastomer layer and α_2 and β_2 for the backing plate; and c_{s_1} and c_{s_2} are the shear wave speeds in the elastomer layer and backing plate, respectively. Note that the expressions α_1 and α_2 used in the coefficients a_{mn} ($m, n = 1, 8$) are different from the constants α_1 and α_2 used in the turbulent wall pressure spectrum in Eq. (9).

Using the constants $A_1^{(1)}$, $B_1^{(1)}$, $A_2^{(2)}$, and $B_2^{(2)}$ obtained from the solution of Eq. (58), the normal stress in the elastomer layer is written as

$$\begin{aligned} \tau_{zz}^{(1)} &= \left[\left(\rho_1 c_{s_1}^2 (k_x^2 - \beta_1^2) \cos(\alpha_1 z) \right) A_1^{(1)} \right. \\ &+ \left(\rho_1 c_{s_1}^2 (k_x^2 - \beta_1^2) \sin(\alpha_1 z) \right) B_1^{(1)} \\ &+ \left(2i\rho_1 c_{s_1}^2 k_x \beta_1 \sin(\beta_1 z) \right) A_2^{(1)} \\ &\left. + \left(-2i\rho_1 c_{s_1}^2 k_x \beta_1 \cos(\beta_1 z) \right) B_2^{(1)} \right] \exp[-i(k_x x - \omega t)]. \quad (59) \end{aligned}$$

Then, the transfer function can be obtained using Eq. (31). It should be mentioned that the transfer function for the elastomer layer backed by a perfectly rigid plane wall can be obtained by solving a system of the following linear algebraic equations for the

constants $A_1^{(1)}$, $B_1^{(1)}$, $A_2^{(1)}$, and $B_2^{(1)}$ in terms of f_o :

$$\begin{bmatrix} a_{11} & a_{12} & a_{13} & a_{14} \\ a_{21} & a_{22} & a_{23} & a_{24} \\ 0 & a_{32} & a_{33} & 0 \\ a_{41} & 0 & 0 & a_{44} \end{bmatrix} \begin{bmatrix} A_1^{(1)} \\ B_1^{(1)} \\ A_2^{(1)} \\ B_2^{(1)} \end{bmatrix} = \begin{bmatrix} b_1 \\ 0 \\ 0 \\ 0 \end{bmatrix}, \quad (60)$$

where $a_{11}, a_{12}, \dots, a_{24}$, and b_1 are given in Eq. (58). However, note that other coefficients that are different from those given in Eq. (58) are given as follows: $a_{32} = \alpha_1$, $a_{33} = -ik_x$, $a_{41} = -ik_x$, and $a_{44} = -\beta_1$.

Evaluation of Turbulent Flow Noise Levels

Turbulent Flow Noise Level Received by a Point Hydrophone Flush-Mounted on a Rigid Surface. The frequency spectral density for this case represents the response of a point hydrophone to the turbulent wall pressure spectrum $P(k_x, k_y, \omega)$ and is written as

$$Q(\omega) = 2\pi \int_{-\infty}^{+\infty} \int_{-\infty}^{+\infty} P(k_x, k_y, \omega) dk_x dk_y. \quad (61)$$

Eq. (61) is simply the integration evaluated for the integrand $P(k_x, k_y, \omega)$ shown in Eq. (9) in the directions of k_x and k_y . The analytically evaluated frequency spectral density is given by [1]:

$$Q(\omega) = 2\pi a_o \rho_o^2 v_*^4 / \omega. \quad (62)$$

Turbulent Noise Level Received by a Finite Hydrophone Flush-Mounted on a Rigid Surface. In this case, the frequency spectral density for a finite hydrophone represents the response of a finite hydrophone to the wall pressure spectrum and is written as

$$Q(\omega) = 2\pi \int_{-\infty}^{+\infty} \int_{-\infty}^{+\infty} P(k_x, k_y, \omega) S(k_x, k_y) dk_x dk_y, \quad (63)$$

where $S(k_x, k_y)$ is the hydrophone function shown in Eq. (23). Eq. (63) is the integration of the product of $P(k_x, k_y, \omega)$ and $S(k_x, k_y)$ in the directions of k_x and k_y . The analytically evaluated frequency spectral density is given by [1]:

$$Q(\omega) = 2\pi [P_o(\omega) \bullet Q_x(\omega) \bullet Q_y(\omega)], \quad (64)$$

where

$$P_o(\omega) = a_o \rho_o^2 v_*^4 \alpha_1 \alpha_2 k_c^2 / (\pi^2 \omega), \quad (65)$$

$$Q_x(\omega) = \frac{\pi}{2\alpha a^2 (\zeta^2 + \alpha^2)^2} \{ 2\alpha a (\zeta^2 + \alpha^2) + (\zeta^2 - \alpha^2) \\ - \exp(-2\alpha a) [(\zeta^2 - \alpha^2) \cos(2a\zeta) + 2\alpha \zeta \sin(2a\zeta)] \}, \quad (66)$$

$$Q_y(\omega) = \frac{\pi}{2b^2 \beta^3} [2b\beta + \exp(-2b\beta) - 1], \quad (67)$$

where $\alpha = \alpha_1 k_c$, $\beta = \alpha_2 k_c$, $a = L_x/2$, $b = L_y/2$, and $\zeta = k_c$.

Turbulent Noise Level Received by an Array of Finite Hydrophones Flush-Mounted on a Rigid Surface. The frequency spectral density for the rectangular array of rectangular hydrophones represents the response of an array of hydrophones to the wall pressure spectrum and is written as

$$Q(\omega) = 2\pi \int_{-\infty}^{+\infty} \int_{-\infty}^{+\infty} P(k_x, k_y, \omega) S(k_x, k_y) A(k_x, k_y) dk_x dk_y. \quad (68)$$

The analytically evaluated frequency spectral density is given by [1]:

$$Q(\omega) = 2\pi [P_o(\omega) \bullet Q_x(\omega) \bullet Q_y(\omega)], \quad (69)$$

where $P_o(\omega)$ is given by Eq. (65), and

$$Q_x(\omega) = \frac{\pi}{2\alpha a^2 (\zeta^2 + \alpha^2)^2 M^2} \sum_{m=1-M}^{M-1} (M - |m|) G(d|m|), \quad (70)$$

where

$$G(d|m|) = 2(a - d|m|) \alpha (\zeta^2 + \alpha^2) + \exp(-2d|m|\alpha) \\ \times [(\zeta^2 - \alpha^2) \cos(2d|m|\zeta) + 2\alpha \zeta \sin(2d|m|\zeta)] - (\zeta^2 - \alpha^2) \\ \times \exp(-2\alpha a) [\cos(2a\zeta) \cos(2d|m|\zeta) \cosh(2d|m|\alpha) \\ + \sin(2a\zeta) \sin(2d|m|\zeta) \sinh(2d|m|\alpha)] \\ - 2\alpha \zeta \exp(-2\alpha a) [\sin(2a\zeta) \cos(2d|m|\zeta) \cosh(2d|m|\alpha) \\ - \cos(2a\zeta) \sin(2d|m|\zeta) \sinh(2d|m|\alpha)] \quad (71)$$

for $a \geq d|m|$, and

$$G(d|m|) = \exp(-2d|m|\alpha) [(\zeta^2 - \alpha^2) \cos(2d|m|\zeta)$$

$$\begin{aligned}
& -\cos(2a\zeta)\cos(2d|m|\zeta)\cosh(2\alpha\alpha) \\
& -\sin(2a\zeta)\sin(2d|m|\zeta)\sinh(2\alpha\alpha)] \\
& +2\alpha\zeta[\sin(2d|m|\zeta)+\sin(2a\zeta)\cos(2d|m|\zeta)\sinh(2\alpha\alpha) \\
& -\sin(2d|m|\zeta)\cos(2a\zeta)\cosh(2\alpha\alpha)]\}
\end{aligned} \quad (72)$$

for $a < d|m|$.

$$Q_y(\omega) = \frac{\pi}{2b^2\beta^3N^2} \sum_{n=1-N}^{N-1} (N-|n|)G(e|n|), \quad (73)$$

where

$$\begin{aligned}
G(e|n|) &= 2(b-e|n|)\beta - \exp(-2e|n|\beta) \\
&+ \exp(-2b\beta)\cosh(2e|n|\beta)
\end{aligned} \quad (74)$$

for $b \geq e|n|$, and

$$G(e|n|) = \exp(-2e|n|\beta)[\cosh(2b\beta) - 1] \quad (75)$$

for $b < e|n|$.

It should be noted that the conditions of $a > d|m|$ (Eq. (71)) and $b > e|n|$ (Eq. (74)) represent the cases where the dimensions of each hydrophone exceed the corresponding separations. This implies that adjacent rectangular hydrophones are overlapping in both the x and y directions.

Turbulent Noise Level Received by an Array of Finite Hydrophones Embedded Within an Outer Decoupler. The frequency spectral density for this case represents the response of an array of hydrophones embedded within a layer of elastomer to the wall pressure spectrum and is given by Eq. (1). Unlike the case of flush-mounted hydrophone arrays, analytical expressions are not available for frequency spectral densities. Therefore, the integration of Eq. (1) can be solved only by the numerical integration method.

Numerical Results

Wavenumber-Frequency Spectra for Corcos Model. In the numerical calculations the following baseline data were used:

$$U = 20 \text{ knots},$$

$$v_* = 0.035 U, \quad (76)$$

$$\rho_o = 1.0 \text{ g/cm}^3,$$

$$c_o = 150,000 \text{ cm/s}.$$

Figure 4(a) shows the numerically calculated results of the Corcos turbulent wall pressure spectrum as a function of the wavenumbers k_x and k_y for the frequency of 100 Hz. As shown in Eq. (9), the peak of the wall pressure spectrum occurs at the convective wavenumber ($k_c = \omega / u_c$) that carries most of the turbulent flow energy. The value of u_c was calculated from Eq. (13). Note that the wall pressure spectrum is expressed in $\text{dB} / (\text{dynes/cm}^2)^2 \text{ cm}^2 \text{ s}$. Figure 4(b) presents the calculated wall pressure spectra as a function of k_x with $k_y = 0$ for the frequencies of 100, 500, and 1000 Hz. As anticipated, the peak of the wall pressure spectrum moves to a high wavenumber as the frequency increases. Notice that the spectrum is inversely proportional to ω^3 .

Turbulent Flow Noise Level Received by the Point Hydrophone. The turbulent flow noise level can be calculated by evaluating the frequency spectral density shown in Eq. (62). Figure 5 presents turbulent flow noise levels in $\text{dB}/\mu\text{Pa}^2\text{Hz}^{-1}$ as a function of frequency in Hz calculated for various flow speeds. The solid, dashed, and chain-dotted curves are the results for $U = 30, 20$, and 10 knots, respectively. It is shown in the figure that the noise level decreases as the freestream velocity decreases. As shown in Eq. (62), the noise level is proportional to U^4 and inversely proportional to ω . The noise level expressed in $\text{dB}/\mu\text{Pa}^2\text{Hz}^{-1}$ (M.K.S. unit) was obtained by adding 100 dB to the results calculated using the C.G.S. units.

Turbulent Flow Noise Level Estimate for the Flush-Mounted Rectangular Hydrophone. The turbulent flow noise level for a finite hydrophone can be calculated by evaluating the frequency spectral density shown in Eq. (63). Although the evaluation of Eq. (63) can be made easily using Eq. (64), it is important to analyze the integrand in order to understand spatial filtering. Figure 6 shows the turbulent wall pressure spectrum (chain-dotted line) of 20-knot freestream velocity for 500 Hz, the hydrophone function of $L_x = 2$ in. (dashed line), and the product of the two functions (solid line), as a function of k_x with $k_y = 0$. Remember that the wall pressure spectrum is expressed in $\text{dB} / (\text{dynes/cm}^2)^2 \text{ cm}^2 \text{ s}$. If the dimension of the hydrophone becomes 4 in., then the beamwidth of

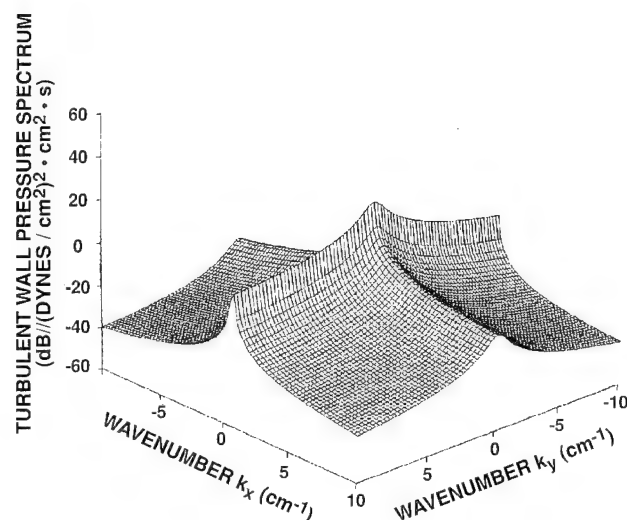


Figure 4(a). Corcos Turbulent Wall Pressure Spectra (at 100 Hz) as Functions of k_x and k_y

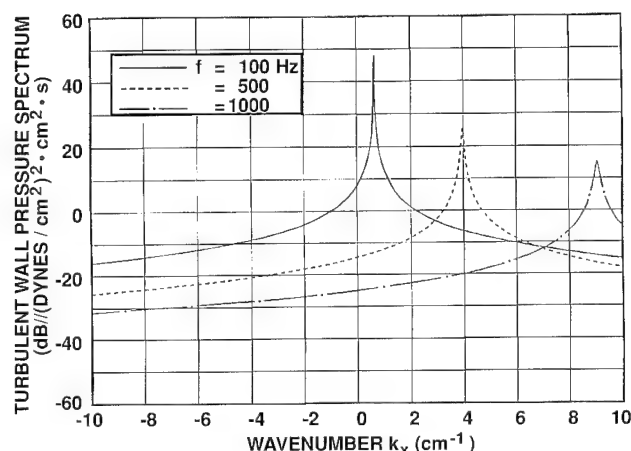


Figure 4(b). Turbulent Wall Pressure Spectra as a Function of k_x for Different Frequencies ($k_y = 0$)

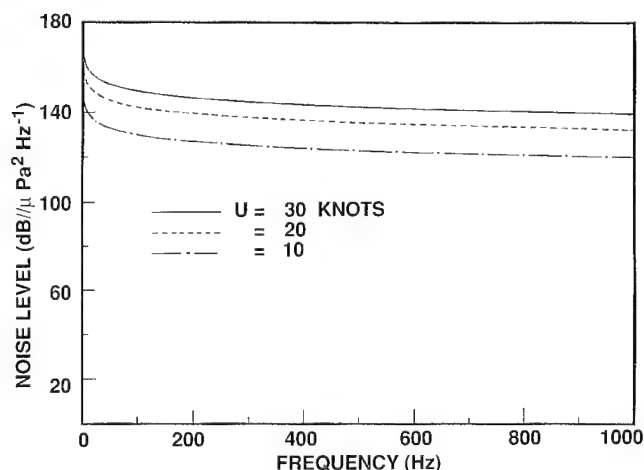


Figure 5. Turbulent Flow Noise Levels Received by a Point Hydrophone as a Function of Frequency for Different Freestream Velocities

the hydrophone becomes one half of the width shown in the figure, making the product much lower than that shown in the figure. This implies that the integrand becomes smaller as the dimension of the hydrophone becomes larger. Therefore, a larger hydrophone serves as a better wavenumber filter in controlling turbulent flow noise. Similar discussions can be made for the dimension of the hydrophone in the k_y direction with $k_x = 0$.

The noise reduction is defined as

$$NR = 10 \log_{10} \left| \frac{[Q(\omega)]}{[Q(\omega)]_0} \right| \text{ dB}, \quad (77)$$

where $[Q(\omega)]$ is the frequency spectral density calculated for a given hydrophone using Eq. (64) and $[Q(\omega)]_0$ is that calculated for a point hydrophone using Eq. (62).

Figure 7 presents the turbulent flow noise reductions calculated for single hydrophones having the area of 1 in.² as a function of frequency in Hz, using $U = 20$ knots and $v_w = 0.035 U$. The solid, chain-dotted, dashed, chain-dashed, and double chain-dotted lines are the turbulent flow noise reductions calculated for the 1-in. x 1-in., 2-in. x 0.5-in., 4-in. x 0.25-in., 0.5-in. x 2-in., and 0.25-in. x 4-in. hydrophones, respectively. It is shown in the figure that the flow noise decreases as the aspect ratio (L_x / L_y) of the hydrophone increases. This confirms the measured data (effect of transducer size and shape) of turbulent boundary layer pressure fluctuations by Recine [23] and White [24]. The peaks in the curve correspond to locations where the convective wavenumber is aligned with the major and sidelobe level peaks of the beam pattern. Conversely, the valleys in the curve correspond to locations where the convective wavenumber is aligned with the nulls ($k_x = \pm 2m\pi / L_x$, $m = 1, 2, 3, \dots$) of the beam pattern.

Figure 8 shows the turbulent flow noise reductions obtained for the 1-, 5-, and 20-in.-square hydrophones mounted on a rigid surface. The freestream velocity is 20 knots. The effects of various hydrophone shapes and of shaded hydrophones on the flow noise reduction are presented in [17] and [25], respectively.

Turbulent Flow Noise Estimate for the Flush-Mounted Rectangular Array. The turbulent flow noise level for an array of finite hydrophones can be calculated by evaluating the frequency spectral density shown in Eq. (68). Although the evaluation of Eq. (68) can be made easily using Eq. (69), it is important to analyze the integrand in order to understand spatial filtering through an array of finite hydrophones. Figure 9 shows the turbulent

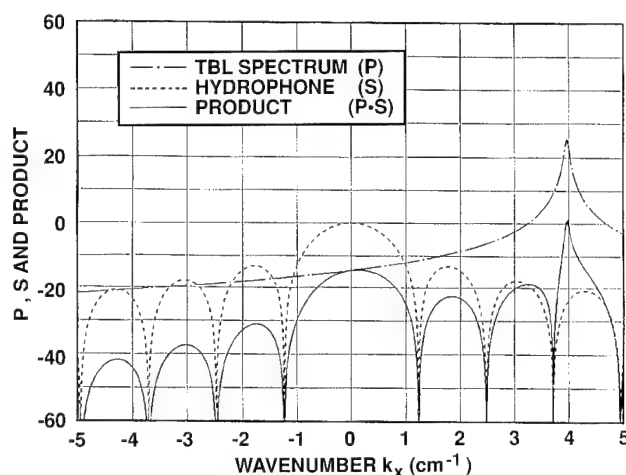


Figure 6. Turbulent Wall Pressure Spectrum at 500 Hz, Hydrophone Function for $L_x = 2$ in., and Their Product

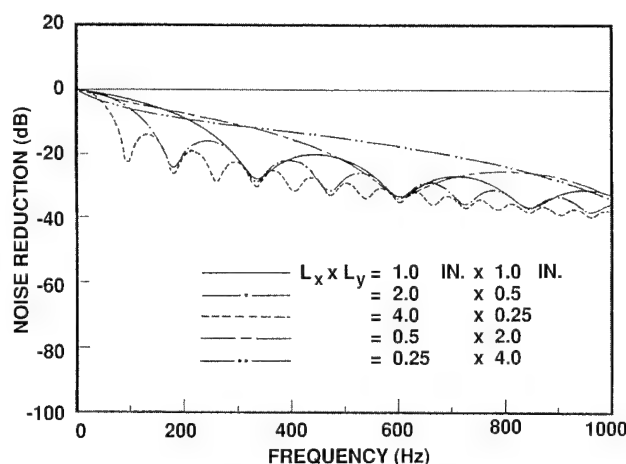


Figure 7. Effect of Aspect Ratio on Turbulent Flow Noise Reduction

wall pressure spectrum (chain-dotted line) at 500 Hz for a freestream velocity of 20 knots, the hydrophone function for $L_x = 2$ in. (dashed line), the array function for $N_x = 5$ (dotted line), and the product of the three functions (solid line), as a function of k_x . Remember that the wall pressure spectrum is expressed in $\text{dB}/(\text{dynes}/\text{cm}^2)^2 \text{cm}^2 \text{s}$. As can be seen in the figure, the aliasing lobes of the array with $N_x = 5$ and $d_x = 2$ in. are canceled by the nulls of the hydrophone beam pattern with $L_x = 2$ in. This is because the array aliasing lobes occur at $(k_x = \pm 2n\pi/d_x, n = 1, 2, 3, \dots)$ and the hydrophone nulls occur at $(k_x = \pm 2m\pi/L_x, m = 1, 2, 3, \dots)$. Then, the integrand becomes smaller as shown in the figure.

Figure 10 presents the turbulent flow noise reductions as a function of frequency calculated for

the 5×5 and 40×40 array elements having 2-in.-square hydrophones without gaps between hydrophones. These results were calculated using $U = 20$ knots and $v_* = 0.035 U$. The solid and chain-dashed curves represent the 5×5 and 40×40 arrays, respectively. As shown in the figure, the flow noise is further reduced as the number of array elements increases. The peaks in the curve correspond to locations where the convective wavenumber is aligned with the array sidelobes. Remember that, in practice, there are gaps between hydrophones even though they may be hairline thin.

Figure 11 presents the turbulent flow noise reductions as a function of frequency calculated for the 5×5 and 40×40 array elements with 2-in.-square hydrophones having 1-in. gaps between adjacent hydrophones. These results were

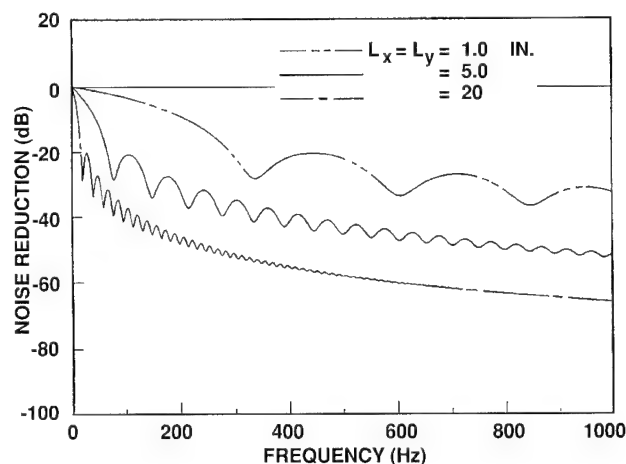


Figure 8. Effect of Hydrophone Dimensions (Flush-Mounted) on Turbulent Flow Noise Reduction

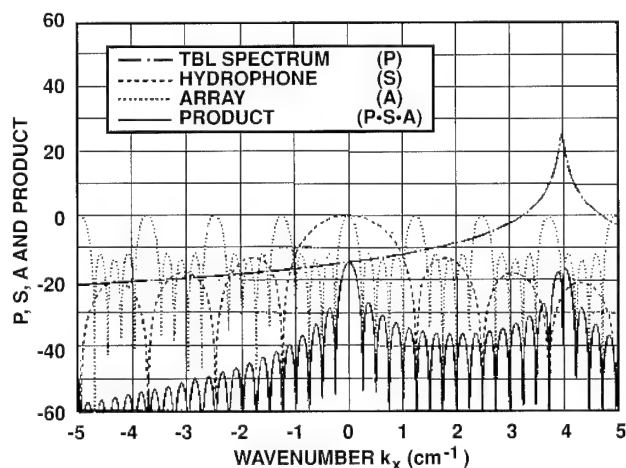


Figure 9. Turbulent Wall Pressure Spectrum, Hydrophone Function for $L_x = 2$ in., Array Function for $N_x = 5$, and Their Product

calculated using $U = 20$ knots and $v_* = 0.035 U$. The solid and chain-dashed curves represent the 5×5 and 40×40 arrays, respectively. As shown in the figure, the flow noise is further reduced as the number of hydrophones in the array increases. The peaks in the curves correspond to locations where the convective wavenumber is aligned with (1) the sidelobes of the array and the hydrophone (lower peaks) and (2) the array aliasing lobes (higher peaks). The valleys in the curves correspond to the nulls of the array and the hydrophone. In the present case, $L_x = 2$ in. and $d_x = 3$ in., and thus, the array aliasing lobes occurring at k_x with $n = 3, 6, 9, \dots$ are canceled by the hydrophone nulls occurring at k_x with $m = 2, 4, 6, \dots$. The curves show that every third aliasing lobe has been canceled by every other hydrophone null.

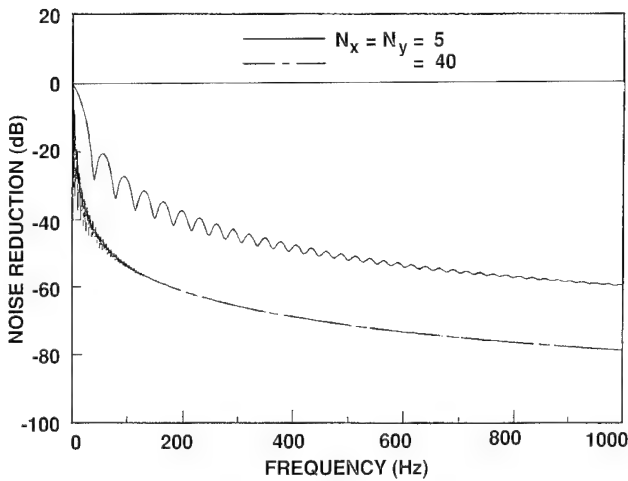


Figure 10. Effect of the Number of Hydrophones in an Array (Without Inter-Hydrophone Spacing) on Noise Reduction

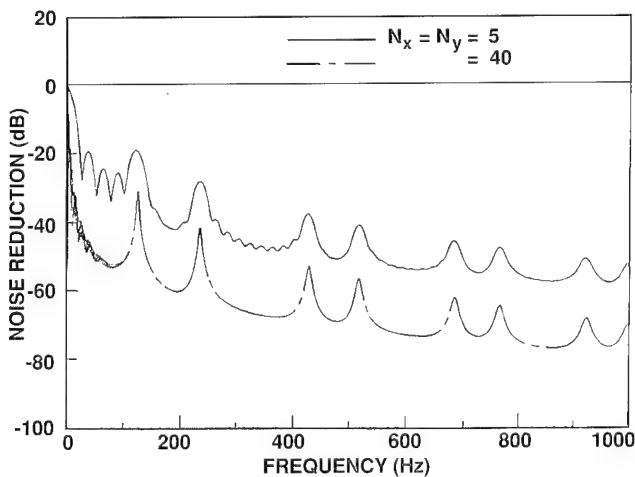


Figure 11. Effect of the Number of Hydrophones in an Array (with Inter-Hydrophone Spacing) on Noise Reduction

Turbulent Flow Noise Estimate for an Array of Hydrophone Embedded Within the Outer Decoupler. In calculating the transfer function given by Eq. (31), it is necessary to use the properties of the elastomer layer and backing plate as well as the geometry. The major parameters required in the evaluation of Eq. (58) are the material density, the compressional and shear wave speeds in the material, and the densities and acoustic wave speeds of the fluid media in contact with the elastomer layer and the backing plate. Note that compressional and shear wave speeds are given by Eqs. (38) and (39). The Lamé constants λ and μ shown in both equations can be expressed in terms of elastic constants as follows:

$$\lambda = E\sigma / [(1 + \sigma)(1 - 2\sigma)] \text{ and } \mu = E / [2(1 + \sigma)], \quad (78)$$

where E is Young's modulus and σ is Poisson's ratio. The elastomer layer (rubber) has a Young's modulus ranging on the order of 10^7 to 10^9 dynes/cm² as a function of frequency. Poisson's ratio σ for the rubber material is normally 0.5. Rubber is a lossy material whose Young's modulus has an imaginary part. The complex (dynamic) Young's modulus is given by $E = E_r + iE_i$, where E_r and E_i are the real and imaginary parts of the Young's modulus, respectively. Actual values of E_r and E_i for a given material can be obtained from measurements. The ratio of E_i to E_r for rubber ranges from 0.1 to 1.0, depending on the frequency. As can be seen in Eq. (78), λ cannot be defined for rubber-like materials because λ is infinite when $\sigma = 0.5$. Therefore, the compressional wave speed cannot be obtained from Eq. (38), but the shear wave speed can be obtained from Eq. (39). An alternative expression for the compressional wave speed in rubber is

$$c_c = [(B + 4\mu / 3) / \rho]^{1/2}, \quad (79)$$

where B is the complex bulk modulus of the material and is not directly obtained from elastic constants. Note that $|B| \gg |\mu|$. The loss factor associated with the compressional wave is normally very small and is weakly dependent on frequency. The complex compressional and shear wave speeds for the elastomer layer are now written as follows:

$$c_{c_1} = c_{c_0} (1 + i\zeta_{c_1})^{1/2} \quad (80)$$

and

$$c_{s_1} = c_{s_0} (1 + i\zeta_{s_1})^{1/2}, \quad (81)$$

where c_{co_1} and c_{so_1} are the compressional and shear wave speeds in the elastomer layer, and ζ_{c_1} and ζ_{s_1} are the loss factors associated with compressional and shear wave speeds. The backing plate used in the present study is made of steel and its Lamé constants λ and μ can be expressed in terms of E and σ as shown in Eq. (78). Normally, the Young's modulus of a steel plate is real because it is not considered as lossy material. However, most structures are subject to structural damping. Thus, a frequency-independent small loss factor can be assigned in the calculation of the transfer function. Then, the complex compressional and shear wave speeds in the backing plate can be directly obtained by using Eqs. (38) and (39) in terms of the complex Young's modulus and Poisson's ratio, and are written as follows:

$$c_{c_2} = c_{co_2} (1 + i\zeta_{c_2})^{1/2} \quad (82)$$

and

$$c_{s_2} = c_{so_2} (1 + i\zeta_{s_2})^{1/2}, \quad (83)$$

where c_{co_2} and c_{so_2} are the compressional and shear speeds, and ζ_{c_2} and ζ_{s_2} are the loss factors associated with compressional and shear wave speeds. The baseline data used in the calculation of the transfer function are as follows:

ρ_o (water density)	1.0 g/cm ²
c_o (sound speed in water)	150,000 cm/s
ρ'_o (air density)	0.00121 g/cm ²
c'_o (sound speed in air)	34,000 cm/s
h_1 (elastomer layer thickness)	7.62 cm (3 in.)
ρ_1 (elastomer density)	1.2 g/cm ³
c_{so_1} (shear wave speed in elastomer)	2000 cm/s
c_{co_1} (compressional wave speed in elastomer)	200,000 cm/s
ζ_{s_1} (shear loss factor of elastomer)	0.3
ζ_{c_1} (compressional loss factor of elastomer)	0.03
h_2 (backing plate thickness)	5.08 cm (2 in.)
ρ_2 (steel density)	7.8 g/cm ³
E_2 (Young's modulus of steel)	19.5×10^{11} dyne/cm ²
σ_2 (Poisson's ratio of steel)	0.3
ζ_{s_2} (shear loss factor of steel)	0.005

ζ_{c_2} (compressional loss factor of steel)	0.001
d (standoff distance)	0

Figure 12 shows the transfer function calculated using the above set of data for different frequencies. The transfer functions for 100, 500, and 1000 Hz are given by the solid, dashed, and chain-dotted lines, respectively. Note the case of 500 Hz. The valley (dip) shown in the figure occurs at the acoustic wavenumber $k_o = \omega / c_o = 0.02094 \text{ cm}^{-1}$. The sharp peak following the valley occurs at the flexural wavenumber originating from the backing plate. The flexural wavenumber at 500 Hz for a 2-in.-steel backing plate is 0.0705 cm^{-1} as shown in the figure.

Figure 13 presents the transfer functions calculated at 1000 Hz for the 3-in.-thick elastomer layer backed by various thicknesses of the steel plate. The solid line is the calculated result for the 3-in.-thick elastomer layer backed by an infinitely rigid wall. The calculated results for the 0.5-, 2-, and 5-in. plate thicknesses are given by the dashed, chain-dotted, and chain-dashed lines, respectively. As shown in the figure, the flexural wavenumber for the steel plate increases as the plate thickness decreases. The flexural wavenumber at 1000 Hz for the 2-in. steel backing plate is 0.0985 cm^{-1} . The transfer functions fall off rapidly beyond the respective flexural wavenumbers. It is noticed that the transfer function for a 3-in.-thick elastomer layer backed by a perfectly rigid surface (solid line) does not exhibit flexural vibration of the plate.

Figure 14 presents the calculated transfer functions with various thicknesses of the elastomer layer for 1000 Hz. The calculated results for the 0.05-, 1-, 2-, 3-, 5-, and 10-in. layer thicknesses are given by the solid, dashed, chain-dotted, chain-dashed, double chain-dotted, and double chain-dashed lines, respectively. The effectiveness of the

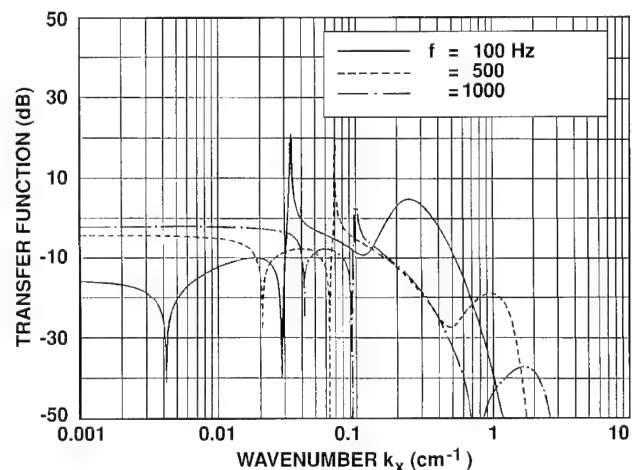


Figure 12. Transfer Functions for Different Frequencies

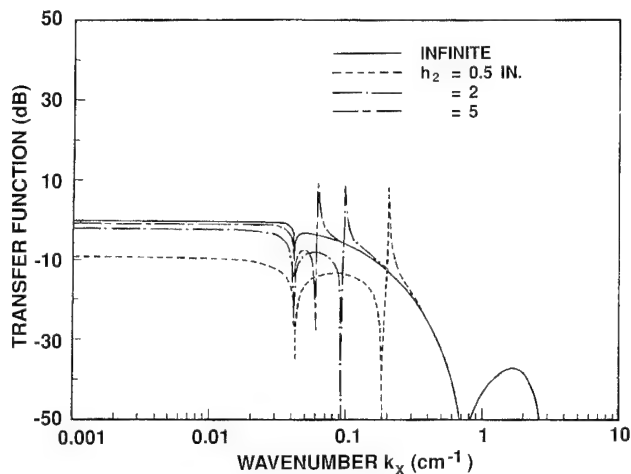


Figure 13. Effect of Backing Plate Thickness h_2 on the Transfer Function at 1000 Hz

elastomer layer as a wavenumber filter is clearly demonstrated beyond the flexural wavenumber. The transfer function falls off faster as the elastomer layer thickness increases. The trend shown in the figure indicates that the transfer function for an infinitely thick elastomer layer is composed of solely the flexural wave region (which is greater than the acoustic region).

In calculating the turbulent flow noise reduction through a layer of elastomer, it is necessary to integrate numerically the integrand shown in Eq. (1), with $S(k_x, k_y) = 1$ and $A(k_x, k_y) = 1$. The baseline data used in calculating noise reductions are the same as those listed earlier, except for the following parameters:

h_1 (elastomer layer thickness)	5.08 cm (2 in.)
d (standoff distance)	1.27 cm (0.5 in.)
$L_x = L_y$ (hydrophone dimension)	5.08 cm (2 in.)

Figure 15 shows the wavenumber-dependent functions necessary for computing the frequency spectral density. The turbulent wall pressure spectrum at 500 Hz, transfer function at 500 Hz ($h_1 = 2$ in., $d = 0.5$ in.), and their product are given by the chain-dotted, dashed, and solid lines, respectively. Remember that the sharp peak shown in the transfer function is the flexural wavenumber at 500 Hz. As mentioned earlier, an elastomer layer is used to minimize the area under the solid line curve by filtering wavenumbers through the layer thickness. Figure 16 shows the flow noise reduction curves calculated for various thicknesses of the elastomer layer. The results shown in the figure are for the point hydrophone with the standoff distance $d = 0.5$ in. as a function of frequency. The frequency interval used for the calculation of these results is 100 Hz. The results calculated for the 1-,

2-, 3-, 5-, and 10-in.-thick elastomer layer are denoted by the solid, dashed, chain-dotted, chain-dashed, and double chain-dotted lines, respectively. As can be seen in the figure, more noise is attenuated as the layer thickness increases for all the frequencies considered here. However, the maximum achievable noise reduction is limited by the transfer function composed solely of the flexural wave region, as shown in Figure 14.

Figure 17 shows the effect of shear wave speed in the layer on the turbulent noise reduction. The results calculated for the shear wave speeds of 2000, 6000, and 10000 cm/s are denoted by the solid, dashed, and chain-dotted lines, respectively. As can be seen in the figure, more noise is attenuated as the shear wave speed increases for the low frequency range. On the other hand, noise is less attenuated as the shear wave speed increases for the high frequency range. It should be remembered that the

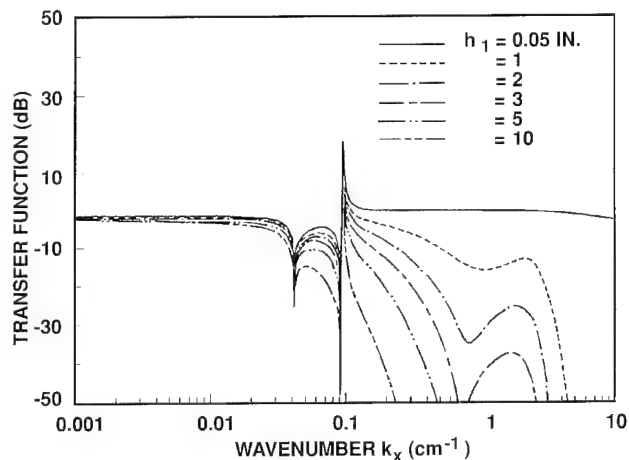


Figure 14. Effect of Elastomer Layer Thickness h_1 on the Transfer Function at 1000 Hz

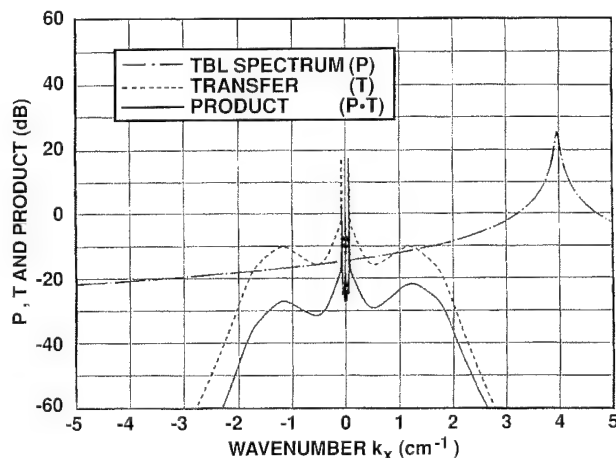


Figure 15. Turbulent Wall Pressure Spectrum, Transfer Function, and Their Product at 500 Hz

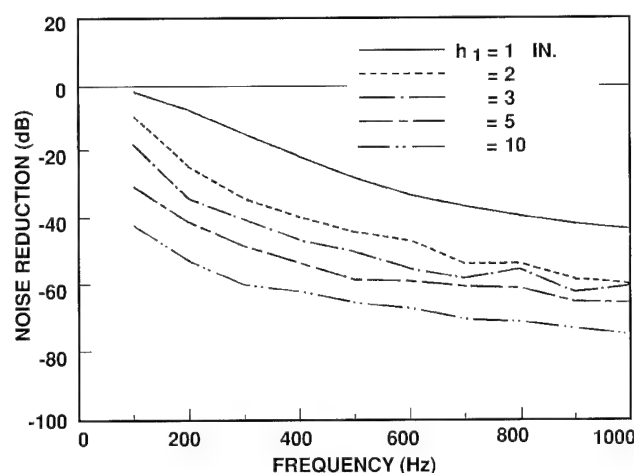


Figure 16. Effect of Elastomer Layer Thickness on Noise Reduction

shear wave speed in the elastomer layer is a function of frequency. Therefore, this particular phenomenon cannot be generalized.

Figure 18 shows the effect of the loss factor associated with shear wave on the turbulent noise reduction. The results calculated for the loss factors of 0.2, 0.6, and 1.0 are denoted by the solid, dashed, and chain-dotted lines, respectively. The figure indicates that as the loss factor increases noise attenuation increases, as expected. However, further noise reduction cannot be achieved beyond a certain value of the loss factor. Because the loss factor is a function of frequency, this phenomenon cannot be generalized.

In calculating the turbulent flow noise reduction using an array of hydrophones embedded within a layer of elastomer, it is necessary to integrate numerically the integrand shown in Eq. (1). Figure 19 shows the wavenumber-dependent functions necessary for computing the frequency spectral density. The turbulent wall pressure spectrum at 500 Hz, hydrophone function ($L_x = 2$ in.), array function ($N_x = 5$), and transfer function at 500 Hz ($h_1 = 2$ in., $d = 0.5$ in.), and their product are given by the chain-dotted, dashed, dotted, chain-dashed, and solid lines, respectively. As mentioned earlier, the use of an elastomer layer is to minimize the area under the solid line curve by filtering wavenumbers through the layer thickness.

Figure 20 shows a comparison of the flow noise reduction curve calculated for a flush-mounted, 1-in.-square hydrophone with that calculated for a 1-in.-square hydrophone embedded within a 2-in.-thick elastomer layer. The standoff distance d is 0.5 in. The noise reduction calculated for the flush-mounted hydrophone is given by the solid line. The calculated result for the flush-mounted hydrophone shown in the figure starts at 1 Hz and has a 1-Hz

frequency interval. The calculated results for the embedded hydrophone are denoted by solid circles starting at 100 Hz and having a 100-Hz frequency interval. As expected, the embedded hydrophone gives more noise reduction. This is due to the filtering effect of the elastomer layer thickness in addition to the spatial averaging of the hydrophone. In practice, hydrophones are covered with a layer of elastomer; thus, the peaks and valleys shown in the flush-mounted hydrophone performance will not appear when hydrophones are embedded within the layer having a reasonable thickness.

Figure 21 shows the effect of hydrophone dimensions on the turbulent noise reduction. The frequency interval used for the calculation of these results is 100 Hz. The solid, dashed, and chain-dotted lines are the noise reductions achieved by 1-, 5-, and 20-in.-square hydrophones, respectively, embedded within a 2-in.-thick elastomer layer with

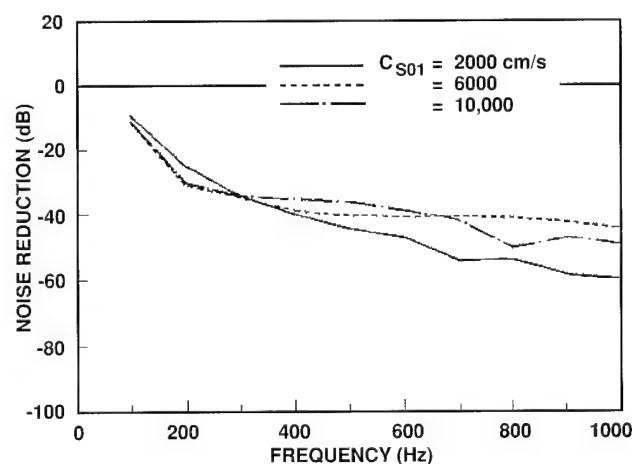


Figure 17. Effect of Shear Wave Speed on Noise Reduction

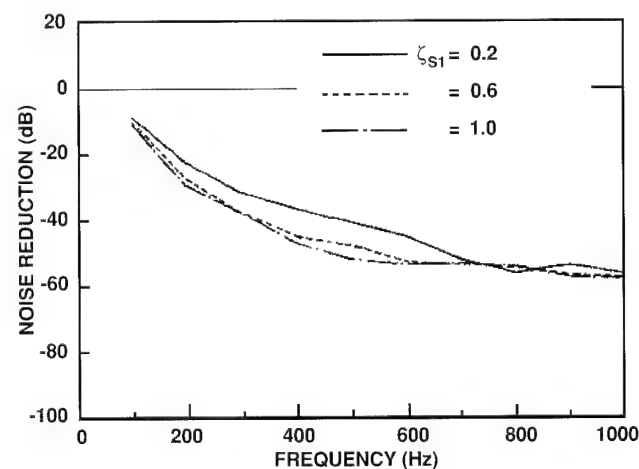


Figure 18. Effect of Loss Factor on Noise Reduction

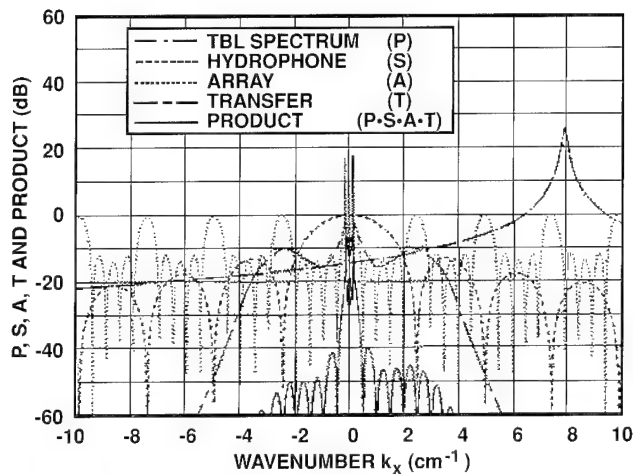


Figure 19. Turbulent Wall Pressure Spectrum, Transfer Function, Hydrophone Function, Array Function, and Their Product at 500 Hz

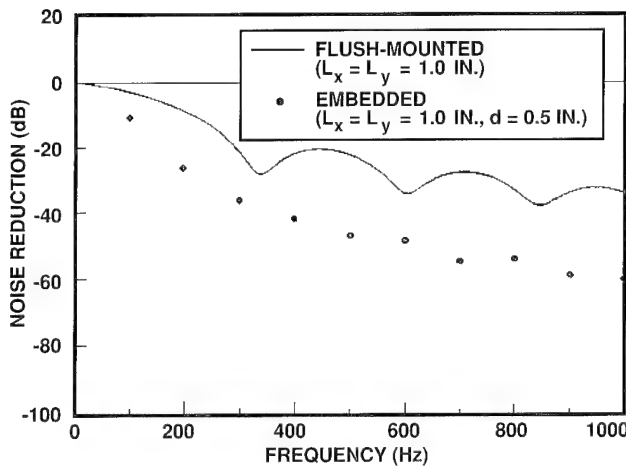


Figure 20. Comparison of Noise Reduction by an Embedded Hydrophone with a Flush-Mounted Hydrophone

a standoff distance of 0.5 in. As can be seen in the figure, more noise is attenuated as the hydrophone dimensions increase within the layer for all frequencies up to 1000 Hz.

Figure 22 illustrates the effect of the number of hydrophones in an array on the turbulent noise reduction. The results shown in the figure are for various arrays of 2-in.-square hydrophones embedded within a 2-in.-thick elastomer layer with a standoff distance of 0.5 in.. The solid, dashed, chain-dotted, and chain-dashed curves are the noise reductions achieved by the 5 x 5, 10 x 10, 20 x 20, and 40 x 40 arrays of 2-in.-square hydrophones with no spacings between adjacent hydrophones. Notice that when the length of the array is doubled, the area that covers the hydrophone array becomes four times larger. This fact is reflected in the noise reduction curves showing a 6-dB difference between

successive curves, except in the low frequency range. Figure 23 presents the noise reductions achieved by the 5 x 5, 10 x 10, 20 x 20, and 40 x 40 arrays of 2-in.-square hydrophones, respectively, with 1-in. spacings between adjacent hydrophones. It is also shown in the figure that there is a 6-dB difference between successive curves.

It is important to mention that the noise reduction is limited by the area that covers the hydrophone array with zero inter-element spacing. This applies to both flush-mounted and embedded hydrophone arrays. Specifically, for a given area of 80 in.², the following arrangements of hydrophone arrays will provide the same amount of turbulent flow noise reduction.

Hydrophone Dimensions	Array Dimensions
1-in. x 1-in.	80 x 80
2-in. x 2-in.	40 x 40
4-in. x 4-in.	20 x 20
8-in. x 8-in.	10 x 10
16-in. x 16-in.	5 x 5

If there is no inter-element separation, then $d_x = L_x$ and $d_y = L_y$. In this case, the product of $S(k_x, k_y)$ and $A(k_x, k_y)$ is written as

$$S(k_x, k_y)A(k_x, k_y) = \left[\frac{\sin(k_x L_x / 2)}{k_x L_x / 2} \times \frac{\sin(k_y L_y / 2)}{k_y L_y / 2} \right]^2$$

$$\times \left[\frac{\sin(N_x k_x L_x / 2)}{N_x \sin(k_x L_x / 2)} \times \frac{\sin(N_y k_y L_y / 2)}{N_y \sin(k_y L_y / 2)} \right]^2$$

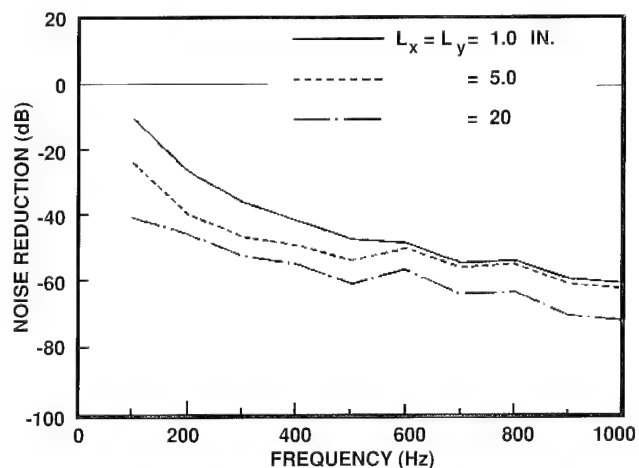


Figure 21. Effect of Dimensions of a Hydrophone Embedded Within a 2-in. Elastomer Layer

$$= \left[\frac{\sin(N_x k_x L_x / 2)}{(N_x k_x L_x / 2)} \times \frac{\sin(N_y k_y L_y / 2)}{(N_y k_y L_y / 2)} \right]^2. \quad (84)$$

Note that the above equation is identical with the hydrophone function $S(k_x, k_y)$ having an axial dimension of $N_x L_x$ and a lateral dimension of $N_y L_y$. In practice, there exists a hair-thin separation between elements for the hydrophone array with zero inter-element spacing.

Conclusions

A study has been made for predictions of the flow noise level received by an array of rectangular hydrophones (1) flush-mounted on a rigid surface and (2) embedded within a layer of elastomer backed by an elastic plate of a finite thickness. The other side of the elastomer is exposed to turbulent flow. The present work describes techniques for reducing

turbulent boundary layer pressure fluctuations using wavenumber filters, such as finite hydrophones or an array of hydrophones or an elastomer layer. The baseline turbulent wall pressure spectrum that represents the flow excitation function is based on the Corcos model modified to fit a 40-dB difference between the peak and the low wavenumber region. The occurrence of the convective ridge wavenumber is estimated by using a convective flow speed that is a function of frequency. Based on this study, the following conclusions are made:

1. The frequency spectral density that represents the hydrophone array response has been obtained by evaluating the double integral. In the flush-mounted case, the double integral is reduced to the product of two single integrals. The two single integrals have been evaluated analytically by using the contour integral. In the embedded case, the double integral has been evaluated numerically via Simpson's rule.

2. More noise is attenuated as (a) the hydrophone dimensions increase and (b) the number of array elements increases. This performance applies to the array configurations with and without inter-hydrophone spacings.

3. More noise is attenuated as the thickness of an elastomer layer increases. However, it should be remembered that the maximum noise reduction using the elastomer layer backed by an elastic plate is limited by the transfer function composed only of the flexural wave region and, thus, the noise cannot be reduced without bound as the thickness increases.

4. The peaks and valleys seen in the noise reduction curves for the flush-mounted case will not appear when a hydrophone or an array of hydrophones is embedded within a layer of elastomer.

5. More noise is attenuated as (a) the loss factor of an elastomer layer increases and (b) the shear wave speed in the layer increases (for the low frequency region). Because a frequency-independent value for the shear wave speed is used in calculating the noise reduction, this performance cannot be generalized. It is suggested that measured values for both shear wave speeds and loss factors be used for predicting turbulent flow noise levels.

6. The techniques described for the flush-mounted case provide a tool for the quick estimate of the response of an array of hydrophones to turbulent boundary layer pressure fluctuations. In practice, an array of hydrophones is covered with a layer of elastomer that protects the array and serves as a wavenumber filter.

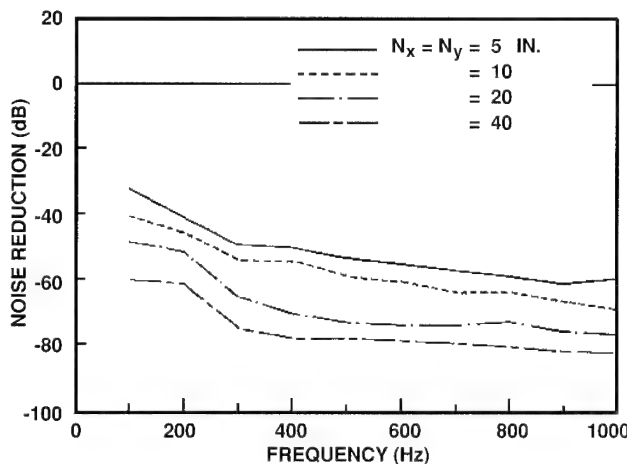


Figure 22. Effect of Number of Hydrophones (Without Inter-Hydrophone Spacing) Embedded Within a 2-in. Elastomer Layer

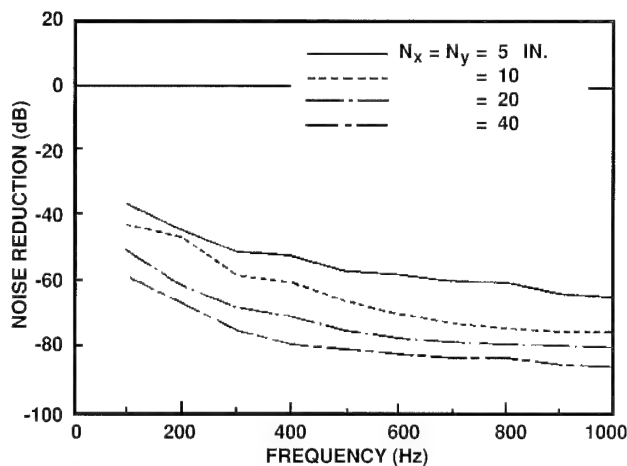


Figure 23. Effect of Number of Hydrophones (with Inter-Hydrophone Spacing) Embedded Within a 2-in. Elastomer Layer

7. The noise reduction is virtually limited by the area that covers an array of hydrophones without inter-element spacing. Specifically, the turbulent flow noise reduction that can be achieved by an array of hydrophones occupying the same area is equal, regardless of hydrophone size incorporated in the array.

8. It is recommended that the original Corcos model with $\alpha_1 = 0.01$ and $\alpha_2 = 1.0$ (in lieu of $\alpha_1 = 0.09$ and $\alpha_2 = 0.63$) be used as a turbulent wall pressure spectrum (an excitation function) in calculating the flow noise reduction.

Acknowledgment

The author would like to express his appreciation to Dr. Howard H. Schloemer for his encouragement and helpful discussion.

References

- [1] S. H. Ko and A. H. Nuttall, "Analytical Evaluation of Flush-Mounted Hydrophone Array Response to the Corcos Turbulent Wall Pressure Spectrum," *Journal of the Acoustical Society of America*, vol. 90, no. 1, 1991, pp. 579-588.
- [2] W. Thompson and Z. E. Montgomery, "Approximate Evaluation of the Spectral Density Integral for a Large Planar Array of Rectangular Sensors Excited by Turbulent Flow," *Journal of the Acoustical Society of America*, vol. 93, no. 6, 1993, pp. 3201-3207.
- [3] S. H. Ko and H. H. Schloemer, "Calculations of Turbulent Boundary Layer Pressure Fluctuations Transmitted into a Viscoelastic Layer," *Journal of the Acoustical Society of America*, vol. 85, no. 4, 1989, pp. 1469-1477.
- [4] S. H. Ko and H. H. Schloemer, "Flow Noise Reduction Techniques for a Planar Array of Hydrophones," *Journal of the Acoustical Society of America*, vol. 92, no. 6, 1992, pp. 3409-3424.
- [5] D. M. Chase and R. Stern, "Turbulent-Boundary-Layer Transmitted into an Elastic Layer," BBN Technical Memorandum No. 382, Bolt Beranek and Newman, Inc., Cambridge, MA, November 1977.
- [6] G. Maidanik and D. W. Jorgensen, "Boundary Wave-Vector Filters for the Study of the Pressure Field in a Turbulent Boundary Layer," *Journal of the Acoustical Society of America*, vol. 42, no. 2, 1967, pp. 494-501.
- [7] W. K. Blake and D. M. Chase, "Wavenumber-Frequency Spectra of Turbulent-Boundary-Layer Pressure Measured by Microphone Arrays," *Journal of the Acoustical Society of America*, vol. 49, no. 3, 1971, pp. 862-877.
- [8] G. M. Corcos, "The Structure of the Turbulent Pressure Field in Boundary Layer Flows," *Journal of Fluid Mechanics*, vol. 18, 1964, pp. 353-378.
- [9] D. M. Chase, "Modelling the Wave-Vector Frequency Spectrum of Turbulent Boundary Wall Pressure," *Journal of Sound and Vibration*, vol. 70, no. 1, 1980, pp. 29-67.
- [10] J. Ffowcs Williams, "Boundary-Layer Pressure and Corcos Model: A Development to Incorporate Low Wavenumber Constraints," *Journal of Fluid Mechanics*, vol. 125, 1982, pp. 9-25.
- [11] J. M. Witting, "A Spectral Model of Pressure Fluctuations at a Rigid Wall Bounding an Incompressible Fluid, Based on Turbulent Structures in the Boundary Layer," *Noise Control Engineering Journal*, vol. 26, no. 1, 1986, pp. 28-43.

- [12] M. K. Bull, "Wall-Pressure Fluctuations Associated with Subsonic Turbulent Boundary Layer Flow," *Journal of Fluid Mechanics*, vol. 28, 1967, pp. 719-754.
- [13] H. Schlichting, *Boundary Layer Theory*, McGraw-Hill, New York, 1968, p. 602.
- [14] C. H. Sherman, S. H. Ko, and B. G. Buehler, "Measurement of the Turbulent Boundary Layer of Wave-Vector Spectrum," *Journal of the Acoustical Society of America*, vol. 88, no. 1, 1990, pp. 386-390.
- [15] N. C. Martin and P. Leehey, "Low Wavenumber Wall Pressure Measurements Using a Rectangular Membrane as a Spatial Filter," *Journal of Sound and Vibration*, vol. 52, no. 1, 1977, pp. 95-120.
- [16] W. K. Blake, *Mechanics of Flow-Induced Sound and Vibration*, vol. II, Academic Press, Inc., New York, 1986.
- [17] S. H. Ko, "Performance of Various Shapes of Hydrophones in the Reduction of Turbulent Flow Noise," *Journal of the Acoustical Society of America*, vol. 93, no. 3, 1993, pp. 1293-1299.
- [18] B. D. Steinberg, *Principles of Aperture and Array System Design*, John Wiley and Sons, New York, 1976.
- [19] S. H. Ko, "Application of Elastomeric to the Reduction of Turbulent-Boundary-Layer Pressure Fluctuations (Three-dimensional Analysis)," *Journal of Sound and Vibration*, vol. 159, no. 3, 1992, pp. 469-481.
- [20] H. Kolsky, *Stress Wave in Solids*, Dover Publications, Inc., New York, 1963.
- [21] T. R. Meeker and A. H. Meizler, "Guided Wave Propagation in Elongated Cylinders and Plates," in *Physical Acoustics*, W. P. Mason (ed.), Academic Press, New York, 1964.
- [22] J. D. Achenbach, *Wave Propagation in Elastic Solid*, North Holland Publishing Co., New York, 1973.
- [23] E. C. Recine, "Measured Discrimination of Boundary Layer Pressure Fluctuations by Round, Square, and Rectangular Transducers," *Journal of the Acoustical Society of America*, vol. 51, no. 1, 1972, pp. 369-377.
- [24] P. H. White, "Effect of Transducer Size, Shape, and Surface Sensitivity on the Measurement of Boundary Layer Pressure," *Journal of the Acoustical Society of America*, vol. 41, 1967, no. 5, pp. 1358-1363.
- [25] S. H. Ko, "Performance of Shaded, Rectangular Hydrophones in the Reduction of Turbulent Flow Noise," *Journal of the Acoustical Society of America*, vol. 94, no. 3, 1993, pp. 1681-1687.



SUNGHWAN KO is a research physicist in the Submarine Sonar Department at NUWC's New London Detachment. He is currently responsible for the reduction of the turbulent flow noise received by an array of hydrophones embedded within an outer decoupler mounted on a submarine hull. Dr. Ko received a B.S. degree from the

Republic of Korea Merchant Marine Academy and M.S. and Ph.D. degrees from the University of Rochester. His principal areas of work have included the following: hydrodynamic instability, acoustic waveguides as applied to aircraft engine noise reduction and to the reduction of ship piping noise, structure-fluid interaction problems, hydrophone modeling, flexural wave baffling, aero- and hydroacoustics, and hull-mounted array design and development of the self-noise reduction techniques that have a direct impact on sonar systems. He has published 32 refereed journal articles, mainly in the field of acoustics. Dr. Ko has been a NUWC staff member since 1972, prior to which he was employed by the Boeing Aircraft Company and General Dynamics. Dr. Ko is a Fellow of the Acoustical Society of America and the recipient of the 1991 Excellence in Science Award of the Naval Underwater Systems Center (NUWC's predecessor organization).

Compressive Strength of Continuous Fiber-Reinforced Composite Components in the Hydrospace Environment

Francis C. Spicola and Neil J. DuBois
Naval Undersea Warfare Center Division Newport

Abstract

To satisfy the requirement to carry ever-increasing payloads to deep depths, continuous fiber-reinforced composite material components must be designed so that internal stress fields are within structural failure design limits for tensile, shear, and compressive stresses. The focus of this article concerns the first-article failure observations of greatest interest in hydrospace applications, namely, continuous fiber-reinforced flat plate components subjected to either uniaxial or biaxial compressive loading and filament-wound, right circular cylindrical shells subjected to external hydrostatic pressure loads. Inconsistencies in experimental results, which make failure prediction for composite hydrospace components a very difficult and costly process, motivated the development of a general analysis tool that would predict failure loads with a high enough confidence level to eliminate the need for full-scale model testing prior to first article fabrication. The analysis, developed at the Naval Undersea Warfare Center (NUWC) Division Newport, appears useful in the prediction of composite shell failure. Significant progress has been made in exposing the hidden physics of compressive failure in continuous fiber-reinforced materials.

The promise of lightweight, high-strength composite materials as the solution to small-scale autonomous vehicle payload limitations in hydrospace has never been fulfilled. To satisfy the requirement to carry ever-increasing payloads to deep depths, continuous fiber-reinforced composite material components must be designed so that internal stress fields are within structural failure design limits for tensile, shear, and compressive stresses. Failure levels for tensile and shear stresses in fiber-reinforced composites are reasonably well understood; thus, they do not pose significant problems for the experienced developer. However, the same cannot be said for compressive stresses. The vagaries of compressive failure in composite material components inhibit realizing the full potential of lightweight, high-strength composite materials in hydrospace.

The analysis of compressive failure in composites requires many considerations. Principal among these are the compressive strength of the composite material based on fiber strength with no instability; global buckling, which is usually predicted and observed in very-thin-walled components; and microbuckling, a phenomenon unique to compressively loaded, continuous fiber-reinforced structural components. Other considerations are the effects of brittle fiber kinking, initial fiber waviness, void content, broken fibers, fiber misalignment, fiber resin interface bond, seawater and other liquid saturation, cosmic ray

impingement, and resin strain to failure. Each of these considerations contributes in some way to deterioration in compressive strength, leading to failures at load levels significantly below those generally predicted with existing analytical tools (i.e., extensions of isotropic, homogeneous structural analysis methods).

It is generally accepted that microbuckling is the prime mover in the compressive failure of continuous fiber-reinforced composite material components. However, most developers either ignore the phenomenon or design around it. Those who ignore it (and they make up the majority of developers) are usually surprised with low-level failures following first-article fabrication. The primary reasons for ignoring microbuckling are the absence of both the necessary analytical tools and the lack of understanding of the physics of the phenomenon. Those few who design around the microbuckling produce significantly overdesigned products and, thus, never realize the full potential of weight savings.

The first-article failure observations of the greatest interest in hydrospace applications (and the focus of this article) are continuous fiber-reinforced flat plate components subjected to either uniaxial or biaxial compressive loading and filament-wound, right-circular cylindrical shells subjected to external hydrostatic pressure loads. For the flat plate, compressive failures occur at levels well below

smear property predictions. These results are readily observed in ASTM test sample geometries for both unidirectional and bidirectional loading. In the case of unidirectional loading, compressive strength is inversely proportional to sample thickness and directly proportional to matrix (resin) modulus of elasticity. For bidirectional loading, the trend of the relationship with respect to sample thickness and matrix modulus is similar, but the level of strength at failure falls off in the major fiber direction as transverse loading is increased. In the case of right-circular cylindrical shells, the strength levels at failure are observed to be below those of flat plates; however, unlike flat plates, a relative increase in apparent strength is observed as thickness increases. The low stress level failures in cylindrical shells appear to be pure compressive failures and are well below global buckling predictions, except for very-thin-walled samples.

These inconsistencies make failure prediction for composite hydrospace components a very difficult and costly process, requiring up-front, full-scale model testing to ensure structural integrity. As a result, a decision was made at the Naval Undersea Warfare Center (NUWC) Division Newport to try to develop a general analysis tool that addresses and reliably predicts failure stresses for compressively loaded, continuous fiber-reinforced composite components. The goal was to generate an analysis that predicts failure loads with a high enough confidence level to eliminate full-scale model testing prior to first-article fabrication. The kernel of the analysis was developed utilizing an energy approach for the prediction of buckling in an axially loaded, continuous fiber embedded in a composite continuum of parallel fibers and a matrix [1]-[4] (see Figure 1).

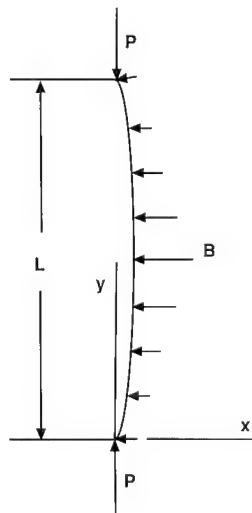


Figure 1. Buckling of a Fiber in an Elastic Continuum

To initiate the development of the energy solution for the buckling of the fiber shown in Figure 1, the general expression for the fiber deflection is represented by the series

$$y = a_1 \sin\left(\pi \frac{x}{L}\right) + a_2 \sin\left(2\pi \frac{x}{L}\right) + a_3 \sin\left(3\pi \frac{x}{L}\right) + \dots \quad (1)$$

The strain energy of bending for the fiber is

$$\Delta U_1 = \frac{E_f}{2} I_f \int_0^L \left(\frac{d^2 y}{dx^2} \right)^2 dx, \quad (2)$$

$$\Delta U_1 = \frac{\pi^4 E_f}{4L^3} I_f \sum_{n=1}^{\infty} n^4 a_n^2.$$

The total energy of deformation for the fiber/matrix continuum is

$$\Delta U_2 = \frac{B}{2} \int_0^L y^2 dx, \quad (3)$$

$$\Delta U_2 = \frac{BL}{4} \sum_{n=1}^{\infty} a_n^2,$$

where B is a measure of the composite continuum's stiffness per unit length of fiber.

The work done by the compressive force P is

$$\Delta T = \frac{P\pi^2}{4L} \sum_{n=1}^{\infty} n^2 a_n^2. \quad (4)$$

Because the work done by the compressive force equals the sum of the strain energies

$$\Delta T = \Delta U_1 + \Delta U_2,$$

$$P = \frac{\pi^2 E_f}{L^2} I_f \left[\frac{\sum_{n=1}^{\infty} n^4 a_n^2 + \frac{BL^4}{\pi^4 E_f} I_f^{-1} \sum_{n=1}^{\infty} a_n^2}{\sum_{n=1}^{\infty} n^2 a_n^2} \right].$$

The critical value of P is found when all coefficients a_n , except one, are made equal to zero:

$$P_{cr} = \frac{\pi^2 E_f}{L^2} I_f \left[n^2 + \frac{BL^4}{n^2 \pi^4 E_f} I_f^{-1} \right]. \quad (5)$$

From Eq. (5), the equation for critical stress can be formulated:

$$S_{cr} = \frac{\pi^2 E_f}{L^2 A_f} I_f \left[n^2 + \frac{BL^4}{n^2 \pi^4 E_f} I_f^{-1} \right], \quad (6)$$

where

E_f = modulus of elasticity of the fiber,

I_f = moment of inertia of the fiber,

A_f = cross-sectional area of the fiber,

L = length of the fiber,

n = number of half wavelengths in the buckled fiber, and

B = transverse support stiffness per unit length of fiber.

A three-point flexure test sequence was conducted to verify Eq. (6). Eight unidirectional S2 fiberglass/epoxy sets of five small-scale beams were fabricated. Four sets had a cross-section that measured 0.500 in. by 0.100 in., with matrices having four different moduli (410, 480, 550, 620 ksi), one for each set of five samples. The second group of four was fabricated with the same width and moduli distribution, but a thickness of 0.200 in. (See Figure 2 for a sketch of the test sample and fixture.) The experimental results obtained are presented in Figure 3. Figure 3 includes the prediction of Eq. (6), as well as the predictions of the best available analyses outside of NUWC [5],[6].

The curves presented in Figure 3 indicate that the NUWC analysis is in close agreement with the ultimate compression strengths observed in the three-point verification bending tests. This close agreement is consistent for the variations in strength as a function of epoxy resin modulus and as a function of test sample thickness. The analytical results show an increase in compressive strength with increase in matrix modulus and a decrease in compressive strength with increase in sample thickness. The transverse support stiffness term, B in Eq. (6), is responsible for the sensitivity

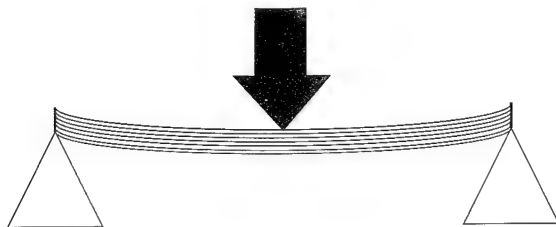


Figure 2. Simply Supported Beam with Transverse Mid-Span Load and Unidirectional Reinforcement Fibers

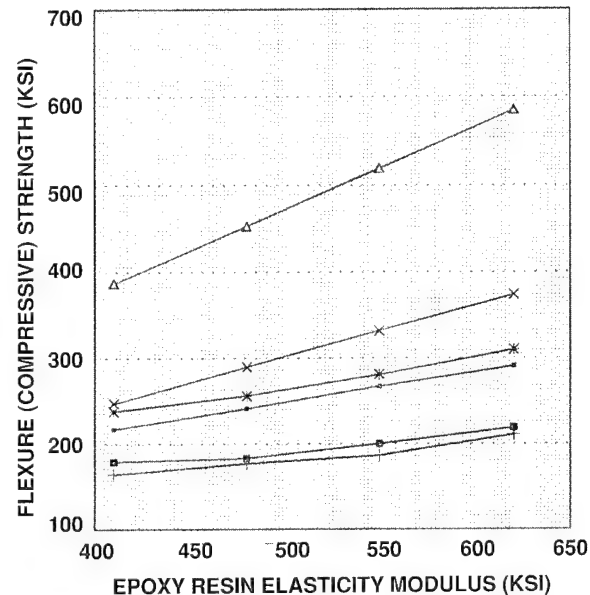
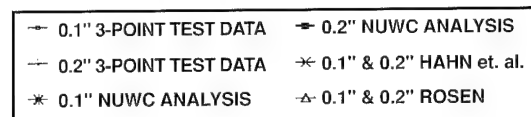


Figure 3. Unidirectional S2 Fiberglass/Epoxy Three-Point Flexure Test Data Compared to NUWC, Rosen [5] and Hahn and Williams [6] Microbuckle Analyses

of the NUWC analysis to the physics of composite material compression failure levels. It decreases in value with increasing transverse support material depth or thickness, and it increases in value as matrix elasticity modulus is increased.

Neither the analysis by Rosen [5] nor Hahn and Williams [6] agrees with experimental results. With respect to variations in resin modulus, the two analyses do not agree quantitatively, nor do they exhibit the same trend as the experimental results. In addition, the analyses of both Hahn and Rosen are insensitive to variations in sample thickness. Consider the equations presented in these works. From Rosen [5],

$$S_{cr} = \frac{G_m}{1 - v_f}, \quad (7)$$

where

G_m = shear modulus of the matrix, and

v_f = fiber fraction by volume.

From Hahn and Williams [6],

$$S_{cr} = v_f \left(\frac{G_m}{1 - v_f} \right). \quad (8)$$

In Eqs. (7) and (8), there are no terms for transverse support; and the relationship between critical stress and shear modulus is a smeared properties relationship, which has been shown to be incorrect, both analytically and experimentally.

In addition to the fiberglass/epoxy bending test, Eq. (6) has been applied to several different geometries, other reinforcing fibers, and different loading formats. The NUWC analysis was verified a second time in a three-point bending test with carbon fibers rather than fiberglass. Carbon fibers are much stiffer than fiberglass in the axial direction, but they are much less stiff in the transverse direction, making them very anisotropic and, thus, providing a very different bending test. ASTM-type compression tests (pure column compression tests) were performed with both fiberglass and carbon fiber and different matrix moduli with very good agreement. Close agreement was observed when fiber reinforcements were alternately laid up in flat plates in an orthogonal format. Initial research with composite cylinders under external hydrostatic pressure has been very encouraging. It appears that the basic NUWC analysis can be used to predict composite shell

failure by assuming the global buckle shape provided by traditional stability theory and smeared properties, and then testing local high stress regions with a modified version of Eq. (6). There also seems to be a potential for predicting biaxially loaded flat plate failure if Eq. (6) can be reformulated with additional work and energy terms.

While significant progress has been made in exposing the hidden physics of compressive failures in continuous fiber-reinforced materials, much remains to be done. Mechanical properties databases have to be expanded/developed. Accurate analytical methods for establishing composite mechanical properties from constituent properties must be improved/developed to compensate for shortfalls in empirical databases. Compression fixtures that minimize fixture effects have to be improved/developed. The analysis of cylindrical shells has to be completed. Microbuckle theory has to be extended to biaxially loaded flat plates. Irregular shapes and nonorthogonal reinforcing fiber orientations have to be addressed, and a structured algorithm has to be developed that is capable of addressing all continuous fiber-reinforced materials subjected to compression loading.

References

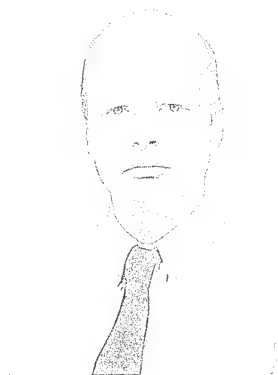
- [1] F. C. Spicola and N. J. Dubois, "An Algorithm for the Analysis of Critical Stresses in Unidirectional Continuous Fiber Laminates," *ASME Computers in Engineering Conference Proceedings*, vol. 2, August 1990, pp. 691-698.
- [2] F. C. Spicola and N. J. Dubois, "An Algorithm for the Analysis of Critical Stresses in Continuous Filament Reinforced Flat Plates Subjected to Unidirectional Compressive Loading," *Eighth International Conference on Composite Materials Proceedings*, July 1991, pp. 4-D-1 to 4-D-10.
- [3] F. C. Spicola, N. J. Dubois, W. C. Tucker, J. C. Butts, and T. Juska, "Compressive Strength of Fiber Reinforced Composites as a Function of Matrix Modulus of Elasticity and Component Wall Thickness," *Ninth International Conference on Composite Materials Proceedings*, vol. VI, July 1993, pp. 573-580.
- [4] F. C. Spicola, N. J. Dubois, W. C. Tucker, and J. C. Butts, "Structural Failure in Filament Wound Right Circular Cylindrical Shells Subjected to Biaxial External Pressure," *Ninth International Conference on Composite Materials Proceedings*, vol. V, July 1993, pp. 209-216.
- [5] B. W. Rosen, "Mechanics of Composite Strengthening," *Fiber Composite Materials*, American Society for Metals, 1965, pp. 37-75.
- [6] T. H. Hahn and J. G. Williams, "Compression Failure Mechanisms in Unidirectional Composites," *Composite Materials: Testing and Design (Seventh Conference)*, ASTM STP 893, 1986, pp. 115-139.

FRANCIS C. SPICOLA

is a mechanical engineer in the Solid Mechanics and Design Branch at NUWC Division Newport. He earned B.S. (1962) and M.S. (1967) degrees in Mechanical Engineering from the University of Rhode Island and has been a NUWC employee for almost 30 years. Mr. Spicola is presently involved in research and development in the area of Composite Materials applications for advanced undersea vehicles and in advancing the state-of-the-art in structural analysis for continuous, fiber-reinforced composite materials.

**NEIL J. DUBOIS**

is a mechanical engineer in the Solid Mechanics and Design Branch at NUWC Division Newport. He received a B.S. degree in Mechanical Engineering Design from Worcester Polytechnic Institute and an M.S. degree in Solid Mechanics from Brown University. His principal duties include vibration isolation design and structural acoustic analysis/testing.



Simplified Structural Acoustic Characterization of External Compliant Coatings on Submerged Surfaces

Bruce E. Sandman and Jeffrey E. Boisvert
Naval Undersea Warfare Center Division Newport

Abstract

Experimental and theoretical analyses have demonstrated that the introduction of a compliant layer at the interface between the structure and fluid medium provides a substantial reduction in the radiated noise due to internal and/or external excitation of the structure. This article derives the appropriate equations in a simplified first-order analysis that identifies the essential parameters governing external compliant coating noise reduction performance, in order to implement an initial near-optimum coating design.

Introduction

The radiation efficiency of submerged structures with extended surfaces such as plates and shells is a critical parameter in the radiated noise produced by both internal and external force and pressure fluctuations. Both experimental and theoretical analyses have demonstrated that the introduction of a compliant layer at the interface between the structure and fluid medium produces a substantial reduction in the radiated noise that results from internal and/or external excitation of the structure. To design and implement an external acoustic decoupling coating with near-optimal noise reduction performance considering the constraints of sub-structure thickness/stiffness, depth pressure, coating thickness, and temperature, it is appropriate to outline a simplified first-order analysis that identifies the essential parameters that control external compliant coating noise reduction potential.

This article derives the appropriate equations that govern external coating noise isolation in terms of simplified structural parameters and geometries. Although the approach is not intended to capture the specific details of a given structural configuration, the analysis provides the essential parametric sensitivities needed for the initial "near-optimum" coating design.

Massless Point Reacting Coating

Consider a continuous and macroscopically homogeneous layer of finite thickness h_c and transverse modulus E_c that exhibits infinitesimal transverse shear transfer. This coating layer is shown in Figure 1. Because the layer is assumed to be massless and point-reacting, the fundamental

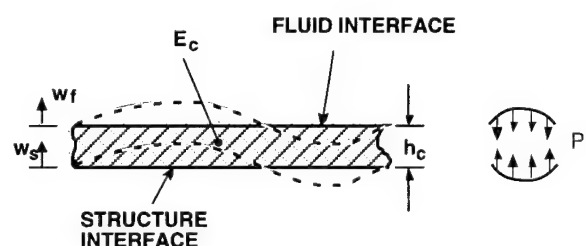


Figure 1. Compliant Point-Reacting Layer Schematic

equation relating the transverse deformation of the layer is given by

$$\tilde{P}_f(\bar{x}, \omega) = \frac{E_c}{h_c} [\tilde{w}_s(\bar{x}, \omega) - \tilde{w}_f(\bar{x}, \omega)] \quad (1)$$

where it is shown that the dependent variables have been transformed to the frequency ω domain. The coordinate vector \bar{x} describes the geometry of the structure and its spatial characteristics. Thus, it is seen that the pressure \tilde{P}_f produces a compression of the coating $\Delta\tilde{w} = \tilde{w}_s - \tilde{w}_f > 0$. This is the specific result that is termed velocity reduction across a compliant layer or coating.

Eq. (1) can be written in the form

$$\tilde{w}_f = \tilde{w}_s - Y_c \tilde{P}_f \quad (2)$$

where $Y_c = h_c / E_c$ denotes the compliance or mobility of the coating layer. The displacements \tilde{w}_f and \tilde{w}_s are measures of motion at the fluid and structural interfaces, respectively. The \bar{x} -

dependence is suppressed in order to present the following simplified characterization of the transmissibility exhibited by the point-reacting compliant layer. The reaction of the fluid to the surface motion of the coating can be represented [1] by the relationship

$$\tilde{P}_f = \rho_f c_f Z_f(i\omega) \tilde{w}_f, \quad (3)$$

where ρ_f and c_f are, respectively, the density and speed of sound in the fluid media. The fluid impedance Z_f may be represented by the form

$$Z_f = R_f + iM_f, \quad (4)$$

which separates the impedance into resistive and reactive components. Note that Z_f of Eq. (4) is nondimensional. A specific form for Z_f will be presented for numerical analysis. Eq. (3) may be combined with Eq. (2) to produce the result

$$[1 + \rho_f c_f(i\omega) Z_f Y_c] \tilde{w}_f = \tilde{w}_s, \quad (5)$$

or

$$\tilde{P}_f = \frac{\rho_f c_f(i\omega) Z_f}{1 + \rho_f c_f(i\omega) Z_f Y_c} \tilde{w}_s. \quad (6)$$

From Eq. (6) it is seen that, if the compliance of the coating becomes zero, the pressure produced in the fluid is directly related to the motion \tilde{w}_s of the structural surface. The motion of the structural surface can be related to forces or pressures by the following generalization:

$$\tilde{w}_s = Y_s \tilde{P}_a - Y_s \tilde{P}_f, \quad (7)$$

where Y_s represents the structural mobility, \tilde{P}_a is the applied pressure that drives the structure, and \tilde{P}_f is the pressure field on the structure induced by the motion in the fluid. By combining Eqs. (7), (6), and (3), it is determined that

$$[1 + \rho_f c_f(i\omega) Z_f (Y_c + Y_s)] \tilde{w}_f = Y_s \tilde{P}_a. \quad (8)$$

This equation governs the motion of the fluid/compliant layer interface for a given pressure input \tilde{P}_a to the structure.

Radiated Acoustic Power

The radiated power produced at the fluid/compliant layer interface is expressed as

$$\hat{\Pi}_{rad} = \frac{1}{2} \text{Re} \left\{ \iint_A P_f V_f^* dA \right\}. \quad (9)$$

It is now assumed that the pressure P_f and velocity V_f do not vary significantly over the area. Thus, the radiating area is acting as an equivalent piston. From the relationship that $V_f^* = (-i\omega) \tilde{w}_f^*$ with $*$ denoting the complex conjugate, it is found that Eq. (9) yields

$$\hat{\Pi}_{rad} = \frac{1}{2} \rho_f c_f \omega^2 R_f |\tilde{w}_f|^2, \quad (10)$$

where $\hat{\Pi}$ is the power per unit area and R_f is the resistive part of the fluid acoustic impedance Z_f defined by Eq. (4). From Eq. (8) it may be verified that

$$|\tilde{w}_f|^2 = \frac{|Y_s|^2}{|1 + \rho_f c_f(i\omega) Z_f (Y_c + Y_s)|^2} \tilde{P}_a^2, \quad (11)$$

and the radiated acoustic power per unit area is directly related to the squared amplitudes of applied force, structural/coating mobility, and fluid impedance. As a refined definition of parameters, it is assumed that the structure acts as a rigid piston and the corresponding mobility is

$$Y_s = -\frac{1}{\rho_s h_s \omega^2}, \quad (12)$$

where ρ_s is the mass density and h_s is the thickness of the rigid circular plate. In addition, the coating compliance is taken to be of the form

$$Y_c = \frac{h_c(1 - i\eta_c)}{\hat{E}_c}, \quad (13)$$

with $\hat{E}_c = E_c(1 + \eta_c^2)$ being the magnitude of the dynamic modulus and η_c denoting the loss factor of the compliant coating material. With the introduction of Eqs. (12) and (13) into Eq. (11), the radiated power of Eq. (10) takes the specific form

$$\hat{\Pi}_{rad} = \frac{1}{2} (\rho_f c_f \omega^2 R_f / |\tilde{D}|^2) \tilde{P}_a^2, \quad (14a)$$

where

$$|\tilde{D}|^2 = [(\rho_s h_s \omega^2 + \rho_f c_f M_f \omega) - \rho_f c_f \omega (M_f - \eta_c R_f) \rho_s h_s \omega^2 / \hat{E}_c]^2$$

$$+\rho_f^2 c_f^2 \omega^2 [(R_f + \eta_c M_f) \rho_s h_s h_c \omega^2 / \hat{E}_c - R_f]^2 \quad (14b)$$

Since $\hat{\Pi}_{rad}$ is the acoustic pressure intensity, the farfield acoustic pressure can be related to the acoustic intensity by

$$|\tilde{P}_{rad}|^2 = \rho_f c_f \hat{\Pi}_{rad} \quad (14c)$$

Eq. (14a) can be written in the form

$$|\tilde{P}_{rad}|^2 / \tilde{P}_a^2 = \frac{1}{2} \rho_f^2 c_f^2 \omega^2 R_f / |\tilde{D}|^2 \quad (14d)$$

which describes the radiated pressure in terms of the input pressure for a rigidly backed compliant coating.

It is also relevant to determine the quantity of acoustic power that is admitted into the base structure. The input power per unit area is

$$\hat{\Pi}_i = \frac{1}{2} \tilde{P}_a \operatorname{Re}(-i\omega \tilde{w}_s^*) \quad (15)$$

From Eqs. (5) and (8), it is found that

$$\tilde{w}_s = \frac{1 + \rho_f c_f (i\omega) Z_f Y_c}{1 + \rho_f c_f (i\omega) Z_f (Y_c + Y_s)} Y_s \tilde{P}_a \quad (16)$$

Substitution of Eq. (16) into Eq. (15) yields

$$\hat{\Pi}_i = \frac{1}{2} \frac{\rho_f c_f \omega^2 (R_f + \rho_f c_f \omega |Z_f|^2 h_c \eta_c / \hat{E}_c)}{|\tilde{D}|^2} \tilde{P}_a^2 \quad (17)$$

where $|\tilde{D}|^2$ is defined in Eq. (14b), and $|Z_f|^2 = (R_f)^2 + (M_f)^2$. Dividing Eq. (14a) by Eq. (17) gives the power ratio:

$$\hat{\Pi}_{ratio} = \frac{\hat{\Pi}_{rad}}{\hat{\Pi}_i} = \frac{R_f}{R_f + \rho_f c_f |Z_f|^2 h_c \eta_c / \hat{E}_c} \quad (18)$$

If $\eta_c = 0$, the coating material exhibits no dissipative losses and the power ratio is equal to unity, i.e., no power is absorbed in the coating. Eqs. (14) and (18) form the basis for numerical studies of the noise

reduction performance of an external coating mounted on a simple structure exhibiting rigid body motion. This analysis resembles pulse-tube evaluations of compliant layers.

Numerical Parametric Analysis

To evaluate the above equations in a form that provides meaningful results, the fluid acoustic impedance given by Eq. (4) must be determined. Note that the present analysis is consistent with the physics of a compliant coating backed by a rigid circular plate. For this case, approximate values for the fluid resistance and reactance are utilized. An asymptotic derivation [2] yields the limiting values:

$$R_f = \begin{cases} \frac{1}{2} (f/f_o)^2 & f/f_o \rightarrow 0 \\ 1 & f/f_o \rightarrow \infty \end{cases} \quad (19a)$$

and

$$M_f = \begin{cases} \frac{8}{3\pi} (f/f_o) & f/f_o \rightarrow 0 \\ \frac{2}{\pi} (f_o/f) & f/f_o \rightarrow \infty \end{cases} \quad (19b)$$

where $f_o = c_f / 2\pi a$ may be considered as the acoustic coincidence frequency for a circular plate of radius $r = a$. For f_o large, the plate dimension or source size is small relative to the acoustic wavelength; for f_o small, the plate becomes an efficient radiator. For the numerical studies presented in this article, reference values of $f_o = 10$ Hz and $f_o = 20$ kHz are used to examine the extremes of frequency-dependent compliant coating noise reduction performance. To provide a meaningful assessment of the coating's acoustic performance, it is appropriate to remove the effect of the rigid backing plate. This is accomplished by forming the ratio

$$|\tilde{P}_{rad}|_C^2 / |\tilde{P}_{rad}|_B^2 = (\hat{\Pi}_{rad})_C / (\hat{\Pi}_{rad})_B = |\tilde{D}_B|^2 / |\tilde{D}_C|^2 \quad (20)$$

of acoustic radiated power from Eq. (14). The subscripts C and B denote coated and bare plates, respectively. The term $|\tilde{D}_C|^2$ is found in Eq. (14b) directly, and

$$|\tilde{D}_B|^2 = (\rho_s h_s \omega^2 + \rho_f c_f M_f \omega)^2 + \rho_f^2 c_f^2 \omega^2 R_f^2 \quad (21)$$

is obtained by setting $h_c = 0$ in Eq. (14b). Thus, $|\tilde{D}_B|^2$ is the square amplitude of the fluid-loaded rigid plate impedance referenced to displacement. Also, Eq. (18) provides the acoustic energy absorbed by the coating material.

In terms of decibels, Eqs. (18) and (20) may be written as

$$(\Delta \hat{\Pi}_{o/i})_{dB} = 10 \log(\hat{\Pi}_{rad}) - 10 \log(\hat{\Pi}_i) \quad (22a)$$

and

$$(\Delta \hat{\Pi}_{C/B})_{dB} = 10 \log(\hat{\Pi}_{rad})_C - 10 \log(\hat{\Pi}_{rad})_B \quad (22b)$$

respectively. Numerical evaluation of Eqs. (14), (20), (21), and (22b) for $\eta_c = 0$, coating stiffnesses of $E_c/h_c = 1000, 2000, 4000, 6000$, and $10,000$ produced the graphs shown in Figure 2a for $f_o = 10$ Hz (efficient radiation) and in Figure 2b for $f_o = 20$ kHz (inefficient radiation). It is seen that the compliant external layer acts as a classical vibration isolator for forced vibration of the base plate. It is noted that the isolation performance of the coating layer displays improved performance in the region of heavy fluid loading and efficient structural radiation ($f_o = 10$ Hz). This is seen by comparing Figure 2a with 2b. Since the system acts like a vibration absorber, the low frequency region

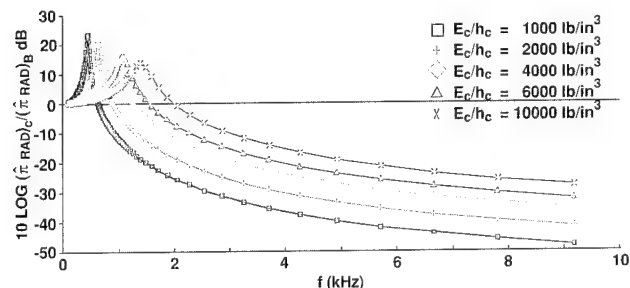


Figure 2a. Coating Insertion Loss vs. Coating Stiffness for 1/2-in. Aluminum Backing Plate with $f_o = 10$ Hz, $\eta_c = 0$

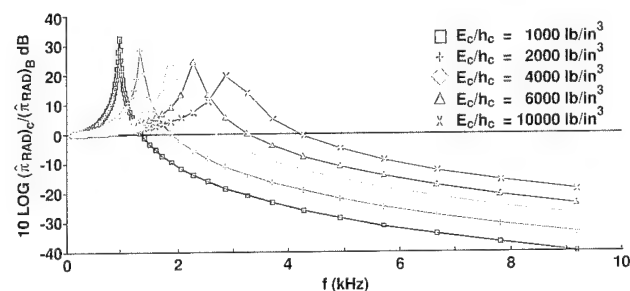


Figure 2b. Coating Insertion Loss vs. Coating Stiffness for 1/2-in. Aluminum Backing Plate with $f_o = 20$ kHz, $\eta_c = 0$

near the fundamental resonance exhibits an amplification due to resonant response. The coating material loss factor η_c has a major impact on the amplitude of resonant response and radiated power, as shown in Figures 3a and 3b. Although the coating material loss factor has a substantial effect on the fundamental resonant amplification, it has little impact on the high frequency noise isolation of the coating. Figure 4 provides a direct indication of the effect of coating damping on the overall noise reduction performance.

Comparing Eqs. (17) and (14a), one sees that the compliant layer produces a reduction of the input power of the force that is similar in form to the radiated power reduction. The power ratio of Eq. (18) shows that if $\eta_c = 0$, then the radiated power

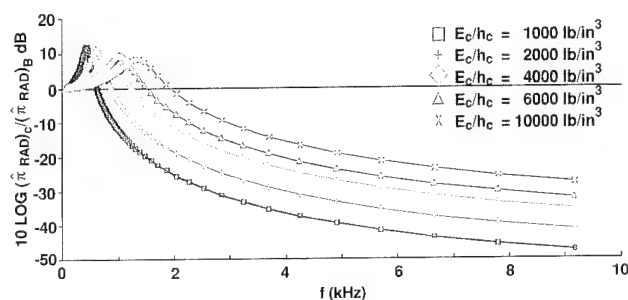


Figure 3a. Coating Insertion Loss vs. Coating Stiffness for 1/2-in. Aluminum Backing Plate with $f_o = 10$ Hz, $\eta_c = 0.2$

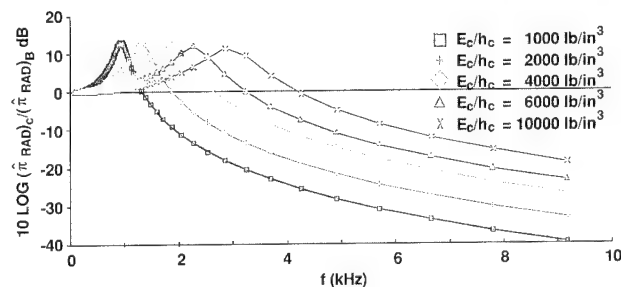


Figure 3b. Coating Insertion Loss vs. Coating Stiffness for 1/2-in. Aluminum Backing Plate with $f_o = 20$ kHz, $\eta_c = 0.2$

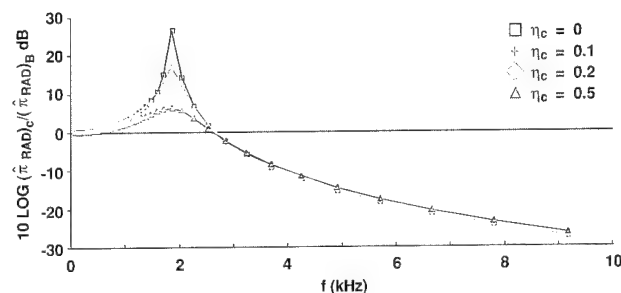


Figure 4. Coating Insertion Loss vs. Loss Factor for 1/2-in. Aluminum Backing Plate with $f_o = 20$ kHz, $E_c/h_c = 4000$ lb/in.³

and input power are identical. Figures 5a and 5b depict the effect of the coating loss factor on the amount of acoustic power that is absorbed by the compliant coating. It is seen that the ability of the coating to absorb energy is directly proportional to the coating's compliance and it is also enhanced by the higher value of fluid "virtual" mass in the subsonic structural wave region. These curves are particularly important when considering the performance of a compliant external coating on the noise attenuation of a source whose acoustic power may be considered as a constant. A source such as machinery airborne noise may be considered as a

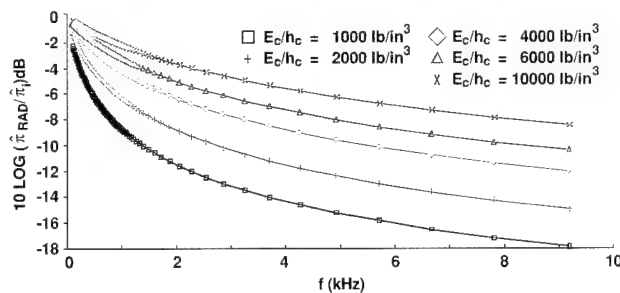


Figure 5a. Acoustic Power Absorption vs. Coating Stiffness for 1/2-in. Aluminum Backing Plate with $f_0 = 10$ Hz, $\eta_c = 0.2$

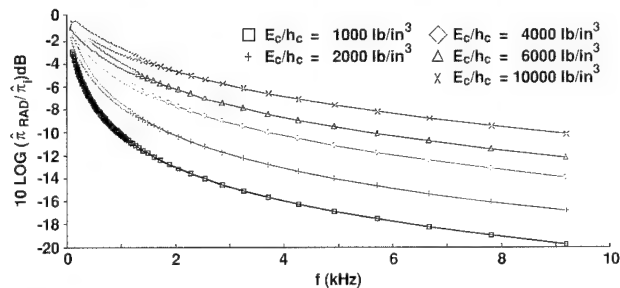


Figure 5b. Acoustic Power Absorption vs. Coating Stiffness for 1/2-in. Aluminum Backing Plate with $f_0 = 20$ kHz, $\eta_c = 0.2$

source with a fixed amount of available acoustic power. Fixed acoustic power levels and force levels must be predetermined attributes of a noise source in order to make an appropriate assessment of the noise reduction that will result with the application of a particular compliant acoustic decoupling layer.

From the form of Eqs. (14), it is seen that the impedance of the backing plate, i.e., $\rho_s h_s \omega$, has a direct impact on the insertion loss exhibited by the coating. In fact, if $\rho_s h_s = 0$, then

$$|\tilde{P}_{rad}|^2 / \tilde{P}_a^2 = \frac{1}{2} R_f / |M_f|^2,$$

which is the result that describes the radiation of the force acting directly on the fluid. Figure 6

provides the sensitivity of the coating insertion loss to various backing plate thicknesses. From this result, it must be concluded that the performance of a coating material is strongly dependent on the characteristic impedance of the backing structure. Experiments and analysis that are performed to determine acoustic coating performance must address the potential impact of the substructure or backing plate on predicted *in situ* performance. This factor could produce substantial errors in extrapolating coating performance from a test configuration to an actual application.

To demonstrate the relevancy of deriving the equations that govern the noise attenuation introduced by a compliant external layer, the

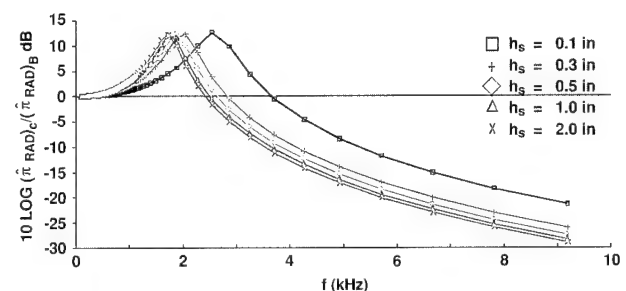


Figure 6. Coating Insertion Loss vs. Backing Plate Thickness with $E_c/h_c = 4000$ lb/in.³, $\eta_c = 0.2$, $f_0 = 20$ kHz

insertion loss given by Eq. (20) is compared with experimental pulse tube data in Figure 7. The sample material, of thickness 0.5 in. and dynamic Young's modulus of 8400 lb/in.², was mounted on a 3/8-in. steel backing plate inside a 6-in. diameter ($f_0 = 3100$ Hz) water-filled pulse tube. It is seen in Figure 7 that the simple model provides characteristics that closely approximate the actual measured performance, except in the region of the fundamental resonance. The area of disagreement is related to the fact that the equations presented here do not model the acoustic characteristics of the pulse tube, which is essentially a cylindrical waveguide. The radiation resistance and reactance

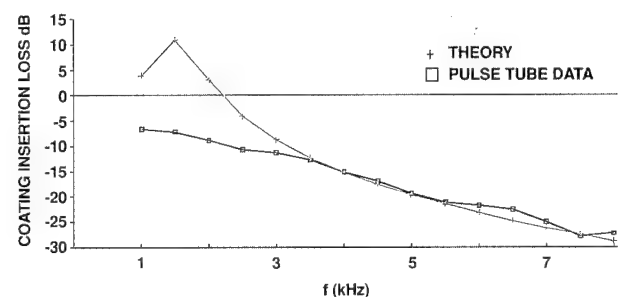


Figure 7. Coating Insertion Loss Theory vs. Experiment for 3/8-in. Steel Backing Plate with $E_c/h_c = 16,800$ lb/in.³, $\eta_c = 0.2$, $f_0 = 3.10$ kHz

of the confined fluid in the pulse tube are substantially different from those quantities presented here, which are approximations for an infinite body of fluid.

Summary and Conclusions

The equations of a compliant layer presented here provide a basis of a theory for predicting the insertion loss or radiated acoustic noise reduction that a relatively soft coating will produce. The basic characteristic that "makes the coating work" may be extracted from Eq. (5) of the text. The velocity reduction, i.e.,

$$|V_f|^2 / |V_s|^2 = \frac{1}{\left[1 + \rho_f c_f (i\omega) Z_f h_c (1 - i\eta_c) / \hat{E}_c\right]^2},$$

is an equation that provides the basic parametric sensitivity of the noise attenuation produced by a compliant layer mounted on a surface with a fixed value of velocity. The fundamental fluid mass/coating compliance resonant frequency is determined by

$$1 - \rho_f c_f \omega M_f h_c / \hat{E}_c = 0.$$

Thus, the coating's compliance h_c / \hat{E}_c and virtual fluid mass M_f control the location of the fundamental resonance,

$$\omega_r^c = 1 / \rho_f c_f M_f (h_c / \hat{E}_c),$$

for the coating and fluid mass system. If the compliance is small by virtue of $h_c \ll 1$ or $\hat{E}_c \gg 1$, then the resonance will be relatively high in

frequency and the coating will exhibit poor noise reduction performance. Environmental parameters such as ambient pressure and temperature directly affect the coating layer's compliance. Specifically,

$$h_c = h_o (1 - P_a^s / \hat{E}_c),$$

and

$$\hat{E}_c = \hat{E}_c^o \left[1 + \sum_n \alpha_n (P_a^s)^n\right],$$

where h_o and \hat{E}_c^o are uncompressed thickness and material stiffness, respectively. The above equations indicate that thickness decreases with increasing ambient pressure, and that the ambient pressure induces a nonlinear hardening of the coating modulus. Thus, thickness, modulus, and ambient pressure are the fundamental parameters for acoustic compliant coating design. The graphical representation of coating insertion losses presented here can be used as a guide for preliminary design.

Finally, the Fourier decomposition of Eqs. (1) and (2),

$$\tilde{P}_{mn}^f = E_c / h_c (\tilde{w}_{mn}^s - \tilde{w}_{mn}^f)$$

or

$$\tilde{w}_{mn}^f = \tilde{w}_{mn}^s - \frac{h_c}{E_c} \tilde{P}_{mn}^f,$$

set the format for integrating the simplified acoustic coating model with a generalized structural acoustic model for shells, where m and n are the discrete wavenumbers that represent the fluid-structural response spectra.

References

- [1] B. E. Sandman, "Fluid Loading Influence Coefficients for a Finite Cylindrical Shell," *Journal of the Acoustical Society of America*, vol. 60, 1976, pp. 1256-1264.
- [2] P. M. Morse and K. U. Ingard, *Theoretical Acoustics*, McGraw Hill, 1968, pp. 383-384.



BRUCE E. SANDMAN is head of the Advanced Technology Division at NUWC Division Newport. He directs broad programs of research and exploratory development in the areas of structure-borne acoustic energy damping, flow-noise damping, and composite materials as they apply to the Navy's critical programs in torpedoes, missiles, submarine launching systems, and

submarine sonar systems. Dr. Sandman has published more than 40 scientific reports and journal articles in the areas of structural mechanics and acoustics and is an internationally recognized expert in flow-noise generation and structural noise propagation. He earned a B.S. degree in Mathematics from Cornell University, and an M.S. in Mechanical Engineering and a Ph.D. in Applied Mechanics from Kansas State University.



JEFFREY E. BOISVERT is a mechanical engineer in NUWC Division Newport's Advanced Technology Division. Since joining NUWC in 1982, he has been working in the area of structural acoustics and analytical acoustic noise modeling. His current research interests include acoustic radiation, vibration isolation/noise reduction, and incident wave excitation of submerged

structures. Mr. Boisvert received a B.S. in Mechanical Engineering and Applied Mechanics from the University of Rhode Island in 1980, and a Sc.M. in Engineering from Brown University in 1982. He is a member of the American Society of Mechanical Engineers.

Considerations on the Use of Advanced Materials in a Marine Environment

Wayne C. Tucker
Naval Undersea Warfare Center Division Newport

Abstract

A new blistering mechanism generated by seawater corrosion reactions in graphite/polymers is examined in light of what is known to occur in fiberglass composite blistering. Other consequences of seawater corrosion reactions and electric fields in composites with conductive fibers are presented. Environmental stresses induced by ocean environments are examined and evaluated as risks when occurring alone and in combination.

Introduction

Degradation of polymer matrix materials in the marine environment is known to occur in several ways [1]-[4]. It is known that resins must resist diffusion of moisture and fibers must be properly sized to avoid wicking of moisture into the composite [5], [6]. Also, water solubles within the composite system must be minimized [7]. Absorption of excessive moisture into the composite system will cause swelling of the matrix, debonding of the fibers, and plasticization of the resin [1]. Water solubles reacting with moisture within the composite may cause the material to blister in seawater [8]. With proper selection of resin/fiber systems and with proper maintenance, a composite system will not encounter severe reduction of mechanical properties due to these known mechanisms [9]. Consideration must also be given to the long-term fatigue durability of the material in seawater. Cyclic stressing due to wave action will be encountered in material systems used in the ocean environment. Waves constantly subject the material to bending and normal stresses, which, in combination with exposure to seawater, are known to degrade material properties in metals and composites. When corrosion is also present, the degradation effect is often dramatically accelerated.

Until recently, degradation of reinforced plastics was not thought to be caused by corrosion. While fiberglass/polymer composites are galvanically inert, graphite/polymer composites are not. Graphite is an efficient cathode that is noble to every metal except platinum and gold. The virtual nobility of graphite would seem to eliminate the prospect of corrosion-induced degradation in the composite because the anode is sacrificial during corrosion.

However, aragonite crystals (a form of calcium carbonate (CaCO_3)) will grow upon graphite/polymer composites galvanically coupled with some metals in seawater [10]. Also, certain graphite/polymer composites will blister as a result of the corrosion process [11]. Thus, it is evident that cathodic reaction plays a significant role in the degradation of graphite/polymer composites.

Moisture uptake in some composites is exacerbated by deep submergence [12], and recent unpublished results [11] indicate surface microcracking in composites that are alternately exposed to sunlight during the day and deep submergence at night. The focus of current work is the evaluation of the effects of these potentially degrading phenomena on the performance of these materials in the ocean environment.

Water/Composite Interactions

Data Samples. Absorption curves for water pickup in graphite/vinyl ester composites are shown in Figure 1. The diffusion coefficients calculated from these data are given in Table 1. The data for pure water and 3-percent sodium chloride (NaCl) solutions were taken at 40°C. The samples, which are 1-1/4-in. squares, 0.07-in.-thick, cut parallel and perpendicular through the fiber layers, are carefully hand-lapped to minimize preparation damage. Preliminary desorption data are in general agreement with these data and, although the results are not final, a similarity in these values suggests that the diffusivity is not concentration-dependent.

The saturation value M_∞ of water in the samples is 1.7-1.75 weight percent for pure water

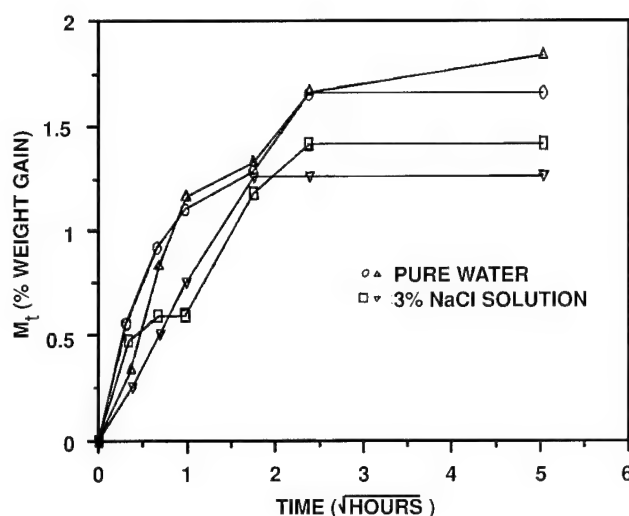


Figure 1. Diffusion Curves for Absorption of Pure Water and 3-Percent NaCl Solution in Vinyl Ester Neat Resin (as Cast) (Temperature = 40°C)

Table 1. Average Diffusional Data from Absorption Experiments at 40°C

CARBON/VINYL ESTER COMPOSITE				
SOLVENT	D_p ($\times 10^{-8}$ cm ² /s)	D_N ($\times 10^{-8}$ cm ² /s)	D_p/D_N	M_{sat} (wt %)
Pure Water	1.56	0.91	1.82	2.6
3% NaCl Soln	1.72	1.20	1.53	2.4
NEAT RESIN - VINYL ESTER				
Pure Water				1.75
3% NaCl Soln				2.4

D_p = Diffusion coefficient parallel to fiber layers
 D_N = Diffusion coefficient normal to fiber layers
 M_{sat} = Percent weight gain at equilibrium saturation

and approximately 1.5 weight percent for the 3-percent solution of NaCl. The saturation value is determined by the holding capacity of the polymer, the temperature, and the partial pressure of water in the solution. Because the presence of salt reduces the water partial pressure, a drop in M_{∞} is expected; however, the value is greater than that predicted. (The reason is not known and the experiment will be duplicated.) The value of 1.75 weight percent, which must be adjusted upward because of fiber volume, is approximately twice the saturation value for vinyl ester observed in an earlier study at 40 percent.

Data are also being collected on the effects of galvanically coupling samples to metal to determine the effect of the electrochemical phenomena on water uptake. Although diffusion data are not complete, coupled samples all show blisters, while uncoupled samples do not. The blisters are of two types: (1) first, tiny blisters (which rupture quickly) form above near-surface carbon fibers; (2) a second generation of blisters forms shortly thereafter, near glass fiber tows. These latter blisters appear to form at this

position either because of some water/glass interaction (they would include water soluble binders on the glass) or because the vinyl ester is thickest at this point and acts like a gel coat.

The absorption curves appear to reach a saturation value and then drop back (weight loss) before beginning a secondary water pickup. This behavior has been observed in earlier studies [12] and by Lee and Rockett and is consistent with the water interaction behavior mechanisms discussed below. Finally, water absorbed by capillarity into surface defects and microcracks between fibers and the matrix were observed to result in an instantaneous weight change upon immersion. There is virtually no such change associated with these samples. The hand-lapping prevented surface damage.

Discussion. Many well-documented water/polymer interactions occur upon exposure of a composite to aqueous solutions, and other mechanisms have been postulated. The fit of data to a Fick's law diffusion profile proves that water diffusion in these samples moves by activated jump – the rate determined through diffusion (resistance to movement) and the concentration gradient (or, more properly, the activity gradient). If both sides of the sample are exposed to a high relative humidity, the sample will saturate throughout; if only one side is exposed, a steady-state gradient is established. There are swelling stresses associated with water uptake. Stress birefringent effects have been observed but have not been quantified.

Water in the polymer acts as a plasticizer; it lowers the glass transition value of the polymer and can lead to a relaxation of the polymer network. This relaxation can lead to a supersaturation of water in the polymer, which can lead to a water loss after saturation, resulting in possible nucleation of interval microcracks known as disk cracks [3].

Disk cracks can also nucleate blisters. The solution in the disk cracks can become concentrated and lead to osmotic swelling and blister growth. Blisters can also be nucleated by water soluble units in a polymer that forms the initial solution, which then undergoes osmotic growth. Fiber binders have been repeatedly implicated in this type of blister formation. Growing blisters act as stress concentrations in a composite and can weaken a structure, causing cracks that remain after drying. Disk cracks, on the other hand, can heal after drying and only small strength losses are noted. Blister growth produces a secondary weight gain that is observed on absorption curves. Leaching of residual constituent is also observed in many solutions. The extraction puts the surface in tension, can lead to crazing, and can reduce strength severely.

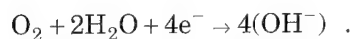
Ion diffusion in polyesters has been established for both the potassium and sulfate ion. Because both the cation and anion are considerably larger than sodium or chloride, there is almost certainly ion transport in these samples. How much, and what effect this will have on the absorption curves, is not known.

Finally, in samples that are galvanically coupled, blisters are strongly alkaline. Most blisters in fiber-reinforced plastics (FRP) materials are acidic, containing organic acids produced by breakdown of polyesters. The exact mechanism for hydroxyl ion (OH^-) production is still under investigation, but the presence of the anion in the vinyl ester matrix could cause polymer degradation. Ester and ether linkages are both known to be subject to alkaline attack. Evidence for strength loss due to this mechanism has not been found, but the possibility does exist.

Metal/Graphite Couples in the Marine Environment

The corrosion possibilities when metals are coupled with graphite/polymer composites in a marine environment can be separated into three cases, with the response of the composite being dependent on the control exerted by the metal reaction. The first case is where all the components are electrochemically inert. The second case is where only the metal is degraded. The third case occurs when a galvanic couple is made between a graphite composite and a metal that can actively corrode in the marine environment without a galvanic couple. In the first two cases, little damage due to electrochemical reactions occurs in the composite. However, in the third case, the reaction may cause damage in the composite.

In the first case, the metal is noble and therefore inert to the cathodic reaction. The reduction of oxygen in water to form the hydroxyl ion is given by



If no crevice corrosion site is created in the galvanic couple, then no reaction in either the metal or the composite will occur.

In the second case, the corrosion potential (E_{corr}) of a passivating metal is less than the potential of the reduction of oxygen from water. The passive film may or may not break down under geometrically controlled corrosion, such as crevice corrosion. In this case, the composite is effective only in inducing corrosion in metals susceptible to crevice corrosion by the type of interface between the composite and the metals. The metal surface

can provide cathodic sites outside the anodic crevice region. Examples of this were observed for monel and stainless steel when crevice corrosion was induced in the metallic material in contact with a vinyl ester/graphite fiber composite [13]. In the same study, a titanium alloy Ti-6Al-4V, which is very resilient to crevice corrosion, did not show any corrosion when coupled to the composite by an interference fit. No composite damage resulted from these couples.

In the third case, the metal actively corrodes in the marine environment prior to any coupling to the composite. This category of metals includes low alloy steels and 2000 and 7000 aluminum alloys. When these active metals are coupled to the graphite composite, the area for the cathodic site becomes larger because the carbon fibers in the composite become possible cathodic sites. However, two possible cathodic reactions are feasible, depending on the exposed sites in the composite materials and the pH of the solution. If carbon fibers are exposed to the marine environment, the reduction of oxygen to form hydroxyl ions is possible. In addition, at potentials more negative than the decomposition of water potential, hydrogen gas evolution is a possible reaction at exposed fibers. The breakdown potential for water is pH-dependent. Water decomposition to form hydrogen and hydroxyl ions is given by

$$E_{\text{H}^+/\text{H}} = -0.242 - 0.059 (\text{pH at } 25^\circ\text{C})$$

for a saturated calomel electrode (SCE).

The pH of seawater is approximately 8, so that $E_{\text{H}^+/\text{H}} = -0.722\text{V}$ (SCE); for 0.5N NaCl and de-ionized water the pH is 6, so that $E_{\text{H}^+/\text{H}} = -0.602\text{V}$ (SCE). Both of these potentials are similar to the free corrosion potentials reached by steel and aluminum in the respective solutions. The possibility of hydrogen ion reduction from the breakdown of water at the cathodic site is, therefore, a second cathodic reaction. The hydrogen reaction may be the reaction that controls damage in composites when coupled to active metals. No damage was found in composites when crevice corrosion was proceeding and when the cathodic reaction was reduction of dissolved oxygen. Damage in the form of blisters in the composite was found only when active corrosion was taking place in mild steel and Al 2024 alloys. Hydrogen ion reduction may have been occurring in the latter case; a simple cathodic polarization test indicated the presence of hydrogen. A section of a carbon fiber composite with a resin-rich surface exposed to solution was maintained at a potential of -5V (SCE). Immediately, gas bubbles were nucleated in a regular pattern, correlating with the closest location of the carbon

fibers to the exposed surface and solution. The low negative potential would ensure that hydrogen production is the favored cathodic reaction and that the bubbles observed were hydrogen. The decomposition of water to form hydrogen leaves hydroxyl ions free to increase pH in the solution adjacent to the composite surface.

It has been shown that the corrosion process will promote the growth of aragonite crystals on the cathodic graphite material and, in certain composites, blistering will occur as a result of the corrosion reaction [13]. Consider the chemistry of natural seawater; calcium carbonate occurs in a 0.01M concentration and the total alkalinity is approximately 2.0 meg/kg. At pH 8 (normal for seawater), this is actually a supersaturated condition by about 20 percent for CaCO_3 . If the corrosion reaction at the cathode raises the pH at the graphite/polymer composite, then the already supersaturated seawater solution will deposit CaCO_3 on the cathode. The crystals have been observed to grow preferentially on exposed graphite fibers (Figure 2). However, in time, the crystals will spread to cover the plastic surface. Once formed, the crystals adhere quite well to the composite and grow to visible size within three weeks. The potential degrading factors that may be attributed to crystal growth on plastics in seawater include unexpected weight gain (Figure 3), increased drag forces on structures in moving seawater, and reduced fatigue endurance.

Because aragonite crystals prefer to grow upon exposed fibers during corrosion, crack growth may

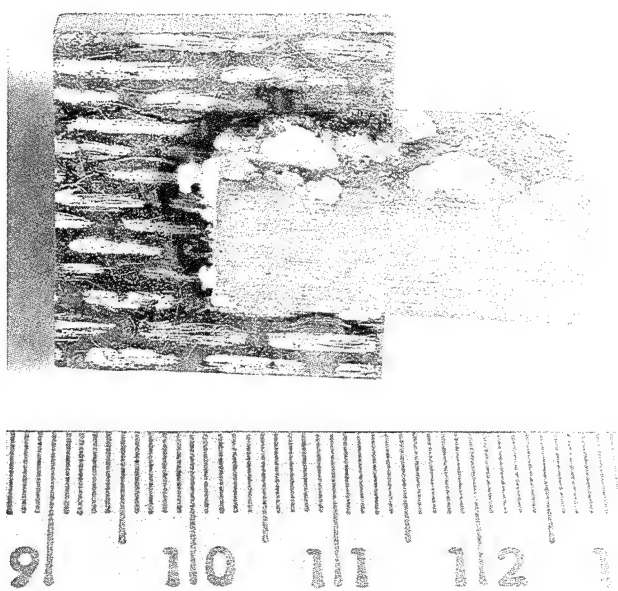


Figure 2. Aragonite Crystals Growing on Exposed Fibers Seen as White Ovals

be enhanced by the crystals growing upon exposed fibers within the crack. The wedging effect of crystalline material inside crack boundaries may be expected to enhance crack growth, even during periods where cyclic loading is not occurring.

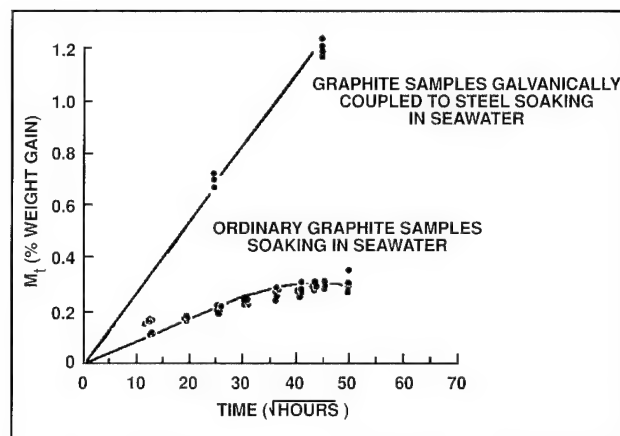


Figure 3. Weight Gain of Epoxy Samples in Seawater (Eyeball Fit Through Data)

Blistering is known to severely degrade composite materials. In fiberglass boat hulls, blistering has been extensively examined [7] and is known to be caused by an osmotic process. In graphite composites, however, blistering is driven by the corrosion process with a markedly different chemistry (Figure 4). Whereas blisters on fiberglass composites have a pH of 3-4, corrosion-induced blisters on graphite composites have an alkaline chemistry of 11.

The impact of blistering as a result of corrosion reactions has not been investigated. Because blistering is a near-surface defect, it will likely affect mechanical properties, especially the initiation of fatigue cracks. The alkaline chemistry of corrosion-induced blistering may also affect polymer stability.

Obviously, electrical isolation from corrosion reactions may be the way to eliminate crystal growth and blistering in graphite/polymer composites. However, if the corrosion reaction drives crystal formation and blistering, then stray or impressed electrical currents may also be a danger. Therefore, whenever a composite material has conductive fibers in a polymer matrix, electrical currents could generate damage to the material. Cathodic protection systems on some ocean structures use impressed electrical currents. Whenever electric welding takes place on or under the water, stray electrical currents may pass through seawater. Improperly grounded battery or electrical systems onboard ship or ocean structures may cause unwanted electrical currents to pass through the material. These types of electrical fields would be

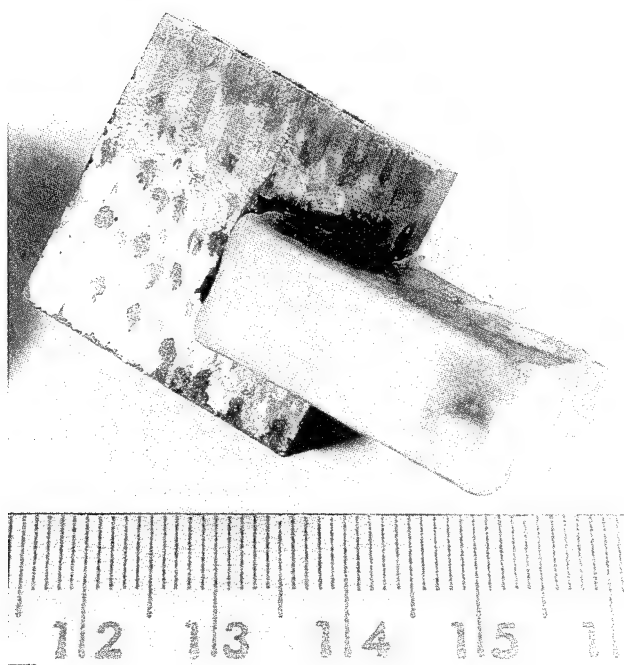


Figure 4. Blisters Evident on the Composite Surface After Galvanic Coupling to Al 2014

much stronger than those created by corrosion and could cause severe and rapid damage to the polymer composite with conductive fibers.

Damage Associated with Deep Submergence

Because the actual use of a composite in the ocean environment will undoubtedly involve stresses induced by static and dynamic loading, and because deep submergence will subject the composite to high ambient water pressure, damage-dependent mechanisms cause (1) capillary flow of moisture along the fiber-matrix interface and (2) the influx of moisture through cracks, pores, or small channels present in the material. These two mechanisms are active in addition to diffusion [14]. However, the surface area over which diffusion may take place can be significantly increased by the presence of moisture inside the composite, on interfacial boundaries, and inside cracks [9]. It should be noted, however, that although moisture penetration is determined by three mechanistically different components, the overall empirical picture is one of Fickian diffusion [14].

Elevated ambient water pressure would not be expected to induce higher diffusion by molecular transport because the transport of water molecules into a solid depends on the vapor pressure at the water/solid interface and the free volume of the polymer. Vapor pressure is relatively unaffected by elevated ambient pressure in the range of testing depths (0-2000 feet of seawater (fsw)), but does depend on temperature and salinity, which was verified experimentally by Loos and Springer [5].

Hydrostatic pressure might be expected to drive the flow of moisture in damage-dependent mechanisms and could, therefore, accelerate this overall uptake of moisture into a composite.

External loading (stress) would normally be expected to alter both molecular diffusion and moisture absorption by damage-dependent mechanisms. Diffusion involves the transport of water molecules through holes in the polymeric molecular structure. Larger holes facilitate molecule transport mobility. The size of the holes is dependent on the free volume in the polymer, which is the difference between the specific volume and the actual volume of the polymeric molecules.

Presumably, the effect of external loading on the diffusion process will result from changes in the free volume due to volumetric strain. Therefore, under hydrostatic pressure, a lowered diffusion rate may be expected by molecular transport because the compressive volumetric strain will tend to shrink the polymer network and lower the free volume. However, damage-dependent mechanisms, namely, capillary flow and flow through microdamage, would likely be enhanced by external loading to the extent that such loading would tend to promote further damage.

Figure 5 illustrates moisture curves for a graphite/polymer composite immersed in seawater at 1 atm and at 2000 fsw. From the outset, it was evident that samples subjected to a 2000-fsw pressure attained a higher moisture content than samples soaking at the surface under otherwise identical conditions. Analysis of diffusion coefficients indicates that, although higher moisture content is attained by samples under pressure, the diffusion coefficients remain the same. This is consistent with the supposition that higher ambient pressure in the range of 2000 fsw will not accelerate molecular transport at the liquid/solid interface.

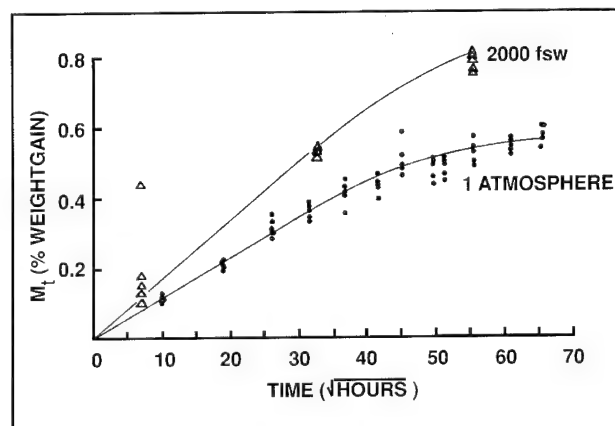


Figure 5. Moisture Curves for Vinyl Ester Graphite Composite in Seawater at 1 Atmosphere and at 2000 ft of Seawater

This supposition was recently verified with neat resin samples [15]. Moisture accumulation by damage-dependent mechanisms would become significant, however, and this accounts for the added moisture retained in defects.

Table 2 indicates the loss in flexure strength and stiffness after four months of exposure to high ambient seawater pressure. Ordinary samples soaking in seawater at 1 atm display no loss of strength or stiffness after six months. Apparently, damage accumulation by high ambient seawater pressure is the cause for not only higher moisture uptake, but also significant strength and stiffness

Table 2. Flexure Strength and Stiffness

Medium	Flexure Strength (KSI)	Tangent Modulus (KSI)
Dry	63	3959
3 Months in Seawater	63	4263
6 Months in Seawater	62	4200
Four Months @ 2000 fsw	51	3415

reduction.

Damage Accumulation from Cyclic Environmental Stresses

A preliminary investigation of extreme environmental effects was conducted in which samples of graphite/polymer composites were subjected to cyclic pressure loading (0-2000 fsw) and sunlight [11]. The samples were pressurized to 2000 fsw at night, then placed in direct sunlight during the day. The experiment was conducted during the summer months in Panama City, FL, where the air temperature reached well above 90°F every day. However, temperatures on the black plastic surface were much higher due to heat absorption. This combination of environmental stresses subjected the material system to several conditions:

- Ultraviolet radiation
- Thermal cycling
- Pressure cycling
- Alternate wetting and drying.

It is unclear at this time which of the above conditions or combination of conditions causes material degradation. What is clear is that the alternate exposure to deep submergence and sunlight degrades the surface of the material. In a magnified area of the composite, microcracks have appeared on the surface, and the damage is visible to the naked eye as very faint areas of discoloration on the surface. ASTM flexure tests of these specimens indicated a loss of strength and stiffness, but further studies are being conducted to substantiate initial findings and determine the cause of microcracking. Possibilities for cracking include:

- Differences in thermal expansion between fibers and matrix
- Ultraviolet radiation
- Cyclic stresses due to pressure
- Alternate wet and dry deposits salts in voids
- Combinations of the above.

Conclusions

Environmental stress due to real ocean conditions has clearly been shown to degrade graphite/polymer composite materials. Seawater chemistry is complex and cannot be duplicated by NaCl solutions or accelerated laboratory experiments with boiling distilled water. Valid material tests for the ocean environment must account for the overall chemical nature of seawater. Systems likely to encounter electric fields or to undergo electrochemical reactions in seawater must be evaluated for possible destructive mechanisms.

In addition, extreme environmental stresses are just beginning to show areas for concern. Since there is evidence to suggest that deep submergence may degrade composites of poor quality (i.e., high void content, delaminations, etc.), a good quality composite that sustains some impact damage may be susceptible to further damage upon submergence.

Degrading mechanisms in combination with loading conditions encountered in the ocean may cause system failure much sooner than predicted if materials are subjected to test programs that oversimplify the extreme exposures of the ocean environment. Clearly, extensive research is required to fully evaluate the impact of the ocean on graphite/polymer composite materials.

References

- [1] J. M. Augl and A. E. Berger, "The Effect of Moisture on Carbon Fiber Reinforced Epoxy Composites, I," NSWC/WOL/TR-76, Naval Surface Weapons Center, White Oak, MD, 1976.
- [2] K. E. Hofer and G. Skaper, "Fatigue Endurance of Glass Reinforced Plastic Laminate Material in a Marine Environment," *40th Annual Conference on Reinforced Plastics/Composites Institute*, The Society of the Plastic Industry, Inc., 28 January-1 February 1985.
- [3] A. Macander and M. Silverman, "Effect of Marine Environment on Stressed and Unstressed Graphite/Epoxy Composites," *Naval Engineering Journal*, vol. 89, no. 4, 1977, pp. 65-72.
- [4] S. K. Rege and S. C. Lakkad, "Effect of Salt Water on Mechanical Properties of Fibre Reinforced Plastics," *Fibre Science and Technology*, 1983, 0015-568183.
- [5] A. C. Loos and G. S. Springer, "Moisture Absorption of Graphite Epoxy Composites Immersed in Liquids and in Humid Air," *Journal of Composite Materials*, vol. 13, 1979, p. 131.
- [6] J. G. S. Spring, "Environmental Effects on Epoxy Matrix Composites," *Composite Materials Testing and Design* (Fifth Conference), ASTM STP 674, S. W. Tsai (ed.), 1979, pp. 291-312.
- [7] T. J. Rockett, "The Cause of Boat Hull Blisters," University of Rhode Island Report for U.S. Coast Guard, Grant No. 1502, 83, 1987.
- [8] R. Davis, J. S. Ghotta, T. R. Mahli, and G. Prichard, "Blister Formation in Reinforced Plastics: The Origin of Osmotic Pressure," *Proceedings of the 38th Annual Conference on Reinforced Plastics Institute*, The Society of the Plastics Institute, Session 17-B, 1983, pp. 1-10.
- [9] Private communication with T. Rockett, Department of Chemical Engineering, University of Rhode Island, Kingston, RI, March/April 1987.
- [10] W. Tucker, "Crystal Growth on Graphite/Polymer Composites," *Journal of Composite Materials*, vol. 22, no. 8, 1988, pp. 792-797.
- [11] W. Tucker and R. Hughes, "Extreme Environmental Effects," 1988 (unpublished).
- [12] W. Tucker and R. Brown, "Moisture Absorption of Graphite/Polymer Composites under 2000 Feet of Seawater," *Journal of Composite Materials*, vol. 23, no. 8, August 1989, pp. 787-797.
- [13] W. Tucker, R. Brown, and L. Russell, "Galvanic Corrosion Between a Carbon Fibre Composite and Metals," *Journal of Composite Materials*, vol. 24, no. 1, 1990, pp. 92-102.
- [14] G. Marom, "The Role of Water Transport in Composite Materials," *Polymer Permeability*, Elsevier, NY, 1985, pp. 342-362.
- [15] W. Tucker, S. B. Lee, and T. J. Rockett, "The Effects of Pressure on Water Transport in Polymers," *Journal of Composite Materials*, vol. 27, no. 8, 1993, pp. 756-763.

WAYNE C. TUCKER

conducts materials research, testing and evaluation for the Solid Mechanics and Design Branch in the Weapons Technology and Undersea Systems Department at NUWC Division Newport. He is responsible for evaluating material performance in submersible applications. He earned a B.S. degree from the University of Massachusetts Dartmouth in 1969, and M.S. (1971) and Ph.D. (1987) degrees from the University of Rhode Island.



Low Frequency Target Physics

Carlos M. Godoy
Naval Undersea Warfare Center Division Newport

Abstract

Certain structural details of submarines produce characteristic low-frequency acoustic scattering mechanisms that provide clues for submarine classification and identification. To gain an understanding of the fundamental scattering mechanisms that contribute to the low frequency (<1.5 kHz) active acoustic response of a submarine, an integrated theoretical and experimental research program using scale-model submarines was conducted. The scale models, which are simple but well-defined submarine-like structures, were used to systematically study submarine scattering mechanisms as a function of structural detail and waveform design. Full-scale measurements on actual submarines have validated the scale-model methodology and results.

Introduction

One of the highest priority research items in the U.S. Navy's low frequency (100 Hz to 1.5 kHz) active initiative is active classification of submarines. This initiative supports a wide range of new and developing tactical systems designed to offset the emerging quiet threat and yet retain a long-range detection capability. This use of the frequency spectrum below 1.5 kHz has uncovered a host of new and difficult problems to be addressed by the acoustic research community, not the least of which is a better understanding of submarine active acoustic response in this frequency regime. The frequency regime spans ka of 2 to 20, from a region where the acoustic backscattering from a target is dominated by the structural elastic response to one in which rigid body specular returns dominate.

A complete understanding of submarine active acoustic response is a key element in the design and development of low frequency active sonar systems. Target strength studies in the low frequency arena are very complex because of the complex properties of the target echo, including both temporal and spectral characteristics, and their interaction with the system and environment. Combining theoretical analysis (analytical and finite element models) with scale model experiments and then comparing both with newly acquired and ongoing full-scale measurement data would clearly provide a better understanding of target active response at low frequency. This understanding of target active response will be used to better predict the performance of newly emerging low frequency active systems.

Research Objectives and Approach

The objective of this research was to gain an understanding of the fundamental scattering mechanisms that contribute to the low frequency active response of a submarine. More precisely, the structural details and resulting acoustic scattering mechanisms that provide clues for the low frequency active classification of submarines were identified and characterized. Figure 1 summarizes the objective and transition mechanism of this effort to the naval community.

Previous research by the author established and successfully demonstrated an integrated theoretical and experimental research methodology. The contributions of fundamental mechanisms to the target strength of a submarine as a function of aspect, frequency, and geometry were identified and characterized. Figures 2 and 3 depict and summarize a sample of the results obtained. The

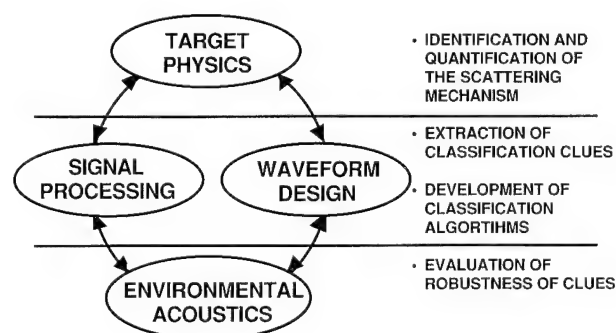


Figure 1. Development of Classification Clues

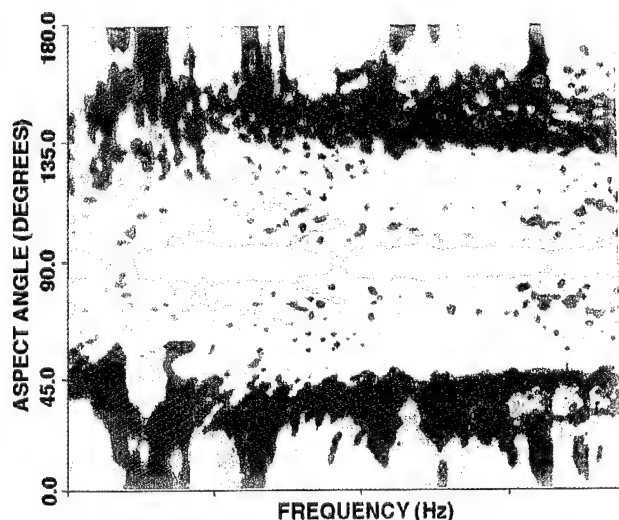


Figure 2. Mock 0 Model Response

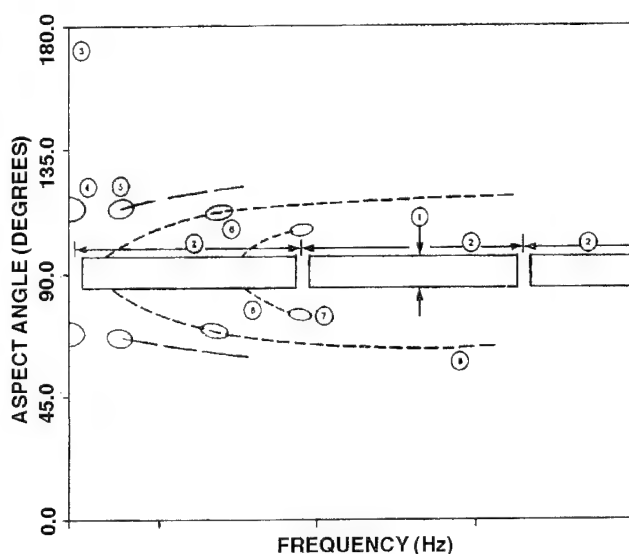


Figure 3. Mock 0 Model Target Strength Mechanisms

approach consisted of a systematic theoretical and experimental study using scale models of submarine-like structures of evolving structural complexity.

Simple, well-defined, submarine-like structures known collectively as Mock models served as the baseline for this study. By design, these models exhibit many of the structural components expected in real submarines (i.e., conical sections, internal and external ribs, cylinders of different lengths and radii, hemispherical endcaps, bulkheads, etc.), yet they remain well enough defined to be modeled analytically and numerically.

It is important to note that for the purposes of this study, it was not necessary that the model be an exact replica of an actual submarine (i.e., same material, shape and structure) as the objective was

to identify mechanisms and not to predict full-scale performance. In fact, measurement programs that purport to predict full-scale results based on small-scale replicas may be seriously flawed due to their inability to model the extreme level of detail needed to accurately represent the full-scale structure.

Results

At each level of structural complexity, numerical and, when possible, analytical models were constructed and validated against scale-model experimental data. Observed scattering phenomena were identified and characterized. Based on the knowledge gained from available modeling techniques, the underlying scattering mechanisms were identified.

This research methodology successfully integrated a variety of resources available at the Naval Undersea Warfare Center (NUWC) Division Newport (scale models, acoustic test facilities, finite element modeling capability, and advanced computational laboratory) with full-scale measurement programs in a systematic and technically correct approach to the low frequency scattering problem.

The focus of the research effort shifted from identifying and characterizing target strength mechanisms (i.e., integrated energy response) to the study of the causes of individual highlights in an echo return. To achieve this goal, an understanding of the scattering mechanisms permitting energy to travel through the body of a submarine and be re-radiated at discontinuities was required. Figure 4 shows the response of the Mock 0 target as a function of aspect, echo structure, and highlight target strength. Target strength studies throughout the frequency range with different waveforms allowed for identification and characterization of the scattering mechanisms (Figure 5). A theoretical

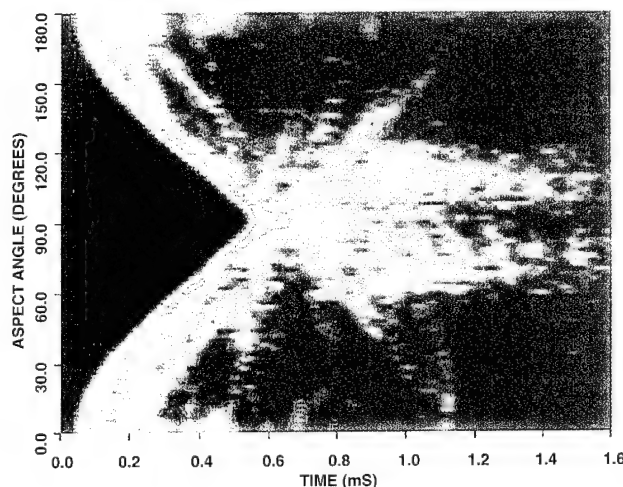


Figure 4. Mock 0 Monostatic Response

model of the Mock 0 target was developed and the results of the model at 400 Hz are shown in Figure 6.

Several major mechanisms contributing to the low frequency active response of a submarine were identified. The occurrence in time of these mechanisms was correctly predicted based on the symmetric and antisymmetric wave speeds in the structure. Additionally, a first cut formulation of the coupling of an incident wave with the structure was accomplished.

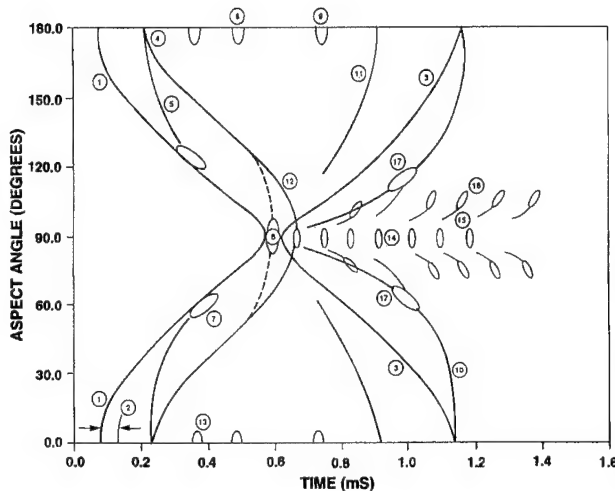


Figure 5. Mock 0 Monostatic Mechanisms

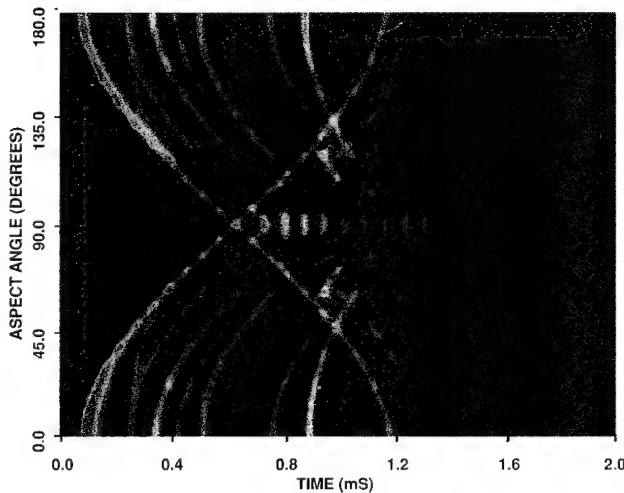


Figure 6. Echo Model



CARLOS M. GODOY

heads the Environmental and Target Modeling Branch in the Weapons System Analysis Department at NUWC Division Newport. In addition, Mr. Godoy is the senior researcher and coordinator for all low frequency target physics research carried out at the Division. Other responsibilities include providing continuous focusing and coupling of

NUWC's target physics research with Navy-wide programs for basic research, exploratory development, and advanced developmental efforts. Mr. Godoy also serves as the Center's principal research scientist in the area of scale-model experimental research and is responsible for validation against full-scale measurements. He earned B.S. and M.S. degrees in Electrical Engineering from Tufts University and has undertaken post-graduate studies at the University of Rhode Island.

The Modal Decomposition of an Impedance Tube

Andrew J. Hull
Naval Undersea Warfare Center Division Newport

Abstract

Impedance tubes usually consist of long ducts, with a speaker mounted either at one end or in the duct wall and with the material placed in the other end. Holes are drilled in the tube at various locations to allow pressure measurements with microphones. In the past, a steady-state continuous model has been used to predict the response of an impedance tube for pressure excitation at one end and an unknown acoustic impedance at the other end. The work presented here extends the modeling of impedance tubes by developing an eigenvalue-based model of the tube in modal space that can incorporate transient or steady-state response of velocity sources on the spatial domain and pressure sources at the end of the tube. Experimental verification is included for several different test configurations. Further, the inverse problem — determining acoustic impedance from the eigenvalues of the measured system response — is solved.

Introduction

The dynamic response of an enclosed acoustic system is determined by both the governing differential equations and associated boundary conditions. The problem was first addressed as early as 1878 by Rayleigh [1] when he modeled one-dimensional acoustic response. More current research has treated the response of hard-walled ducts with idealized reflecting and/or nonreflecting terminations to point source excitation [2]-[6].

Ducts with idealized, totally reflective boundary conditions result in self-adjoint differential operators that yield a standing wave model with mutually orthogonal modes. However, models of ducts with totally absorbent (nonreflecting) boundary conditions do not resonate, and wave propagation models are frequently used. Actual acoustic systems have nonidealized, partially reflective boundary conditions, yielding some combination of propagating and standing wave components in their acoustic pressure response [7]-[9].

The available analytical techniques, however, do not provide for the possibility that the acoustic response could be a combination of standing and propagating waves, nor do they consider the effect of partially absorptive boundary conditions on duct models. The partially absorptive boundary condition produces a nonself-adjoint differential operator. Thus, traditional methods of orthogonal mode shape discretization for this class of problems cannot be applied because the eigenfunctions are not

orthogonal with the conventional inner product over the domain of the operator, and the conventional eigenfunction inner product does not decouple the state equations of the model.

This article develops an infinite order, diagonal, state-space model of a duct with a partially absorptive boundary condition by deriving a new method to orthogonalize the state equations. Mathematically, the model of duct pressure at some location in the spatial domain divided by the forcing function is a complex transfer function obtained by manipulating the nonself-adjoint differential operator of the system. The model is experimentally verified for several different test configurations. As described at the end of this article, the model also provides a method for evaluating duct endpoint impedances based on the system eigenvalues.

System Model

The system model is a one-dimensional, hard-walled duct excited by either a pressure input at one end or a particle velocity input into the spatial domain. The boundary conditions are a pressure release boundary condition at one end and a generalized impedance boundary condition at the other. This partially reflective boundary allows the acoustic response model to include standing and propagating wave responses simultaneously. This occurs when some energy in the duct is dissipated out of the duct, while the remainder is reflected back into the duct.

The forced, linear, second-order, wave equation for modeling particle displacement in a one-dimensional hard-walled duct is [10]-[12]

$$\frac{\partial^2 u(x,t)}{\partial t^2} - c^2 \frac{\partial^2 u(x,t)}{\partial x^2} = \frac{P(t)\delta(x)}{\rho} + \frac{\partial V(t)}{\partial t} R(x-x_s) \quad (1)$$

where $u(x,t)$ is the particle displacement (m), c is the acoustic wave speed (m/s), x is the spatial location (m), t is time (s), ρ is the density of the medium (kg/m^3), $P(t)$ is the pressure excitation at $x=0$ (N/m^2), $V(t)$ is the particle velocity excitation at $x=x_s$ (m/s), $\delta(x)$ is the Dirac delta function (1/m), and $R(x-x_s)$ is the rectangular function (dimensionless). The rectangular function is defined as unity for $x=0$ to $x=x_s$ and as zero everywhere else. The left-hand side of Eq. (1) represents the dynamics of the duct, and the right-hand side represents the forcing functions acting on the duct. The wave equation assumes an adiabatic system, no mean flow in the duct, a uniform duct cross-section, and negligible air viscosity effects. The hard-wall assumption models the duct as having no dissipation on the domain. The one-dimensional assumption requires the diameter of the duct to be small compared with its length, which is valid when $f < 0.586(c/d)$, where f is the frequency (Hz) and d is the diameter of the duct (m) [13], [14].

The boundary condition at the location $x=L$ is a generalized condition that corresponds to the acoustic impedance at the end of the duct. It is expressed as the relationship between the spatial gradient and the time gradient of particle displacement [10], [15] as follows:

$$\frac{\partial u(L,t)}{\partial x} = -K \left(\frac{1}{c} \right) \frac{\partial u(L,t)}{\partial t} \quad (2)$$

where K is the acoustic impedance of the termination end (dimensionless). For a steady-state response in the duct, K can be a complex number. For a transient response, K is a real number. Implicit in Eq. (2) is the analogy with electrical systems, where acoustic velocity corresponds to current and duct pressure to voltage. When $\text{Re}(K)$ equals zero or infinity, the termination end of the duct reflects all the acoustic energy, and the response is composed of standing waves only. When $K = 1 + 0i$, the termination end of the duct absorbs all the acoustic energy, and the response is composed of propagating waves. All other values of K yield some mixed combination of propagating and standing wave response. In general, the reflection

coefficient $(1-K)/(1+K)$ gives the relative magnitude of the reflected pressure wave off the termination end. The real part of K (acoustic resistance) is associated with energy dissipation and is sometimes called a loss coefficient because it is a measure of the amount of energy leaving the duct. The imaginary part of K (acoustic reactance) is associated with conservative fluid compliance and/or inertia effects.

The duct end at $x=0$ is modeled as a pressure release boundary condition:

$$\frac{\partial u(0,t)}{\partial x} = 0 \quad (3)$$

At low frequencies, this equation corresponds to an open duct end or one with an excitation speaker. The acoustic pressure of the system is related to the spatial gradient of the particle displacement by [10]

$$P(x,t) = -\rho c^2 \frac{\partial u(x,t)}{\partial x} \quad (4)$$

Eqs. (1)-(4) represent a mathematical model of the duct for one-dimensional motion. An impedance tube with two excitation sources is shown in Figure 1, although only one source is typically used for an experiment.

A Decoupled Solution

A decoupled set of ordinary differential equations that model the dynamic response are now developed. These equations will incorporate the boundary conditions (Eqs. (2) and (3)) as well as the initial conditions in the duct. The eigenvalues and eigenfunctions of the model are found by applying separation of variables to Eqs. (2) and (3) and to the homogeneous version of Eq. (1).

Separation of variables assumes that each term of the solution is a product of a function in the spatial domain multiplied by a function in the time domain:

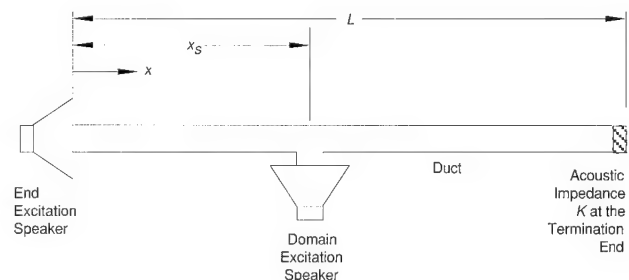


Figure 1. A Typical Impedance Tube with Excitation Sources

$$u(x, t) = X(x)T(t) . \quad (5) \quad \Lambda_n = c\lambda_n , \quad (12)$$

Substituting Eq. (5) into the homogeneous version of Eq. (1) produces two independent ordinary differential equations, each with complex-valued separation constant λ ; namely,

$$\frac{d^2 X(x)}{dx^2} - \lambda^2 X(x) = 0 , \quad (6)$$

and

$$\frac{d^2 T(t)}{dt^2} - c^2 \lambda^2 T(t) = 0 . \quad (7)$$

The separation constant $\lambda = 0$ is a special case, where $X(x) = T(t) = \text{a constant}$ to satisfy Eqs. (2) and (3). Because the pressure field is proportional to the spatial derivative of the particle displacement, the separation constant $\lambda = 0$ (and its associated particle displacement term) will not contribute to the pressure field. The spatial ordinary differential equation (Eq. (6)) is solved for $\lambda \neq 0$ with the boundary condition given in Eq. (3):

$$X(x) = e^{\lambda x} + e^{-\lambda x} . \quad (8)$$

The time-dependent ordinary differential equation (Eq. (7)) yields the following general solution:

$$T(t) = Ae^{c\lambda t} + Be^{-c\lambda t} . \quad (9)$$

Applying the boundary condition of Eq. (2) to Eqs. (8) and (9) results in $B = 0$ and the integer-indexed separation constants

$$\lambda_n = \frac{1}{2L} \log_e \left(\frac{1-K}{1+K} \right) - \frac{n\pi i}{L} , \quad (10)$$

$$n = \dots -3, -2, -1, 0, 1, 2, 3, \dots ,$$

where i is equal to the square root of -1 and λ has units of inverse meters. Inserting the indexed separation constants into Eq. (8) produces the complex-valued spatial eigenfunctions

$$\varphi_n(x) = e^{\lambda_n x} + e^{-\lambda_n x} . \quad (11)$$

The eigenvalues of the system are equal to the separation constant multiplied by the wave speed as follows:

where Λ_n has units of radians/s. A plot of the eigenvalues in the complex plane is shown in Figure 2. The indexed eigenvalues are equally spaced and parallel to the imaginary axis. The $n=2$ eigenfunction is shown in Figure 3 for acoustic impedances of $K = 0.5 + 0i$ and $K = 0 + 0i$. Unless the acoustic impedance K is zero or infinity, the eigenfunctions are not mutually orthogonal on $[0, L]$, conventional modal analysis of the forced wave equation is not possible, and the time response cannot be found.

As discussed earlier, traditional methods of orthogonal mode shapes cannot be applied here because of the nonself-adjoint operator. However, by extending the problem definition onto a virtual duct and then redefining the equations over $[-L, L]$, the time and space modes will decouple and a solution to the problem can be found. This technique is explained next.

The particle displacement (or solution) to the forced wave equation is now written as a series solution plus a time-dependent term arising from the $\lambda = 0$ separation constant. This expression is

$$u(x, t) = G(t) + \sum_{n=-\infty}^{\infty} a_n(t) \varphi_n(x) , \quad (13)$$

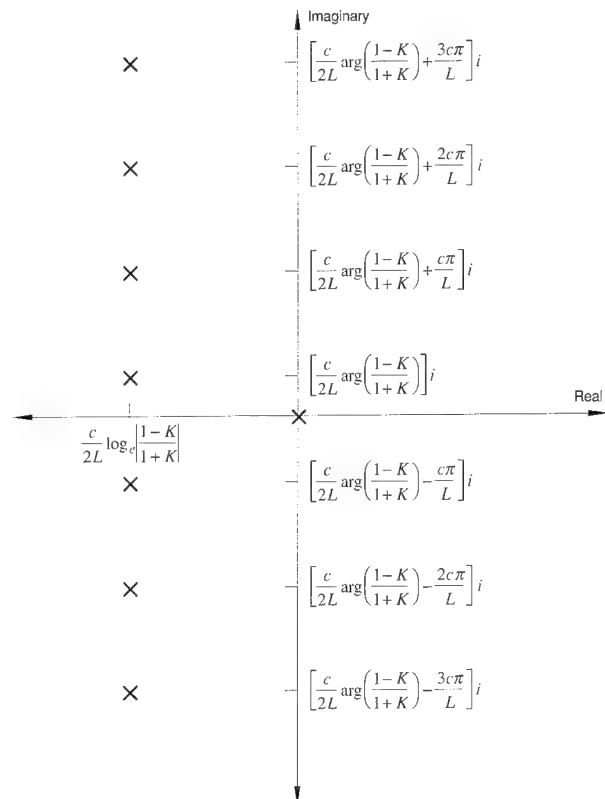


Figure 2. System Eigenvalues Λ_n for Constant K

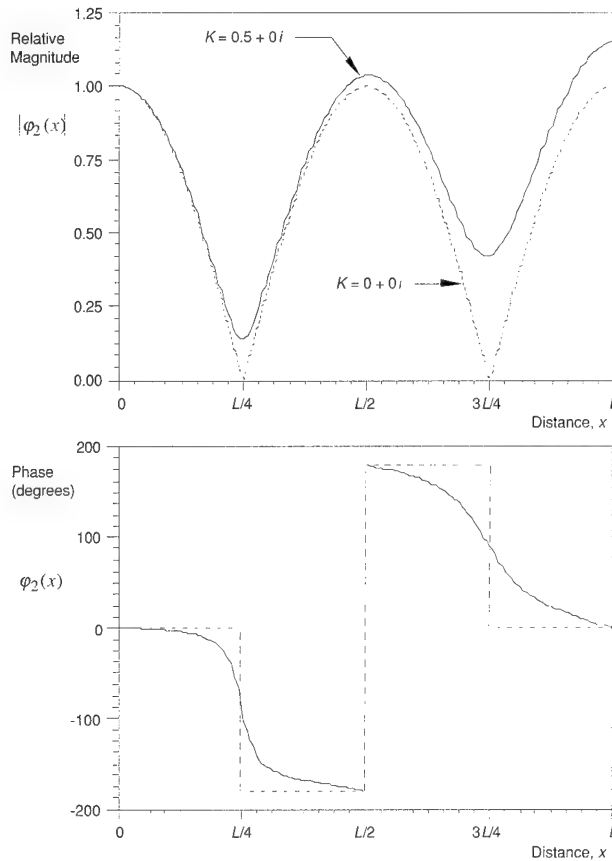


Figure 3. Second Eigenfunction with End Impedances of $K = 0.5 + 0i$ and $K = 0 + 0i$

where $G(t)$ and $a_n(t)$ are generalized coordinates (state variables), and $\varphi_n(x)$ represents the spatial eigenfunctions defined in Eq. (11). The coordinate $G(t)$ will not contribute to the pressure response in the duct because the pressure response is dependent only on the spatial partial derivative. Derivation of a solution that decouples the time and space modes requires the time derivative (velocity) of the particle displacement to be written in two different forms. The first form is the time derivative of Eq. (13) and yields

$$\frac{\partial u(x,t)}{\partial t} = \frac{dG(t)}{dt} + \sum_{n=-\infty}^{\infty} \frac{da_n(t)}{dt} \varphi_n(x). \quad (14)$$

The second, developed by using Eqs. (5), (9), and (12), is written as

$$\frac{\partial u(x,t)}{\partial t} = \sum_{n=-\infty}^{\infty} \Lambda_n a_n(t) \varphi_n(x). \quad (15)$$

Equating (14) and (15) produces

$$\frac{dG(t)}{dt} + \sum_{n=-\infty}^{\infty} \left[\frac{da_n(t)}{dt} - \Lambda_n a_n(t) \right] \varphi_n(x) = 0. \quad (16)$$

The assumption is now made that differentiation will distribute over the summation, which will be validated by the decoupled space and time modes. The forced wave equation (Eq. (1)) is rewritten with the equations (13)-(16). The second partial time derivative is found from the time derivative of Eq. (15), and the second partial spatial derivative is found from the second spatial derivative of Eq. (13). Inserting these derivatives into the left-hand side of Eq. (1) yields

$$\sum_{n=-\infty}^{\infty} \left[\frac{da_n(t)}{dt} - \Lambda_n a_n(t) \right] \Lambda_n \varphi_n = \frac{P(t)\delta(x)}{\rho} + \frac{\partial V(t)}{\partial t} R(x - x_s). \quad (17)$$

Eq. (16) is now differentiated with respect to x and multiplied by the wave speed c . The result is then added to Eq. (17) to form

$$\sum_{n=-\infty}^{\infty} \left[\frac{da_n(t)}{dt} - \Lambda_n a_n(t) \right] \Lambda_n 2e^{\lambda_n x} = \frac{P(t)\delta(x)}{\rho} + \frac{\partial V(t)}{\partial t} R(x - x_s), \quad x \in [0, L], \quad (18)$$

and is subtracted from Eq. (17) to give

$$\sum_{n=-\infty}^{\infty} \left[\frac{da_n(t)}{dt} - \Lambda_n a_n(t) \right] \Lambda_n 2e^{-\lambda_n x} = \frac{P(t)\delta(x)}{\rho} + \frac{\partial V(t)}{\partial t} R(x - x_s), \quad x \in [0, L]. \quad (19)$$

The interval of Eq. (19) is changed from $[0, L]$ to $[-L, 0]$ by substitution of $-x$ for x , producing

$$\sum_{n=-\infty}^{\infty} \left[\frac{da_n(t)}{dt} - \Lambda_n a_n(t) \right] \Lambda_n 2e^{\lambda_n x} = \frac{P(t)\delta(-x)}{\rho} + \frac{\partial V(t)}{\partial t} R(-x - x_s), \quad x \in [-L, 0]. \quad (20)$$

Combining Eqs. (18) and (20) into a single equation and breaking the exponential into terms that contain the index n and terms that do not contain the index n results in

$$\sum_{n=-\infty}^{\infty} \left[\frac{da_n(t)}{dt} - \Lambda_n a_n(t) \right] 2\Lambda_n e^{\frac{-in\pi x}{L}}$$

$$= \begin{cases} e^{\frac{-1}{2L} \log_c \left(\frac{1-K}{1+K} \right) x} \left[\frac{P(t)\delta(-x)}{\rho} + \frac{\partial V(t)}{\partial t} R(-x-x_s) \right] & x \in [-L, 0] \\ e^{\frac{-1}{2L} \log_c \left(\frac{1-K}{1+K} \right) x} \left[\frac{P(t)\delta(x)}{\rho} + \frac{\partial V(t)}{\partial t} R(x-x_s) \right] & x \in [0, L] \end{cases} \quad (21)$$

The exponential function $e^{im\pi x/L}$ (where m is an integer) is now multiplied on both sides of Eq. (21), and the resulting equation is integrated from $-L$ to L . The left-hand side of the equation can be expressed as

$$\int_{-L}^L \left[\frac{da_n(t)}{dt} - \Lambda_n a_n(t) \right] 2\Lambda_n e^{\frac{-in\pi x}{L}} e^{\frac{im\pi x}{L}} dx$$

$$= \begin{cases} \left[\frac{da_n(t)}{dt} - \Lambda_n a_n(t) \right] 4\Lambda_n L & , \quad n = m \\ 0 & , \quad n \neq m \end{cases} \quad (22)$$

Use of the reflection property of integrals and the bound of $0 < x_s < L$ results in the right-hand side of Eq. (21) becoming

$$\int_{-L}^0 e^{-\lambda_n x} \left[\frac{P(t)\delta(-x)}{\rho} + \frac{\partial V(t)}{\partial t} R(-x-x_s) \right] dx$$

$$+ \int_0^L e^{-\lambda_n x} \left[\frac{P(t)\delta(x)}{\rho} + \frac{\partial V(t)}{\partial t} R(x-x_s) \right] dx$$

$$= \frac{2P(t)}{\rho} + \frac{1}{\lambda_n^2} \frac{d\varphi_n(x_s)}{dx} \frac{\partial V(t)}{\partial t} \quad (23)$$

Eqs. (22) and (23) can be equated (for $n = m$) to form ordinary differential equations for the generalized coordinates a_n as

$$\frac{da_n(t)}{dt} - \Lambda_n a_n(t)$$

$$= \frac{P(t)}{2\Lambda_n L \rho} + \frac{1}{4\Lambda_n L \lambda_n^2} \frac{d\varphi_n(x_s)}{dx} \frac{\partial V(t)}{\partial t} \quad (24)$$

An explicit solution to Eq. (24) cannot be found until a time-dependent forcing function has been specified.

The initial conditions of the generalized coordinates can be determined from the initial conditions of the duct with a method similar to the above derivation. This equation is

$$a_n(0) = \frac{1}{4\Lambda_n L} \int_0^L \frac{\partial u(x,0)}{\partial t} \varphi_n(x) dx$$

$$+ \frac{1}{4\lambda_n^2 L} \int_0^L \frac{\partial u(x,0)}{\partial x} \frac{d\varphi_n(x)}{dx} dx, \quad (25)$$

where $\partial u(x,0)/\partial t$ is the initial velocity of the acoustic medium (m/s) and $\partial u(x,0)/\partial x$ is the initial acoustic strain in the duct (dimensionless), which is proportional to initial pressure (Eq. (4)).

Accuracy of Truncated Solution

The exact series solution must be truncated to a finite number of terms. The effect of this truncation on steady-state pressure excitation (at $x = 0$) will now be examined since a closed-form solution already exists for this case. The exact steady-state series solution for pressure excitation at $x = 0$ is found by solving Eq. (24) using $P(t) = P_0 e^{i\omega t}$ (where ω = frequency in radians/s) and $V(t) = 0$ and then inserting the resulting generalized coordinates $a_n(t)$ into Eq. (4). The transfer function between pressure in the domain $P(x,t)$ and the amplitude of the excitation P_0 is

$$\frac{P(x,t)}{P_0} = \frac{-c}{2L} \left[\sum_{n=-\infty}^{\infty} \frac{e^{\lambda_n x} - e^{-\lambda_n x}}{(i\omega - \Lambda_n)} \right] e^{i\omega t}, \quad (26)$$

which is truncated to a $2N + 1$ term series by

$$\frac{P(x,t)}{P_0} = \frac{-c}{2L} \left[\sum_{n=-N}^N \frac{e^{\lambda_n x} - e^{-\lambda_n x}}{(i\omega - \Lambda_n)} \right] e^{i\omega t}. \quad (27)$$

The exact steady-state response for the system described in Eqs. (1)-(4) has been independently calculated [8] for harmonic pressure excitation at $x = 0$ in continuous, closed-form solution as

$$\frac{P(x,t)}{P_0} = \left[\frac{(K+1)e^{\frac{i\omega}{c}(L-x)} + (K-1)e^{\frac{-i\omega}{c}(L-x)}}{(K+1)e^{\frac{i\omega}{c}L} + (K-1)e^{\frac{-i\omega}{c}L}} \right] e^{i\omega t}. \quad (28)$$

This exact steady-state response model is valid only for the special case of harmonic pressure excitation at $x = 0$. It cannot model the velocity excitation in the domain, nor can it model transient responses. It is used here only for comparison with the more general result of Eq. (26).

Quantitative information on the accuracy of a truncated, steady-state, series solution (Eq. (27)) is

found here by comparing it to an exact, steady-state frequency response (Eq. (28)). Figure 4 shows the frequency response of a 1.524-m (5-ft) duct at a location of $x = 0.4267$ m (1.4 ft) from pressure excitation at $x = 0$. The impedance at $x = L$ is $K = 0.3 + 0.2i$, and a truncated series model with 11 terms is used to approximate the exact solution. The solid line is the truncated steady-state series solution (Eq. (27)) and the dashed line is the continuous solution (Eq. (28)). The mean relative error up to the fifth duct resonance is only 3.2 percent (-30 dB). Numerical simulations suggest that the state-space model requires one state to model zero frequency response plus two states to model each duct resonance. The model yields acceptable accuracy up to the highest duct resonance modeled.

Model Validation Experiments

The state-space model developed above will now be experimentally verified for four different test cases: (1) steady-state pressure excitation with frequency-invariant (constant) acoustic impedance, (2) steady-state velocity excitation with frequency-invariant acoustic impedance, (3) steady-state pressure excitation with frequency-dependent acoustic impedance, and (4) transient pressure excitation with constant impedance. In all experiments, the impedance at the end of the duct

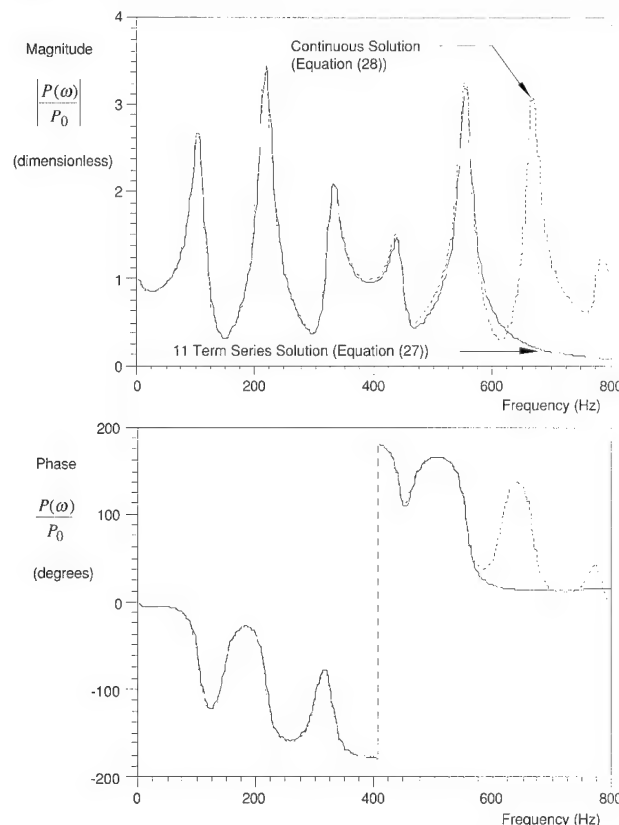


Figure 4. Theoretical Frequency Responses with Acoustic Impedance $K = 0.3 + 0.2i$

was calculated from the experimental system transfer functions. This impedance measurement technique is described next.

Steady-State Pressure Excitation With Frequency-Invariant Acoustic Impedance

The first experiment involved steady-state pressure excitation at $x = 0$ with a constant, frequency-invariant acoustic impedance at the termination end. The impedance was produced by inserting a flat piece of packing foam that had a nearly constant impedance at all frequencies of interest (approximately $K = 0.285 + 0.079i$ from zero to 400 Hz). The theoretical response of the system is given by Eq. (27). The experiment used a 76-mm (3-in.) circular PVC schedule-40 duct that was 2.60 m (8.52 ft) long driven by a 254-mm (10-in.) diameter speaker (Realistic 40-1331B). Input pressure of the speaker was measured at its exit plane with a Bruel and Kjaer Type 4166 1/2-in. microphone attached to a Hewlett Packard 5423A digital signal analyzer. At a location of $x = 0.792$ m (2.60 ft) from the speaker, the response of the tube was measured with another Bruel and Kjaer Type 4166 1/2-in. microphone. The output of the response measurement microphone was then connected to the signal analyzer (Figure 5). Both microphones were calibrated using a Bruel and Kjaer Type 4230 sound level calibrator. The results of the experiment are shown in Figure 6. The measured responses are marked by X's and the theoretical response by a solid line. There is a high degree of accuracy in the magnitude and phase data. The disagreement between the experimental data and the theory is possibly due to a slight nonlinearity of the packing foam impedance.

Steady-State Velocity Excitation With Frequency-Invariant Acoustic Impedance

The experiment was rerun with velocity excitation in the domain. The truncated steady-state transfer function of the system with a velocity excitation of $V(t) = V_0 e^{i\omega t}$ at x_s is

$$\frac{P(x,t)}{V_0} = \frac{-i\omega pc^2}{4L} \left[\sum_{n=-N}^N \frac{(e^{\lambda_n x_s} - e^{-\lambda_n x_s})(e^{\lambda_n x} - e^{-\lambda_n x})}{(i\omega - \Lambda_n)\Lambda_n} \right] e^{i\omega t}. \quad (29)$$

A Realistic 102-mm (4-in.) speaker was located in the wall of the duct at $x_s = 1.58$ m (5.17 ft) with a schedule-40 test tee. The input signal was measured with a Bruel and Kjaer Type 3544 helium neon laser velocity measurement system attached to the signal analyzer. The test tee had a Plexiglas window inserted in its side so that the laser could illuminate the speaker cone face in order to measure speaker velocity. The length of the duct tested was 4.42 m

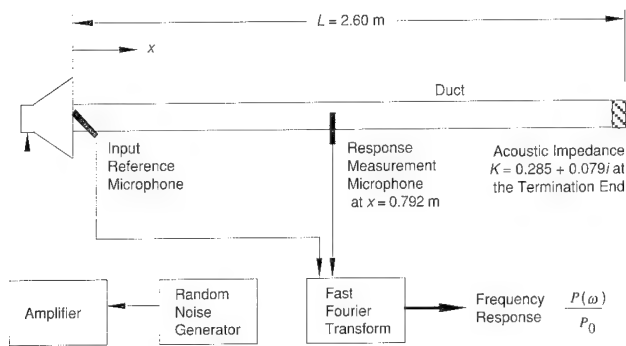


Figure 5. Laboratory Configuration for First Experiment

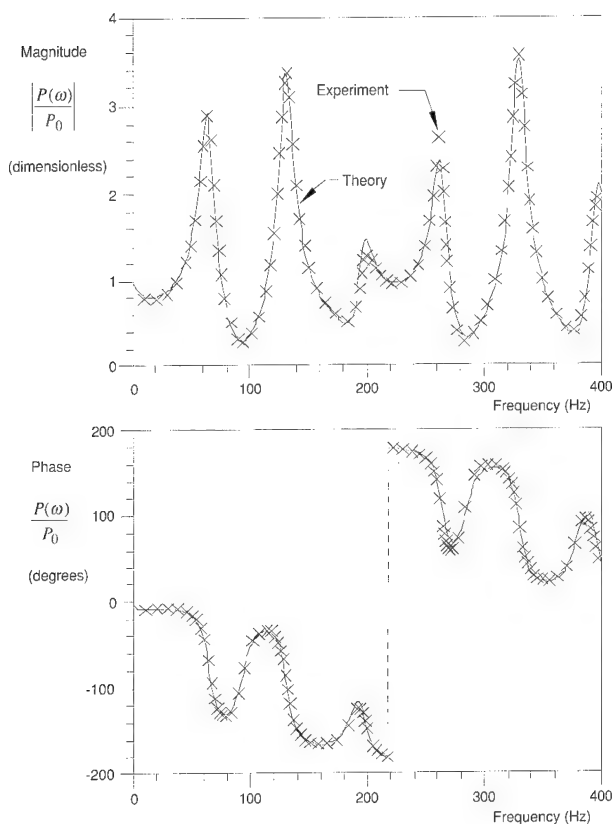


Figure 6. Theoretical and Experimental Frequency Responses for First Test

(14.5 ft), and the response was measured at $x = 0.762$ m (2.50 ft). The foam used in the first experiment was again used in this one. A diagram of the laboratory configuration is shown in Figure 7; the results of the experiment are shown in Figure 8. The solid line denotes the theory (Eq. (29)), and the X's show the experimental data.

Steady-State Pressure Excitation With Frequency-Dependent Acoustic Impedance

The acoustic impedance discussed here is given in Eq. (2), where it is assumed that acoustic impedance is frequency-invariant. For some

termination ends, the impedance is frequency-dependent. For these systems, Eq. (2) is written as

$$\frac{\partial u(L, t)}{\partial x} = -K(\omega) \left(\frac{1}{c} \right) \frac{\partial u(L, t)}{\partial t} \quad (30)$$

Although the separation of variables method is for a constant K , the termination ends where K is a function of frequency can be approximated by the expression

$$\left. \frac{\partial u(L, t)}{\partial x} \right|_{\omega=\omega_n} \approx -K_n \left(\frac{1}{c} \right) \left. \frac{\partial u(L, t)}{\partial t} \right|_{\omega=\omega_n} \quad (31)$$

With the relationship in Eq. (31), the state-space model derived above can be used to approximate systems with frequency-dependent terminations, as shown in the next experiment.

The third test involved pressure excitation at $x = 0$ with a nonconstant acoustic impedance in the termination end. The nonconstant termination was produced by placing a hemisphere of foam with a diameter equal to the duct diameter in the end of the duct at $x = L$. The resulting acoustic wave was affected by the presence and the shape of the material, which produced a nonconstant acoustic impedance. The impedance values listed in Table 1 were found by obtaining the frequency response of the system from zero to 800 Hz and then solving the inverse problem for K at each duct eigenvalue (described below). The length of the duct was 1.59 m (5.22 ft), and the response was measured at $x = 1.09$ m (3.56 ft). The experimental setup (with different physical dimensions) was the same as that shown in Figure 5. The state-space model was assembled with the individual acoustic impedance

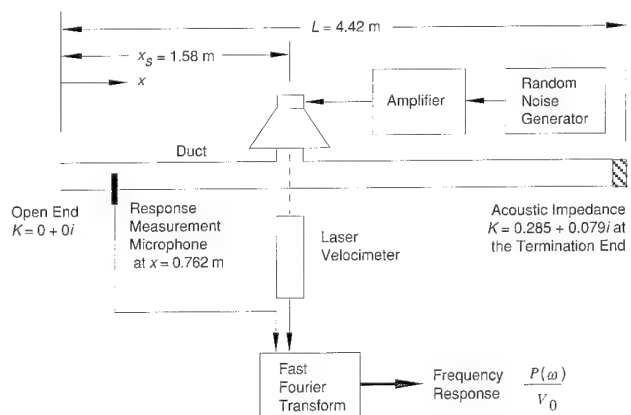


Figure 7. Laboratory Configuration for Second Experiment

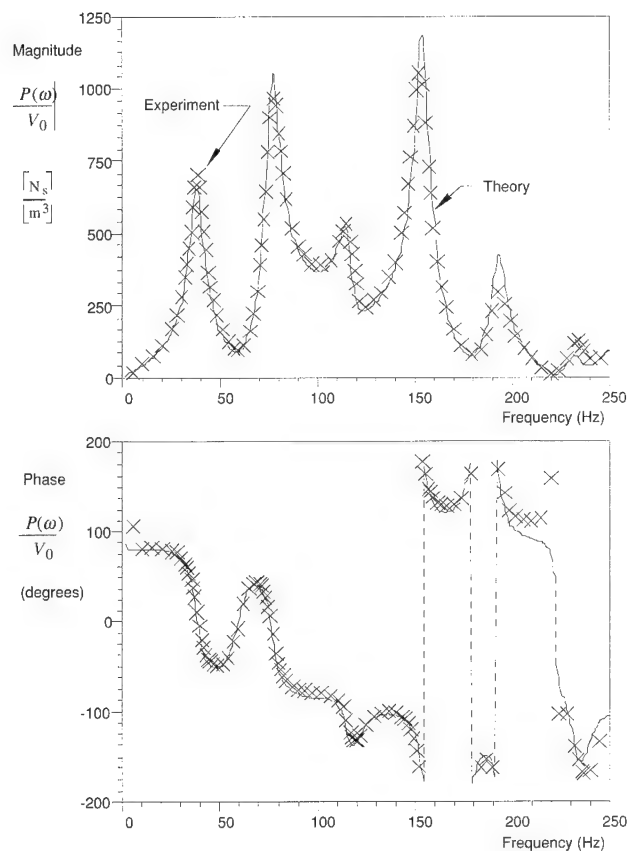


Figure 8. Theoretical and Experimental Frequency Responses for Second Test

measurements of K at each resonant frequency, rather than at a single constant value. The eigenvalues of the system are nonconjugate complex values since K is complex. A comparison of the theoretical transfer function and the experiment is shown in Figure 9. This figure demonstrates that for a nonconstant impedance end, the linear state-space model is reasonably accurate and can predict resonant peak locations as well as system phase angles. The errors tend to be minimized near the natural frequencies, but maximized between them. This result occurred because the modal impedances K_n were measured at the natural frequencies. The model does not account for varying values of the acoustic impedance between the modes.

Transient Pressure Excitation With Constant Acoustic Impedance

The transient response of the system was next verified. The experiment was initiated by attaching a pulse generator to the amplifier in order to excite the speaker. The electrical impulse produced was converted to one cycle of sine wave acoustic energy at approximately 500 Hz (Figure 10). The system input pressure and response pressure were measured by Bruel and Kjaer Type 4166 1/2-in. microphones attached to an Apple Macintosh IIX

Table 1. Calculated Acoustic Impedance

Eigenvalue (n)	f_n (Hz)	$\text{Re}(K_n)$	$\text{Im}(K_n)$
1	104.8	0.599	0.066
2	213.8	0.585	0.054
3	314.6	0.594	0.206
4	424.2	0.522	0.198
5	533.5	0.491	0.182
6	645.0	0.508	0.104
7	754.6	0.459	0.081

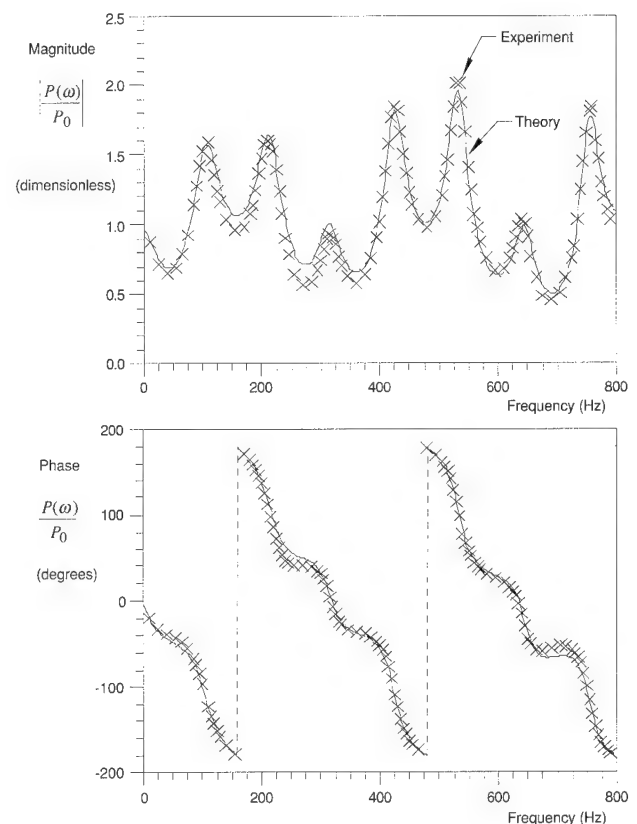


Figure 9. Theoretical and Experimental Frequency Responses for Third Test

computer running National Instruments Labview software and an NB-MIO-16L analog-to-digital converter. The length of the duct in this test was 2.44 m (8.00 ft), and the response was measured at $x = 0.792$ m (2.60 ft). The packing foam used in the first and second experiments was also used here to provide a nonzero acoustic impedance at the end of the duct. The measured time domain experimental data were compared to the theoretical model response. Only the real part of K was used in the theoretical formulation.

Figure 11 is a plot of the experimental data and theoretical state-space model. The solid line shows the experimental data and the dashed line depicts the theoretical model. The theoretical model response was computed using a fifth-order Adams integration method with 51 states. The forcing function in the Adams integration routine was the measured system input at $x = 0$. The integration step size was $\Delta t = 0.000035$ second, which matched the Labview sampling rate of 28571 Hz. There is an excellent match between the theoretical model and experimental data from $t = 0$ to $t = 0.015$ second. After that, the experimental data and theoretical prediction deviate because the propagating pressure pulse is reflected off the now inactive speaker and is affected by its impedance. The theoretical model does not account for impedance at the inactive speaker (zero velocity); however, Figures 6, 8, and 9 illustrate that an active speaker used in this experiment has little effect on the impedance at the source end ($x = 0$) for the test frequencies used here.

Acoustic Impedance Measurement

The acoustic impedance K of the termination end can be determined at each duct resonance from the eigenvalue corresponding to that resonance. This computation assumes that the eigenvalues of the system are known. Measuring these duct system eigenvalues is discussed below. Directly solving for K in terms of Λ is very difficult; therefore, an intermediate variable β is introduced to simplify the acoustic impedance computation. The variable β_n is related to the n th eigenvalue Λ_n from Eqs. (10) and (12) as

$$\begin{aligned} & \text{Re}(\Lambda_n) + i \text{Im}(\Lambda_n) \\ &= \frac{c}{2L} \log_e [\text{Re}(\beta_n) + i \text{Im}(\beta_n)] - \frac{n\pi c i}{L}, \end{aligned} \quad (32)$$

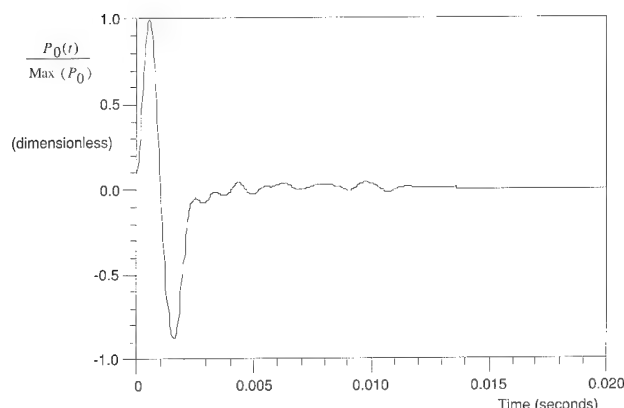


Figure 10. System Pressure Input at $x = 0$

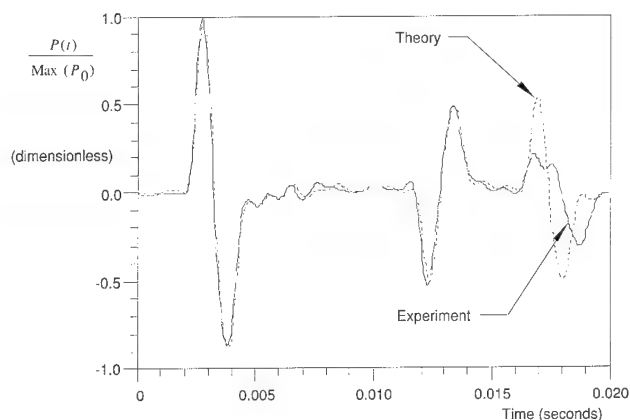


Figure 11. Transient Response of Duct at $x = 0.792$ m

where $\text{Re}(\cdot)$ denotes the real part, $\text{Im}(\cdot)$ denotes the imaginary part, and the subscript n denotes the n th term. Eq. (32) is now divided into two parts, one equating the real coefficients and the other equating the imaginary coefficients. The complex logarithm on the right-hand side is rewritten as

$$\log_e [\text{Re}(\beta_n) + i \text{Im}(\beta_n)] = \log_e |\beta_n| + i \arg(\beta_n), \quad (33)$$

where $|\beta_n|$ is the magnitude of β_n and $\arg(\beta_n)$ is the argument of β_n , i.e., the arctangent of $[\text{Im}(\beta_n)/\text{Re}(\beta_n)]$.

The intermediate variable β_n is now solved for in terms of the real and imaginary parts of the eigenvalues. The real part of β_n is

$$\text{Re}(\beta_n) = \pm \left[\frac{\exp\left(\frac{4L \text{Re}(\Lambda_n)}{c}\right)}{1 + \tan^2\left(\frac{2L d_n}{c}\right)} \right]^{\frac{1}{2}}, \quad (34a)$$

where

$$d_n = \text{Im}(\Lambda_n) - \frac{nc\pi}{L}. \quad (34b)$$

The sign of the right-hand side of Eq. (34a) is determined by

$$\text{sgn}[\text{Re}(\beta_n)] = \begin{cases} +1 & \text{if } 0 \leq |\Delta| \leq 0.25 \\ -1 & \text{if } 0.25 \leq |\Delta| \leq 0.50 \end{cases}, \quad (35a)$$

where

$$\Delta = d_n \left(\frac{L}{c\pi} \right). \quad (35b)$$

If the value of Δ is less than -0.5 or greater than 0.5, the eigenvalue index n is incorrect and corresponds to an eigenvalue other than the n th one. The value of n must then be changed to produce a Δ between -0.5 and 0.5, which will correspond to the correct eigenvalue index. Once $\text{Re}(\beta_n)$ is found, $\text{Im}(\beta_n)$ can be solved using

$$\text{Im}(\beta_n) = \text{Re}(\beta_n) \tan\left(\frac{2Ld_n}{c}\right), \quad (36)$$

where $\text{Re}(\beta_n)$ is given in Eq. (34a).

Use of Eqs. (10) and (32) now allows the term $(1-K)/(1+K)$ to be equated to the intermediate variable β_n as

$$\text{Re}(\beta_n) + i\text{Im}(\beta_n) = \frac{1 - \text{Re}(K_n) - i\text{Im}(K_n)}{1 + \text{Re}(K_n) + i\text{Im}(K_n)}, \quad (37)$$

where $\text{Re}(K_n)$ is the real part of K and $\text{Im}(K_n)$ is the imaginary part of K corresponding to the n th eigenvalue. Breaking Eq. (37) into two equations and solving for K_n as a function of β_n yield the acoustic impedance as

$$\text{Re}(K_n) = \frac{1 - [\text{Re}(\beta_n)]^2 - [\text{Im}(\beta_n)]^2}{[\text{Re}(\beta_n) + 1]^2 + [\text{Im}(\beta_n)]^2}, \quad (38)$$

and

$$\text{Im}(K_n) = \frac{-2\text{Im}(\beta_n)}{[\text{Re}(\beta_n) + 1]^2 + [\text{Im}(\beta_n)]^2}. \quad (39)$$

Acoustic impedance measurement K_n represents the acoustic impedance at the n th resonant frequency.

Because steady-state eigenvalue measurements are amplitude dominated rather than phase dominated, the impedance measurement technique developed here does not require phase-matched microphones, nor does it require compensation for phase-mismatched microphones. Phase mismatch in the microphones is neglected since the measurements are made at a duct resonant frequency, i.e., the measurements are made when the system phase angles are changing rapidly through 180° . Microphones operating under 500 Hz

rarely have a phase error greater than 5° [16]. The distance between the microphones is also not critical because the duct eigenvalues are independent of measurement location, unlike in previous methods [17]-[19], where microphone spacing is a required parameter in the analysis and phase-matched microphones (or a compensation function) are necessary because wave propagation across the microphones is detected. The computation of acoustic impedance from duct eigenvalues is a closed-form solution. Thus, errors in the method developed here are only a function of errors associated with measuring the eigenvalues of the duct, the duct length, and the speed of sound. In addition, because this method uses the input microphone as an amplitude reference, the excitation speaker does not require a flat response around the frequency of interest since the response is normalized by the pressure input reference when the fast Fourier transform is computed.

The 5423A structural dynamics analyzer used in this research is capable of providing a number of real-time analyses, including determination of the transfer function (frequency response) of a system and calculation of the corresponding eigenvalues. The analyzer accomplishes this by curve-fitting a single-mode vibration model (two first-order states) to the experimental data. Included in the single-mode vibration model is compensation for other modes, that may be overlapping at that particular frequency. During the curve-fitting process, the real and imaginary parts of the eigenvalues are calculated. Although it is beyond the scope of this article to describe the process, modal parameter extraction from the transfer function of the system is a common function of commercial fast Fourier analyzers [20], [21].

Conclusions

The modal decomposition of an impedance tube was theoretically demonstrated and experimentally verified. The new model incorporates pressure at the end or velocity input in the spatial domain, as well as unknown impedance at the termination end. The model is valid for both steady-state and transient responses. Several experiments have shown that the model is extremely accurate. The acoustic impedance at the termination end could be determined by using the eigenvalues from the steady-state experiments.

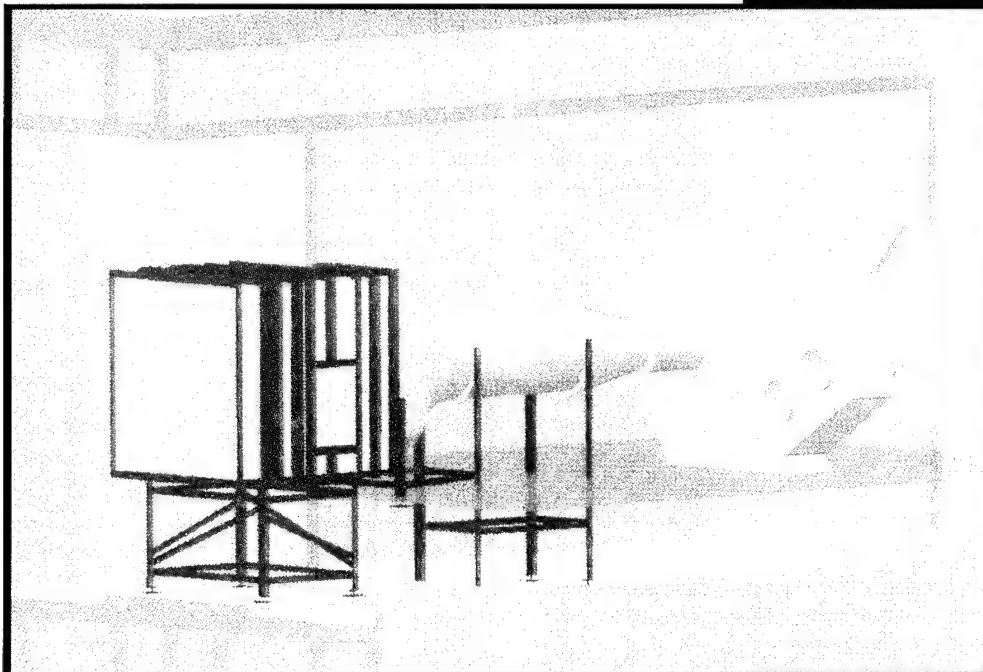
References

- [1] J. W. S. Rayleigh, *The Theory of Sound, Volume II*, Dover Publications, New York, 1878, pp. 49-68.
- [2] J. C. Snowdon, "Mechanical Four Pole Parameters and Their Application," *Journal of Sound and Vibration*, vol. 15, no. 3, 1971, pp. 307-323.
- [3] P. E. Doak, "Excitation, Transmission and Radiation of Sound from Source Distributions in Hard-Walled Ducts of Finite Length (II): The Effects of Duct Length," *Journal of Sound and Vibration*, vol. 31, no. 2, 1973, pp. 137-174.
- [4] M. A. Swinbanks, "The Active Control of Sound Propagation in Long Ducts," *Journal of Sound and Vibration*, vol. 27, no. 3, 1973, pp. 411-436.
- [5] M. C. J. Trinder and P. A. Nelson, "Active Noise Control in Finite Length Ducts," *Journal of Sound and Vibration*, vol. 89, no. 1, 1983, pp. 95-105.
- [6] J. Tichy, G. E. Warnaka, and L. A. Poole, "A Study of Active Control of Noise in Ducts," *Journal of Vibration, Acoustics, Stress, and Reliability in Design*, vol. 106, 1984, pp. 399-404.
- [7] D. D. Davis, Jr., G. M. Stokes, D. Moore, and G. L. Stevens, Jr., "Theoretical and Experimental Investigation of Mufflers With Comments on Engine Exhaust Design," NACA Report 1192, National Advisory Committee for Aeronautics, 1954.
- [8] C. E. Spiekermann and C. J. Radcliffe, "Decomposing One-Dimensional Acoustic Response into Propagating and Standing Waves," *Journal of the Acoustical Society of America*, vol. 84, no. 4, 1988, pp. 1536-1541.
- [9] C. E. Spiekermann and C. J. Radcliffe, "Stripping One-Dimensional Acoustic Response into Propagating and Standing Wave Components," *Journal of the Acoustical Society of America*, vol. 84, no. 4, 1988, pp. 1542-1548.
- [10] W. W. Seto, *Theory and Problems of Acoustics*, McGraw-Hill Book Company, New York, 1971.
- [11] P. E. Doak, "Excitation, Transmission and Radiation of Sound From Source Distributions in Hard-Walled Ducts of Finite Length (I): The Effects of Duct Cross-Section Geometry and Source Distribution Space-Time Pattern," *Journal of Sound and Vibration*, vol. 31, no. 1, 1973, pp. 1-72.
- [12] P. M. Morse and K. U. Ingard, *Theoretical Acoustics*, McGraw-Hill Book Company, New York, 1968, pp. 469-471.
- [13] The American Society for Testing and Materials, "Standard Test Method for Impedance and Absorption of Acoustical Materials by the Impedance Tube Method," Annual Book of ASTM Standards, Designation: C 384-85, vol. 04-06, 1985, pp. 144-156.
- [14] The American Society for Testing and Materials, "Standard Test Method for Impedance and Absorption of Acoustical Materials Using a Tube, Two Microphones, and a Digital Frequency Analysis System," Annual Book of ASTM Standards, Designation: E 1050-85a, vol. 04-06, 1985, pp. 910-917.
- [15] A. D. Pierce, *Acoustics: An Introduction to Its Physical Principles and Applications*, McGraw-Hill Book Company, New York, 1981, pp. 111-113 and p. 321.
- [16] Bruel and Kjaer, "Condenser Microphones and Microphone Preamplifiers," Bruel and Kjaer Instruments, Inc., Naerum, Denmark, 1982.
- [17] A. F. Seybert and D. F. Ross, "Experimental Determination of Acoustic Properties Using a Two-Microphone Random-Excitation Technique," *Journal of the Acoustical Society of America*, vol. 61, no. 5, 1977, pp. 1362-1370.
- [18] J. Y. Chung and D. A. Blaser, "Transfer Function Method of Measuring In-Duct Acoustic Properties. I. Theory," *Journal of the Acoustical Society of America*, vol. 68, no. 3, 1980, pp. 907-913.
- [19] J. Y. Chung and D. A. Blaser, "Transfer Function Method of Measuring In-Duct Acoustic Properties. II. Experiment," *Journal of the Acoustical Society of America*, vol. 68, no. 3, 1980, pp. 914-921.
- [20] Hewlett-Packard, "User's Guide, 5423A Structural Dynamics Analyzer," Hewlett-Packard Company, Santa Clara, CA, 1979.
- [21] Structural Dynamics Research Corporation, "User Manual for MODALANALYSIS 8.0," Structural Dynamics Research Corporation, Milford, OH, 1983.




ANDREW J. HULL earned his B.S. (1983), M.S. (1985), and Ph.D. (1990) degrees, all in Mechanical Engineering, from Michigan State University. He joined NUWC in 1990 and presently works in the Towed Array Exploratory Development Branch at the NUWC Detachment in New London, CT. His research interests are in the areas of acoustics,

vibrations, and boundary value problems.



Acoustic Facilities



The divider figure illustrates measurement of turbulence characteristics at the torpedo slide valve as part of internal flow studies in the water intake plenum of a submarine model in the acoustic wind tunnel.

Target Response Measurement System (TRMS)

David M. Deveau
Naval Undersea Warfare Center Division Newport

Abstract

The Target Response Measurement System (TRMS) at the Naval Undersea Warfare Center (NUWC), Seneca Lake Detachment, in Dresden, NY, provides a full-spectrum target response measurement capability. Seneca Lake's accessibility enables the testing of virtually all targets, regardless of scale, and the TRMS takes full advantage of the platforms and support capabilities at the facility.

Introduction

The Target Response Measurement System (TRMS) facility is designed to meet the needs of the target physics community and expanded to measure the target strength of full-scale torpedoes, unmanned underwater vehicles (UUVs), and mines over several bands of interest. Utilizing the existing Naval Undersea Warfare Center (NUWC), Seneca Lake Detachment, in Dresden, NY, TRMS has capitalized on existing moored platforms to address a wide range of test parameters. TRMS consists of a self-contained 8-foot x 20-foot measurement enclosure that houses test personnel, data acquisition, post-processing, signal generation, and support systems. A variety of directional acoustic projectors have been designed to be interchangeable within a fully instrumented steel frame. Central to the system design is the capability to perform measurements in the acoustic farfield with a 90° arc of bistatic sensors 333-m from the target. This configuration allows for the full exploitation of inexpensive scale model targets such as our 1/8-scale (6-m) submarine inner pressure hull. The flexibility of Seneca Lake's barges allows for ranges of up to 91 m when the 333-m range is not required. Scaled coatings and additional structures can be added to the scaled submarine hull and compared with their full-scale counterparts without sacrificing fidelity. In addition, mines, UUVs, and torpedoes can be measured at their full size over the surveillance and tactical regions while still in the acoustic farfield.

Active Acoustics

Creation of active interrogation signals proved to be a unique systems problem. Reflections from the target supports (lines, shackles), the lake surface

and bottom, and even the water itself all backscatter energy; it became necessary to create very directive acoustic beams coupled with directional receivers. Parabolic and parametric sources are our primary focus and were selected to handle specific frequency ranges. Two air-backed parabolic sources, designed at Division Newport, provide a directional capability similar to that of a flexural disk, but require only a single low-cost element placed at the parabola's focal point. The 42-in. unit covers the range from 800 Hz to 16 kHz and the 17-in. unit covers the range from 15 kHz to 50 kHz. The parametric source was chosen because of its extremely narrow beam and no side or back lobes. The parametric unit covers the range from 800 Hz to 6 kHz, overlapping the 42-in. parabola. This overlap was necessary because the 42-in. parabola's wider beam below 3 kHz created an excessive amount of environmental clutter when used 333 m from the target. Frequencies below 800 Hz are supported by flexensional units such as LTS. Above 50 kHz, we utilize a combination of high-frequency parametric sources, run at their primary frequencies. Currently, TRMS is researching two high-frequency concepts: (1) planar source, which utilizes polyvinylidene fluoride (PVDF) polymer technology, and (2) a diced ceramic element used in 1920s torpedo technology and currently used in medical analysis systems.

Acoustic Receivers

Further reduction of environmental and man-made reflections is achieved with vertical line arrays which provide a wide measure of surface and bottom rejection. Our typical monostatic receiver is a rugged 3-foot line array suspended with the

projector. This receiver is currently being moved to a backup role as transmit/receive (T/R) switches are introduced into the parabolic/parametric sources. The switches will be timed such that the source will become a highly directive receiver with the same benefits as their active counterparts. The 3-foot line arrays and parabolas become omnidirectional below approximately 2 kHz, making them susceptible to reverberant clutter. For most targets, this does not present a problem; however, excessive clutter and ambient below 1 kHz requires the receive array to have gain and surface rejection. To achieve this goal, eight 3-foot line arrays are placed together to form a 40-foot line array with each array output individually stored for later recombination. Post-processing of the individual lines allows the sensor outputs to be shaded and summed to create a better noise and off-axis clutter rejection. Higher frequencies are supported by hydrophone probes, again providing a high directivity.

Three additional sensors are utilized which (1) monitor the projector output (MONITOR); (2) measure the source level near the target, but off on an angle (OFF-AXIS); and (3) allows assessment of target alignment (ALIGN). The monitor hydrophone is placed 50 feet in front of the target and measures the amount of source level directed at the target. This output is corrected to the target's face and used

as the source level for computation of target strength. The monitor is also used in conjunction with the off-axis hydrophone to pass source level information to the target alignment system. The alignment sensor provides a simple method to orientate projector to target in both the vertical and horizontal planes. This is done at the highest frequency of interest and the sensor is removed once the projector is peaked on the target. These three sensors are generally small 2-in. omnidirectional balls.

Bistatic Receivers

Suspended at the 91-m depth are 19 line arrays forming a permanent 90° arc about the target when deployed at a range of 333 m (Figure 1). Spaced at 5° increments (relative to source-target-receiver path), the 19 permanently moored arrays give TRMS a multistatic measurement capability for each active interrogation. The receivers are terminated in an underwater electronics enclosure which filters and amplifies the signals prior to their transmission to the surface. A 700-m cable carries the signals from the underwater enclosure to a permanent barge-mounted termination panel. Activation of the bistatic array requires the attachment of a multiconductor cable between the data acquisition system and the barge termination panel. Because

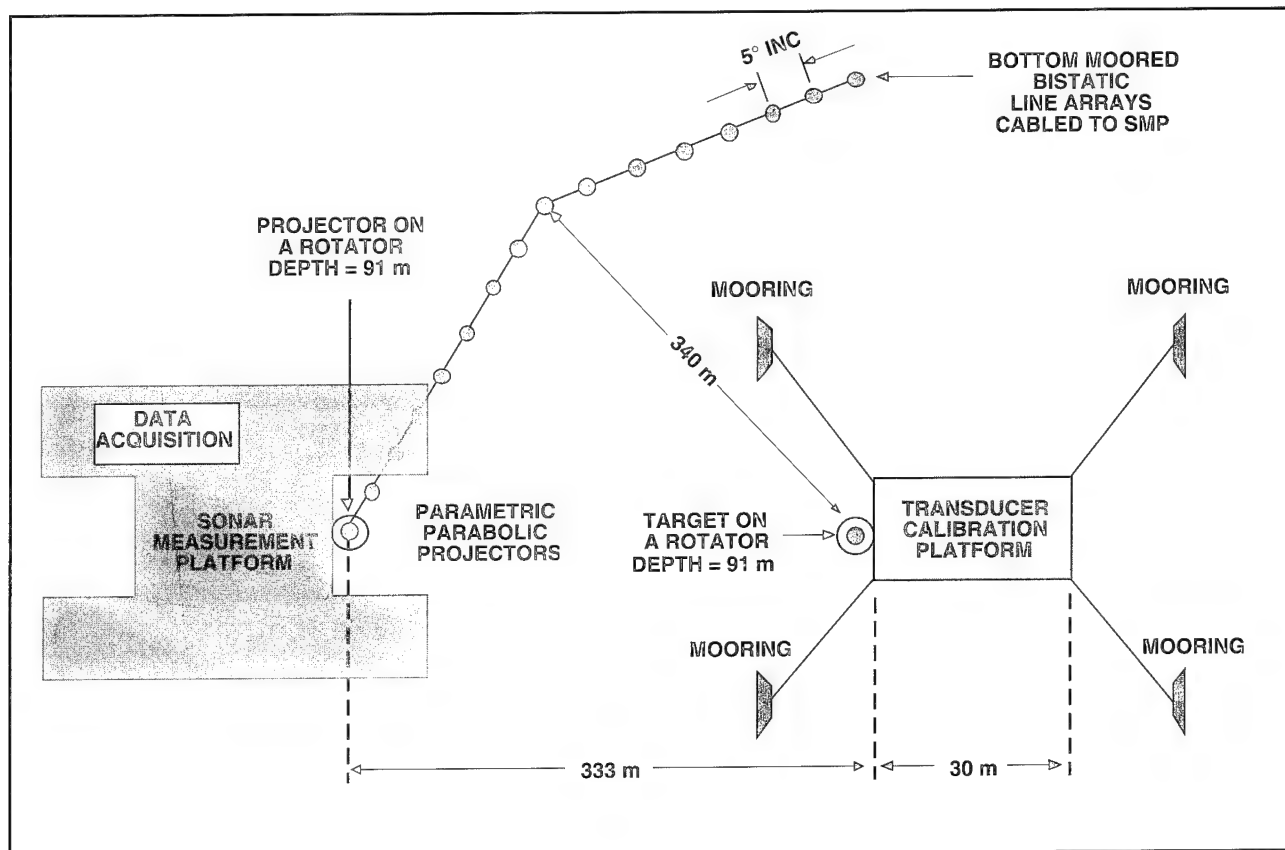


Figure 1. Bistatic System Overview

the array and its termination are permanent, activation requires only one hour of setup and calibration to place the system on-line. As previously stated, the bistatic array can support frequencies up to 15 kHz, with a lower cutoff of 800 Hz.

In addition to the receiver array, single relocatable bistatic receivers are available for deployment. A line array is moored at the user's desired location with the receiver cable brought to the surface. The cable is terminated on a small range craft and its output is transmitted using an FM carrier over a wideband analog radio frequency (RF) link. The RF link allows for placement of the bistatic receiver without the concern of long temporary cable runs on the lake surface or bottom.

Barge Local

A target's physical size, frequency range, or user requirements can also be supported by docking one of several Seneca Lake barges next to the main moored barge, the sonar measurement platform (SMP). This configuration creates two very stable platforms from which the measurement can be conducted (Figure 2). A maximum separation of 91 m, source to target, can be adjusted to meet acoustic requirements. A reduction in required source level and acoustic reverberation are the advantages achieved at short distances. This configuration can be combined with the 333-m range to enhance detectability over a wide-frequency range.

Data Acquisition

The multiple TRMS acoustic sensors (22 total) require a sophisticated suite of acquisition hardware and the ability to be quickly reconfigured to meet a wide variety of applications. Digitizing all channels

provided the ability to perform several real-time processing functions, but also presented a formidable challenge for handling the projected wide range of frequencies and then to store this information to a fast low-cost storage medium. The system developed into a bank of dedicated external hardware connected to and controlled by a personal computer (PC)-based system. To accomplish the data storage task, a dedicated high-density hard disk was coupled with an optical disk for real-time data storage and data archive, respectively.

Precision Filters, Inc., was selected to provide the external hardware. The system consisted of several independent modules which can be replaced on a channel-by-channel basis without long down time (<1/2 hour). The hardware suite consists of (1) a differential input preamplifier, (2) a lowpass filter bank, (3) a base band translator (BBT), and (4) the 16-bit analog-to-digital converter (ADC) (Figure 3). The BBT provides the system with its ability to handle a wide range of frequencies without having to modify the ADC. The BBT shifts any bandlimited signal from its original frequency to the same bandwidth centered about 0 Hz and produces two outputs for each input: the 'I' (in-phase) and 'Q' (quadrature) signals. These two signals carry all the information necessary to properly process the translated signal. In addition, because the original bandwidth and center frequency are known, the original signal frequency can be recreated in post-processing. Shifting to the original frequency is not necessary for processing the target strength; however, it does provide the user a better view of the target's response in the time domain. The ADC has a maximum per-channel sample rate of 40 kHz, which is sufficient to digitize the maximum translator bandwidth of 12 kHz. The BBT can be bypassed should a user's frequency be low enough (<10 kHz) that translation is not required. The ADC

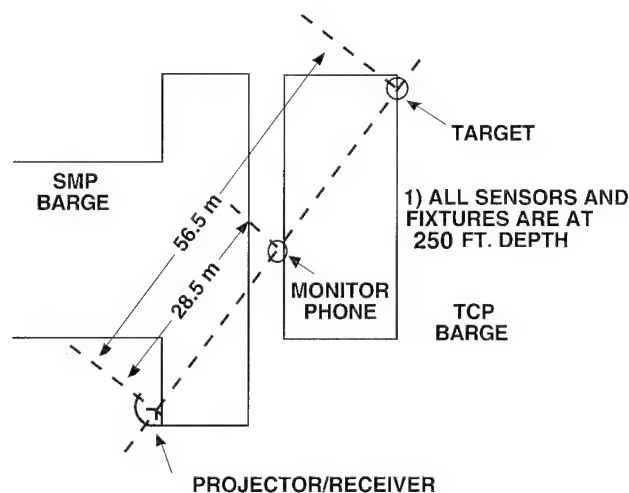


Figure 2. Local Barge Configuration

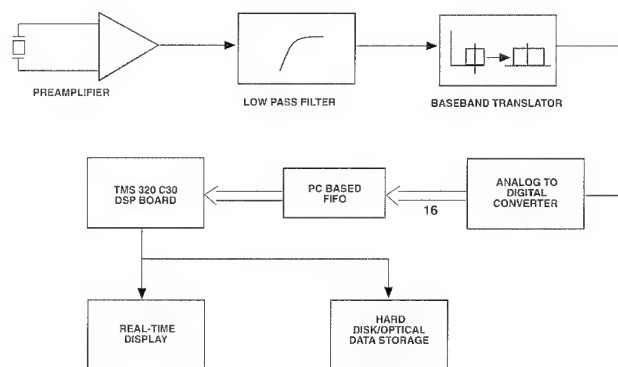


Figure 3. Data Acquisition Block Diagram

is externally gated to acquire a time period long enough to characterize the target. The gating process reduces the overall amount of data stored and analyzed in post-processing. Digital data are transferred over a high-speed parallel bus to a first-in/first-out (FIFO) interface located with the PC.

The PC is a 486/66 MHz IBM compatible unit that controls all system hardware, processes and displays real-time data, and stores all information to an internal 1-Gbyte hard disk. The PC tasks are all accomplished within the standard acoustic ping repetition rate of one ping per second. The PC program, written in C, is menu-driven, allowing the user to easily change hardware settings and not requiring intimate knowledge of the hardware systems. All raw analog information is digitized and stored in real time for later review/processing of the active signature. The data acquisition computer system displays all channels in real time and utilizes the TMS320C30 digital signal processor to compute the receive level and target strength of each active channel. Graphically, the user can view the captured time series from any channel and the target's polar response pattern.

Signal generation is accomplished with an arbitrary waveform generator (ARB). This is also controlled by the PC and the operator can select from several different canned waveforms (CW, FM Sweep, White Noise) or enter in a file name which would cause the PC to download a compatible datafile to the ARB for generation. Utility programs are available for creation of user-defined signals from mathematical expressions.

Post-Processing Capabilities

Post-test analysis of target response data is an important feature within the system configuration. Because targets do not behave the same at all frequencies, it is essential that the user be able to quickly evaluate an individual target's performance and determine which frequencies or signals would better exploit the target's acoustical features.

Post-processing of data involves recovering the stored raw time series information, hardware configuration, and calibration results. This information was stored in real time by the data acquisition computer and updated regularly during measurement. A second post-processing PC utilizes a series of algorithms to recover this information from the optical disk and place it in a format usable to the MatLab digital signal processing program. Once in the MatLab environment, the user can select from a standard processing set that includes integrated target strength, root mean square (RMS) and peak target strength, and fast Fourier transform (FFT) computed target strength (Figure 4). Data

acquired using FM sweeps and similar complex signals can be presented as color contour or waterfall plots (Figure 5). Time series plots (Figure 6) of all active pings are available. The MatLab environment allows easy modification of our processing suite to accommodate a request for additional processing or the user can incorporate his/her own processing algorithm.

Support Systems

Coordinating the underwater position of the projector and target requires several sensors that must be continually monitored. To accomplish this, a virtual control panel was created under the National Instruments LabView environment and placed on a 486/66 MHz PC (Control), separate from the data acquisition and post-processing computers.

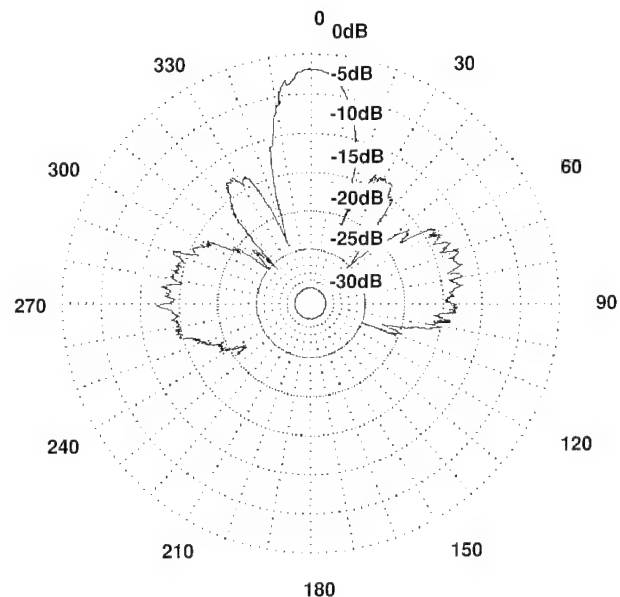


Figure 4. Sample Target Beampattern

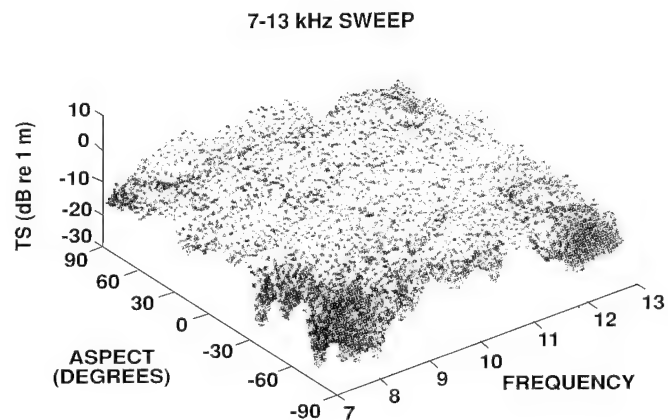


Figure 5. FM Sweep

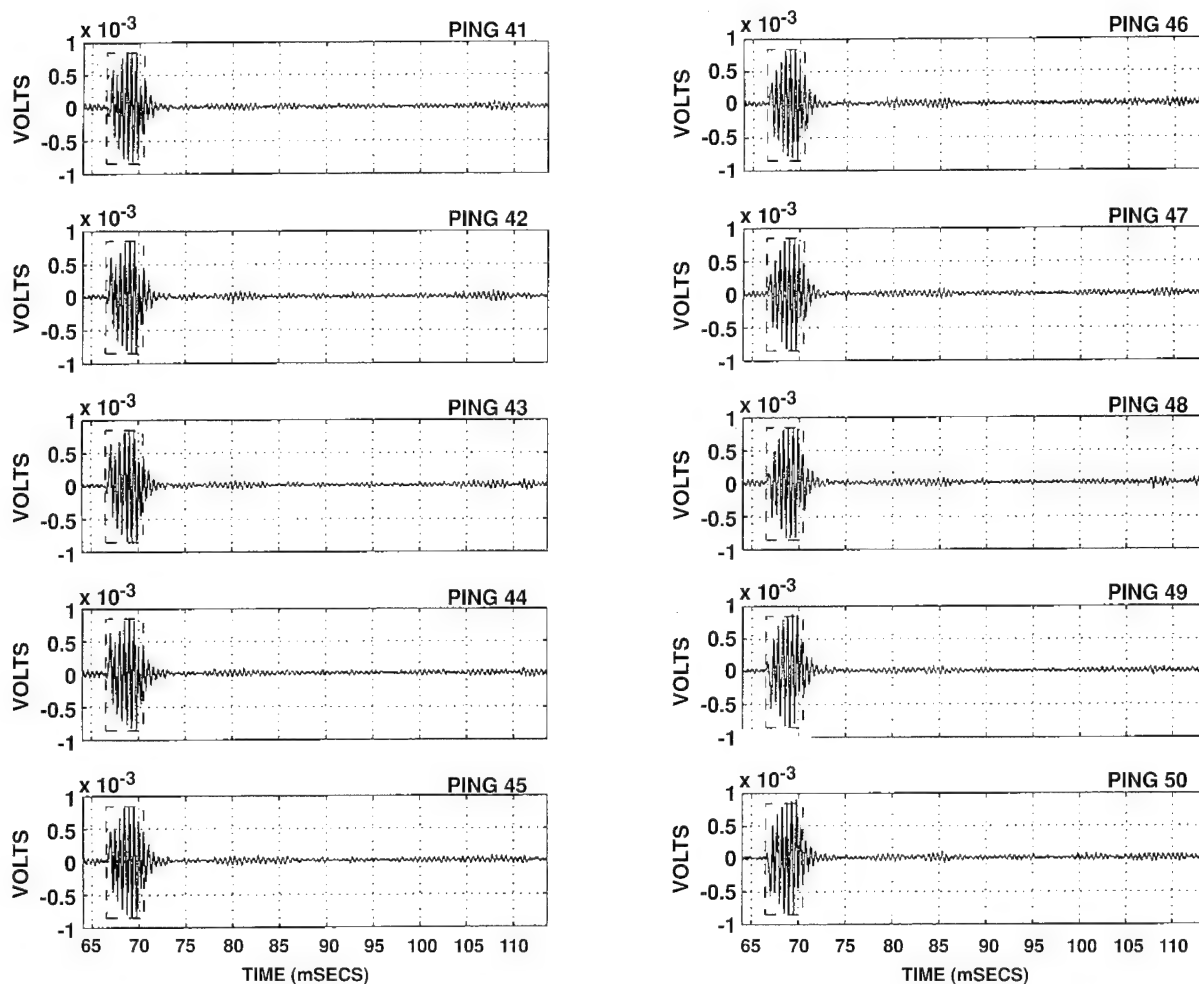


Figure 6. Target Response

All sensor outputs and support system controls are placed on the screen, providing the user with only required access to the hardware. Tilt sensors and underwater compasses are placed on the target and projector to ensure proper orientation after deployment. The individual azimuthal rotators of the target and projector are controlled from the computer. All control functions and sensors relative to the target are transmitted to the Control computer via serial and analog RF links.

The Control computer also handles the target alignment task using the Monitor and Off-Axis hydrophones. When the projector is peaked on the target, the levels are stored along with the compass and tilt sensor information. The Control computer continually checks the Monitor phone level and determines a course of action should this level drop. If the Monitor level decreases (increases) but the Off-Axis level increases (decreases), the system determines that the projector to target orientation has shifted and commands the target rotator to

slowly redirect the projector to peak on the target. Tilting of the projector is also handled by the Control computer via an electric tilt motor mounted on the projector frame. Once the desired tilt is achieved, the electric tilt motor is powered off and simultaneously engages a normally closed disc brake to hold the projector in place without the need for power.

Performance Specifications

TRMS is designed to interrogate targets in the acoustic farfield. At the 333-m range (Barge Remote), the farfield requirement specifies a maximum target size and frequency range. Measurements taken with the system deployed from adjacent platforms (Barge Local) are done at higher (lower) frequencies with smaller (larger) targets. Whether the 333 m/remote, local, or a combination of both configurations is required depends on the particular test requirement.

General Specifications

Target Aspect Angle	$0 < f < 360^\circ$
Aspect Angular Resolution	$< 1^\circ$
Acoustic Sources	Parametric/ Parabolic
Acoustic Receivers	Line Arrays
Target Rotation Speed	0.1° per second
Max Ping Interrogation Rate	1 per second

Specifications of the Barge Remote Bistatic Range

Frequency Range	800 Hz - 15 kHz
Ping Type	CW, FM sweeps, user-defined
Operational Depth	300 feet
Max Target to Sensor Distance	333 m nominal
Number of Bistatic Sensors	19
Bistatic Measurements	0 to 90° , 5° increments

Specifications of the Barge Local Configuration

Frequency Range	200 - 400 kHz
Ping Type	CW, FM sweeps, user-defined, broadband
Operational Depth	250 feet; variable
Max Target to Sensor Distance	91 m nominal
Placement of Bistatic Sensors	User-defined

Sample Bistatic Measurement Scenario

The parabolic/parametric projectors are deployed to the nominal 91-m depth using available crane assets. Once at depth, a horizontal rotator is placed on the pipes to give the projector a full 360° rotational field of view. The target is deployed to the same depth utilizing a 6-ton winch to lower the target with low stretch Dacron or small diameter wire rope support lines. Shackles and other hardware are kept to a minimum about the target. A small hydrophone is also lowered with the target to aid in aligning the projector at the target. The hydrophone is removed once the alignment is complete. The support lines will place the target at a depth of 150 feet, at which point a strongback is attached and pipes are used to lower the target the remaining distance. An electronics package containing the target's tilt sensor and compass relays information on the target's orientation. Support lines are not used for the entire distance to eliminate backlash as the target is rotated. Once at depth, a horizontal rotator is attached to the pipes. The target's rotator is controlled within the TRMS

measurement system via an RF link. The monitor phone is lowered to the same deployment depth between the projector and target. Typical monitor phone placement is 50 feet in front of the target to prevent the target's response from mixing with the direct signal. This completes the system deployment, but now the projector must align with both the target and the monitor phone. This is accomplished by monitoring the target's hydrophone and the monitor phone as the projector is active and moved in both the vertical and horizontal planes. Once the peak is established at the same azimuthal and inclination angle on both the target and monitor phone, the target's hydrophone is removed and the system is ready to begin the measurement. Target rotation is continuous at a rate of 0.1° per second. The system waits approximately one minute to allow the target to stabilize its speed to begin data acquisition. After a full rotation or a nonrotating target's ping set is complete, the acquisition computer's data are off-loaded to an optical disk for transfer to the MatLab post-processing computer. The data acquisition computer is cleared and ready to begin a new test.

Recent Measurements

TRMS has taken measurements for NUWC Division Newport's target physics program, Commander Submarine Force, U.S. Atlantic Fleet; Commander, Space and Naval Warfare; and the AMDS submarine sonar program. Bistatic data have been taken on the 1/8-scale model target of a submarine inner pressure hull and compared with 1/100-scale model data taken at the Division's Acoustic Test Facility. COMSUBLANT and SPAWAR data have been gathered over a wide frequency for several different classes of mines and mine training shapes.

Conclusions

TRMS is designed to meet a wide variety of customer requirements. The data acquisition and post-processing systems have the capability to meet virtually any user requirements covering target strength measurements to target imaging. Operating as part of an existing facility allows the system to operate at a very low cost while still providing the equipment necessary to meet complex test parameters. The facility will enhance any active measurements program by being able to evaluate full-scale weapons, UUVs, mines, or realistically sized vehicles in a real environment.



DAVID M. DEVEAU is a project engineer for the Target Response Measurement System (TRMS) in the Shore Systems Branch of the Test and Evaluation Department at NUWC Division Newport. In his ten years at NUWC, Mr. Deveau has also been a project engineer and system designer for the AUTEC Site 1 Modular Range Tracking System (MRTS), a data acquisition/control system designer for the Weapon Noise Measurement (WNM) system, and has designed several data acquisition and control systems for the ICEX and SHAREM exercises. He currently holds three patents for systems related to data acquisition and acoustic simulators. Mr. Deveau received a B.S. degree in Electrical Engineering from the University of Rhode Island in 1984.

Acoustic Test Facility

The Acoustic Test Facility in Newport is the Navy's primary test bed for the acoustic evaluation of underwater sonars for vehicles and targets. Capabilities include the measurement, characterization, modeling, analysis, and reduction of complete underwater weapon systems as well as individual system components. The facility consists of a large test tank, associated mechanical support equipment, a 3-axis probe positioning system, a fully automatic data gathering and control system, and a graphite fiber pressure vessel.

General Features and Capabilities

The Acoustic Test Facility features a 700,000-gallon test tank that measures 60 ft long, 40 ft wide, and 35 ft deep. The tank is fitted with viewing and access ports and is supported by a variety of handling and positioning equipment, including overhead cranes, rotators, and movable test bridges. The test tank provides a maximum 50-ft test distance, with 2 ms of reflection-free test time. One-man operation is possible with minimal setup time, and two or more simultaneous test setups can be accommodated. Tests are controlled and test data collected by the facility's integrated computer system, called the Acoustic Evaluation System.

The facility's mechanical support equipment can handle test specimens weighing up to 3 tons and can rotate specimens in three dimensions to a computer-controlled accuracy of 0.001°. The two overhead cranes are electrically driven and are capable of X-Y travel throughout the building; each has a lifting capacity of 3 tons. The test bridges, which support the facility's rotational equipment and shaftwork, have a weight capacity of 5 tons. They are designed to accommodate the rotators in a variety of test wells within the tank. This flexibility permits multiple test setups and allows tailoring to various test requirements. Laser alignment of test devices is available when it is necessary to establish precise mechanical alignments independent of the acoustic main response axis. Both underwater and topside laser alignment can be done.

An X-Y-Z positioner is available with a capability of 6 feet of travel in each axis and an accuracy within ± 0.001 in. An underwater rotator can be used with this positioner to provide roll or tilt rotations in synchrony with X-Y-Z positions.

The Acoustic Evaluation System provides computerized, fully automatic test control and data gathering. It comprises a Hewlett Packard 9000 computer; a Real Time Systems, Inc., data generation, acquisition, and transfer subsystem; and a host of supporting instruments and controls.

A graphite pressure vessel serves as an acoustically transparent test vessel for performing acoustic tests at pressures up to 1000 psi at temperatures from 35°F. The pressure vessel opening is 32 in. in diameter and has a test window length of 60 in.

Testing and Data Reduction Capabilities

Transmit Transfer Functions

- Impedance and phase
- Resistance vs. reactance
- Admittance and phase
- Conductance vs. susceptance
- Transmit linearity/constant amplitude
- Transmit voltage response
- Transmit current response
- Transmit current-voltage response
- Transmit power response and efficiency
- Fast Fourier Transform (FFT) capabilities on all of the above

Reciprocity

- Transmit and receive

Beam Patterns

- Polar
- Rectangular
- Multipole (phase required)
- Directivity index
- Frequency or spectrum vs. angle
- Three-Dimensional

Receive Transfer Functions

- Receive voltage response
- Receive linearity and constant level
- FFT capabilities

Target Analysis

- FFT
- Scale model analysis (monostatic or bistatic)
- Target strength and contour mapping in three dimensions
- Acoustic holography using the 3-axis positioning system

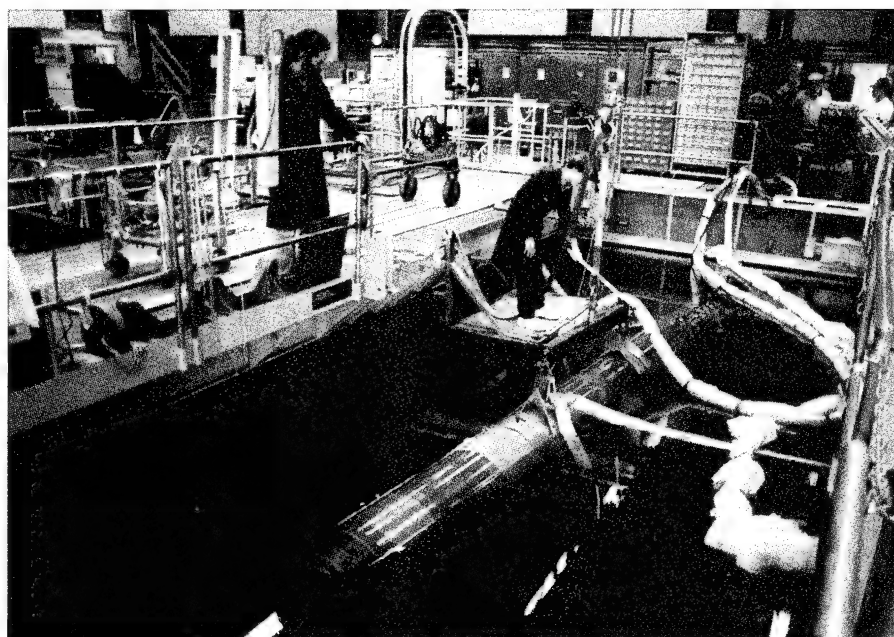


Figure 1. Acoustic Test Facility Reverberant Test Tank

Radiated Noise Measurements

- Reverberant tests
- Acoustic holography using the 3-axis positioning system

Mechanical Features

- 3-ton weight-handling capacity
- Three-dimensional rotation of test specimens
- Rotators:
 - one 5-ton
 - three 1-ton
 - one submersible 1-ton for pitch and roll axis rotation
 - one coaxial rotation system with 0.001° accuracy
 - one submersible 200-pound stepper motor for pitch and roll axis rotation
- 3-axis probe positioner with pitch and roll capabilities
- two or more simultaneous test setups
- maximum 50-ft test distance with 2 ms of reflection-free test time, 1000 psi with temperature control from 35°F to 120°F.
- laser alignment fixture for precise mechanical alignments
- tank capacity of 700,000 gallons
- anechoic lining system (with frequency range of 300 Hz to 100 kHz)

Signal Generation, Reception, and Data Analysis Features

Frequency range: 10 Hz to 3 MHz

Dynamic range: ≥ 100 dB

Linearity: $\pm 1/4$ dB

Power out:

50 W to 500 kHz

75 W to 1 MHz

2 kW to 4 kW

Point of Contact:



Claude A. Ledoux
Naval Undersea Warfare Center
Division Newport
Newport, RI 02841
(401) 841-2237
FAX (401) 841-2482

Claude A. Ledoux is a senior specialist in the area of underwater acoustic measurements technology and has worked in the field of acoustic testing for 34 years. As a member of NUWC Division Newport's Acoustic Systems Technology Branch, Mr. Ledoux serves as manager of the Division's Acoustic Test Facility. He is responsible for the development of unique instrumentation and software to perform underwater acoustic measurements. These original developments have gained wide acceptance in other acoustic test facilities. Mr. Ledoux advises and assists Navy, commercial, and foreign organizations in setting up and modifying acoustic test facilities.

Acoustic Wind Tunnel

The Acoustic Wind Tunnel in Newport has the lowest ambient noise levels of any known equivalent facility. Specifically conceived to perform basic investigations in the areas of hydrodynamics and hydroacoustics on small-diameter underwater vehicles, the wind tunnel was designed to be a general-purpose research tool for advanced studies in propulsor hydrodynamics, hydroacoustics, in-flow analysis, boundary layer turbulence, and wake studies.

It is supported by independent high/low rate and digital data acquisition systems. These systems allow multi-channel measurements capability of flow induced phenomena, including acoustic radiation and directivity, turbulence, velocity, and pressure distributions; and steady and fluctuating aerodynamic forces in a very quiet acoustic and flow background environment.

Construction

- Overall room footprint: 110 ft long x 34 ft wide x 34 ft high.
- 60 ft long with variable cross sectional components.
- Fabricated using 3/4-in. oak veneer plywood surrounded by 5-ft aluminum angle frames and elevated with adjustable steel base structures. All joints and seams sealed internally.
- 12-1/2-ft long diffuser section contains three screens (8 mesh size with .028-in. diameter - 304 stainless).

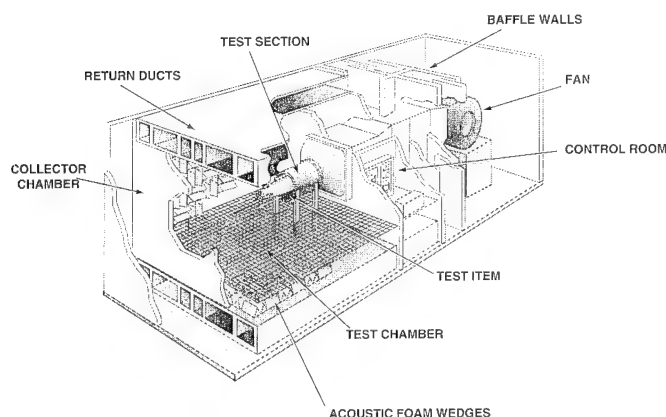


Figure 1. Acoustic Wind Tunnel

- 15-ft long muffler section contains two banks of in-line mufflers. The mufflers in the first bank are oriented horizontally; the mufflers in the second bank are oriented vertically to improve performance.
- 5-ft long first contraction section. Flexible duct connector used to join muffler section. Mainframe for the sting assembly located in this section.
- 11-ft settling chamber contains two screens and two flow filters. Screens consist of 16 mesh size with .018-in. diameter - 304 stainless and 23 mesh size with .009-in. diameter - 304 stainless. Flow filters consist of 1/2-in. diameter honeycomb hexcell, 5 in. thick and 1/8-in. diameter cylindrical tubes 8 in. thick. Coarse filters and screens are followed by finer mesh filters and screens. Up to four additional screens can be incorporated.
- 8-ft long contraction nozzle constructed of hand laid 3/16-in. E-type fiberglass over 1-in. urethane foam core ($3 \frac{1}{2} \text{ lb/ft}^3$). Surface finish of 63μ in.
- 8-ft long test section constructed of hand laid 3/16-in. E-type fiberglass over 3/4-in. split balsa wood core. Surface finish of 63μ in.

Technical Characteristics

Test Section

- Standard Configuration: 4-ft diameter open jet following 9-ft long fiberglass duct.
- Full size tactical scale vehicles up to 26-in. diameter.
- Capable of modifying open jet discharge from 0 to 100 ft^2 .
- Collection chamber enables free jet to pass undisturbed through acoustic test chamber.

Flow

- Square to round 8:1 fiberglass contraction nozzle; 63μ -in. finish.
- 0-200 fps with standard 4-ft diameter circular test section.
- Spatial uniformity > 99.5 percent at 150 fps - standard configuration.
- Turbulence Intensity < 0.3 percent at 150 fps - standard configuration.
- Sting-mounted test item; no balance, strut, or fairings in upstream flow.

Acoustic Chamber

- 100 Hz to 40 kHz anechoic chamber 33 ft wide x 43 ft long x 25 ft high.

- 35,500 ft³ volume 34-in. foam wedges on all surfaces.
- Equipped with rotating boom directional microphone and fixed microphones.
- Wire suspension flooring 7 ft-1 in. below centerline of tunnel.
- Removable aluminum floor grating capable of supporting a distribution load of 2000 pounds.
- 5-ton crane on rails capable of moving test items into test chamber.
- 50 hard points on floor and ceiling capable of supporting 2000-pound point loads.

Environmental

- 100-ton capacity internal heat exchangers in low velocity return air section of wind tunnel to maintain constant temperature and humidity (constant Reynolds Number).

Silencing

- Fan room covered with absorptive lining and panel damping.
- Fan mounted on 160-ton concrete pedestal isolated from building foundation.
- Two banks of in-line mufflers absorb sound energy produced by the fan and eliminate sound contamination in the acoustic chamber (IAC model 5 LFS silencers).
- Tunnel mechanically isolated from building partitions, fan discharge housing, and specific tunnel sections.
- Absorptive linings in sinuous return air paths and collection chamber.
- Electric motor with isolation coupling.
- Seamless metal return air plenum externally damped.
- All internal exposed surfaces covered with 2-in. thick sound foam.

Powering

- 500 HP variable frequency fan drive.
- 0-960 RPM fan with 78-in. diameter wheel and air foil blades.
- Fan delivers 136,000 scfm at 900 RPM and 14-in. H₂O static pressure.

Model Support

- Nose sting 14-in. diameter x 25-ft long cantilever anchored on separate foundation (standard configuration).
- Permits formation of natural boundary layer without interference from struts or guy wires.
- Sting position and slope are adjustable or removable, if desired.
- Can support models weighing as much as 1000 pounds.

Model Propulsor Power

- Contra- and single-rotating shafts, individually operated from control room; each vibration system isolated and cooled.

- Dynamometer internal to test item, capable of measuring propulsor thrust and torque.

Unique Features

- Test section discharges along centerline of the anechoic test chamber, allowing accurate low frequency noise measurements. Wire suspension floor allows access to model while floor wedges are in place.
- Tunnel has no collector downstream of the test section. Collector noise would limit acoustic performance. Instead the tunnel uses a free stream diffuser configuration where the exiting air jet is brought to rest normal to a plane smooth wall.
- Vehicle models weighing up to 1000 pounds are supported by a cantilever nose sting which obviates the need for support struts and/or suspension wires. The flow noise of these appendages is totally avoided, as are the disturbances they would create in the inflow to a propulsor.
- Tunnel is secured to the Top Secret level to meet data acquisition and reduction requirements of current and future Navy programs. Closed circuit TV monitors entire area.
- Facility cranes can support loads up to 5000 pounds, meeting the needs for most model testing requirements.

Point of Contact:



Pierre J. Corriveau
Naval Undersea Warfare Center
Division Newport
Newport, RI 02841
(401) 841-7085
FAX (401) 841-1144

Pierre J. Corriveau is the head of the Solid Mechanics and Design Branch within the Advanced Technology Division at NUWC Division Newport. He received a B.S. degree in Mechanical Engineering from the University of New Hampshire in 1976 and an M.S. degree in Ocean Engineering in 1978 and a Ph.D. in Mechanical Engineering and Applied Mechanics in 1991, both from the University of Rhode Island. His research interests are in the area of radiated noise measurements and modeling of underwater vehicles. Of particular current interest is the modeling of hydroacoustic propulsor radiated noise sources, including the excitation mechanisms and the fluid-loaded structural response. Dr. Corriveau has published in the areas of radiated noise measurements of free running vehicles and laboratory subsystems, the modeling of hydroacoustic sources, and empirical techniques to measure structural response functions.

Anechoic Chamber

Description

The Anechoic Chamber is a calibrated (in accordance with the National Voluntary Laboratory Accreditation Program (NVLAP)) facility built to support NUWC Division Newport's lead role in the research and development of tactical scale underwater vehicles. It is geared specifically to advanced studies in active noise cancellation, target strength, acoustic directivity, and measurements of the sound power level produced by full-scale, small diameter vehicles, as well as components and subsystems for submarine scale hardware. The unique combination of acoustic and radio frequency (RF) measurements within a common enclosure allows the entire range of tactical signatures to be established in a cost-effective manner. The versatility designed into this facility allows investigations into such areas as environmental/community noise studies, consumer appliance,

automobile noise, and commercial product airborne sound certification.

The unobstructed 64,000-ft anechoic chamber is acoustically anechoic from 80 Hz to 40 kHz. The walls of the chamber are completely covered with acoustic wedges and acoustic reflections are reduced to an extremely low level, emulating a free field environment. The chamber is RF shielded from 14 kHz to 2 GHz. Electromagnetic shielding is accomplished by surrounding measurement volume with a contiguous metallic enclosure. Redundant ground loops guarantee that the earth's magnetism, as well as stray electrical currents, are suppressed to enable the measurement of low level RF signals. The anechoic chamber and electromagnetic shield are suspended by 7 Hz pneumatic mounts in order to be mechanically isolated from the host facility.

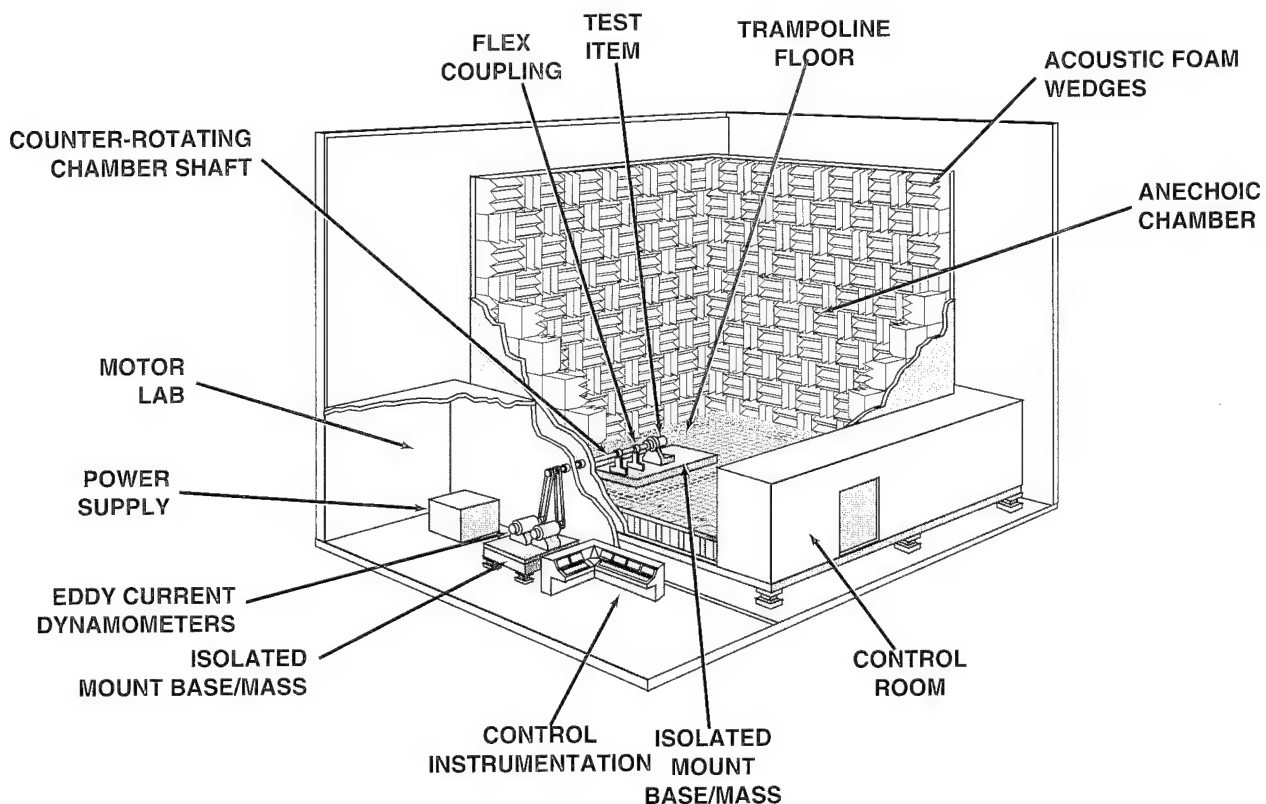


Figure 1. Anechoic Chamber

This results in an extremely low background noise level within the facility. Quiet low power dynamometers, located outside the chamber, allow hardware to be tested under similar in-water conditions. Vehicles or components weighing up to 5000 pounds may be suspended within the chamber for testing.

Technical Characteristics

Acoustic Characteristics

- 80 Hz to 40 kHz anechoic chamber, 40 ft wide x 40 ft long x 40 ft high
- 64,000 test volume, 30-in. foam wedges on all surfaces
- Convertible to hemi-anechoic mode
- Equipped with rotating boom directional microphone and fixed microphones
- 14 kHz to 2 GHz electromagnetic shielded

Construction

- Shielding 4-in. thick, 65 dB TL @ 1 kHz, 100 dB TL @ 14 kHz, Magnetic 100 dB TL @ 1 mHz, Electric 100 dB TL @ 50 mHz, Plane Wave 100 dB TL @ 2 GHz
- Entire chamber isolated from host facility by self-compensating 7 Hz pneumatic mounts
- Removable aluminum floor grating capable of supporting a line load of 20 lbs/ft²
- Wire suspension flooring 4 feet above chamber floor
- Two 8-in., four 4-in. mechanical communication, four 2-in. electric communication/instrumentation

Environmental

- Automatic temperature/humidity control, 4600 SCFM quiet low velocity air exchange

Test Item Support

- 110, 220V AC, variable DC
- Component cooling
- Low power (200 HP) low noise single and counter-rotating dynamometry sets. Dynamometers located outside test volume, completely isolated (vibration and airborne sound)
- 140 hard points on floor and ceiling capable of supporting 2000-pound load; center points capable of suspending 5000 pounds.
- Facility accepts full-scale tactical vehicles and scale models up to 25 ft in length
- 3-ton crane capability

The NUWC Anechoic Chamber is supported by a complete suite of specialized instrumentation and independent high and low rate digital data acquisition systems. The instrumentation and acquisition systems allow multi-channel measurements capability of noise directivity, and

steady and fluctuating acoustic forces in a very quiet acoustic environment.

The chamber is designed to be a turn-key facility, requiring one technician along with one investigator. The extremely low operating cost of this facility, i.e., passive room, will allow access to a multitude of programs with limited resources.

The entire laboratory is secured to the Top Secret level in order to facilitate data acquisition and reduction in support of present and future Navy-wide program requirements.

Point of Contact:



John D. Muench
Naval Undersea Warfare Center
Division Newport
Newport, RI 02841
(401) 841-7085
FAX (401) 841-1144

John D. Muench is a member of the Advanced Technology Division at NUWC Division Newport. He received his B.S. degree in Mechanical Engineering in 1985 from the University of Hartford, his M.S. degree in Ocean Engineering in 1991 from the University of Rhode Island, and is pursuing a Ph.D. in Mechanical Engineering and Applied Mechanics at the University of Rhode Island. His research interests are in the field of experimental acoustics and hydrodynamics related to torpedo radiated noise reduction. Of particular current interest is the design, construction, and calibration of the NUWC Anechoic Chamber and Acoustic Wind Tunnel. Mr. Muench has published in the areas of structural acoustics, radiated noise measurements, and empirically based radiated noise modeling.

Materials Analysis Laboratory

The Materials Analysis Laboratory is an engineering test facility dedicated to working with the scientific community for development of mechanical properties of materials and components for use in Navy submarine and surface ship systems.

This facility is capable of performing static and dynamic measurements on most engineering materials. In addition to mechanical property measurements, it is involved in studying corrosion and fatigue mechanisms as they pertain to Navy applications, as well as failure analysis of mechanical components.

The Materials Analysis Laboratory has two static test instruments, both Instron Universal Testing Machines: a Model 1125 and a Model 4206. The 1125 Instron has a 20-Kip load frame and several load cells that give it accurate load measuring capacities from 5 pounds to 20,000 pounds at speeds of 0.002 in. per minute (ipm) to 20 ipm. This machine is equipped with a high deformation extensometer for measuring the elongation of elastomers up to 1000 percent and is capable of performing load or displacement controlled experiments, stress relaxation, and cyclic measurements. The 1125 can conduct tests in both compression and tension and data can be recorded on an XY recorder, a strip chart, or by computer acquisition.

The Model 4206 Instron Machine has a 30-Kip load frame and is microprocessor controlled. Like the 1125, this machine has several load cells that provide accurate load measurements from 5 pounds to 30,000 pounds. This machine is easily set up and calibrated and, as such, is normally used for most of the metal testing conducted at the Materials Analysis Laboratory. It is equipped with strain gage extensometers of various gage lengths capable of measuring strains up to 50 percent. It is also equipped with tape extensometers that measure in preset increments of elongation and a video extensometer for special work. The 4206 has an infinite speed range from approximately 0.001 ipm to 20 ipm. This too can test in both tension and compression and has controls that allow for load, displacement or strain control, as well as break detection, automatic peak record features, and crosshead motion controls. A chamber, capable of operating in the range of $\pm 150^{\circ}\text{C}$, is available for conducting experiments and tests at different temperatures. Use of the chamber imposes serious

limitations on the test configuration, strain measurements, and amount of elongation that can be placed on samples.

Many fixtures and grips are used by the Materials Analysis Laboratory, and they are usually designed to be compatible with both machines. Typical fixtures used include a sliding 90° peel fixture, compression platens, and rotating 90° peel fixtures. Typical grips available consist of wedge grips, pneumatic grips, and elastomeric grips. There are variations of each of these items.

The laboratory is also equipped with a servo-hydraulic Interlaken test machine, a dynamic version of the Instron machines. It has a 22-Kip load frame capable of testing and measuring data in the range of $\pm 11,000$ pounds, can measure strains up to 50 percent at frequencies up to 20 Hz (depending on imposed displacement), and has two load cells with ranges between 5 pounds and 11,000 pounds. The grips and fixtures used with this machine were designed to be compatible with the Instron Machines.

These instruments are used to conduct numerous tension, compression, shear, and peel tests. Some tests are performed in accordance with American Standards for Testing and Materials (ASTM) specifications and with Navy specifications. Most of the tests performed are such that no standards are exactly applicable because they deal with specialized components and assemblies. A sample configuration is dependent upon the load ranges of the instruments as well as the ability to fixture them. They provide such information as ultimate and yield tensile strengths, shear strengths, and moduli values. They can develop stress relaxation curves and are used to investigate hysteresis of various materials. They have been used to test metals and nonmetals alike, including composites, elastomers, urethanes, gels, liquids, and adhesives. Components for periscopes, towed arrays, and hull arrays for both submarines and surface ships have been successfully tested.

The Materials Analysis Laboratory is also home to some unique dynamic testing instruments. The Metravib Viscoanalyzer is a versatile tool used to develop the tensile and shear properties of viscoelastic materials as a function of temperature and frequency. It is capable of testing from 5 Hz to 1000 Hz over a temperature range of $\pm 200^{\circ}\text{C}$. The

Metravib provides such information as the Real, Imaginary and Complex (E' , E'' , E^*) components of both the tensile and shear moduli along with the loss tangent ($\tan \delta$). It also has the capability to perform dynamic viscosity measurements. This instrument can perform temperature shifts that allow the dynamic data to be extrapolated to very high frequencies. Transitions can also be approximated by the Metravib. It can be run in such a way that properties as a function of time can be monitored. Tests and results can be tailored to the specific needs of the customer. Generally, small samples are used in the Metravib, but since it is a stiffness controlled apparatus, geometry is varied to bring the sample into acceptable measurement limits.

Another dynamic test apparatus, the Dynamic Modulus Measurement System (DMMS) is also found in the Materials Analysis Laboratory. The DMMS is a resonant vibrational mode instrument that can be used to determine the dynamic Young's and shear moduli (E and G , respectively). It also measures damping properties of nonferrous materials that can be cast, drawn, or machined into the shape of a bar of circular, rectangular, or elliptical cross section.

The Materials Analysis Laboratory has a temperature chamber that covers the range of $\pm 100^\circ\text{C}$. It is used for preconditioning samples that will undergo temperature testing and also for long-

term exposure tests. An accelerated corrosion test is currently underway in this chamber.

The laboratory is equipped with a stereo microscope and photographic capabilities. This equipment is used extensively in failure analysis of Navy components. It has provided support to such programs as periscopes, towed arrays, and hull arrays. The laboratory can also perform a limited amount of metallographic preparation for microscopic examination.

Hardness measurements for both metals and polymers can be made within this facility. A New Age Hardness Tester with Rockwell ranges of C, D, A, G, B, and F is used for metals. Polymer hardness measurements are made using either a Shore A (soft) or Shore D (hard) Durometer. These measurements can be used to evaluate and verify material stiffness, treatments, and mechanical properties.

Corrosion evaluation is conducted in a pair of tanks with artificial seawater. Air is pumped into the tanks to prevent stagnation. The tanks are used to monitor the long-term effects of an ocean environment on various submarine and surface ship components.

The Materials Analysis Laboratory works closely with other NUWC facilities, including Code 2131 Chemistry Laboratory, the Pressure Laboratory, the Vibration Laboratory, and the Machine Shop.

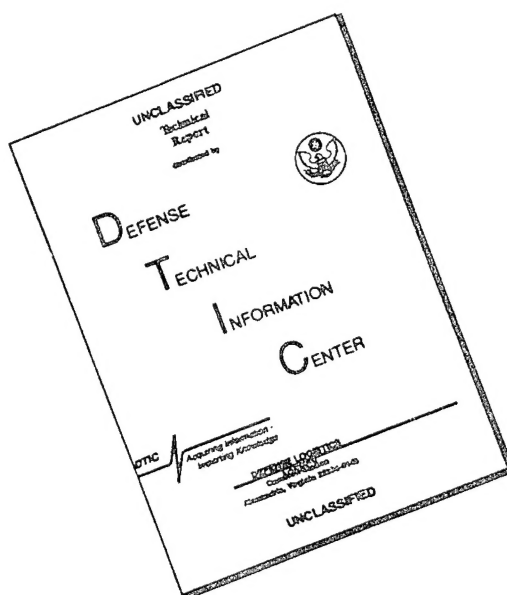
Point of Contact:



Robert A. Lafreniere
Naval Undersea Warfare Center
New London Detachment
New London, CT 06320
(203) 440-4221
FAX (203) 440-5383

Robert Lafreniere is a research mechanical engineer in the Mechanical Engineering Division at NUWC Division Newport. Since joining NUWC in 1985, he has been working in the area of static, modal, and dynamic analysis of structures using finite element methods; micro and macro analysis of composite structures; materials behavior; and numerical analysis. Dr. Lafreniere earned degrees in Mechanical Engineering, a B.S. from Rutgers University and M. S. from the University of Connecticut, and a Ph.D. in Applied Mechanics from the University of Connecticut.

DISCLAIMER NOTICE



THIS DOCUMENT IS BEST QUALITY AVAILABLE. THE COPY FURNISHED TO DTIC CONTAINED A SIGNIFICANT NUMBER OF PAGES WHICH DO NOT REPRODUCE LEGIBLY.